Modelling and Simulation of Solidification of High Grade Steel Ingot Castings

Dissertation zur Erlangung des Grades
"Doktor der montanistischen Wissenschaften"

vorgelegt von

Dipl.-Math.-Ing. Anton Ishmurzin

am Lehrstuhl für
"Modellierung und Simulation metallurgischer Prozesse"
Department Metallurgie
Montanuniversität Leoben

Leoben, Dezember 2009

Gutachter: O.Univ.-Prof. Dr.rer.nat. Andreas Ludwig
Ao.Univ.-Prof. Dr.rer.nat. Clemens Brand

Eidesstattliche Erklärung

Ich erkläre an Eides statt, dass ich diese Arbeit selbständig verfasst, andere als die angegebenen Quellen und Hilfsmittel nicht benutzt und mich auch sonst keiner unerlaubten Hilfsmittel bedient habe.

Abstract

In the work presented an approach to simulate ingot solidification of highly alloyed steels was developed. It includes simplified simulation of initial mould filling with the melt, followed by a subsequent simulation of the solidification course within the framework of multiphase multicomponent computational fluid dynamics.

The multiphase multicomponent solidification model was developed, based on the previous models for binary alloys. In order to allow the multicomponent capability, the governing multiphase flow equations were reconsidered, that include equations describing conservation of mass, momentum, energy as well as alloying components (species) and grain density transport. Source terms for the equations were reformulated to reflect multicomponent kinetic and thermodynamic relations.

An approach to couple multicomponent/multiphase thermodynamics and kinetics with multiphase/multicomponent flow model was developed. It has a form of a nonlinear algebraic equation system, relating temperature and composition of the bulk melt with solid and liquid compositions at the interface at the solid–liquid phase interface. A Newton-type iterative method was used for solving the equation system.

The coupling approach was validated using alloys from Fe–C–Cr, Fe–C–Mn and Cu–Sn–P systems. The necessary thermodynamic functions, the liquidus temperature and tie-line relations were approximated as piecewise-linear as well as interpolated using bivariate splines.

The implementation of the model for ternary alloys was used for carrying out simulations of solidification of Fe–C–Cr alloys in two different ingot geometries taking into account two- and three-phase flow. The thermal convection was found to be the predominant effect influencing the course of solidification, solutal convection did not influence the solidification significantly.

The modelling and simulation methods of multiphase multicomponent alloy solidification presented can be used for simulation of a wide range of multicomponent solidification processes.

Abstract

In der vorliegenden Arbeit wurde eine Methode entwickelt, Kokillenerstarrung hochlegierter Stähle zu simulieren. Die Arbeit beinhaltet eine vereinfachte Simulation anfänglicher Formfüllung mit der Schmelze, und weiters eine Simulation des Erstarrungsverlaufs im Rahmen von rechenbetonter Mehrphasen- und Mehrkomponenten- Fluiddynamik. Das Mehrphasen-Mehrkomponenten-Erstarrungsmodell wurde auf Grundlage vorangehender Modelle für binäre Legierungen entwickelt. Um die Mehrkomponentenfähigkeit zu ermöglichen, wurden die herrschenden Mehrphasengleichungen, einschließlich der Gleichungen die die Erhaltung von Masse, Impuls und Energie sowie Legierungsbestandteile (Legierungselemente) und Korndichtentransport beschreiben, erörtert. Quellterme für die Gleichungen wurden neu dargelegt, um die mehrkomponentenkinetischen und thermodynamischen Verhältnisse widerzuspiegeln. Eine Methode, Mehrkomponenten-/Mehrphasenthermodynamik und -kinetik mit einem Mehrphasen-/Mehrkomponentenströmungsmodell zu koppeln, wurde entwickelt. Diese Methode besitzt die Form eines nicht linearen algebraischen Gleichungssystems, und bringt Temperatur und Beschaffenheit der Schmelze in Verbindung mit den Zusammensetzungen der jeweiligen Phasen an der Schnittstelle der Feststoff- Flüssigkeit-Phase. Eine Newton'sche iterative Methode wurde benutzt, um das Gleichungssystem zu lösen. Die Kopplungsmethode wurde mittels Legierungen von Fe-C-Cr, Fe- C-Mn und Cu-Sn-P Systemen bestätigt. Die erforderlichen thermodynamischen Funktionen, die Liquidustemperatur und die Konodenverhältnisse wurden als stückweise-linear eingeschätzt sowie mittels bivariaten Splines interpoliert. Das Modell wurde für Dreistofflegierungen implementiert und für die Ausführung von Erstarrungssimulationen von Fe-C-Cr Legierungen in zwei verschiedenen Kokillengeometrien unter Berücksichtigung der Zweiphasen- und Dreiphasenströmung eingesetzt. Es stellte sich heraus, dass die Wärmekonvektion den größten Einfluss auf den Erstarrungsverlauf ausübte: solutale Konvektion nahm keinen bedeutenden Einfluss auf die Erstarrung. Die vorgelegten Modellierungs- und Simulierungsmethoden für Mehrphasen- Mehrkomponenten-Legierungserstarrung können zur Simulation einer großen Vielfalt von Mehrkomponentenerstarrungsprozessen angewendet werden.

Acknowledgements

First of all the author would like to express gratitude to the Austrian Christian Doppler research society and Böhler Edelstahl GmbH & Co KG for their support of this work. Special thanks to Prof. Andreas Ludwig, who made this dissertation work possible and for his excellent supervision, support and invaluable discussions; Prof. Clemens Brand for his invaluable insights, suggestions and comments; Dr. Menghuai Wu, Dr. László Könözsy, Dr. Wolfgang Schützenhöfer, Dipl.-Ing. Robert Tanzer for their outstanding scientific cooperation; Dr. Sven Eck, Dr. Autumn Fjeld, Dr. Abdellah Kharicha, Dr. Monika Grasser, Dipl.-Ing. Florian Mayer, Dipl.-Chem. Mihaela Stefane Kharicha, Dr. Claudia Pfeiler, Dipl.-Ing. Günter Unterreiter, Dipl.-Ing. Johann Mogeritsch and Georg Nunner for being great colleagues in daily work and discussions; computer system administrators Klaus Otto, Jasmin Grasenegger and Sabine Kerschbäumer for providing the excellent technical support; secretary Jennifer Dorner for her kind and patient assistance in everyday work and organisational activity. Also, I would like to thank Dipl.-Chem. Stefan Kleditsch of FLUENT-ANSYS Inc. for his technical and other support and assistance.

Last, but not the least, I would like to express my warmest love and many thanks to my family for their love and emotional support as well as my girlfriend Helen for her patience and kindest support during these years.

Contents

List of Figures

List of Tables

Chapter 1

Introduction

All of metallurgical production chains include the intrinsic step of solidification. During its course, as temperature decreases, the growth of the dendrites and equiaxed grains happens, driven by the undercooling. Due to different reasons (solute rejection, shrinkage, different flow phenomena) initially uniform macroscale distributions of alloying elements become non-uniform, macrosegregation appears. The interplay of different microscale, mesoscale and macroscale factors affects these processes. Increasing the knowledge of phenomena taking place during solidification is of utter importance for finding ways for improving the quality of the end product, which directly depends on the macrosegregation and primary microstructure at the end of solidification.

The negative effect of uneven distribution of alloying elements were known for several centuries, for example in the 1850s american railroad engineers knew that "steel too high in carbon or phosphorous might be brittle" |Aldrich99|. Nowadays these negative effects have been studied thoroughly. For instance in |Lesoult05| we can find the following:

> Several examples are available in the literature of detrimental effects of macrosegregation in steel continuous casting (CC) slabs. Sheets and plates for pipeline or pressurised vessels are more or less sensitive to "hydrogen induced cracking" (HIC). This type of cracking is observed in regions segregated in Mn and P |Nakai79|. Weldability, impact strength, and toughness of large diameter steel pipe can also

be affected by local segregations that are inherited from solidification |Devillers88|.

(...)

The production of large steel ingots with improved structural and chemical homogeneity is of great concern for steelmakers. Indeed final properties of forgings can be strongly affected by metallurgical structures, segregations, and defects of as-cast ingots |Blondeau91|. Fig. 4 (Fig. 1.1 in this work) illustrates the different types of segregation in a steel ingot of 65 t the nominal carbon content of which is 0.22 wt.%. It shows also the schematic pattern of grain structure: columnar zone near the surface, globular equiaxed grains in the centre from the bottom up to 75% of the total height, and dendritic equiaxed grains on the top of the ingot. The columnar zone has a homogeneous chemical composition, which differs little from the nominal analysis. The carbon content at the bottom of the ingot is less than the nominal one. This region is called the "negative segregation cone". It occupies more than 50% of the height in the centre of the ingot, like the globular equiaxed zone. The top of the ingot corresponds to an intense positive segregation. Onto this major segregation are superimposed mesosegregations. "A" segregations pointing towards the top of the casting are located near the boundary between globular and dendritic equiaxed grains. "V" segregations are visible in the central part of the globular equiaxed zone.

The intrinsic conditions of a solidification process such as high temperatures and pressures as well as the amount of hard material to process (in certain cases up to 20-50 ton of hard highly alloyed steel in case of ingot casting) after solidification to prepare samples for further investigations such as etching or chemical analysis makes experimental investigation of the solidification processes very expensive. Moreover, certain phenomena such as primary solidification and further solid state phase changes cannot be observed in place on the industrial scale, due to prohibitive properties of the casting processes mentioned above.

This is why employing the methodology of mathematical modelling is of utmost importance, providing a relatively cheap and reliable alternative to expen-

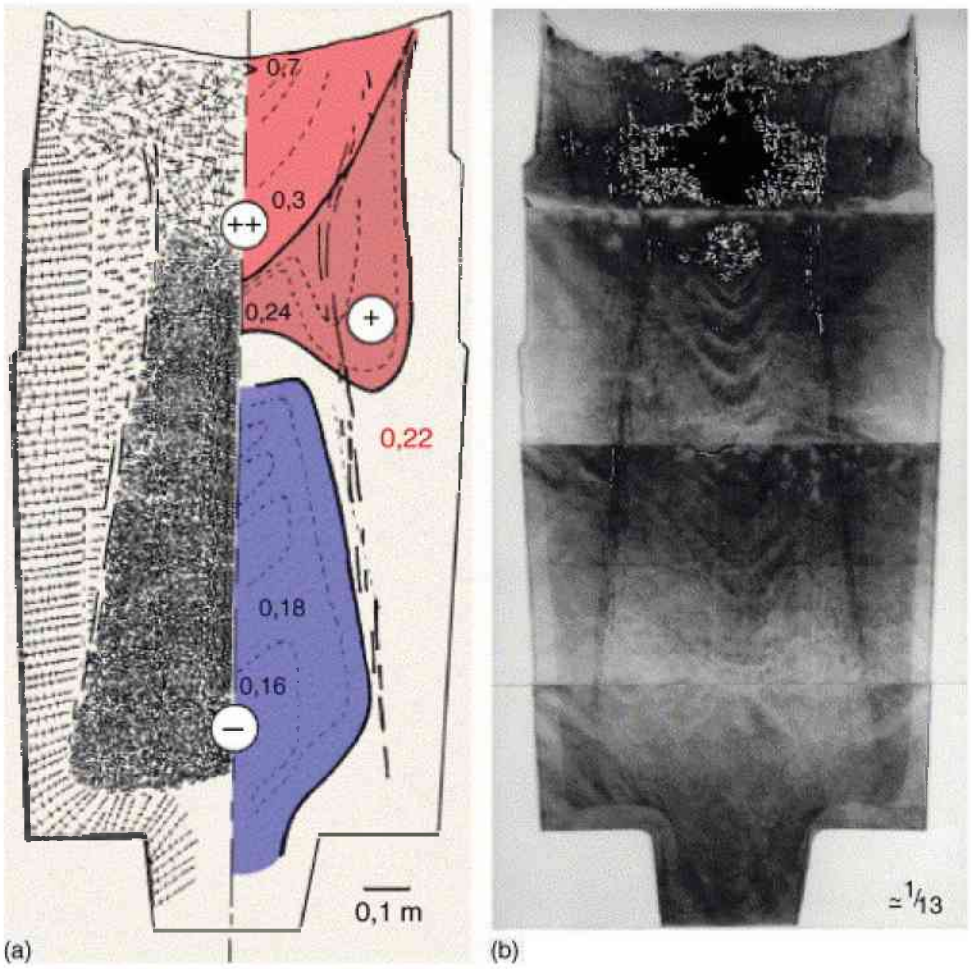

Figure 1.1: Longitudinal section of a 65 t steel ingot: (a) macrostructure and carbon macrosegregation; (b) sulphur print. Taken from |Lesoult05|.

sive experimental investigations as well as the possibility to study the solidification phenomena using mathematical models in dynamics, as they occur at high temperatures, as opposed to a posteriori investigations of casted ingots at room temperature. Indeed, the best results in understanding solidification are only possible to achieve by combining both experimental investigations and simulations.

According to |Lesoult05|,

> Most of the empirical knowledge on steel ingots was built early in the last century |Hultgren29|, |Gray56|, |Roques60| and |Kohn67|. The cost in time and money of full-scale trials was then an effective driving force for developing the first theoretical models of the formation of segregations in ingots, by Hultgren |Hultgren73|, Oeters and co-workers |Ebneth74|, Chuang and Schwerdtfeger |Chuang75|, den Hartog et al. |denHartog75|, Flemings |Flemings76|, and Fredriksson and Nilsson |Fredriksson78| for instance. The first numerical models of macrosegregation came soon after |Ohnaka86|.

One of the most promising ways to model solidification phenomena is to employ the multiphase fluid dynamics framework. A good survey on the multiphase flow dynamics development is given in |Kolev02|. Numerous research of different metallurgical processes involving metallurgical flows and solidification employing methods of multiphase fluid dynamics has been done for example in continuous casting of steels |Thomas90, Thomas94, Yuji99, Hardin99, Zhang00, Thomas01, Yu02, Javurek05, Pfeiler05, Yuan05, Mayer07|, direct-chill casting of bronze |Ludwig06a, Gruber-Pretzler06, Gruber-Pretzler07b| and casting of other alloys, for example hypermonotectic ones |Ludwig06b, Gruber-Pretzler07a|, direct-chill casting of aluminium alloys |Du07, Nadella08, Reddy97, Rousset95, Vreeman00b, Vreeman00a|, and other areas.

In this work, the Eulerian multiphase fluid dynamics framework was chosen to model the ingot casting solidification process. The solidifying melt is modelled as multiphase multicomponent Newtonian fluid consisting of interpenetrating continua (representing liquid, columnar and equiaxed phases) which flow mechanics described by governing partial differential equations of multiphase flow including modelled source terms. The governing system of equations consists of the partial differential equations expressing the conservation of mass, momentum, energy,

solute components and equiaxed number density on the macroscale. A number of multiphase models for solidification based on the volume averaging approach, that consider different phases (liquid, solid equiaxed and/or columnar phases) as spatially coupled and interpenetrating continua |Beckermann88, Beckermann93, Beckermann97, Ni91, Ludwig02, Ludwig05a, Wu06, Wu07| have been developed.

In order to connect the description of the multiphase flow phenomena at macroscale with solidification and thermodynamic phenomena happening at the mesoscale, it is necessary to take into account the closure relations on the liquid–solid interfacial scale (mesoscale), describing the relations between the far-field macroscale mass fractions of solute components and their concentrations at the interface between the solidifying dendrite or grain and the melt surrounding it (also called the solid–liquid interface). These relations define mass and solute transfer between the phases due to solidification. In order to describe these closure relations in thermodynamically consistent way, access to the thermodynamic data during solidification simulation is required.

Most of the previous work was done for binary systems. A few trials were performed on multicomponent systems using simplified thermodynamics and also online coupling with thermodynamic software, both for Eulerian models |Bennon87, Felicelli98, Du07, Han07, Ganguly07| and other models like cellular automata – finite difference methods (CAFD) |Lee04, Thuinet06, Lee07|, Lagrangian models |Appolaire08|. Linearised phase diagrams with constant liquidus slope and constant partitioning coefficients are usually used |Schneider95c, Schneider95b, Ciobanas07a, Ciobanas07b|. For the case of ternary alloys, see for example |DuPont06|.

At the same time great progress has been achieved in the field of computational thermodynamics |Sundman85, Andersson02|. Using the so-called CALPHAD method |Sundman85, Andersson02| and programming interfaces to access the thermodynamic data provided |Chen05|, it is possible to predict phase evolutions and solidification paths taking into account effects of cooling rate, back diffusion, and coarsening |Kraft97, Jie05, Larouche07|. Those methods, however, are limited to cases of small specimen solidifying under given conditions. Combeau and co-workers proposed a micro—macro segregation model |Combeau96, Doré00, Thuinet04|, in which an 'open specimen', corresponding to

the volume element in a larger system, was considered. The overall solute in the volume element is allowed to exchange with the neighbouring elements. Hence, the access to thermodynamic data is given through the so-called mapping files.

The work presented deals with modelling and simulation of solidification processes taking place in a solidifying ingot of highly alloyed steels, using multiphase fluid dynamics and computational fluid dynamics, based on previous research [Ludwig02, Ludwig05b].

This work addresses the following major questions that were not addressed in the literature/previous research done in this field:

- derivation of the closure laws connecting macroscopic Eulerian multiphase model with multicomponent alloy thermodynamics and kinetics, which result in an nonlinear system of equations coupling macroscale quantities (temperature and bulk melt composition) with mesoscale ones (mass fractions of alloying components in solid and liquid phases at the solid–liquid phase interface) and analysis of the resulting nonlinear system of equations

- formulation of thermodynamics and kinetic relations for multicomponent alloys based on Gibbs phase rule for primary and peritectic solidification and generalising binary solidification growth kinetic relations for columnar and equiaxed morphologies

- address the problem of intrinsic discontinuity of solubilities of the solute components (for instance, solubility of carbon changes with a jump from ferrite to austenite in the Fe–C system) by using spline interpolations of the tabulated solubility functions, thus employing thermodynamic data which are much closer to the reality than the idea of linearising liquidus surfaces and/or linear solubilities used by many authors.

Addressing the major questions mentioned, several auxiliary problems were successfully solved:

- analysis of the coupling system of nonlinear equations, numerical implementation of the Newton-type solver for solving it

- development of the method of constructing piecewise-linear approximations of thermodynamic functions for different steels necessary for simplified cou-

pling between macroscale and mesoscale quantities and its numerical implementation

- development of a method to represent the intrinsically discontinuous solubilities of solute elements in the solid phases using spline interpolations and its numerical implementation

- performing validations of both piecewise-linear and spline representations of phase diagrams by comparing the results produced by these models with Thermo-Calc–Scheil model results

The model developed and implemented was used for performing simulations of alloyed steel ingot solidification of different sizes and compositions to study different effects influencing the course of solidification and final distributions of alloying elements as well as the primary macrostructure development.

In spite of the fact that this work is focused on modelling and simulation of solidification in ingot casting, the methods developed can be used for simulating other solidification processes, for example direct-chill casting of a tin bronze [Gruber-Pretzler08, Ishmurzin08].

A note on the temperature units: all temperatures in the work are given in degrees Kelvin if not stated otherwise.

Chapter 2

Solidification model description

Note on scales

In order to simplify the following discussion, let us consider three length scales: microscale, mesoscale and macroscale. Table 2.1 shows typical objects as well as approximate dimension ranges, relevant objects and quantities of these scales.

2.1 Eulerian multiphase solidification model

For the general discussion of different models of multiphase flows see, for example, |Kolev02| or |Brennen05|.

As modelling framework for our studies we have chosen the Eulerian multiphase model with exchange terms appropriately modified to model solidification kinetics as developed first for globular equiaxed solidification |Ludwig02| and then extended to the three phase case taking columnar-to-equiaxed transition into account |Ludwig05b|. The model is three-dimensional, incorporating three phases: liquid, columnar and equiaxed, as in the aforementioned literature.

Below we introduce the governing equations of this model, as well as the necessary closure assumptions and relations.

Further, we will restrict the discussion to a ternary case for the sake of simplicity. The derivation of governing equations for an arbitrary number of components is straightforward.

scale	typical objects	dimensions (m)	relevant objects and quantities
micro	atom, group of atoms	$10^{-10} \ldots 10^{-7}$ m	solid–liquid interface
meso	crystallite, group of crystallites	$10^{-6} \ldots 10^{-3}$ m	element concentrations in/adjacent to a crystalline
macro	ingots, castings	$10^{-2} \ldots 10^{-1}$ m	bulk mass fractions of elements

Table 2.1: Different scales, their typical objects, dimensions and corresponding quantities and relevant objects.

2.1.1 Governing equations

Continuity equations

Conservation of mass of three phase flow is expressed with the following equations

$$\frac{\partial}{\partial t}(f_l \rho_l) + \nabla \cdot (f_l \rho_l \vec{u}_l) = -(M_{le} + M_{lc}), \tag{2.1}$$

$$\frac{\partial}{\partial t}(f_e \rho_e) + \nabla \cdot (f_e \rho_e \vec{u}_e) = M_{le}, \tag{2.2}$$

$$\frac{\partial}{\partial t}(f_c \rho_c) + \nabla \cdot (f_c \rho_c \vec{u}_c) = M_{lc}. \tag{2.3}$$

Here f_l, f_c and f_e are volume phase fractions of liquid, columnar and equiaxed phases; ρ_l, ρ_c and ρ_e are densities of the liquid, columnar and equiaxed phase respectively; $\vec{u}_l$, $\vec{u}_c$ and $\vec{u}_e$ are velocities of the phases, M_{lc} and M_{le} are mass transfer rates from the liquid phase to the columnar phase and from the liquid phase to the equiaxed phase. Another possible mass transfer rate M_{ce} characterises *fragmentation*, which happens when a columnar dendrite breaks up and thus forms equiaxed crystallites. Fragmentation is considered to be a minor effect and it is thus neglected, so $M_{ce} = 0$. For the mass transfer rates the following

holds:

$$M_{cl} = -M_{lc}, \tag{2.4}$$

$$M_{el} = -M_{le}. \tag{2.5}$$

A mass transfer rate from one phase to another consists of two parts, one representing the mass transfer due to phase change and the second due to diffusion:

$$M_{ji} = M_{ji}^{(p)} + M_{ji}^{(d)}. \tag{2.6}$$

The mass transfer rate due to diffusion is neglected, that is $M_{ji}^{(d)} = 0$, so

$$M_{ji} = M_{ji}^{(p)}. \tag{2.7}$$

Derivation of the mass transfer rate (2.7) is given later in Section 2.1.3 on page 17.

Momentum conservation equations

The conservation of momentum in liquid and equiaxed phases are governed with the following equations:

$$\begin{aligned} \frac{\partial}{\partial t}\left(f_l \rho_l \vec{u}_l\right) + \nabla \cdot \left(f_l \rho_l \vec{u}_l \vec{u}_l\right) &= -f_l \nabla p + \Delta(\mu_l f_l \vec{u}_l) \\ &\quad + \frac{1}{3}\nabla(\nabla \cdot \mu_l f_l \vec{u}_l) \\ &\quad + f_l \rho_{l,\mathrm{ref}} \left(1 - \beta_T (T_l - T_{\mathrm{ref}}) - \sum_{i=1}^{N} \beta_c^i (c_l^i - c_{\mathrm{ref}}^i)\right) \vec{g} \\ &\quad - (M_{le} + M_{lc})\vec{u}_l - K_{le}(\vec{u}_l - \vec{u}_e) - K_{lc}(\vec{u}_l - \vec{u}_c), \end{aligned} \tag{2.8}$$

$$\begin{aligned}\frac{\partial}{\partial t}\left(f_e\rho_e\vec{u}_e\right)+\nabla\cdot\left(f_e\rho_e\vec{u}_e\vec{u}_e\right) &= -f_e\nabla p+\Delta(\mu_e f_e\vec{u}_e) \\ &+\frac{1}{3}\nabla(\nabla\cdot\mu_e f_e\vec{u}_e) \\ &+f_e\rho_e\vec{g} \\ &+\vec{u}_l M_{le}+K_{le}(\vec{u}_l-\vec{u}_e)-K_{ec}(\vec{u}_e-\vec{u}_c),\end{aligned} \tag{2.9}$$

where p is the pressure, which is shared between the phases, μ_l and μ_e are the dynamic viscosities of the liquid and the equiaxed phases. The viscosity of the equiaxed phase is calculated using the following expression |Wu03|:

$$\mu_e=\begin{cases}\frac{\mu_l}{f_e}\left(\left(1-\frac{f_e}{f_e^{\text{limit}}}\right)^{-2.5f_c^{\text{limit}}}-(1-f_e)\right) & \text{when } f_e<f_e^{\text{limit}} \\ \infty & \text{else}\end{cases} \tag{2.10}$$

The Boussinesq approach is used to model both thermal and solutal convection. Parameters of the Boussinesq source terms include: $\rho_{l,\text{ref}}$ – the reference density of the liquid phase; β_T – the thermal expansion coefficient; T_{ref} – the reference temperature at which the density of the liquid is equal to $\rho_{l,\text{ref}}$; β_c^i, $i=1,\ldots,N$ – the solutal expansion coefficients (here N is the number of components in the melt) and c_{ref}^i, $i=1,\ldots,N$ – reference component mass fractions, at which the density of the liquid is equal to $\rho_{l,\text{ref}}$. Vector $\vec{g}$ is the gravitational acceleration vector. Drag is modelled using the following parameters: K_{le} – the drag coefficient that characterises drag force between the liquid and the equiaxed phases, K_{lc} – drag coefficient characterising the drag force between the liquid and the columnar phases and K_{ec} – drag coefficient for the drag force between the equiaxed and the columnar phases. The drag coefficient K_{le} is derived in |Wu03| and it is a combination of the Kozeny-Carman model for small equiaxed volume fractions and Blake-Kozeny for equiaxed volume fractions beyond the packing limit of 0.637 |Wu03|. Details of these drag models can be found in |Ludwig02, Bird60, Wang03|.

Energy conservation equations

Energy conservation for the liquid, columnar and equiaxed phases is governed by the following three energy conservation equations, formulated for enthalpies:

$$\begin{aligned} \frac{\partial}{\partial t}(f_l\rho_l h_l) + \nabla\cdot(f_l\rho_l h_l\vec{u}_l) &= \nabla\cdot(f_l k_l \nabla T_l) \\ &\quad + h_l(M_{el} + M_{cl}) \\ &\quad + H^*((T_e - T_l) + (T_c - T_l)) \end{aligned} \tag{2.11}$$

$$\begin{aligned} \frac{\partial}{\partial t}(f_c\rho_c h_c) + \nabla\cdot(f_c\rho_c h_c\vec{u}_c) &= \nabla\cdot(f_c k_c \nabla T_c) \\ &\quad + h_c M_{lc} \\ &\quad + H^*((T_l - T_c) + (T_e - T_c)) \end{aligned} \tag{2.12}$$

$$\begin{aligned} \frac{\partial}{\partial t}(f_e\rho_e h_e) + \nabla\cdot(f_e\rho_e h_e\vec{u}_e) &= \nabla\cdot(f_e k_e \nabla T_e) \\ &\quad + h_e M_{le} \\ &\quad + H^*((T_l - T_e) + (T_c - T_e)). \end{aligned} \tag{2.13}$$

Here h_l, h_e and h_c are the enthalpies of the liquid, equiaxed and columnar phases respectively, k_l, k_c and k_e are their thermal conductivities and H^* is the volumetric heat transfer coefficient between the three phases. The enthalpies are defined as follows:

$$h_l = \int_{T_{\text{ref}}}^{T} c_{p(l)}dT + h_l^{\text{ref}}, \tag{2.14}$$

$$h_e = \int_{T_{\text{ref}}}^{T} c_{p(s)}dT + h_e^{\text{ref}}, \tag{2.15}$$

$$h_c = \int_{T_{\text{ref}}}^{T} c_{p(s)} dT + h_c^{\text{ref}}, \tag{2.16}$$

where h_l^{ref}, h_c^{ref} and h_e^{ref} are the standard state enthalpies for the liquid, columnar and equiaxed phases respectively, T_{ref} is the standard state temperature; $c_{p(l)}$ is the heat capacity of the liquid phase, $c_{p(s)}$ is the heat capacity of the solid phase, that is of both columnar and equiaxed phase. Note that although the columnar and the equiaxed phase movements are described by different equations, they consist of the same matter. Thermodynamically there is no distinction between the columnar and the equiaxed phases. On the other hand, from the fluid dynamics point of view they are different, because their flow dynamics are different (for example the equiaxed phase is allowed to move, whereas the columnar phase is always at rest.)

Species transport equations

Species transport in the liquid, columnar and equiaxed phases is governed by the following equations:

$$\frac{\partial}{\partial t}\left(f_l \rho_l c_l^i\right) + \nabla \cdot \left(f_l \rho_l c_l^i \vec{u}_l\right) = -\tilde{c}_e^i M_{le} - \tilde{c}_c^i M_{lc} \tag{2.17}$$

$$\frac{\partial}{\partial t}\left(f_c \rho_c c_c^i\right) + \nabla \cdot \left(f_c \rho_c c_c^i \vec{u}_c\right) = \tilde{c}_c^i M_{cl} \tag{2.18}$$

$$\frac{\partial}{\partial t}\left(f_e \rho_e c_e^i\right) + \nabla \cdot \left(f_e \rho_e c_e^i \vec{u}_e\right) = \tilde{c}_e^i M_{el} \tag{2.19}$$

Here, c_l^i are the bulk liquid mass fractions of $i-$th component, $i = 1, \ldots, N$ where N is the number of alloying components. In the case of $N = 1$ a binary system is considered, in case of $N = 2$ a ternary system is considered and so on. The mesoscale quantities $\tilde{c}_c^i$ and $\tilde{c}_e^i$ are mass fractions of the i-th alloying element in the columnar and in the equiaxed phase respectively at the solid–liquid interface. Thermal equilibrium is assumed at the solid–liquid phase, thus $\tilde{c}_c^i$ and $\tilde{c}_e^i$ are equilibrium solid concentrations and are provided by phase diagram

information.

In order to quantify macrosegregation, an additional quantity called mixture mass fraction is used, which is calculated as a weighted mass fraction of a component m among all of the phases

$$c^m_{\text{mix}} = \frac{\sum_{i=1}^{i=K} c^m_i \rho_i f_i}{\sum_{i=1}^{i=K} \rho_i f_i}, \tag{2.20}$$

where K is the number of phases, m is the component index.

Grain density transport and nucleation equation

In order to calculate the mass transfer rate from the liquid phase to the equiaxed phase, the transport of the grain density as well as grain nucleation have to be predicted. Grain density transport and grain nucleation are governed by the following equation incorporating the Oldfield law of nucleation |Oldfield66|:

$$\frac{\partial n}{\partial t} + \nabla \cdot (\vec{u}_e n) = \left(\frac{\partial (\Delta T)}{\partial t} + \nabla \cdot (\vec{u}_l \Delta T) \right) \frac{n_{\max}}{\Delta T_\sigma \sqrt{2\pi}} \exp\left(-\frac{1}{2} \left(\frac{\Delta T - \Delta T_N}{\Delta T_\sigma} \right)^2 \right) \tag{2.21}$$

Here n is the grain number density, $\Delta T = \tilde{T} - T_l$ is the constitutional undercooling, $\tilde{T}$ is the temperature at solid–liquid interface, ΔT_N and ΔT_σ are the mean and the standard deviation of the normal distribution of the nucleation law, $n_{\max}$ is the maximum possible equiaxed grain density.

2.1.2 Solidification growth kinetics

In order to compute the correct mass transfer rate it is necessary to know the grain or dendrite growth velocity due to solidification. Below, the derivation of the growth velocity formulae for columnar (simplified as cylinders) and equiaxed (simplified as spheres) morphologies for binary alloys is presented.

Assume a simple binary phase diagram of two elements A and B with a partitioning coefficient $k = \frac{\tilde{c}_s}{\tilde{c}_l}$, $k < 1$, $\rho_l = \text{const}$. Consider a solidifying cylinder of a radius R and let us consider a thin layer of thickness Δr around this cylinder (see the scheme in Fig. 2.1). The mass fraction of the element A in the liquid

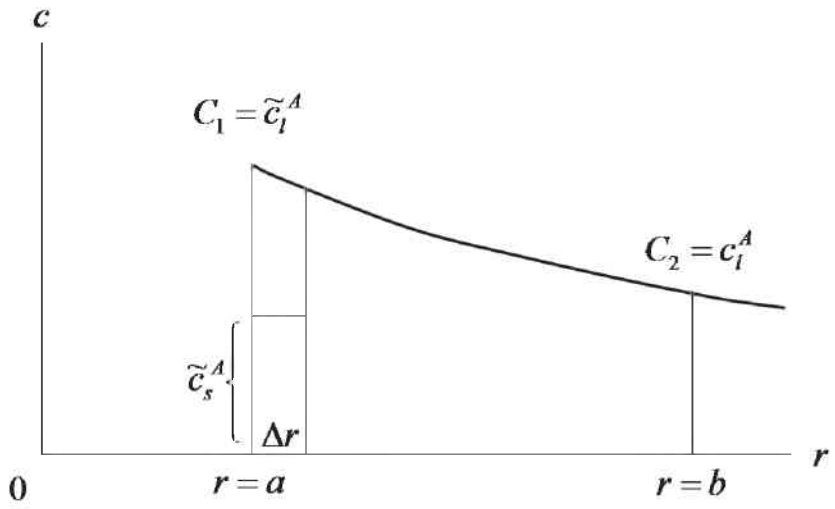

Figure 2.1: Solute redistribution around a solidifying cylinder

adjacent to the solidifying cylinder is $\tilde{c}_l^{\mathrm{A}}$ (at $r = a$). The corresponding mass fraction of the element A in the solid at the cylinder surface is $\tilde{c}_s^{\mathrm{A}}$(at $r = a$). The far-field mass fraction of the element A in the liquid is c_l^{A} and it is considered to be reached at $r = b$. The amount of the alloying component A in this Δr layer of liquid will be $\rho_l \tilde{c}_l^{\mathrm{A}} A \Delta r$ (here A is the area of the cylinder sides). Because of the partitioning coefficient being generally smaller than 1, not all of this amount of alloying component A will be incorporated into the solid: Some of it will be rejected into the liquid. The amount of the incorporated mass of alloying component A is equal to $\rho_l \tilde{c}_s^{\mathrm{A}} A \Delta r$. Now the difference between these two masses $m_{\mathrm{rej}} = (\tilde{c}_l^{\mathrm{A}} - \tilde{c}_s^{\mathrm{A}}) \rho_l A \Delta r$ is the mass of the element A that is rejected into the melt. Let us assume that the rejected mass of alloying component A is diffused within the liquid melt with the diffusion coefficient D_l^{A}. The flux of the rejected mass is thus:

$$q_{\mathrm{rej}} = (\tilde{c}_l^{\mathrm{A}} - \tilde{c}_s^{\mathrm{A}}) \rho_l \frac{\Delta r}{\Delta t}, \tag{2.22}$$

where $\frac{\Delta r}{\Delta t}$ is the velocity of the solidification front or *growth velocity* $v = \frac{\Delta r}{\Delta t}$, so

$$q_{\mathrm{rej}} = (\tilde{c}_l^{\mathrm{A}} - \tilde{c}_s^{\mathrm{A}}) \rho_l v. \tag{2.23}$$

The diffusive flux into the liquid is equal to

$$q_{\text{diff}} = -D_l^{\text{A}} \frac{\mathrm{d}c_l^{\text{A}}}{\mathrm{d}r} \rho_l \tag{2.24}$$

As we said before, the flux of rejected mass of the alloying element A must diffuse into the melt, which means that $q_{\text{diff}} = q_{\text{rej}}$. This leads to the equation expressing the solute balance:

$$(\tilde{c}_l^{\text{A}} - \tilde{c}_s^{\text{A}})\rho_l v = -D_l^{\text{A}} \frac{\mathrm{d}c_l^{\text{A}}}{\mathrm{d}r} \rho_l \tag{2.25}$$

and dividing by ρ_l we get the expression for calculating the growth velocity:

$$v = \frac{-D_l^{\text{A}} \frac{\mathrm{d}c_l^{\text{A}}}{\mathrm{d}r}}{(\tilde{c}_l^{\text{A}} - \tilde{c}_s^{\text{A}})} \tag{2.26}$$

Note that the difference between cylinder and spherical growth is only in the form of the mass fraction gradient $\frac{\mathrm{d}c_l^{\text{A}}}{\mathrm{d}r}$.

Cylindrical growth

In the case of cylindrical growth, the mass fraction gradient of the alloying component A can be estimated by assuming steady state diffusion around the growing cylinder and solving the corresponding steady diffusion equation around a cylinder:

$$\frac{\mathrm{d}}{\mathrm{d}r}\left(r D_l^{\text{A}} \frac{\mathrm{d}c}{\mathrm{d}r}\right) = 0, \; a < r < b \tag{2.27}$$

with the following boundary conditions:

$$c(r = a) = \tilde{c}_l^{\text{A}} \tag{2.28}$$

$$c(r = b) = c_l^{\text{A}} \tag{2.29}$$

The solution of this boundary value problem is (as any computer algebra system confirms):

$$c(r) = \frac{\tilde{c}_l^{\mathrm{A}} \ln(b/r) + c_l^{\mathrm{A}} \ln(r/a)}{\ln(b/a)} \tag{2.30}$$

and the mass fraction gradient:

$$\frac{\mathrm{d}c}{\mathrm{d}r} = \frac{(c_l^{\mathrm{A}} - \tilde{c}_l^{\mathrm{A}})}{r \ln(b/a)} \tag{2.31}$$

Substituting this expression for the gradient into the (2.26) and renaming $a = R$, $b = R_{\max}$ we get the expression for the growth velocity of a cylinder:

$$v_c = \frac{2D_l^{\mathrm{A}}}{d} \frac{(\tilde{c}_l^{\mathrm{A}} - c_l^{\mathrm{A}})}{(\tilde{c}_l^{\mathrm{A}} - \tilde{c}_s^{\mathrm{A}})} \ln^{-1}\left(\frac{R_{\max}}{R}\right), \tag{2.32}$$

where R is the current radius of the growing cylinder and $R_{\max}$ is the maximal radius of the cylinder and $d = R/2$ is the diameter.

Spherical growth

The derivation of the expression for the growth velocity in case of a spherical growth is similar to the derivation of the growth velocity of a cylinder (see, for example |Ludwig05a|) and so the expression for the equiaxed growth velocity becomes:

$$v_e = \frac{2D_l^{\mathrm{A}}}{d} \frac{(\tilde{c}_l^{\mathrm{A}} - c_l^{\mathrm{A}})}{(\tilde{c}_l^{\mathrm{A}} - \tilde{c}_s^{\mathrm{A}})} \tag{2.33}$$

2.1.3 Mass transfer rate computation

The volume averaged mass transfer rate from liquid phase to columnar, used in the conservation equations (1), (2) and (6), (7), can be calculated as:

$$M_{cl} = \rho_l \cdot v_c \cdot S_c \cdot A_{\mathrm{imp},c} \tag{2.34}$$

where ρ_l is the density of the liquid, v_c is the columnar growth velocity, S_c is the total surface area of all growing columnar dendrites per unit volume.

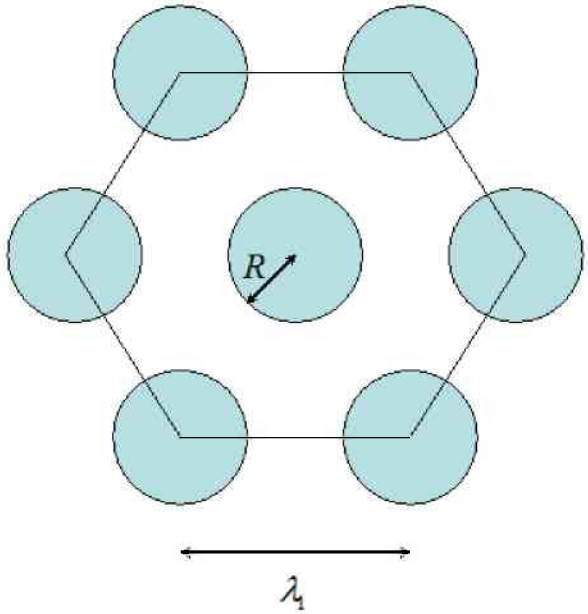

Figure 2.2: Hexagonal arrangement of columnar cylinders with a primary dendrite arm spacing λ_1 and a columnar radius $R = 0.5d_c$.

The idea of Avrami factor [Avrami40] accounting for the impingement during crystallite growth was adapted for the columnar growth case by introducing the impingement factor $A_{\text{imp},c}$. It is derived in [Mayer07] and can be expressed as:

$$A_{\text{imp},c} = \begin{cases} 1, & d_c \leq \lambda_1 \\ f_l / f_{l,\text{crit}} & d_c > \lambda_1 \end{cases} \tag{2.35}$$

where λ_1 is the primary dendrite arm spacing, and both the columnar diameter d_c and the critical liquid volume fraction $f_{l,\text{crit}}$ are calculated assuming a hexagonal arrangement of cylindrical trunks from the geometrical considerations as follows.

The columnar volume fraction is expressed as the ratio between the volume of the columnar phase and the total volume (see Fig. 2.2):

$$f_c = \frac{\frac{3}{4}\pi d_c^2}{\frac{3\sqrt{3}}{2}\lambda_1^2}. \tag{2.36}$$

Note that the height of cylinders cancels out in (2.36). From (2.36) the columnar diameter can be expressed as:

$$d_c = 2\sqrt{\frac{f_c\sqrt{3}}{2\pi}}\lambda_1 \tag{2.37}$$

Now the cylinders are in contact with each other when $d_c = \lambda_1$ and start to impinge when d_c becomes bigger than λ_1, and according to (2.37) the critical liquid fraction corresponding to the condition $d_c = \lambda_1$ is:

$$f_{l,crit} = 1 - f_{c,crit} = 1 - \frac{\pi\sqrt{3}}{6} \tag{2.38}$$

In order to find the surface concentration S_c used in (2.34), let us assume the hexagonal arrangement of columnar cylinders. Then, let us consider an elementary hexagonal cell with the primary dendrite spacing λ_1. In the two-dimensional case, the total area of the hexagonal cell is:

$$A_{\text{cell}} = \frac{3\sqrt{3}}{2}\lambda_1^2. \tag{2.39}$$

The available surface area of columnar cylinders is then (note that in two-dimensional case it is equal to the circumference of three circles with the diameter d_c):

$$s = 3\pi d_c. \tag{2.40}$$

Surface concentration is then the ratio between the total area A_{cell} and the surface s available for mass transfer:

$$S_c = \frac{s}{A_{cell}} = \frac{2\sqrt{3}\pi d_c}{3\lambda_1^2}. \tag{2.41}$$

2.2 Scheil-Gulliver solidification model

A widely used simple solidification model for binary alloys was proposed by Scheil |Scheil42| and Gulliver |Gulliver13, Gulliver22|. Its assumptions are complete

mixing (infinite diffusion) in liquid and absence of diffusion in solid. The former assumption means that the excess solute will be redistributed evenly over the entire volume of fluid. In this case, there will be an interaction with the far end of crucible during the whole solidification process. The entire solute distribution will essentially be a long terminal transient beginning at the solid concentration $c_0 k$. Here c_0 is the initial liquid mass fraction of the alloying element, and k is the solute redistribution coefficient, so that $c_s = k c_l$. This behaviour is described by the Gulliver-Scheil equation (see |Kurz98|):

$$\frac{c_l}{c_0} = \frac{1}{(1 - f_s)^{1-k}}, \tag{2.42}$$

where f_s is the solid volume fraction.

Based on this model, a special module (it will be called Thermo-Calc–Scheil module throughout this work) has been implemented in Thermo-Calc thermodynamics software package |The06a|. The Thermo-Calc User's Guide |The06a| describes this package and its algorithm as follows:

> The module can be applied to any high-order multicomponent system. A simulation is made step by step along the cooling procedure (for instance, with decreasing temperature or extracted heat), and after each step the new liquid composition is used as the "local overall" composition at the next step.
>
> The general procedure of the traditional Scheil-Gulliver model simulation can be illustrated by Fig. 2.3 (in this work) and briefly described as follows:
>
> Start with system that is on the liquidus line at temperature T_1 and overall composition x_1.
>
> The temperature condition is decreased to T_2 and the equilibrium is calculated. This gives a certain amount of solid phase(s) formed and new liquid composition x_2. The system with the overall composition equal to x_2 would be completely liquid at this temperature.
>
> The overall composition is set to x_2. This effectively means that the program "forgets" the amount of solid phase(s) formed previously, and

that the solid phase(s) will remain at the composition at which it was formed.

The simulation is continued from the Step 2, and repeated until the lowest temperature where liquid can exist (either all liquid disappear or a certain fraction of liquid remain in the system) is found.

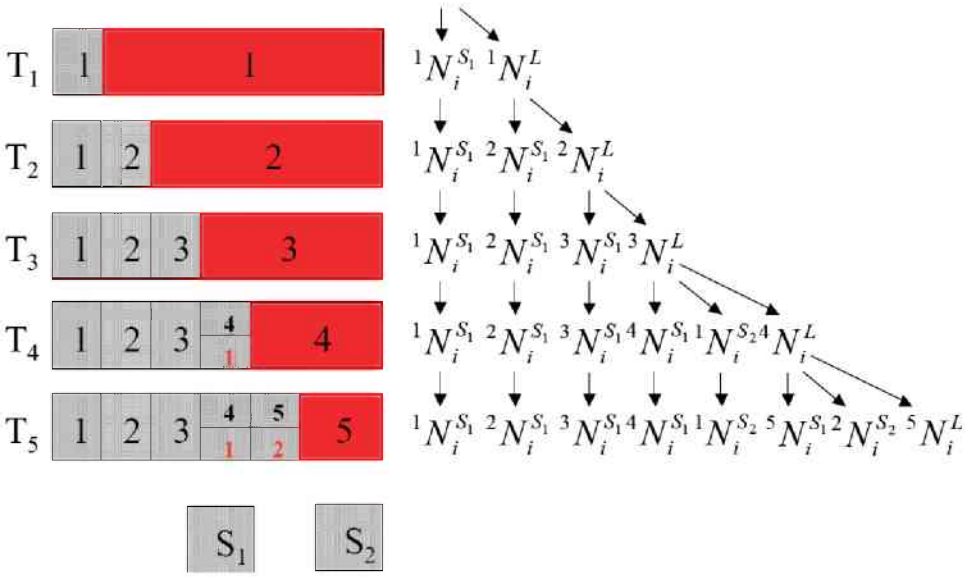

Figure 2.3: The algorithm of the traditional Scheil-Gulliver model for simulation of an alloy solidification process (taken from [The06a])

This Thermo-Calc–Scheil module will be used to validate the approximations of different phase diagrams (thermodynamic functions) described later in Section 3.5.

Chapter 3

Development of the multicomponent solidification model

3.1 Simplified zero-dimensional solidification model

In order to describe the idea of coupling between solidification kinetics, thermodynamics and the multiphase mass transfer, let us consider a simplified zero-dimensional solidification model as it is done in |Ishmurzin08|. By simplifying the multiphase solidification model described in |Ludwig05b, Wu06, Ludwig06a| we want to neglect flow phenomena (melt flow, solid phase movement, sedimentation, convection, and so on) and concentrate only on the thermodynamically consistent modelling of zero-dimensional solidification. Flow phenomena can be adequately incorporated into the model when needed as it is shown in |Ludwig05a, Ludwig07|. On the other hand, the thermodynamical part will be taken into account without simplifications.

The assumptions of the zero-dimensional model are:

- there are only two phases involved during solidification, the liquid phase, denoted by the lower index l and the solid columnar phase, denoted by the lower index c,
- the morphology of the columnar dendrite trunks is assumed to be cylindrical,
- the growth of columnar trunks is controlled by diffusion,

- local thermal equilibrium is assumed at the liquid–solid interface,
- the equilibrium concentrations of alloying elements in liquid and solid phase at the liquid—solid interface are different from the bulk concentrations,
- species transport by back diffusion in the columnar phase is ignored,
- density of the liquid phase ρ_l and of the columnar phase ρ_c are constant.

Taking into account the aforementioned model assumptions, the conservation equations were as follows. The mass conservation equations are

$$\frac{\mathrm{d}f_c}{\mathrm{d}t} = \frac{1}{\rho_c} M_{lc}, \tag{3.1}$$

$$\frac{\mathrm{d}f_l}{\mathrm{d}t} = -\frac{1}{\rho_l} M_{lc}, \tag{3.2}$$

where f_l and f_c are phase volume fractions ($f_l + f_c = 1$), ρ_c and ρ_l are the densities of the phases, and M_{lc} is the mass transfer rate from liquid to solid due to solidification. The formula (2.34) for computation of the mass transfer rate $M_{lc} = -M_{cl}$ is derived in Section 2.1.3. The way to obtain the growth velocity v for this formula in multicomponent case is discussed in the Section 3.4, the actual formula for v is (3.19) which is a multicomponent analog of the columnar growth velocity in the binary case (2.32). The species conservation equations are:

$$\frac{\mathrm{d}}{\mathrm{d}t}(f_c c_c^i) = \frac{1}{\rho_c} C_{lc}^i, \tag{3.3}$$

$$\frac{\mathrm{d}}{\mathrm{d}t}(f_l c_l^i) = -\frac{1}{\rho_l} C_{lc}^i, \tag{3.4}$$

where c_c^i is the mass fraction of the $i-$th solute component in the solid phase, and c_l^i in the liquid phase, $i = 1, \ldots, N-1$, and N is the total number of components. The species transfer rate due to solidification C_{lc}^i is defined as follows:

$$C_{lc}^i = \tilde{c}_c^i M_{lc}, \tag{3.5}$$

where $\tilde{c}_c^i$ is the equilibrium mass fraction of i-th solute component in the solid phase at the liquid–solid interface.

Substituting (3.1) and (3.5) into (3.3), and substituting (3.2) and (3.5) into (3.4), we get

$$\frac{\mathrm{d}c_c^i}{\mathrm{d}t} = -\frac{M_{lc}}{\rho_c f_c}(c_c^i - \tilde{c}_c^i), \tag{3.6}$$

$$\frac{\mathrm{d}c_l^i}{\mathrm{d}t} = \frac{M_{lc}}{\rho_l f_l}(c_l^i - \tilde{c}_c^i). \tag{3.7}$$

Here, the equilibrium mass fraction $\tilde{c}_c^i$ is the thermodynamic quantity which must be determined from thermodynamics according to the local temperature (see the definition of these functions $\tilde{c}_c^i$ for the ternary case ($i = 1, 2$) (3.16) and (3.17)).

The temperature is assumed to decrease linearly with time with constant cooling rate κ, starting with the initial temperature T_0:

$$T = T_0 - \kappa T. \tag{3.8}$$

Note that when taking flow and energy conservation into account, the temperature T is determined by means of the energy equation. Thus, Eq. (3.8) serves as a kind of a rough simplification of a more general energy conservation equation.

For simplicity let us assume a ternary alloying system Fe–C–Cr ($N = 2$ and $i = 1, 2$). In this case, the zero-dimensional solidification model takes the form of the system of three ordinary differential equations. The first equation is (3.1), and the other two are (3.7) for $i = 1, 2$ or $i = \mathrm{C}, \mathrm{Cr}$:

$$\frac{\mathrm{d}c_l^{\mathrm{C}}}{\mathrm{d}t} = -\frac{M_{lc}}{\rho_c f_c}(c_l^{\mathrm{C}} - \tilde{c}_c^{\mathrm{C}}), \tag{3.9}$$

$$\frac{\mathrm{d}c_l^{\mathrm{Cr}}}{\mathrm{d}t} = -\frac{M_{lc}}{\rho_c f_c}(c_l^{\mathrm{Cr}} - \tilde{c}_c^{\mathrm{Cr}}). \tag{3.10}$$

This ordinary differential equation system consisting of equations (3.1), (3.9) and (3.10) together with the initial conditions

$$\begin{aligned} f_c(0) &= \epsilon, \\ c_l^{\mathrm{C}}(0) &= c_{l0}^{\mathrm{C}}, \\ c_l^{\mathrm{C}}(0) &= c_{l0}^{\mathrm{Cr}} \end{aligned} \tag{3.11}$$

make up an initial value problem, which can be integrated numerically. This initial value problem, apart from the illustration of the coupling idea between the flow equations on one side, and thermodynamics and growth kinetics on the other, will be used later for evaluating piecewise-linear approximations of thermodynamic functions (3.15), (3.16) and (3.17), see Chapter 5 for details. Note that when solving (not simplified) equations describing a multiphase flow the problem of their coupling with thermodynamics and kinetics is the same: it is necessary to calculate the mass transfer rate in a correct, thermodynamically consistent way.

3.2 Multiphase/multicomponent flow models summary

Three-phase ternary solidification

The equations of the three-phase Eulerian ternary solidifying flow that will be used in simulations in Chapter 6 are:

- three mass conservation equations (2.1)-(2.3)
- two momentum conservation equations (2.8)-(2.9)
- three energy conservation equations (2.11)-(2.13)
- six alloying component transport equations (2.17)-(2.19)
- one grain density transport equation (2.21)

Two-phase ternary solidification

The equations describing two-phase Eulerian ternary solidifying flow that will be also bee used later in Chapter 6 simulations can be summarised as follows:

- two mass conservation equations (2.1) and (2.3)
- one momentum conservation equation (2.8)
- two energy conservation equations (2.11)-(2.12)
- four alloying component transport equations (2.17)-(2.18)

Mass transfer rates and ternary thermodynamics

The mass transfer rates for both three- and two-phase flows are calculated incorporating ternary phase diagram data in a thermodynamically consistent way as described in Section 3.1.

3.3 Incorporating phase diagram data

In this work our goal is to model multicomponent multiphase solidification. We do not consider any solid phase transformations. We will call the solidification process a *one-phase solidification*, if there only *one* solid phase forms from the liquid phase (for example $L \rightarrow \delta$ in Fe–C diagram, see Fig. 3.1).

Note that peritectic solidification (for example the formation of austenite, $L + \delta \rightarrow \gamma$ in Fe–C diagram) in this sense is also a one-phase solidification, since there is only one solid phase forming from the liquid.

On the other hand, eutectic solidification is not a one-phase solidification, as there are two solid phases forming from the liquid phase (for example $L \rightarrow$ γ+carbide). Only a very small percentage of liquid turns into the eutectic solid at the end of solidification for the steels in question, so the eutectic solidification is not considered here.

The main difference between the one-phase and two-phase reactions is the number of degrees of freedom f: In the case of one-phase solidification it is equal to $f = C - 1$, where C is the number of components, whereas in the case of

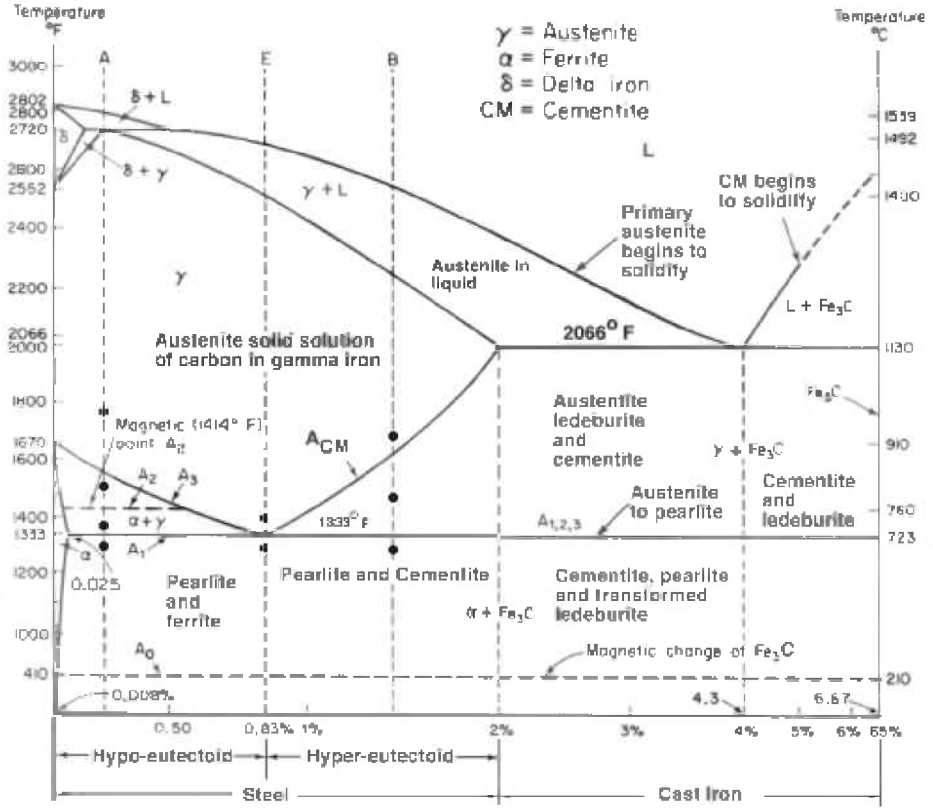

Figure 3.1: $Fe - Fe_3C$ phase diagram [Pollack88]

two-phase reaction (eutectic) one degree of freedom vanishes: $f = C - 2$, since the liquid (on the mesoscale) is in equilibrium with two solid phases in this case.

The following description will be done for the ternary case for simplicity. Alloying elements will be denoted as A and B respectively. Expanding ternary description to the $N-$component case is straightforward and is given later in the Section 8.3.

Between the liquid and a crystallite there is a thin microscopic solid–liquid interface, where solidification takes place. Because of its microscopic thickness (several atoms), we assume solid and liquid phases to be in equilibrium there. This assumption is natural, since cooling rates in ingot solidification are not high.

Thermodynamic information for real multicomponent alloying systems is provided by phase diagrams, which are available from thermodynamic software such

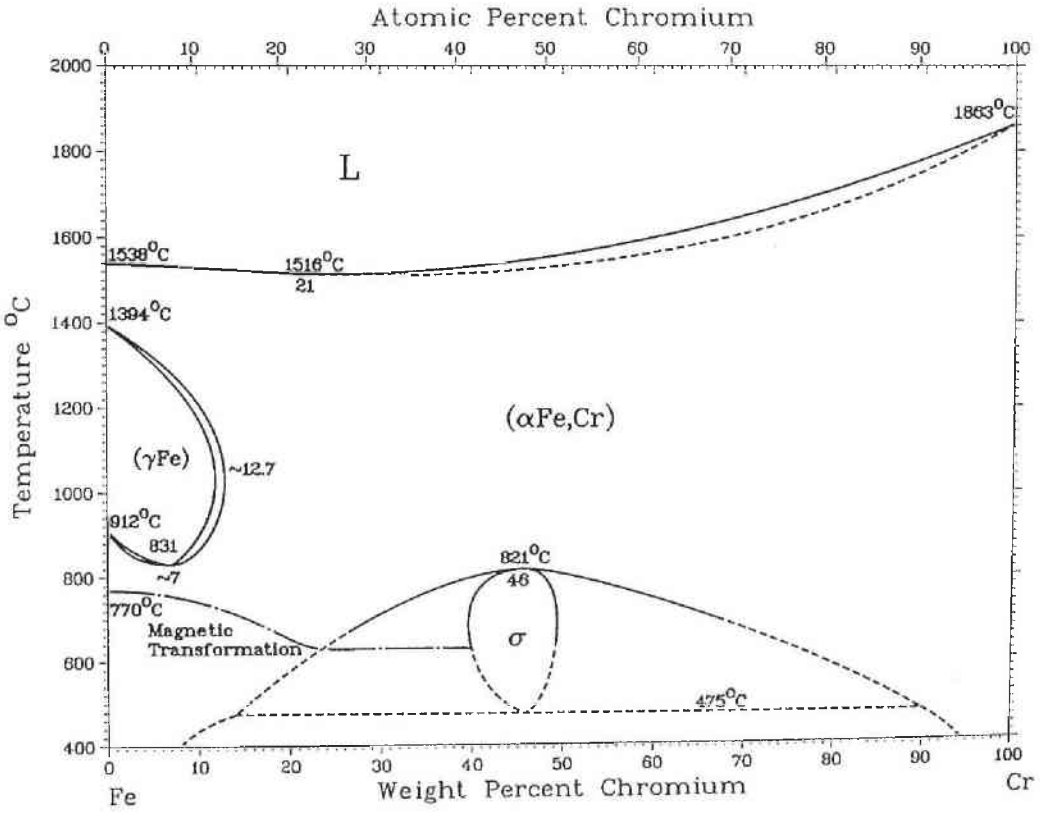

Figure 3.2: Fe – Cr phase diagram

as Thermo-Calc [The06a], ChemSage [Eriksson90], and others. The explanation of how this thermodynamical information is included into the model follows.

The following description is valid for two-phase regions (liquid and primary solid) of the phase diagram. When two phases liquid l and solid s of a three component system consisting of components A, B and C are in thermodynamic equilibrium, we can express the equilibrium condition in terms of equalities of fluxes of these three components between different phases [Steinberg89]:

$$q^s_{\mathrm{A}}(\tilde{c}^{\mathrm{A}}_l, \tilde{c}^{\mathrm{B}}_l, \tilde{T}) = q^l_{\mathrm{A}}(\tilde{c}^{\mathrm{A}}_l, \tilde{c}^{\mathrm{B}}_l, \tilde{T}) \tag{3.12}$$

$$q^s_{\mathrm{B}}(\tilde{c}^{\mathrm{A}}_l, \tilde{c}^{\mathrm{B}}_l, \tilde{T}) = q^l_{\mathrm{B}}(\tilde{c}^{\mathrm{A}}_l, \tilde{c}^{\mathrm{B}}_l, \tilde{T}) \tag{3.13}$$

$$q_{\mathrm{C}}^{s}(\tilde{c}_l^{\mathrm{A}}, \tilde{c}_l^{\mathrm{B}}, \tilde{T}) = q_{\mathrm{C}}^{l}(\tilde{c}_l^{\mathrm{A}}, \tilde{c}_l^{\mathrm{B}}, \tilde{T}) \tag{3.14}$$

where q_i^j, $i = \mathrm{A}, \mathrm{B}, \mathrm{C}$, $j = l, s$ is the number of molecules of component i leaving phase j per unit surface per unit time and $\tilde{T}$ is the equilibrium temperature. The actual form of q_i^j is of no interest for our discussion. The existence of these functional relations is important. Let us consider two thermodynamical relations known from a ternary phase diagram (and available to us by means of thermodynamical software): liquidus surface and the tie-line relation. The first, the liquidus surface, in the case of a ternary system and a two-phase region (liquid plus a forming solid phase) of the phase diagram can be written as:

$$\tilde{T} = \tilde{T}(\tilde{c}_l^{\mathrm{A}}, \tilde{c}_l^{\mathrm{B}}) \tag{3.15}$$

The second relation, the tie-line in the same conditions of two-phase region of a ternary phase diagram can be written as:

$$\tilde{c}_s^{\mathrm{A}} = \tilde{c}_s^{\mathrm{A}}(\tilde{c}_l^{\mathrm{A}}, \tilde{c}_l^{\mathrm{B}}) \tag{3.16}$$

$$\tilde{c}_s^{\mathrm{B}} = \tilde{c}_s^{\mathrm{B}}(\tilde{c}_l^{\mathrm{A}}, \tilde{c}_l^{\mathrm{B}}) \tag{3.17}$$

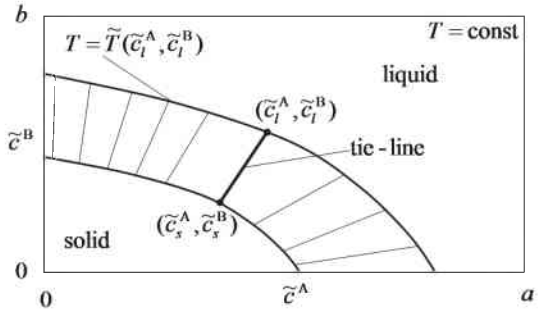

Figure 3.3: Schematic representation of a tie-line relation in a ternary phase diagram

Comparing Eq. (3.12)-(3.14) with (3.15)-(3.17) one can see that the latter three equations express the same relations as the former three, but their advantage is that they are available from thermodynamic software packages, for example |The06a, Eriksson90|.

In the work presented, an extensive use of the Fe–C–Cr phase diagram was made. In the following the way of obtaining the numerical values of these three thermodynamic functions for this alloying system is presented.

Combined experimental and computational investigations of the Fe–C–Cr phase diagram has been quite extensive, see, for example |Westgren28, Kundrat84, Lee92, Sopousek94, Kowalski94|.

The three thermodynamic functions, liquidus temperature, solubility of carbon and solubility of chromium in the solid phases forming from the liquid available from the Fe–C–Cr phase diagram information data provided by Thermo-Calc |Andersson02, Chen05, Sundman85, The06a| are shown below in Figs. 3.4-3.6. They represent the functions defined with (3.15)-(3.17) for the Fe–C–Cr system. The functions depicted are spline-interpolants of these functions, computed as described in Section 4.3.3 for the use in determination of the mass transfer rate terms as described in Section 3.4. They represent the functions defined with (3.15)-(3.17) for the Fe–C–Cr system.

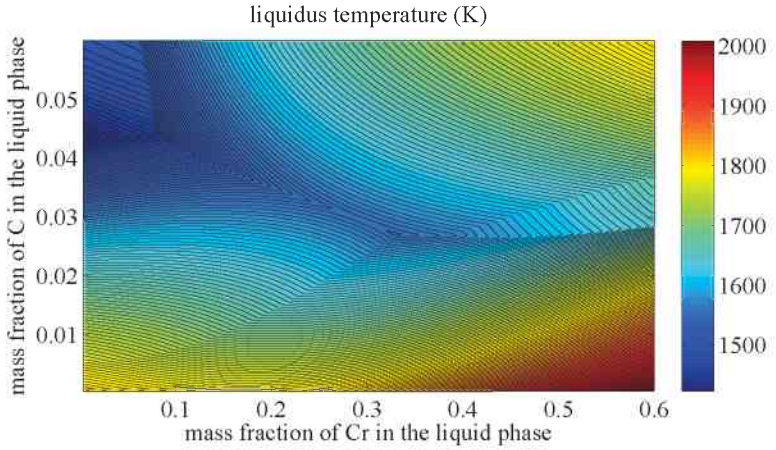

Figure 3.4: Liquidus temperature $\widetilde{T}(\tilde{c}_l^{\mathrm{C}}, \tilde{c}_l^{\mathrm{Cr}})$ in the Fe-rich corner

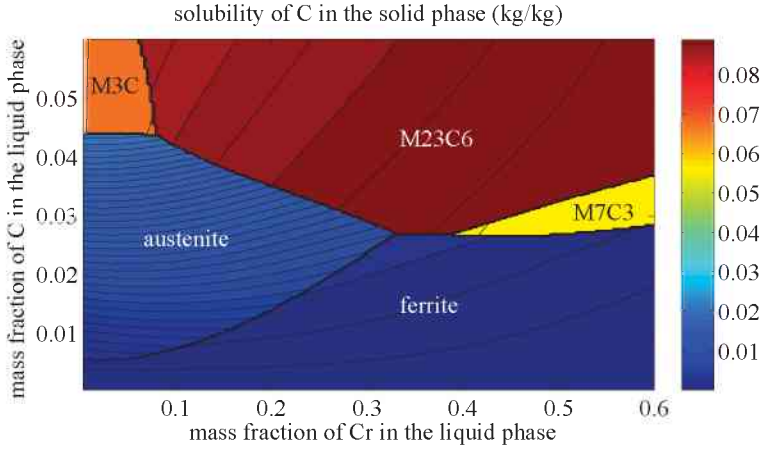

Figure 3.5: Solubility of carbon in the solid phase $\tilde{c}_s^{\mathrm{C}}\left(\tilde{c}_l^{\mathrm{C}}, \tilde{c}_l^{\mathrm{Cr}}\right)$ in the Fe-rich corner

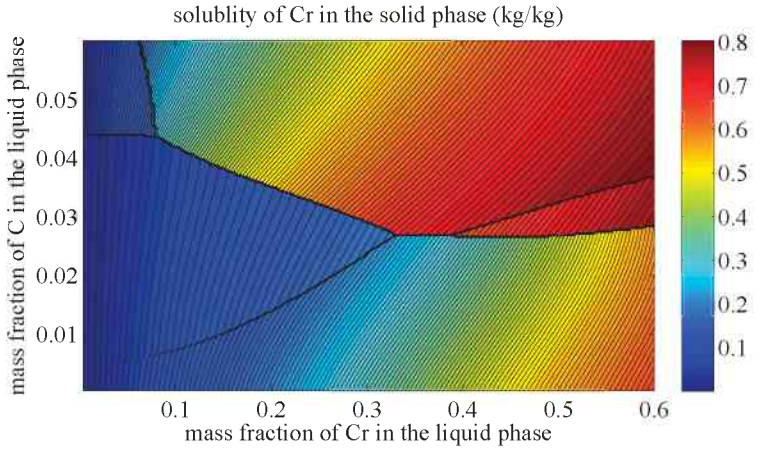

Figure 3.6: Solubility of chromium in the solid phase $\tilde{c}_s^{\mathrm{Cr}}\left(\tilde{c}_l^{\mathrm{C}}, \tilde{c}_l^{\mathrm{Cr}}\right)$ in the Fe-rich corner

For other alloying systems these functions can be acquired analogously.

3.4 Coupling between solidification thermodynamics, kinetics and Eulerian multiphase flow model

In an alloying system with N components $N-1$ expressions for the growth velocity (either columnar or equiaxed) can be written: $v^i,\ i = 1, \ldots, N-1$. Important is that all of these growth velocities are equal to each other:

$$v^1 = v^2 = \ldots = v^{N-2} = v^{N-1}, \tag{3.18}$$

since they all express the velocity of the same solidification front. Thus, in the following, when deriving quantities for the multicomponent case we will often omit the upper index, keeping in mind that the growth velocity can be calculated using any of $N-1$ components:

$$v_c = \frac{2D_l^i}{d}\frac{(\tilde{c}_l^i - c_l^i)}{(\tilde{c}_l^i - \tilde{c}_s^i)}\ln^{-1}\left(\frac{R_{\max}}{R}\right), \tag{3.19}$$

which is a multicomponent analog of the columnar growth velocity (2.32) in the binary case, $i = 1, \ldots, N-1$ is the number of the alloying component.

Further we will consider only ternary systems with two alloying elements A and B, so $i = \mathrm{A}, \mathrm{B}$.

The assumption of the thermal equilibrium at the solid–liquid phase interface can be expressed as:

$$T_l = \widetilde{T}(\tilde{c}_l^{\mathrm{A}}, \tilde{c}_l^{\mathrm{B}}) \tag{3.20}$$

Now together with the equation that expresses the equality of growth velocities calculated based on concentration distributions of both components A and B (see the Section 2.1.2 on growth kinetics)

$$D_l^{\mathrm{A}}\frac{\tilde{c}_l^{\mathrm{A}} - c_l^{\mathrm{A}}}{\tilde{c}_l^{\mathrm{A}} - \tilde{c}_s^{\mathrm{A}}} = D_l^{\mathrm{B}}\frac{\tilde{c}_l^{\mathrm{B}} - c_l^{\mathrm{B}}}{\tilde{c}_l^{\mathrm{B}} - \tilde{c}_s^{\mathrm{B}}} \tag{3.21}$$

all these four equations (3.16), (3.17), (3.20) and (3.21) make up an nonlinear equation system with the unknowns $\tilde{c}_l^{\mathrm{A}}, \tilde{c}_l^{\mathrm{B}}, \tilde{c}_s^{\mathrm{A}}, \tilde{c}_s^{\mathrm{B}}$. This system also includes the three process parameters $T_l, c_l^{\mathrm{A}}, c_l^{\mathrm{B}}$. It is possible to show using the Implicit Function Theorem known from mathematical analysis (see for example |Rudin76|)

that this equation system implicitly defines a functional dependence of unknown mesoscopic parameters $\tilde{c}_l^{\mathrm{A}}, \tilde{c}_l^{\mathrm{B}}, \tilde{c}_s^{\mathrm{A}}, \tilde{c}_s^{\mathrm{B}}$ on known macroscopic parameters $T_l, c_l^{\mathrm{A}}, c_l^{\mathrm{B}}$. The equation system can be written as

$$F(T_l, c_l^{\mathrm{A}}, c_l^{\mathrm{B}}; \tilde{c}_l^{\mathrm{A}}, \tilde{c}_l^{\mathrm{B}}, \tilde{c}_s^{\mathrm{A}}, \tilde{c}_s^{\mathrm{B}}) = \mathbf{0}, \tag{3.22}$$

where

$$F = \begin{pmatrix} \tilde{c}_s^{\mathrm{A}}(\tilde{c}_l^{\mathrm{A}}, \tilde{c}_l^{\mathrm{B}}) - \tilde{c}_s^{\mathrm{A}} \\ \tilde{c}_s^{\mathrm{B}}(\tilde{c}_l^{\mathrm{A}}, \tilde{c}_l^{\mathrm{B}}) - \tilde{c}_s^{\mathrm{B}} \\ \tilde{T}_l(\tilde{c}_l^{\mathrm{A}}, \tilde{c}_l^{\mathrm{B}}) - T \\ r\frac{\tilde{c}_l^{\mathrm{A}} - c_l^{\mathrm{A}}}{\tilde{c}_l^{\mathrm{A}} - \tilde{c}_s^{\mathrm{A}}} - \frac{\tilde{c}_l^{\mathrm{B}} - c_l^{\mathrm{B}}}{\tilde{c}_l^{\mathrm{B}} - \tilde{c}_s^{\mathrm{B}}} \end{pmatrix}, \tag{3.23}$$

and

$$\mathbf{0} = \begin{pmatrix} 0 \\ 0 \\ 0 \\ 0 \end{pmatrix}, \tag{3.24}$$

and $r = {}^{D_l^{\mathrm{A}}}/_{D_l^{\mathrm{B}}}$.

In order to apply the Implicit Function Theorem, let us rewrite the Eq. (3.22) in the following form

$$F(x, y) = 0, \tag{3.25}$$

where $x = (T_l, c_l^{\mathrm{A}}, c_l^{\mathrm{B}})$ and $y = (\tilde{c}_l^{\mathrm{A}}, \tilde{c}_l^{\mathrm{B}}, \tilde{c}_s^{\mathrm{A}}, \tilde{c}_s^{\mathrm{B}})$. Let us fix a point $(a, b) = (T_{l,a}, c_{l,a}^{\mathrm{A}}, c_{l,a}^{\mathrm{B}}; \tilde{c}_{l,b}^{\mathrm{A}}, \tilde{c}_{l,b}^{\mathrm{B}}, \tilde{c}_{s,b}^{\mathrm{A}}, \tilde{c}_{s,b}^{\mathrm{B}})$, then the part of the Jacobian with derivatives of F with respect to the mesoscopic parameters $y = (\tilde{c}_l^{\mathrm{A}}, \tilde{c}_l^{\mathrm{B}}, \tilde{c}_s^{\mathrm{A}}, \tilde{c}_s^{\mathrm{B}})$ of the system (3.22) $J_{F,y}$ at this point is

$$J_{F(a,b),y} = \begin{pmatrix} \partial\tilde{c}_s^{\mathrm{A}}(a,b)/\partial\tilde{c}_l^{\mathrm{A}} & \partial\tilde{c}_s^{\mathrm{A}}(a,b)/\partial\tilde{c}_l^{\mathrm{B}} & -1 & 0 \\ \partial\tilde{c}_s^{\mathrm{B}}(a,b)/\partial\tilde{c}_l^{\mathrm{A}} & \partial\tilde{c}_s^{\mathrm{B}}(a,b)/\partial\tilde{c}_l^{\mathrm{B}} & 0 & -1 \\ \partial\tilde{T}_l(a,b)/\partial\tilde{c}_l^{\mathrm{A}} & \partial\tilde{T}_l(a,b)/\partial\tilde{c}_l^{B} & 0 & 0 \\ r\frac{(c_{l,a}^{\mathrm{A}}-\tilde{c}_{s,b}^{\mathrm{A}})}{(\tilde{c}_{l,b}^{\mathrm{A}}-\tilde{c}_{s,b}^{\mathrm{A}})^2} & \frac{(\tilde{c}_{l,b}^{\mathrm{B}}-c_{l,a}^{\mathrm{B}})}{(\tilde{c}_{l,b}^{\mathrm{B}}-\tilde{c}_{s,b}^{\mathrm{B}})^2} & r\frac{(\tilde{c}_{l,b}^{\mathrm{A}}-c_{l,a}^{\mathrm{A}})}{(\tilde{c}_{l,b}^{\mathrm{A}}-\tilde{c}_{s,b}^{\mathrm{A}})^2} & \frac{(c_{l,a}^{\mathrm{B}}-\tilde{c}_{l,b}^{\mathrm{B}})}{(\tilde{c}_{l,b}^{\mathrm{B}}-\tilde{c}_{s,b}^{\mathrm{B}})^2} \end{pmatrix} \tag{3.26}$$

The function F satisfies the requirements of the Implicit Function Theorem where Jacobian of $J_{F(a,b),y}$ can be be inverted. It means that the following continuously differentiable function G exists everywhere, where the Jacobian $J_{F(a,b),y}$ is invertible:

$$y = G(x) \tag{3.27}$$

or

$$(\tilde{c}_l^{\mathrm{A}}, \tilde{c}_l^{\mathrm{B}}, \tilde{c}_s^{\mathrm{A}}, \tilde{c}_s^{\mathrm{B}}) = G(T_l, c_l^{\mathrm{A}}, c_l^{\mathrm{B}}), \tag{3.28}$$

which means that mesoscopic quantities $\tilde{c}_l^{\mathrm{A}}, \tilde{c}_l^{\mathrm{B}}, \tilde{c}_s^{\mathrm{A}}, \tilde{c}_s^{\mathrm{B}}$ functionally depend on macroscopic ones $T_l, c_l^{\mathrm{A}}, c_l^{\mathrm{B}}$. The actual form of the function G is determined by thermodynamic relations (3.15), (3.16) and (3.17) and growth kinetics relation (3.21) combined together by means of the nonlinear algebraic equation system (3.22). We arrive at an important conclusion that there exists a dependence of the equilibrium concentrations of alloying components A and B in solid and liquid phases at the solid–liquid phase interface on the concentrations of alloying components in the bulk melt and its temperature.

The unknowns $\tilde{c}_l^{\mathrm{A}}, \tilde{c}_l^{\mathrm{B}}, \tilde{c}_s^{\mathrm{A}}, \tilde{c}_s^{\mathrm{B}}$ are the only mesoscopic quantities entering the formulae for growth velocities (2.32) and (2.33). The mass transfer rate depends on the thermodynamics by means of growth velocity and thus on the mesoscopic unknown quantities $\tilde{c}_l^{\mathrm{A}}, \tilde{c}_l^{\mathrm{B}}, \tilde{c}_s^{\mathrm{A}}, \tilde{c}_s^{\mathrm{B}}$ which are functions of macroscopic parameters $T_l, c_l^{\mathrm{A}}, c_l^{\mathrm{B}}$. Which means that the mass transfer rate is in the end a function of known macroscopic parameters $T_l, c_l^{\mathrm{A}}, c_l^{\mathrm{B}}$ and can be calculated by employing three thermodynamic relations expressed with Eqs. (3.15)-(3.17) and an expression for growth velocity ((2.32) for columnar or (2.33) for equiaxed morphology).

In the explicit form the function G can be found in the simplified case when thermodynamic functions (3.15), (3.16) and (3.17) are linear. In this case there are 3 linear functions and 1 nonlinear function in the equation system and it can be solved analytically. It was done using the symbolical algebraic software package Maple V [Maplesoft05, Char93]. See Appendix 8.3 where a way of obtaining this analytical solution is described. However, the solution for this simplified case is of a limited practical use, since the thermodynamic functions (3.15), (3.16) and (3.17) in general case are nonlinear.

Since the thermodynamic functions (3.15)-(3.17) are available only from thermodynamic software packages and since the equation system (3.15)-(3.21) is nonlinear, the solution of this system in general case is possible only numerically (described in the Section 4.2). Based on this, a coupling algorithm was developed, which description follows. The coupling is performed according to the following steps:

1. Get the macroscopic parameters in the bulk melt $T_l, c_l^{\mathrm{A}}, c_l^{\mathrm{B}}$.

2. Solve numerically (see Section 4.2) the nonlinear equation system consisting of equations (3.16), (3.17), (3.20) and (3.21) to get the mesoscopic parameters $\tilde{c}_l^{\mathrm{A}}, \tilde{c}_l^{\mathrm{B}}, \tilde{c}_s^{\mathrm{A}}, \tilde{c}_s^{\mathrm{B}}$ (solid–liquid interface equilibrium mass fractions of the alloying components A and B).

3. Using the values of $\tilde{c}_l^{\mathrm{A}}, \tilde{c}_l^{\mathrm{B}}, \tilde{c}_s^{\mathrm{A}}, \tilde{c}_s^{\mathrm{B}}$ calculated in the previous step (Step 2) and $c_l^{\mathrm{A}}, c_l^{\mathrm{B}}$, calculate the growth velocity (either columnar or equiaxed) according to (2.32) or (2.33).

4. Using the growth velocity calculated at the Step 3, calculate the mass transfer rate using (2.1.3).

Now the mass transfer rate computed can be used for calculating the source terms for the equations of the multiphase solidification model (described in the Section 2.1), thus solving the problem of calculating the mass transfer rate in a thermodynamically consistent way.

A method for solving this equation system was implemented. For details on the numerical techniques employed see Chapter 4.

3.5 Representation of ternary thermodynamic functions

Now let us consider the possibilities of getting the values of the mentioned thermodynamic functions (3.15)-(3.17). The most natural way to evaluate these functions is to use a thermodynamics software package, for example Thermo-Calc |The06a|. This way is the most precise, but also the most time consuming, since the evaluation of these three thermodynamic functions (3.15)-(3.17) has to be performed several times during the iterative process of a Newton-type method (we use the Hybrid Powell's Method described in Section 4.2) for solving the nonlinear equation system (3.16)-(3.21) and this Newtonian iterative process has to be performed for each computational cell on each iteration of the flow solver. On the other hand, the thermodynamic functions describing the tie-line relations (3.16)-(3.17) are intrinsically discontinuous: These functions represent solubilities of the corresponding components in the solid phase, and they naturally change with a jump (for example in the Fe–C system the solubility of carbon in ferrite and in austenite changes with a jump as crystal lattice changes immediately when temperature changes).

The existence of this natural discontinuity affects the numerical use of the functions provided by Thermo-Calc in two ways: firstly, Newton-type methods are not designed to solve equation systems with discontinuous functions so the the behaviour of the Newton-type iterative process is at least unpredictable, and secondly, the existence of this discontinuities makes it necessary to threat those explicitly. In other words, when during the solidification, a solidification path crosses such a discontinuous phase border it has to be treated explicitly: for instance precautions have to be made that the Newton-type iterations *always*stay in the continuous definition domain of functions (3.16)-(3.17) and there must be some kind of artificial treatment to bridge the solidification path from one continuous domain to the other. These two factors make direct use of thermodynamic software packages prohibitive.

In order to overcome the limitations described, two methods to approximate the thermodynamic functions provided by thermodynamic software were developed and implemented, which are described below.

3.5.1 Piecewise-linear interpolation of thermodynamic functions

The simplest way to approximate a function is to linearise it around a point. Let us construct a piecewise-linear approximation of a thermodynamic function f:

$$f = f\left(\tilde{c}_l^{\mathrm{A}}, \tilde{c}_l^{\mathrm{B}}\right),\ 0 \leq \tilde{c}_l^{\mathrm{A}} \leq a,\ 0 \leq \tilde{c}_l^{\mathrm{B}} \leq b \tag{3.29}$$

(which can be any of the functions of interest (3.15)-(3.17)), defined in the domain D:

$$D = \left\{\left(\tilde{c}_l^{\mathrm{A}}, \tilde{c}_l^{\mathrm{B}}\right) \mid 0 \leq \tilde{c}_l^{\mathrm{A}} \leq a,\ 0 \leq \tilde{c}_l^{\mathrm{B}} \leq b\right\} \tag{3.30}$$

around two points $O_1 \in D_1$ and $O_2 \in D_2$ respectively, where D_1 and D_2 are nonintersecting subdomains of the domain $D = D_1 \cup D_2$, and the curve g defining the border between D_1 and D_2 is given with the following equation:

$$\tilde{c}_l^{\mathrm{B}} = g\left(\tilde{c}_l^{\mathrm{A}}\right),\ 0 \leq \tilde{c}_l^{A} \leq a, \tag{3.31}$$

as shown in the Fig. 3.7.

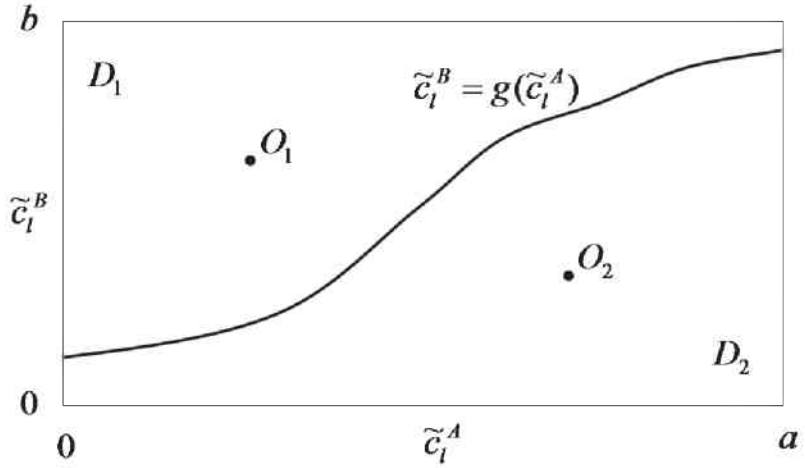

Figure 3.7: A schematic view of a two-phase case with a phase border between the two phase domains D_1 and D_2

Let points O_1 and O_2 have coordinates $O_1\left(\tilde{c}_{l,1}^{\mathrm{A}}, \tilde{c}_{l,1}^{\mathrm{B}}\right)$ and $O_2\left(\tilde{c}_{l,2}^{\mathrm{A}}, \tilde{c}_{l,2}^{\mathrm{B}}\right)$. Now

we can construct a piecewise-linear approximation of the function (3.29). The approximation will consist of two linear pieces: the first piece is valid in the neighbourhood of the point O_1 (subdomain D_1), and the second in the neighbourhood of point O_2 (subdomain D_2), while the Eq. (3.31) will define the border between them.

The linearization of the function of interest around these two points can be done by expanding the function (3.29) using the Taylor Formula and dropping the terms of order higher than $O\left(||r - r_{O_i}||\right),\ i = 1, 2$:

$$\hat{f}_{O_1}\left(\tilde{c}_l^{\mathrm{A}}, \tilde{c}_l^{\mathrm{B}}\right) = f_{O_1} + \left(\frac{\partial f}{\partial \tilde{c}_l^{\mathrm{A}}}\right)_{O_1}\left(\tilde{c}_l^{\mathrm{A}} - \tilde{c}_{l,1}^{\mathrm{A}}\right) + \left(\frac{\partial f}{\partial \tilde{c}_l^{\mathrm{B}}}\right)_{O_1}\left(\tilde{c}_l^{\mathrm{B}} - \tilde{c}_{l,1}^{\mathrm{B}}\right) \tag{3.32}$$

and around O_2:

$$\hat{f}_{O_2}\left(\tilde{c}_l^{\mathrm{A}}, \tilde{c}_l^{\mathrm{B}}\right) = f_{O_2} + \left(\frac{\partial f}{\partial \tilde{c}_l^{\mathrm{A}}}\right)_{O_2}\left(\tilde{c}_l^{\mathrm{A}} - \tilde{c}_{l,2}^{\mathrm{A}}\right) + \left(\frac{\partial f}{\partial \tilde{c}_l^{\mathrm{B}}}\right)_{O_2}\left(\tilde{c}_l^{\mathrm{B}} - \tilde{c}_{l,2}^{\mathrm{B}}\right) \tag{3.33}$$

Now combining these linearizations Eq. (3.32) and (3.33) with the equation (3.31) defining the phase border we construct a piecewise-linear approximation for the whole domain of interest $D = \left\{\left(\tilde{c}_l^{\mathrm{A}}, \tilde{c}_l^{\mathrm{B}}\right) \mid 0 \le \tilde{c}_l^{\mathrm{A}} \le a,\ 0 \le \tilde{c}_l^{\mathrm{B}} \le b\right\}$:

$$\hat{f}\left(\tilde{c}_l^{\mathrm{A}}, \tilde{c}_l^{\mathrm{B}}\right) = \begin{cases} f_{O_1}\left(\tilde{c}_l^{\mathrm{A}}, \tilde{c}_l^{\mathrm{B}}\right), & \text{if } \tilde{c}_l^{\mathrm{B}} \le g\left(\tilde{c}_l^{\mathrm{A}}\right) \\ f_{O_2}\left(\tilde{c}_l^{\mathrm{A}}, \tilde{c}_l^{\mathrm{B}}\right), & \text{otherwise} \end{cases} \tag{3.34}$$

The parameters that need to be estimated using Thermo-Calc are:

$$f_{O_1},\ f_{O_2},\ \left(\frac{\partial f}{\partial \tilde{c}_l^{\mathrm{A}}}\right)_{O_1},\ \left(\frac{\partial f}{\partial \tilde{c}_l^{\mathrm{A}}}\right)_{O_2},\ \left(\frac{\partial f}{\partial \tilde{c}_l^{\mathrm{B}}}\right)_{O_1},\ \left(\frac{\partial f}{\partial \tilde{c}_l^{\mathrm{B}}}\right)_{O_2}$$

whereas the coordinates of the points O_1 and O_2 has to be chosen so that the solidification paths calculated using the approximation given by Eqs. (3.32) and (3.33) deviates as little as possible from the one calculated using the original thermodynamic functions (3.15)-(3.17). For the implementation details (including the choice of O_1 and O_2) see Section 4.3. Analogously one can construct similar piecewise approximation of a given function f in the N-phase case (See

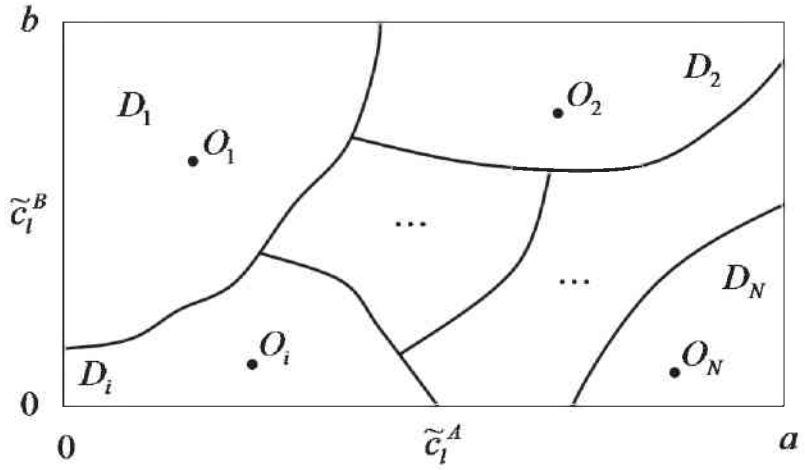

Figure 3.8: Regions with different phases in the N-phase case

Fig. 3.8). Note that the connectivity of the subdomains D_i is only schematic, in reality the connectivity have to be consistent with the Gibbs phase rule.

In this case the domain of interest D is divided into N nonintersecting subdomains:

$$D = \cup_{i=1}^{i=N} D_i \tag{3.35}$$

In each subdomain D_i we linearise the initial function f, getting N linear functions $\hat{f}_i$, $i = 1, \ldots, N$, each defined in its subdomain D_i:

$$\hat{f}_i\left(\tilde{c}_l^{\mathrm{A}}, \tilde{c}_l^{\mathrm{B}}\right) = f_{O_i} + \left(\frac{\partial f}{\partial \tilde{c}_l^{\mathrm{A}}}\right)_{O_i} \left(\tilde{c}_l^{\mathrm{A}} - \tilde{c}_{l,i}^{\mathrm{A}}\right) + \left(\frac{\partial f}{\partial \tilde{c}_l^{\mathrm{B}}}\right)_{O_i} \left(\tilde{c}_l^{\mathrm{B}} - \tilde{c}_{l,i}^{\mathrm{B}}\right) \tag{3.36}$$

Now the function defined in the whole domain D (except the boundaries ∂D_i, for which a special treatment is needed) can be constructed:

$$\hat{f}\left(\tilde{c}_l^{\mathrm{A}}, \tilde{c}_l^{\mathrm{B}}\right) = \begin{cases} \hat{f}_1, & \text{if } x \in D_1, \\ \hat{f}_2, & \text{if } x \in D_2, \\ \dots & \dots \\ \hat{f}_N & \text{if } x \in D_N. \end{cases} \tag{3.37}$$

Note the obvious drawback of the approximation method described: the discontinuity at the borders $\partial D = \cup_{i=1}^{i=N} \partial D_i$ if we apply this method for a continuous function f. Although, among the functions we want to approximate, only the function (3.15) describing the liquidus surface is continuous in the whole domain D, whereas other two functions Eq. (3.16) and (3.17) are naturally discontinuous at ∂D (see the discussion above about the nature of the physical quantities they represent). So this discontinuity is nonphysical only for approximation of the liquidus surface (3.15) and depending on the phase diagram using a special treatment the discontinuity on ∂D can be successfully handled. In order to solve this discontinuity problem in principle we suggest using spline interpolation for approximating thermodynamic functions (3.15)-(3.17) as described in the next section.

3.5.2 Spline interpolation of thermodynamic functions

The other way to represent the phase diagram information given by functions (3.15)-(3.17) considered in this work is the spline interpolation |DeBoor94|. Let us consider again a thermodynamic function f defined above in Eq.(3.29). This function values in general case are available only pointwise, as the values of it are themselves a result of a numerical solution of a minimisation problem |White58; Eriksson71; Eriksson90|. So it is natural to assume that the values of the function f are given for instance on a uniform grid $\Omega_{h_1 h_2}$ in the domain D defined above in (3.30) with spatial steps h_1 and h_2 in directions $\tilde{c}_l^{\mathrm{A}}$ and $\tilde{c}_l^{\mathrm{B}}$ respectively. The grid $\Omega_{h_1 h_2}$ can be defined as:

$$\Omega_{h_1 h_2} = \left\{ \left(\tilde{c}_{l,i}^{\mathrm{A}}, \tilde{c}_{l,j}^{\mathrm{B}}\right) | \tilde{c}_{l,i}^{\mathrm{A}} = i h_1, \tilde{c}_{l,j}^{\mathrm{B}} = j h_2, i = 0,\ 1,\ \dots, N_1,\ j = 0,\ 1,\ \dots, N_2 \right\} \tag{3.38}$$

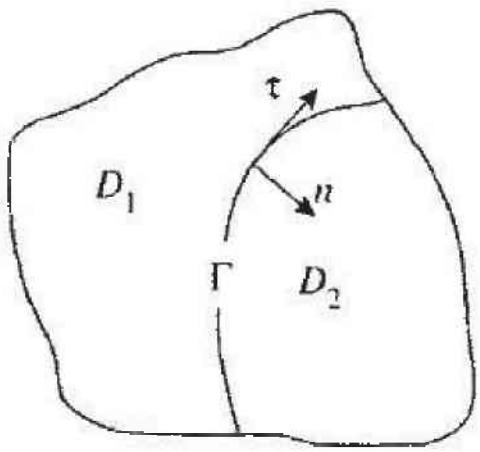

Figure 3.9: Subdomains D_1 and D_2 with the interface Γ [Kounchev01]

In [Kounchev01] the understanding of a multivariate spline is given as follows:

"Assume that a domain $D \subset \mathbb{R}^n$ be given and a disjoint family of subdomains D_j such that $\cup D_j = D$, and the boundaries ∂D_j are smooth enough, so that the normal n exists almost everywhere on ∂D_j. Then a *spline* is a function u, defined in D which is assembled of functions u_j defined on D_j. These pieces are of similar nature and match up to a certain degree d of smoothness on the joint boundaries. Imagine for simplicity that $D \subset \mathbb{R}^2$ and $D = D_1 \cup D_2$, and $\overline{D}_1 \cap \overline{D}_2 = \Gamma$ which is a curve (see Fig. 3.9).

The joint boundary Γ where two pieces match is called the *interface* or *break-surface*.

Then we require that

$$\begin{aligned} u_1 &= u_2 \quad \text{on } \Gamma, \\ \tfrac{\partial}{\partial n} u_1 &= \tfrac{\partial}{\partial n} u_2 \quad on\ \Gamma, \\ &\cdots \\ \tfrac{\partial^d}{\partial n^d} u_1 &= \tfrac{\partial^d}{\partial n^d} u_2 \quad on\ \Gamma, \end{aligned} \tag{3.39}$$

where $\partial/\partial n$ denotes the normal derivative (one of the two directions) on Γ. If we also require more smoothness of the functions u_1 and u_2 on the joint boundary Γ, say $u_1 \in (\overline{D}_1)$ and $u_2 \in (\overline{D}_2)$, if Γ is also smooth enough, we may differentiate the above equalities in the direction τ tangential to Γ and obtain the equalities of the mixed derivatives up to order d_1, i.e.

$$\frac{\partial^l}{\partial \tau^l}\frac{\partial^k}{\partial n^k}u_1 = \frac{\partial^l}{\partial \tau^l}\frac{\partial^k}{\partial n^k}u_2, \tag{3.40}$$

where the indexes l and k satisfy $l + k \leq d_1$ and $0 \leq k \leq d$. Let us fix a point y on Γ. To write the last equalities in a simpler way, let us introduce a local coordinate system on the surface Γ by putting $y = 0$ and by choosing the normal vector (one of two directions) to coincide with the coordinate axis x_2. Then the above equality at the point y will read as follows:

$$\frac{\partial^l}{\partial x_1^l}\frac{\partial^k}{\partial x_2^k}u_1(0) = \frac{\partial^l}{\partial x_1^l}\frac{\partial^k}{\partial x_2^k}u_2(0). \tag{3.41}$$

The really big questions arise if we are given a "data function" f on the set Γ which has to be *interpolated* by the spline u, i.e. if we would like to have

$$u_1 = u_2 = f \quad \text{on } \Gamma. \tag{3.42}$$

Then the problem is a real intellectual challenge. In the present book we provide a solution only for integers $d = 2p - 2 \geq 0$, where $p \geq 1$ is an integer. The functions u_1 and u_2 then satisfy the equations

$$\begin{aligned} \Delta^p u_1 &= 0 \quad \text{in } D_1, \\ \Delta^p u_2 &= 0 \quad \text{in } D_2, \end{aligned} \tag{3.43}$$

where Δ^p is the polyharmonic operator."

After giving this general idea of a multivariate spline, let us take a closer look at

the splines that can help us to interpolate the necessary thermodynamic functions (3.15)-(3.17). These functions are functions of two variables. We will need to construct a spline function of two variables, that interpolates the from Thermo-Calc |The06a, The06b| tabulated pointwise tabulated values of these functions.

The following description is taken from |Kvasov00|, from the section "Spline functions of two variables on a rectangular grid".

Let on a rectangular domain $\Omega = [a, b] \times [c, d]$ a mesh of lines $\Delta = \Delta_x \times \Delta_y$ be introduced with:

$$\Delta_x : \ a = x_0 < x_1 < \ldots < x_N = b,$$

$$\Delta_y : \ c = y_0 < y_1 < \ldots < y_M = d,$$

which divides the domain Ω into the rectangles

$$\Omega_{ij} = \{(x, y) \, | x \in [x_i, x_{i+1}], \ y \in [y_j, y_{j+1}]\},$$

$$i = 0, \ \ldots, \ N - 1; \quad j = 0, \ \ldots, \ M - 1.$$

Let us associate with Δ_x a vector with integer components $\bar{\nu} = (\nu_1, \ \ldots, \ \nu_{N-1})$ and with Δ_y an analogous vector $\bar{\mu} = (\mu_1, \ \ldots, \ \mu_{M-1})$. For integers $k \geq 0$ and $l \geq 0$ let us denote by $C^{k,l}[\Omega]$ the set of continuous on Ω functions f having continuous partial and mixed derivatives $D^{r,s} f \ (r \leq k, \ s \leq l)$. By the symbol $C^{-1,-1}[\Omega]$ we denote the set of piecewise continuous functions whose discontinuities are of first order on some closed curves containing possibly the boundaries of the domain.

*Definition.*The function $S_{n,m,\bar{\nu},\bar{\mu}}$ is called a spline of two variables of order n and of multiplicity ν ($\nu = \max\limits_i \nu_i, \ 0 \leq \nu_i \leq n$) with respect to x, and of order m and of multiplicity μ ($\mu = \max\limits_j \mu_j, \ 0 \leq \mu_i \leq m$) with respect to y with joining lines of the mesh Δ if

(a) in any rectangle Ω_{ij}, the function $S_{n,m,\bar{\nu},\bar{\mu}}$ is a polynomial of order n with

respect to x and of order m with respect to y that is

$$S_{n,m,\bar{\nu},\bar{\mu}} = \sum_{\alpha=0}^{n-1} \sum_{\beta=0}^{m-1} a_{\alpha\beta}^{ij} (x - x_i)^{\alpha} (y - y_i)^{\beta},$$

$$i = 0, \ldots, N-1; \quad j = 0, \ldots, M-1; \tag{3.44}$$

(b) adjacent polynomials are smoothly tied together

$$D^{r,s} S_{n,m,\bar{\nu},\bar{\mu}}(x_i - 0, y) = D^{r,s} S_{n,m,\bar{\nu},\bar{\mu}}(x_i + 0, y),$$

$$r = 0, \ldots, n-1-\nu_i, \; i = 1, \ldots, N-1; \; s = 0, \ldots, m-1-\mu,$$

$$D^{r,s} S_{n,m,\bar{\nu},\bar{\mu}}(x, y_i - 0) = D^{r,s} S_{n,m,\bar{\nu},\bar{\mu}}(x, y_i + 0),$$

$$s = 0, \ldots, m-1-\mu_i, \; j = 1, \ldots, M-1; \; r = 0, \ldots, n-1-\nu,$$

that is

$$S_{n,m,\bar{\nu},\bar{\mu}} \in C^{n-1-\nu, m-1-\mu}[\Omega].$$

We call $\bar{\nu}$ and $\bar{\mu}$ the multiplicity vectors. The i-th component ν_i of $\bar{\nu}$ controls the smoothness of the spline along the mesh line $x = x_i$ and is called the multiplicity of the spline along the mesh line $x = x_i$. Analogously the j-th component μ_j of the vector $\bar{\mu}$ is called the multiplicity of the spline on the line $y = y_i$.

Chapter 4

Numerical implementation

4.1 Computational fluid dynamics of incompressible multiphase flows: phase-coupled SIMPLE method

For the implementation of the ternary solidification model described in the previous chapters the commercial software FLUENT was used |FLU01|. Necessary source terms like mass transfer rate, species transfer rate, etc. as well as function calls to the libraries that provide the Hybrid Powell method and spline interpolation functionality were implemented by means of the User Defined Functions interface |FLU06|. The numerical method for solving the equations of Eulerian multiphase model used in FLUENT is Phase-Coupled SIMPLE method |Vasquez00|, which is a modification of the SIMPLE method of S. V. Patankar |Patankar80| for multiphase flows. A summary of the Phase-Coupled SIMPLE method is given in |Ersayin05|.

The governing equations are discretized by dividing the domain into a finite number of control volumes. In the collocated variables finite volume approach, checkboard splitting of pressure is avoided using a special discretization scheme following Rhie and Chow |Rhie83|. A similar idea was implemented into FLUENT unstructured by Mathur and Murthy |Marthur97|. The idea has also been extended to multiphase flows (Vasquez and Ivanov |Vasquez00|). Similarly, other driving forces like gradients of the volume fraction, or body forces, can be included in the Rhie and Chow |Rhie83| scheme. But, such a velocity reconstruction does

not automatically satisfy mass continuity.

An extended SIMPLE algorithm is used for the pressure-velocity coupling in multiphase flow. To avoid bias towards a heavy phase, the pressure correction is based on the conservation of the total volume. The resulting discretized form of the total volume continuity equation for incompressible fluids and the correction for the volume fluxes, derived from the coupled momentum equations, are used to satisfy local mass continuity and derive pressure corrections. The coefficients of the pressure correction equation implicitly contain the whole effect of the coupling terms of the momentum equations. The algorithm is named Phase-Coupled-SIMPLE and is summarised below:

1. Initialise all variables.
2. Update boundaries and coupling terms.
3. Solve for phase-coupled velocity vectors using a block algebraic multigrid method.
4. Reconstruct the volume fluxes. Use a point matrix solver to get volume fluxes.
5. Build the pressure-correction equation from total volume continuity and solve it.
6. Volume fluxes and velocity corrections preserve the full coupling. Use a matrix solver to correct fluxes and velocities. Correct share pressures.
7. Solve for volume fractions enforcing realizability conditions and update properties.
8. Solve scalar equations.
9. Repeat from Step 2 until convergence.
10. If time dependent, advance to next time step.

The following description is taken from [FLU01] (notation is adapted, plus additional description of terms is given):

"The velocities are solved coupled by phases, but in a segregated fashion. The block algebraic multigrid scheme used by the density-based solver described in |Weiss99| is used to solve a vector equation formed by the velocity components of all phases simultaneously. Then, a pressure correction equation is built based on total volume continuity rather than mass continuity. Pressure and velocities are then corrected so as to satisfy the continuity constraint.

For incompressible multiphase flow, the pressure-correction equation takes the form

$$\sum_{k=1}^{n} \frac{1}{\rho_{rk}} \left\{ \frac{\partial}{\partial t} f_k \rho_k + \nabla \cdot f_k \rho_k \vec{u}'_k + \nabla \cdot f_k \rho_k \vec{u}^*_k - \left(\sum_{l=1}^{n} (\dot{m}_{lk} - \dot{m}_{kl}) \right) \right\} = 0 \tag{4.1}$$

where ρ_{rk} is the phase reference density for the k-th phase (defined as the total volume average density of phase k), $\vec{u}'_k$ is the velocity correction for the k-th phase, and $\vec{u}^*_k$ is the value of $\vec{u}_k$ at the current iteration. The velocity corrections are themselves expressed as functions of the pressure corrections. Also here $\dot{m}_{lk}$ are mass transfer rates from phase k to l.

The volume fractions are obtained from the phase continuity equations"

$$\frac{1}{\rho_{rk}} \left(\frac{\partial}{\partial t} (f_q \rho_q) + \nabla \cdot (f_q \rho_q \vec{v}_q) = \sum_{p=1}^{n} (\dot{m}_{pq} - \dot{m}_{qp}) \right) \tag{4.2}$$

4.2 Numerical solution of the nonlinear equation system for coupling

For solving the nonlinear equation system consisting of (3.16),(3.17),(3.20) and (3.21) the Hybrid Powell's algorithm |Powell70a, Powell70b| implemented within

the GSL Scientific Library |Galassi01| was used. The following quote from [Galassi01] describes this method (in the following description J is the Jacobian of the equation system $f(x) = 0$, dx is an unknown Newton step):

"This is a modified version of Powell's Hybrid method as implemented in the *hybrj* algorithm in minpack. Minpack was written by Jorge J. Moré, Burton S. Garbow and Kenneth E. Hillstrom. The Hybrid algorithm retains the fast convergence of Newton's method but will also reduce the residual when Newton's method is unreliable.

The algorithm uses a generalised trust region to keep each step under control. In order to be accepted a proposed new position x' must satisfy the condition $|D(x' - x)| < \delta$, where D is a diagonal scaling matrix and δ is the size of the trust region. The components of D are computed internally, using the column norms of the Jacobian to estimate the sensitivity of the residual to each component of x. This improves the behaviour of the algorithm for badly scaled functions.

On each iteration the algorithm first determines the standard Newton step by solving the system $Jdx = -f$. If this step falls inside the trust region it is used as a trial step in the next stage. If not, the algorithm uses the linear combination of the Newton and gradient directions which is predicted to minimise the norm of the function while staying inside the trust region,

$$dx = -\alpha J^{-1} f(x) - \beta \nabla |f(x)|^2 \tag{4.3}$$

This combination of Newton and gradient directions is referred to as a dogleg step.

The proposed step is now tested by evaluating the function at the resulting point, x'. If the step reduces the norm of the function sufficiently then it is accepted and size of the trust region is increased. If the proposed step fails to improve the solution then the size of the trust region is decreased and another trial step is computed.

The speed of the algorithm is increased by computing the changes to the Jacobian approximately, using a rank-1 update. If two suc-

cessive attempts fail to reduce the residual then the full Jacobian is recomputed. The algorithm also monitors the progress of the solution and returns an error if several steps fail to make any improvement (it either reports that "the iteration is not making any progress, preventing the algorithm from continuing" or "re-evaluations of the Jacobian indicate that the iteration is not making any progress, preventing the algorithm from continuing")."

Further details about the algorithm and its implementation can be found in |Broyden65, Moré79, Moré81|.

In this work the GNU Scientific Library multidimensional root–finding functions were called from the FLUENT's User Defined Functions |FLU01, FLU06| by means of the provided C programming language interface to solve the nonlinear equation system consisting of four equations (3.16), (3.17), (3.20) and (3.21) to determine the interfacial equilibrium concentrations $\tilde{c}_l^{\mathrm{A}}$, $\tilde{c}_l^{\mathrm{B}}$, $\tilde{c}_s^{\mathrm{A}}$, $\tilde{c}_s^{\mathrm{A}}$ which are the four unknowns of the equation system aforementioned. Note that when taking three phases into account (that is liquid, columnar and equiaxed), then a distinction has to be made between the interfacial equilibrium concentrations, since they will be different for different phases. In the three phase case, the equation system (3.16),(3.17),(3.20) and (3.21) has to be solved twice, once to get interfacial concentrations $\tilde{c}_{l,c}^{\mathrm{A}}$, $\tilde{c}_{l,c}^{\mathrm{B}}$, $\tilde{c}_{s,c}^{\mathrm{A}}$, $\tilde{c}_{s,c}^{\mathrm{A}}$ for the columnar phase and $\tilde{c}_{l,e}^{\mathrm{A}}$, $\tilde{c}_{l,e}^{\mathrm{B}}$, $\tilde{c}_{s,e}^{\mathrm{A}}$, $\tilde{c}_{s,e}^{\mathrm{A}}$ for the equiaxed phase, which are used later for calculating growth velocities for the columnar phase (2.32) and liquid (2.33) phase.

4.3 Numerical representation of the multicomponent phase diagram data

4.3.1 Piecewise-linear approximation of Fe–C–Cr system

Piecewise linear approximation were performed to correctly represent the solidification paths predicted by Thermo-Calc-Scheil module for X30Cr15 alloy. In order to do so, the solidification path for the X30Cr15 alloy was calculated using Thermo-Calc-Scheil module. This solidification path is shown in the Fig. 4.1.

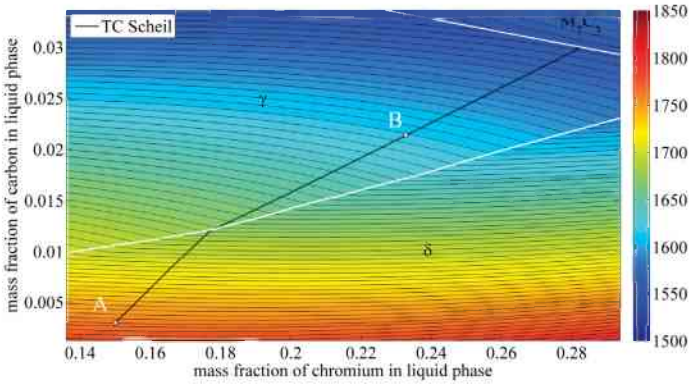

Figure 4.1: The solidification path for the X30Cr15 alloy calculated using the Thermo-Calc-Scheil module and linearization points depicted on top of the contour plot of the liquidus temperature (temperature is given in degrees Kelvin) in the iron-rich corner of Fe-C-Cr phase diagram

The solidification starts with the formation of the ferrite phase, then the solidification path proceeds towards the peritectic line, then the peritectic solidification starts and austenite starts to form. Then the solidification path proceeds to the eutectic grove where eutectic solidification with the formation of the austenite and carbide M_7C_3.

Having these solidification paths, we make the choice of points A and B so that the linearizations resulting make a good representation of the thermodynamic functions (3.15), (3.16) and (3.17) in that sense, that the solidification paths calculated with Thermo-Calc-Scheil module and the solidification path calculated with the multiphase solidification model described above differ as little as possible.

The mass fractions of the elements C and Cr are measured in kg of the element per kg of the melt, so its unit is $\frac{\text{kg}}{\text{kg}} = 1$, and mass fractions $\tilde{c}^{\text{C}}_{l,A}$ and $\tilde{c}^{\text{Cr}}_{l}$ are unitless. The coordinates of the points $A(\tilde{c}^{\text{C}}_{l,A}, \tilde{c}^{\text{Cr}}_{l,A})$ and $B(\tilde{c}^{\text{C}}_{l,B}, \tilde{c}^{\text{Cr}}_{l,B})$ are mass fraction of elements C and Cr in the liquid phase were chosen as

$$A = (\tilde{c}^{\text{C}}_{l} = 0.003,\ \tilde{c}^{\text{Cr}}_{l} = 0.15) \tag{4.4}$$

and

$$B = (\tilde{c}^{\text{C}}_{l} = 0.022,\ \tilde{c}^{\text{Cr}}_{l} = 0.26) \tag{4.5}$$

linearization was done as described in Section 3.5.1. The linearization parameters were calculated using Thermo-Calc and are given in Table 4.1.

around the point A	numeric value	around the point B	numeric value
$\tilde{T}_A$	1759.7046 K	$\tilde{T}_B$	1605.6378 K
$\left(\partial\tilde{T}/\partial\tilde{c}_l^{\mathrm{C}}\right)_A$	-9198.5831 K	$\left(\partial\tilde{T}/\partial\tilde{c}_l^{\mathrm{C}}\right)_B$	-4175.2312 K
$\left(\partial\tilde{T}/\partial\tilde{c}_l^{\mathrm{Cr}}\right)_A$	-76.214187 K	$\left(\partial\tilde{T}/\partial\tilde{c}_l^{\mathrm{Cr}}\right)_B$	-348.79788 K
$\tilde{c}_{s,A}^{\mathrm{C}}$	$4.8618649 \cdot 10^{-4}$	$\tilde{c}_{s,B}^{\mathrm{C}}$	$7.0848973 \cdot 10^{-3}$
$\left(\partial\tilde{c}_s^{\mathrm{C}}/\partial\tilde{c}_l^{\mathrm{C}}\right)_A$	0.15106564	$\left(\partial\tilde{c}_s^{\mathrm{C}}/\partial\tilde{c}_l^{\mathrm{C}}\right)_B$	0.30575641
$\left(\partial\tilde{c}_s^{\mathrm{C}}/\partial\tilde{c}_l^{\mathrm{Cr}}\right)_A$	$-5.2915106 \cdot 10^{-4}$	$\left(\partial\tilde{c}_s^{\mathrm{C}}/\partial\tilde{c}_l^{\mathrm{Cr}}\right)_B$	$-1.2038858 \cdot 10^{-2}$
$\tilde{c}_{s,A}^{\mathrm{Cr}}$	0.14207627	$\tilde{c}_{s,B}^{\mathrm{Cr}}$	0.16559951
$\left(\partial\tilde{c}_s^{\mathrm{Cr}}/\partial\tilde{c}_l^{\mathrm{C}}\right)_A$	-2.2273607	$\left(\partial\tilde{c}_s^{\mathrm{Cr}}/\partial\tilde{c}_l^{\mathrm{C}}\right)_B$	-2.0782296
$\left(\partial\tilde{c}_s^{\mathrm{Cr}}/\partial\tilde{c}_l^{\mathrm{Cr}}\right)_A$	1.0438801	$\left(\partial\tilde{c}_s^{\mathrm{Cr}}/\partial\tilde{c}_l^{\mathrm{Cr}}\right)_B$	0.61073492

Table 4.1: linearization parameters for the linearization of the iron-rich corner of the Fe-C-Cr phase diagram for solidification simulations of X30Cr15 alloy. Note that units of the slopes of the liquidus surface $\left(\partial\tilde{T}/\partial\tilde{c}_l^{\mathrm{C}}\right)_{A,B}$ and $\left(\partial\tilde{T}/\partial\tilde{c}_l^{\mathrm{C}}\right)_{A,B}$ are $\frac{\mathrm{K}}{\mathrm{kg/kg}}$, that is degree Kelvin per unit of mass fraction. Similarly, slopes of solubilities $\left(\partial\tilde{c}_s^{\mathrm{C}}/\partial\tilde{c}_l^{\mathrm{C}}\right)_{A,B}$, $\left(\partial\tilde{c}_s^{\mathrm{C}}/\partial\tilde{c}_l^{\mathrm{Cr}}\right)_{A,B}$, $\left(\partial\tilde{c}_s^{\mathrm{Cr}}/\partial\tilde{c}_l^{\mathrm{C}}\right)_{A,B}$ and $\left(\partial\tilde{c}_s^{\mathrm{Cr}}/\partial\tilde{c}_l^{\mathrm{Cr}}\right)_{A,B}$ are unitless because they describe the change of solid mass fraction of an element (measured in $\frac{\mathrm{kg}}{\mathrm{kg}}$) as the liquid mass fraction of this or the other element (also measured in $\frac{\mathrm{kg}}{\mathrm{kg}}$) changes.

The border line Eq. (3.31), between the ferrite and austenite regions were approximated with a straight line, which is tangential to the real phase border at the point where the solidification path intersects the peritectic line. The equation of the the straight line estimated using Thermo-Calc data is:

$$\tilde{c}_l^{\mathrm{Cr}} = 0.04 + 11.50\tilde{c}_l^{\mathrm{C}}. \tag{4.6}$$

so the thermodynamic functions are approximated by means of the functions of the following form

$$\hat{f}\left(\tilde{c}_l^{\mathrm{C}}, \tilde{c}_l^{\mathrm{Cr}}\right) = \begin{cases} f_A\left(\tilde{c}_l^{\mathrm{C}}, \tilde{c}_l^{\mathrm{Cr}}\right), & \text{if } \tilde{c}_l^{\mathrm{Cr}} \leq g\left(\tilde{c}_l^{\mathrm{A}}\right) \\ f_B\left(\tilde{c}_l^{\mathrm{C}}, \tilde{c}_l^{\mathrm{Cr}}\right), & \text{otherwise} \end{cases} \tag{4.7}$$

where $f_i\left(\tilde{c}_l^{\mathrm{C}}, \tilde{c}_l^{\mathrm{Cr}}\right),\ i = A, B$ are the linearizations around the points A and B with the parameters listed in the Table 4.1, and the function g is defined by (4.6).

For the details on the command sequence used for obtaining the linearization parameters from Thermo-Calc see Appendix 8.3.

4.3.2 Piecewise-linear approximation of Fe–C–Mn system

Similar piecewise-linear approximation was done for thermodynamic functions (3.15), (3.16) and 3.17 for the iron-rich corner of the Fe–C–Mn system. Similarly to the previous Section 4.3.1, two points, A and B were chosen. Their coordinates were:

$$A = (\tilde{c}_l^{\mathrm{Mn}} = 0.014, \tilde{c}_l^{\mathrm{C}} = 0.018) \tag{4.8}$$

and

$$B = (\tilde{c}_l^{\mathrm{Mn}} = 0.02239847,\ \tilde{c}_l^{\mathrm{C}} = 0.0068080346) \tag{4.9}$$

linearization was done as described in Section 3.5.1. The linearization parameters were calculated using Thermo-Calc and are given in Table 4.2.

around the point A	numeric value	around the point B	numeric value
$\tilde{T}_A$	1789.902 K	$\tilde{T}_B$	1748.57 K
$\left(\partial\tilde{T}/\partial\tilde{c}_l^{\mathrm{Mn}}\right)_A$	-503.40987 K	$\left(\partial\tilde{T}/\partial\tilde{c}_l^{\mathrm{Mn}}\right)_B$	-399.14278 K
$\left(\partial\tilde{T}/\partial\tilde{c}_l^{\mathrm{C}}\right)_A$	-7954.6705 K	$\left(\partial\tilde{T}/\partial\tilde{c}_l^{\mathrm{C}}\right)_B$	-6717.6148 K
$\tilde{c}_{s,A}^{\mathrm{Mn}}$	$1.02349830 \cdot 10^{-2}$	$\tilde{c}_{s,B}^{\mathrm{Mn}}$	$1.62194480 \cdot 10^{-2}$
$\left(\partial\tilde{c}_s^{\mathrm{Mn}}/\partial\tilde{c}_l^{\mathrm{Mn}}\right)_A$	0.73438282	$\left(\partial\tilde{c}_s^{\mathrm{Mn}}/\partial\tilde{c}_l^{\mathrm{Mn}}\right)_B$	0.72859525
$\left(\partial\tilde{c}_s^{\mathrm{Mn}}/\partial\tilde{c}_l^{\mathrm{C}}\right)_A$	-0.14228358	$\left(\partial\tilde{c}_s^{\mathrm{Mn}}/\partial\tilde{c}_l^{\mathrm{C}}\right)_B$	-0.13937542
$\tilde{c}_{s,A}^{\mathrm{C}}$	$3.00995580 \cdot 10^{-4}$	$\tilde{c}_{s,B}^{\mathrm{C}}$	$2.19010220 \cdot 10^{-3}$
$\left(\partial\tilde{c}_s^{\mathrm{C}}/\partial\tilde{c}_l^{\mathrm{Mn}}\right)_A$	$-1.15022550 \cdot 10^{-3}$	$\left(\partial\tilde{c}_s^{\mathrm{C}}/\partial\tilde{c}_l^{\mathrm{Mn}}\right)_B$	$-3.47417690 \cdot 10^{-3}$
$\left(\partial\tilde{c}_s^{\mathrm{C}}/\partial\tilde{c}_l^{\mathrm{C}}\right)_A$	0.16776847	$\left(\partial\tilde{c}_s^{\mathrm{C}}/\partial\tilde{c}_l^{\mathrm{C}}\right)_B$	0.35739281

Table 4.2: linearization parameters for the linearization of the iron-rich corner of the Fe–Mn–C phase diagram for solidification simulations of Fe–0.4wt.%Mn–1.8wt.%C alloy. See the note on units of the given values in Table 4.1. Note that the values without units indicated are dimensionless.

The border line Eq. (3.31), between the ferrite and austenite regions were approximated with a straight line, which is tangential to the real phase border at the point where the solidification path intersects the peritectic line. The equation of the the straight line estimated using Thermo-Calc data was:

$$\tilde{c}_l^{\mathrm{C}} = 5.276 \cdot 10^{-3} - 4.162 \cdot 10^{-2}\tilde{c}_l^{\mathrm{Mn}} \tag{4.10}$$

4.3.3 Spline interpolation

To interpolate the pointwise tabulated Thermo-Calc ternary thermodynamics data the SINTEF Spline Library (SISL) was used |SIN06, SIN05|. The SISL Reference Manual describes the SISL library as follows |SIN05|:

> "SISL is a geometric toolkit to model with curves and surfaces. It is a library of C functions to perform operations such as the definition, intersection and evaluation of NURBS (Non-Uniform Rational B-spline) geometries. (...)"

These SISL functions were called from FLUENT's User Defined Functions and from the Hybrid Powell's method described in Section 4.2 nonlinear equation solver functions.

Firstly, the SISL function s1535 is called to create spline interpolations of Thermo-Calc [The06a] tabulated data of values of functions (3.15)-(3.17). Then the SISL function s1506 is called each time the Hybrid Powell's Method nonlinear equation solver functions need to evaluate either the values of the functions (3.15)-(3.17) or the Jacobian of the system of nonlinear equations (3.16)-(3.21) according to its algorithm.

The thermodynamic functions (3.15)-(3.17) values, their first and cross derivatives were tabulated for the iron-rich corner of Fe–C–Cr phase diagram in the rectangular region on a grid $\Omega_{h_1 h_2}$ as defined by Eq. (3.38) with $N_1 = N_2 = 200$, $a = 0.06$, $b = 0.6$, $h_1 = {}^{a}/_{N_1}$, $h_2 = {}^{b}/_{N_2}$, $A = \mathrm{C}$, and $B = \mathrm{Cr}$. Note that a and b have units of mass fraction. The tabulations were performed using a self-written C-program that calls Thermo-Calc routines using Thermo-Calc API [The06b]. Thermo-Calc API provides routines to calculate the values and first derivatives of the thermodynamic functions (3.15)-(3.17). Cross derivatives were estimated numerically using first derivatives on a grid with spatial steps $0.5h_1$ and $0.5h_2$ in directions of both parameters. Then the arrays containing tabulated values of thermodynamic functions, their derivatives and cross derivatives were supplied to the SISL function s1535 to compute B-forms of interpolating splines of two variables of third order, which were used in the numerical procedure of solving the nonlinear equation system (3.15)-(3.17) as described above in Section 4.2. The graphical representation of these functions as contour plots with isolines are shown in Figs. 3.4-3.6.

In order to perform the spline interpolation successfully, one has to make the right choice of the parameters of interpolation: spline order and an appropriate parametrisation. There are two ways to parametrise a B-spline surface using the SISL library: a uniform and arc-length based parametrizations. For our case the uniform parametrisation was used, with the natural choice for the parameters of $(\tilde{c}_l^{\mathrm{C}}, \tilde{c}_l^{\mathrm{Cr}})$.

Determination of the spline order for the interpolation

The other parameter to choose is the order of the spline surface with respect to the first and the second parameter. In order to find out the optimal order of the spline-interpolating surface, interpolating spline surfaces were computed with orders 3rd to 15th (same order for both parameters) on a 200x200 grid of tabulated data. Then, these interpolating spline-surfaces were used to evaluate the values of the thermodynamic functions (3.15), (3.16), (3.17) and their first derivatives on a 600x600 grid and compared with the data tabulated on the same 600x600 grid. The dependence of the accuracy on the spline degree can be illustrated with the Fig. 4.2, where the spline-interpolants of different order created using 200x200 tabulated data for the function (3.16) and the tabulated 600x600 data are compared along a line $\tilde{c}_l^{\mathrm{C}} = 0.0158$. Consider Fig. 3.5 where the function (3.16) is shown : the aforementioned line $\tilde{c}_l^{\mathrm{C}} = 0.0158$ is a coordinate line parallel to the horizontal axis and crosses the phase border between ferrite and austenite near the point with coordinates ($\tilde{c}_l^{\mathrm{C}} = 0.0158$, $\tilde{c}_l^{\mathrm{Cr}} \approx 0.22$). As expected, significant interpolation errors occur near the discontinuity experienced by the function (3.16) along the phase border (see Fig. 4.2).

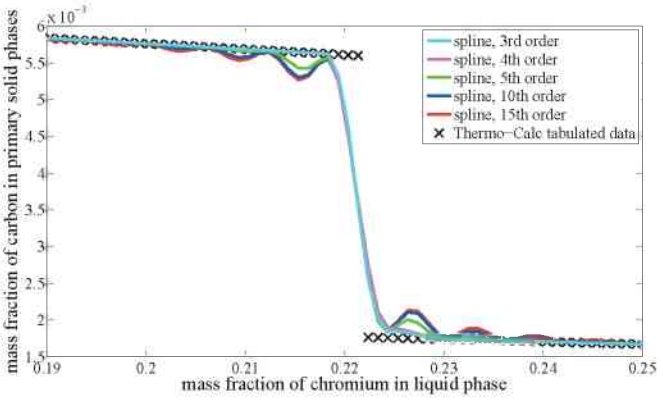

Figure 4.2: Comparison between the spline-interpolants of different order and the tabulated data, projected onto the plane $\tilde{c}_l^{\mathrm{C}} = 0.0158$.

In order to quantify the interpolation error, the relative error vectors with the components

$$\epsilon_{\mathrm{rel},i} = \frac{|f_{i,\mathrm{exact}} - f_{i,\mathrm{interpolated}}|}{|f_{i,\mathrm{exact}}|} \tag{4.11}$$

were calculated. Here $i = 1, \ldots, 600 \cdot 600$ is the number of a data point on a 600x600 grid, $f_{i,\text{exact}}$ is the value of a tabulated function and $f_{i,\text{interpolated}}$ is the value of the spline interpolant at the same point. Function f here represents one of the thermodynamic functions (3.15), (3.16), (3.17) or their first derivative. Further, to quantify the interpolation error, their maximum norms

$$||\epsilon_{\text{rel}}||_\infty = \max_{1 \leq i \leq 360000} |\epsilon_{\text{rel},i}| \tag{4.12}$$

and their Euclidean norms

$$||\epsilon_{\text{rel}}||_2 = \sqrt{\Sigma_{i=1}^{i=360000} (\epsilon_{\text{rel},i})^2} \tag{4.13}$$

were calculated. The dependence of these two norms on spline surface order for functions (3.15), (3.16) is shown in the Figs. 4.3 and 4.4. For other thermodynamic functions and their derivatives these relations are analogous.

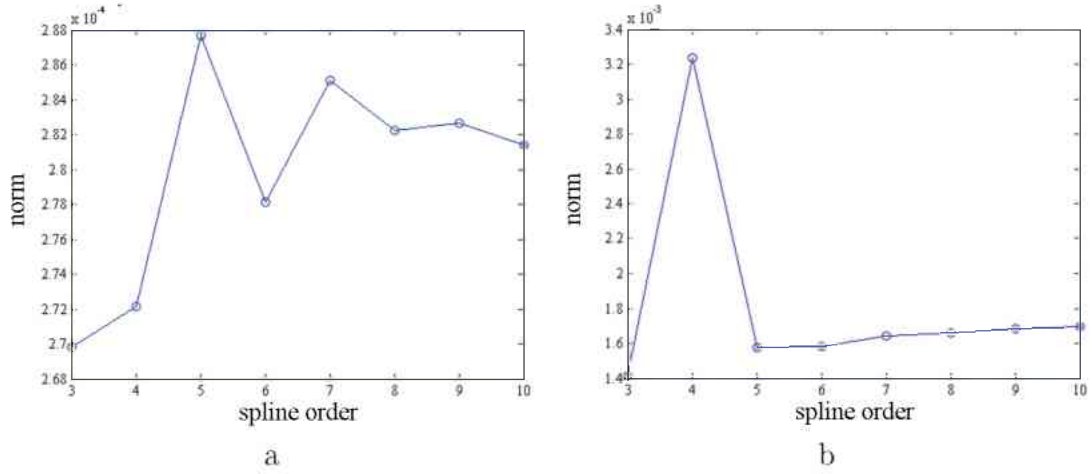

Figure 4.3: Dependence of the norms $||\epsilon_{\text{rel}}||_\infty$ (a) and $||\epsilon_{\text{rel}}||_2$ (b) for the liquidus temperature (3.15) on the interpolating spline surface order

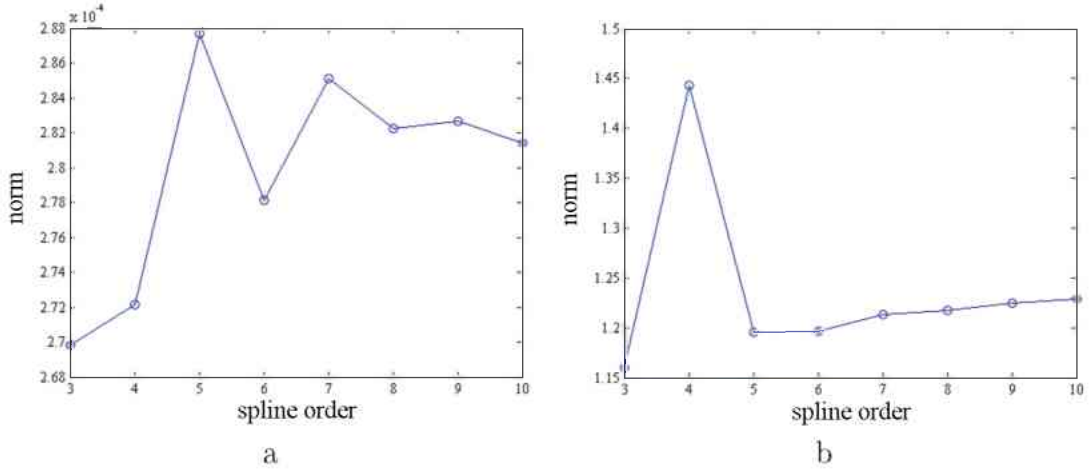

Figure 4.4: Dependence of the norm $||\epsilon_{\text{rel}}||_\infty$ (a) and $||\epsilon_{\text{rel}}||_2$ (b) for the solubility of chromium (3.16) on the spline surface order

As it can be seen from the Fig. 4.3 and Fig. 4.4, the smallest error corresponds to the third order of interpolating spline surfaces and so the third order was used for the interpolation in the simulations.

4.3.4 Error analysis for piecewise-linear interpolation and spline interpolation

Let us investigate the error introduced by the approximation of the three thermodynamic functions of interest $\bar{T}_l(\bar{c}_l^{\text{C}}, \bar{c}_l^{\text{Cr}})$, $\bar{c}_s^{\text{C}}(\bar{c}_l^{\text{C}}, \bar{c}_l^{\text{Cr}})$ and $\bar{c}_s^{\text{Cr}}(\bar{c}_l^{\text{C}}, \bar{c}_l^{\text{Cr}})$, that we will denote here as function $f(\bar{c}_l^{\text{C}}, \bar{c}_l^{\text{Cr}})$ using piecewise-linear approximation and spline interpolation. Let f_{exact} denote the value of the function calculated using Thermo-Calc, the value which we will consider to be exact and f_{approx} to the approximate value of the function f, calculated either using spline tabulation of previously tabulated data or using piecewise-linear approximation.

The relative error of approximation of a thermodynamic function f can be calculated using the following formula:

$$\epsilon_{\text{rel}} = \frac{|f_{\text{exact}} - f_{\text{approx}}|}{|f_{\text{exact}}|}. \tag{4.14}$$

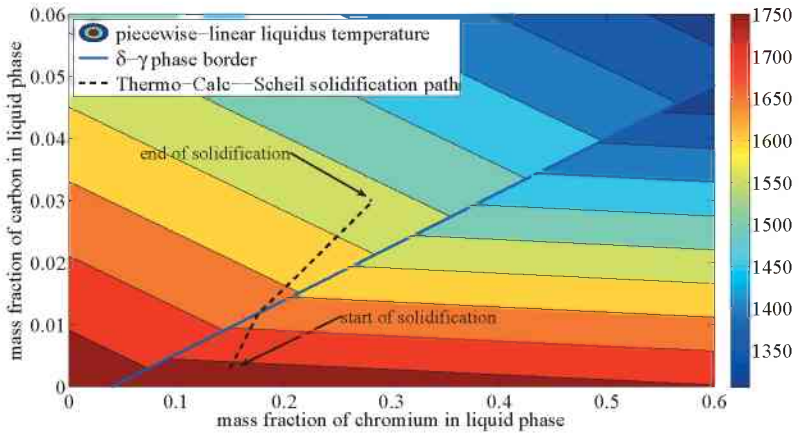

Figure 4.5: Piecewise-linear representation of the liquidus temperature $\tilde{T}_l(\tilde{c}_l^{\mathrm{C}}, \tilde{c}_l^{\mathrm{Cr}})$ for the iron-rich corner of the Fe–C–Cr phase diagram. A discontinuity in the values of the liquidus temperature can be seen along the border between δ and γ phases. Note that in reality the liquidus temperature is continuous. A solidification path calculated using Thermo-Calc–Scheil module for X30Cr15 alloy is shown for reference.

Piecewise-linear approximation

The contour plots of the piecewise-linear approximations of the three thermodynamic functions of interest, $\tilde{T}_l(\tilde{c}_l^{\mathrm{C}}, \tilde{c}_l^{\mathrm{Cr}})$, $\tilde{c}_s^{\mathrm{C}}(\tilde{c}_l^{\mathrm{C}}, \tilde{c}_l^{\mathrm{Cr}})$ and $\tilde{c}_s^{\mathrm{Cr}}(\tilde{c}_l^{\mathrm{C}}, \tilde{c}_l^{\mathrm{Cr}})$ in the iron-rich corner are shown in the Figs. 4.5, 4.6 and 4.7 respectively.

The corresponding Thermo-Calc tabulated functions (not interpolated or approximated) are shown in Figs. 3.4, 3.5 and 3.6 respectively.

The decimal logarithms of the relative error of approximation for piecewise-linear approximations $\log_{10} \epsilon_{\mathrm{rel}}$ were calculated for the iron-rich corner of the Fe–C–Cr for the three thermodynamic functions of interest $\tilde{T}_l(\tilde{c}_l^{\mathrm{C}}, \tilde{c}_l^{\mathrm{Cr}})$, $\tilde{c}_s^{\mathrm{C}}(\tilde{c}_l^{\mathrm{C}}, \tilde{c}_l^{\mathrm{Cr}})$ and $\tilde{c}_s^{\mathrm{Cr}}(\tilde{c}_l^{\mathrm{C}}, \tilde{c}_l^{\mathrm{Cr}})$. They are shown in Fig. 4.8, Fig. 4.9 and 4.10 respectively.

As it can be seen in Figs. 4.8, 4.9 and 4.10 showing the distribution of the approximation error, the smallest error areas are situated around the points where linearizations were done. The further are the areas from these points, the higher gets the approximation error, rendering these piecewise-linear approximation unusable for simulating solidification of alloys with initial concentrations that are far away from the linearization points. Nevertheless, in the neighbourhood of the Thermo-Calc–Scheil solidification path the relative error of approximation is

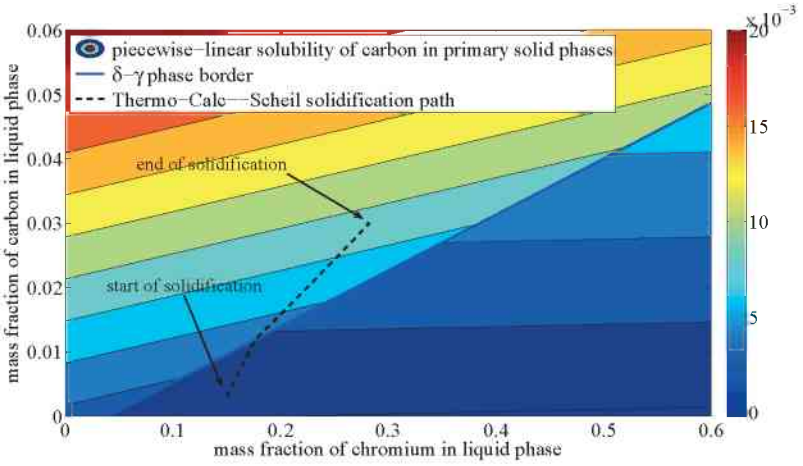

Figure 4.6: Piecewise-linear representation of the solubility of carbon in primary solid phases $\tilde{c}_s^{\mathrm{C}}(\tilde{c}_l^{\mathrm{C}}, \tilde{c}_l^{\mathrm{Cr}})$ in the iron-rich corner of the Fe–C–Cr phase diagram. A discontinuity in the values of the solubility can be seen along the border between δ and γ phases. In reality this function is also discontinuous along the phase borders. A solidification path calculated using Thermo-Calc–Scheil module for X30Cr15 alloy is shown for reference.

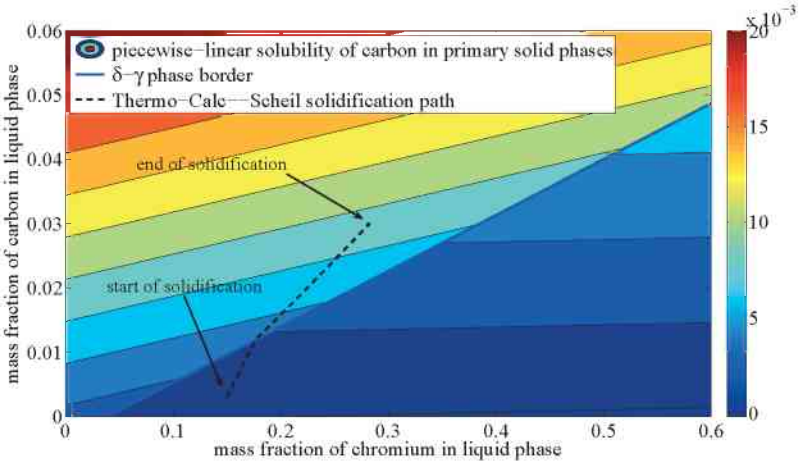

Figure 4.7: Piecewise-linear representation of the solubility of carbon in primary solid phases $\tilde{c}_s^{\mathrm{Cr}}(\tilde{c}_l^{\mathrm{C}}, \tilde{c}_l^{\mathrm{Cr}})$ in the iron-rich corner of the Fe–C–Cr phase diagram. A discontinuity in the values of the solubility can be seen along the border between δ and γ phases. In reality this function is also discontinuous along phase borders. A solidification path calculated using Thermo-Calc–Scheil module for X30Cr15 alloy is shown for reference.

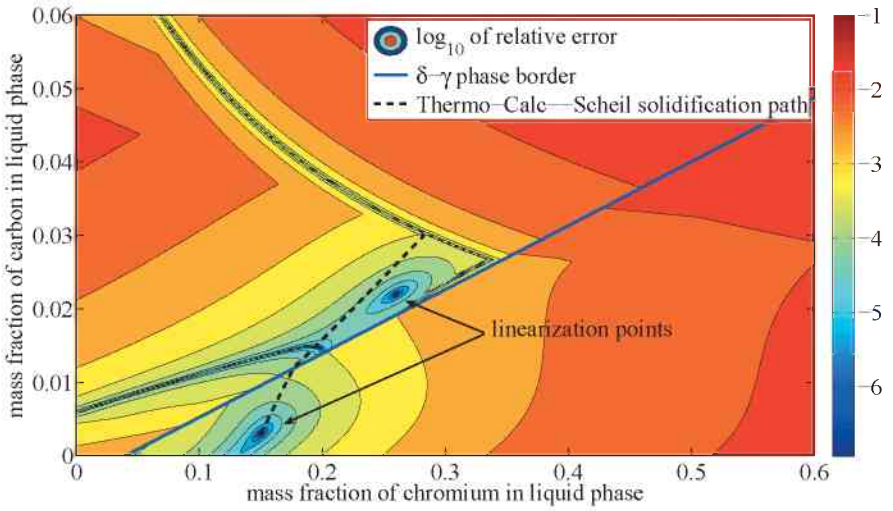

Figure 4.8: Decimal logarithm of the relative error $\log_{10}\epsilon_{\text{rel}}$, Eq. (4.14), for piecewise linear approximation of the liquidus temperature $\tilde{T}_l(\tilde{c}_l^{\text{C}}, \tilde{c}_l^{\text{Cr}})$ for the iron-rich corner of the Fe–C–Cr phase diagram. Note that the points used for linearization and their neighbourhood can be clearly identified by the areas with the lowest error. A solidification path calculated using Thermo-Calc–Scheil module for X30Cr15 alloy is shown for reference.

relatively low: up to 10^{-3} for the liquidus surface (4.5), up to about 10^{-1} for the solubility of carbon in primary solid phases and up to 10^{-2} for the solubility of chromium.

Spline interpolation using 100x100 points for tabulation

The contour plots of the spline interpolations of the three thermodynamic functions of interest $\tilde{T}_l(\tilde{c}_l^{\text{C}}, \tilde{c}_l^{\text{Cr}})$, $\tilde{c}_s^{\text{C}}(\tilde{c}_l^{\text{C}}, \tilde{c}_l^{\text{Cr}})$ and $\tilde{c}_s^{\text{Cr}}(\tilde{c}_l^{\text{C}}, \tilde{c}_l^{\text{Cr}})$ in the iron-rich corner tabulated on a 100x100 grid are shown in Figs. 4.11, 4.12 and 4.13 respectively.

The decimal logarithms of the relative error of approximation for splines on 100x100 grid $\log_{10}\epsilon_{\text{rel}}$ were calculated for the iron-rich corner of the Fe–C–Cr for the three thermodynamic functions of interest $\tilde{T}_l(\tilde{c}_l^{\text{C}}, \tilde{c}_l^{\text{Cr}})$, $\tilde{c}_s^{\text{C}}(\tilde{c}_l^{\text{C}}, \tilde{c}_l^{\text{Cr}})$ and $\tilde{c}_s^{\text{Cr}}(\tilde{c}_l^{\text{C}}, \tilde{c}_l^{\text{Cr}})$. They are shown in Fig. 4.14, Fig. 4.15 and 4.16 respectively.

From these figures depicting the relative error in approximation we see that the liquidus temperature $\tilde{T}_l(\tilde{c}_l^{\text{C}}, \tilde{c}_l^{\text{Cr}})$ (Fig. 4.14) is represented in the whole region of interest with the maximal relative error of 10^{-4} and it is continuous contrary to the piecewise-linear approximation. The $\log_{10}||\epsilon_{\text{rel}}||_2$ (defined by Eq.(4.13)) for

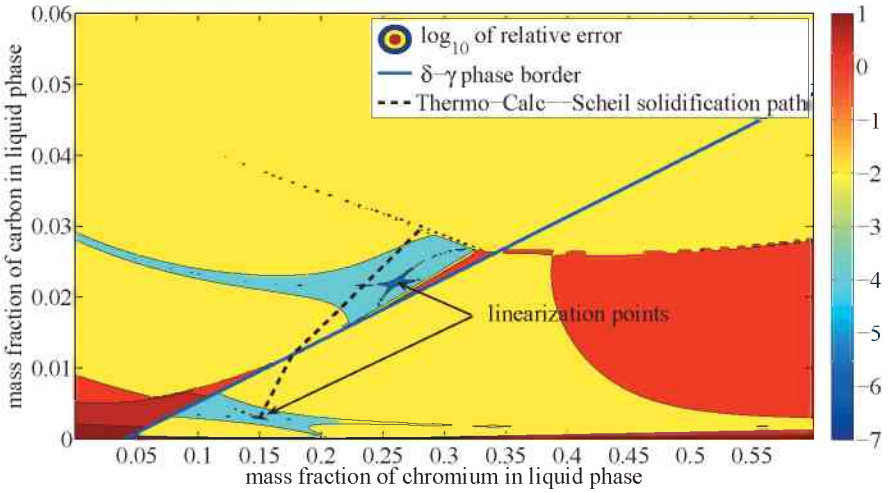

Figure 4.9: Decimal logarithm of the relative error $\log_{10} \epsilon_{\text{rel}}$, Eq. (4.14), for piecewise linear approximation of the solubility of chromium in the primary solid phases $\tilde{c}_s^{\text{C}}(\tilde{c}_l^{\text{C}}, \tilde{c}_l^{\text{Cr}})$ for the iron-rich corner of the Fe–C–Cr phase diagram. Note that the points used for linearization and their neighbourhood can be clearly identified by the areas with the lowest error. A solidification path calculated using Thermo-Calc–Scheil module for X30Cr15 alloy is shown for reference.

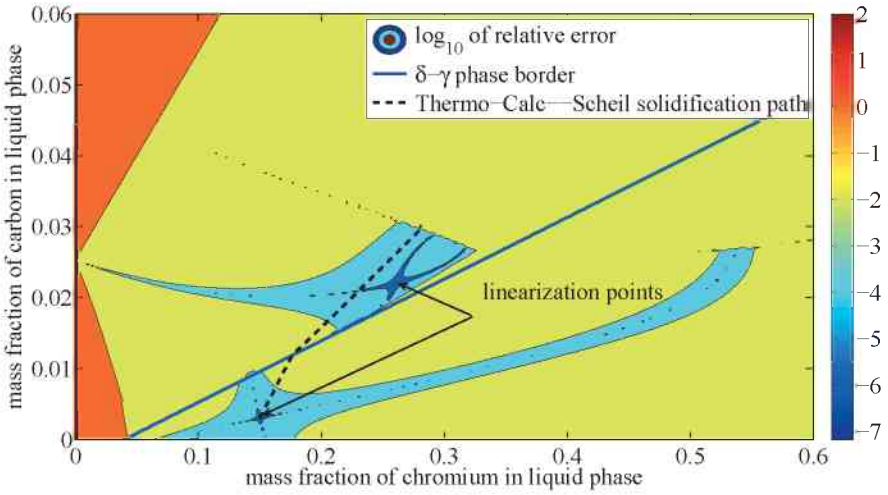

Figure 4.10: Decimal logarithm of the relative error $\log_{10} \epsilon_{\text{rel}}$, Eq. (4.14), for piecewise linear approximation of the solubility of chromium in the primary solid phases $\tilde{c}_s^{\text{Cr}}(\tilde{c}_l^{\text{C}}, \tilde{c}_l^{\text{Cr}})$ for the iron-rich corner of the Fe–C–Cr phase diagram. Note that the points used for linearization and their neighbourhood can be clearly identified by the areas with the lowest error. A solidification path calculated using Thermo-Calc–Scheil module for X30Cr15 alloy is shown for reference.

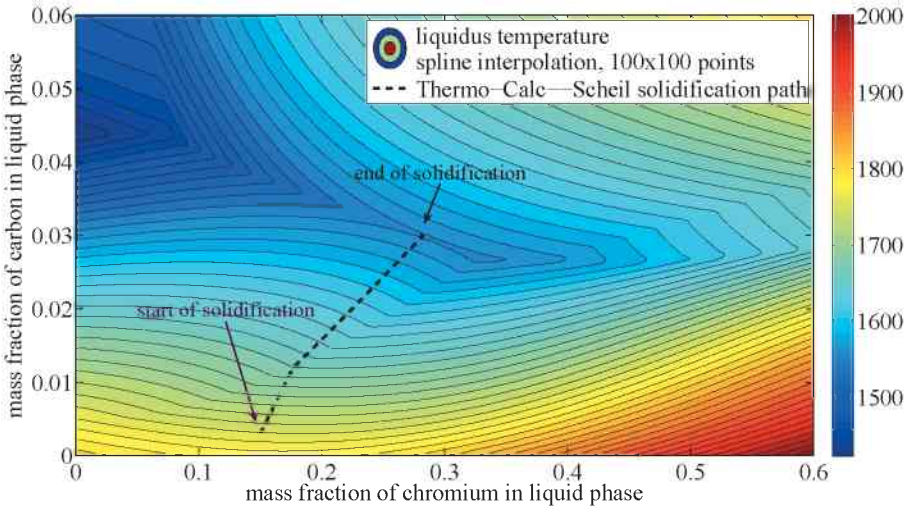

Figure 4.11: Spline interpolation of the liquidus temperature $\tilde{T}_l(\tilde{c}_l^{\mathrm{C}}, \tilde{c}_l^{\mathrm{Cr}})$ for the iron-rich corner of the Fe–C–Cr phase diagram using 100x100 points tabulation. Note the continuity of the approximation. A solidification path calculated using Thermo-Calc–Scheil module for X30Cr15 alloy is shown for reference.

liquidus temperature is equal to -2.1240 for the whole region considered. Calculating the norm of the relative error for solubilities $\tilde{c}_s^{\mathrm{C}}(\tilde{c}_l^{\mathrm{C}}, \tilde{c}_l^{\mathrm{Cr}})$ and $\tilde{c}_s^{\mathrm{Cr}}(\tilde{c}_l^{\mathrm{C}}, \tilde{c}_l^{\mathrm{Cr}})$ is meaningless since it is too big. The situation with spline interpolation of tabulated data for the solubilities of carbon $\tilde{c}_s^{\mathrm{C}}(\tilde{c}_l^{\mathrm{C}}, \tilde{c}_l^{\mathrm{Cr}})$ and chromium $\tilde{c}_s^{\mathrm{Cr}}(\tilde{c}_l^{\mathrm{C}}, \tilde{c}_l^{\mathrm{Cr}})$ is complicated by the discontinuities of these functions at the phase borders. Due to this, there are very small areas which have high relative error up to 10^2. Those areas are situated in the vicinity and at the phase borders, where discontinuities of the solubilities are now smoothed and since splines used are continuous functions, this causes such a big errors, since they do not represent the discontinuous function jumps precisely.

Spline interpolation using 200x200 points for tabulation

The contour plots of the spline interpolations of the three thermodynamic functions of interest $\tilde{T}_l(\tilde{c}_l^{\mathrm{C}}, \tilde{c}_l^{\mathrm{Cr}})$, $\tilde{c}_s^{\mathrm{C}}(\tilde{c}_l^{\mathrm{C}}, \tilde{c}_l^{\mathrm{Cr}})$ and $\tilde{c}_s^{\mathrm{Cr}}(\tilde{c}_l^{\mathrm{C}}, \tilde{c}_l^{\mathrm{Cr}})$ in the iron-rich corner tabulated on a 200x200 grid are shown in the Figs. 4.17, 4.18 and 4.19 respectively.

The decimal logarithms of the relative error of approximation for splines on

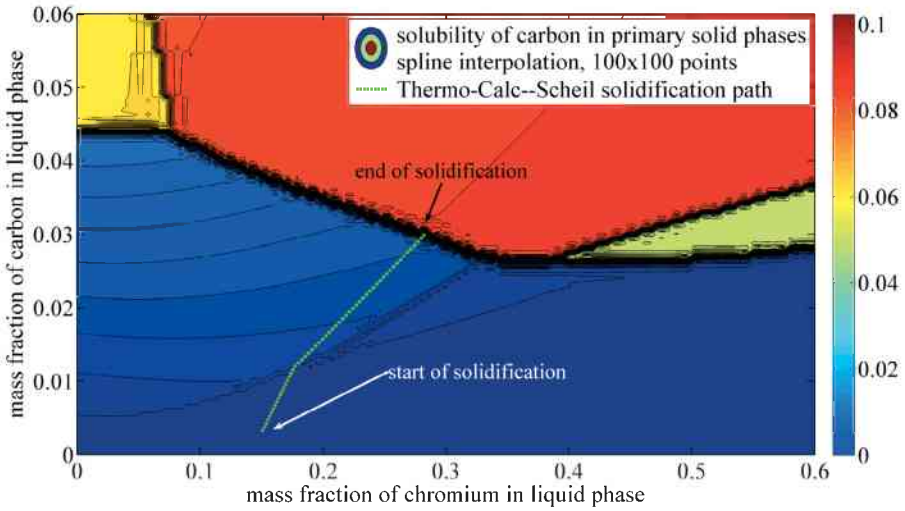

Figure 4.12: Spline interpolation of the solubility of carbon in primary solid phases $\tilde{c}_s^{\mathrm{C}}(\tilde{c}_l^{\mathrm{C}}, \tilde{c}_l^{\mathrm{Cr}})$ for the iron-rich corner of the Fe–C–Cr phase diagram using 100x100 points tabulation. Note that the clear change in the values of the solubility can be seen along the phase borders. A solidification path calculated using Thermo-Calc–Scheil module for X30Cr15 alloy is shown for reference.

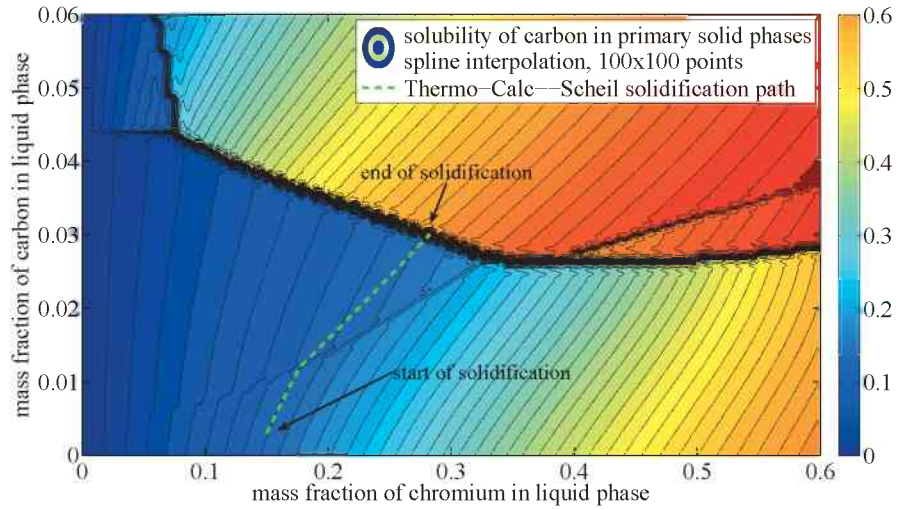

Figure 4.13: Spline interpolation of the solubility of carbon in primary solid phases $\tilde{c}_s^{\mathrm{Cr}}(\tilde{c}_l^{\mathrm{C}}, \tilde{c}_l^{\mathrm{Cr}})$ for the iron-rich corner of the Fe–C–Cr phase diagram using 100x100 points tabulation. Note that the clear change in the values of the solubility can be seen along the phase borders. A solidification path calculated using Thermo-Calc–Scheil module for X30Cr15 alloy is shown for reference.

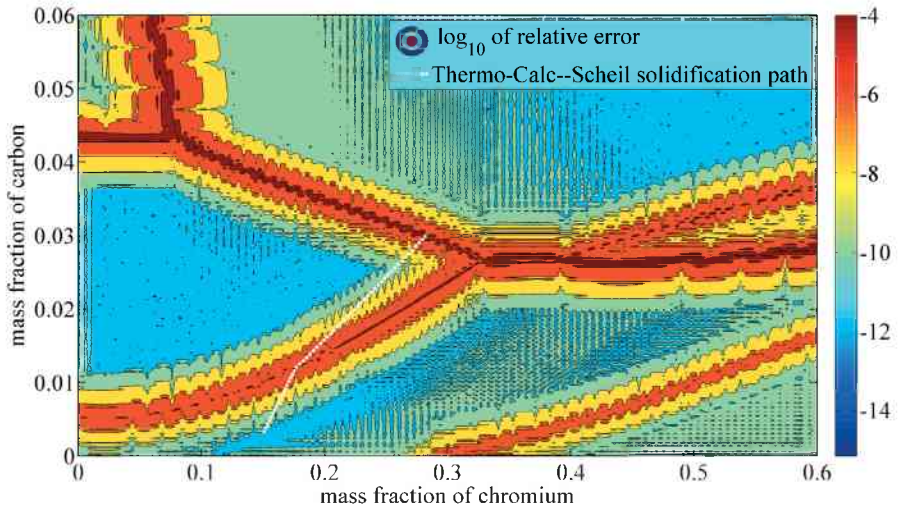

Figure 4.14: Decimal logarithm of the relative error $\log_{10} \epsilon_{\text{rel}}$ for the spline interpolation of the 100x100 tabulation of the liquidus temperature $\tilde{T}_l(\tilde{c}_l^{\text{C}}, \tilde{c}_l^{\text{Cr}})$ for the iron-rich corner of the Fe–C–Cr phase diagram. It can be seen that the error is highest near the phase borders and the error is low away from them. A solidification path calculated using Thermo-Calc–Scheil module for X30Cr15 alloy is shown for reference.

200x200 grid $\log_{10} \epsilon_{\text{rel}}$ were calculated for the iron-rich corner of the Fe–C–Cr for the three thermodynamic functions of interest $\tilde{T}_l(\tilde{c}_l^{\text{C}}, \tilde{c}_l^{\text{Cr}})$, $\tilde{c}_s^{\text{C}}(\tilde{c}_l^{\text{C}}, \tilde{c}_l^{\text{Cr}})$ and $\tilde{c}_s^{\text{Cr}}(\tilde{c}_l^{\text{C}}, \tilde{c}_l^{\text{Cr}})$. They are shown in Fig. 4.20, Fig. 4.21 and 4.22 respectively.

Everything said for 100x100 spline case holds for this 200x200 case. In comparison with the 100x100 case, the 200x200 case provides higher precision in the sense that the areas with the maximal error are smaller. On the other hand, increasing the number of nodes does not decrease the maximal error in the case of solubilities of alloying elements since this error is caused by the discontinuity of this functions and not by the approximation. On the other hand, the overall error of approximation of the liquidus temperature which is continuous, quantified by the $\log_{10} ||\epsilon_{\text{rel}}||_2$, which is equal to -2.6583 is bigger than in the case of the 100x100 tabulation. The norm of the relative error is bigger, but these two values of the norm are not representative to draw the conclusion that the approximation error increases with the number of nodes.

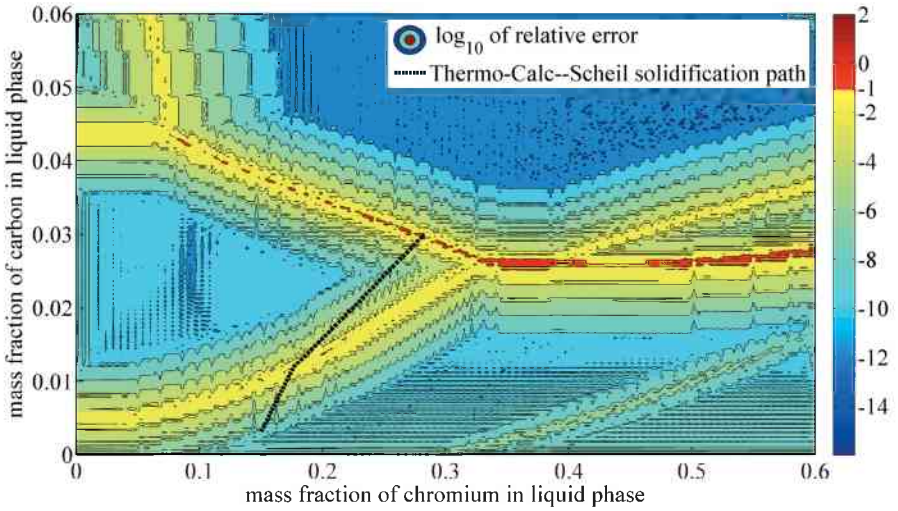

Figure 4.15: Decimal logarithm of the relative error $\log_{10} \epsilon_{\text{rel}}$ for the spline interpolation of the 100x100 tabulation of the solubility of carbon in the primary solid phases $\tilde{c}_s^{\text{C}}(\tilde{c}_l^{\text{C}}, \tilde{c}_l^{\text{Cr}})$ for the iron-rich corner of the Fe–C–Cr phase diagram. It can be seen that the error is highest near the phase borders and the error is low away from them. A solidification path calculated using Thermo-Calc–Scheil module for X30Cr15 alloy is shown for reference.

Conclusion about approximations

Comparing all three considered ways of approximating the liquidus temperature $\tilde{T}_l(\tilde{c}_l^{\text{C}}, \tilde{c}_l^{\text{Cr}})$ and solubilities of carbon $\tilde{c}_s^{\text{C}}(\tilde{c}_l^{\text{C}}, \tilde{c}_l^{\text{Cr}})$ and chromium $\tilde{c}_s^{\text{Cr}}(\tilde{c}_l^{\text{C}}, \tilde{c}_l^{\text{Cr}})$ in primary solid phases, we can draw several conclusions.

The piecewise-linear approximations are quite precise, and in combination with the relative ease of the calculation of their parameters (9 parameters using Thermo-Calc) and implementation (2 equations for each thermodynamic functions) they present an acceptable tool for representing the Fe–C–Cr phase diagram not far away from the linearization points.

The approximation of the thermodynamic functions using splines is precise in the whole iron-rich corner of the Fe–C–Cr phase diagram for the liquidus temperature. For solubilities it is precise in the iron-rich corner apart from the phase borders. The approximation using splines introduces an approximation error connected with smoothing of these functions discontinuities along the phase borders. This is also can be seen in the Fig. 4.2: it is clear that the relatively big value of the error should not be considered as a problem, since the smoothing of

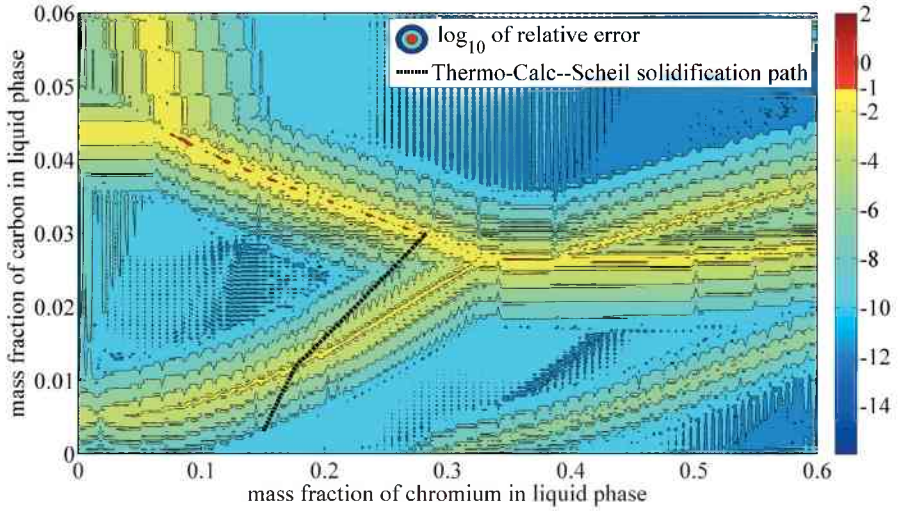

Figure 4.16: Decimal logarithm of the relative error $\log_{10} \epsilon_{\mathrm{rel}}$ for the spline interpolation of the 100x100 tabulation of the solubility of carbon in the primary solid phases $\tilde{c}_s^{\mathrm{Cr}}(\tilde{c}_l^{\mathrm{C}}, \tilde{c}_l^{\mathrm{Cr}})$ for the iron-rich corner of the Fe–C–Cr phase diagram. It can be seen that the error is highest near the phase borders and the error is low away from them. A solidification path calculated using Thermo-Calc–Scheil module for X30Cr15 alloy is shown for reference.

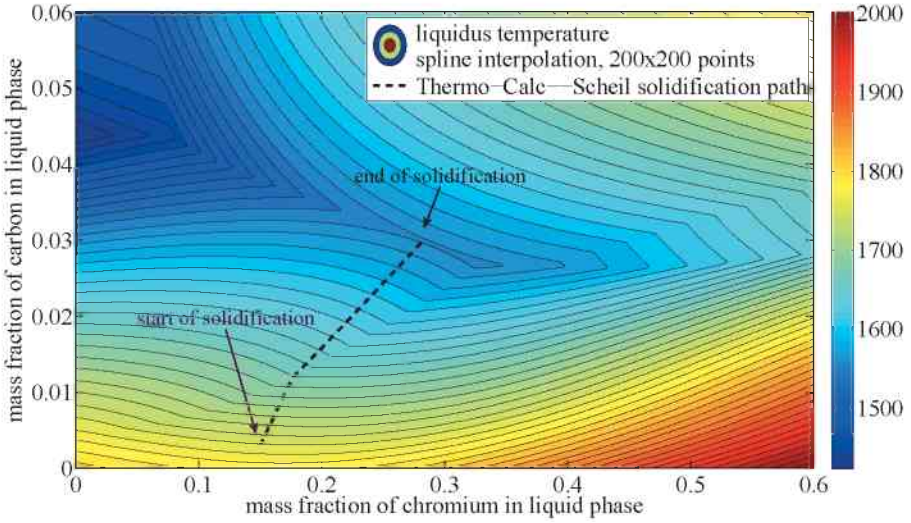

Figure 4.17: Spline interpolation of the liquidus temperature $\tilde{T}_l(\tilde{c}_l^{\mathrm{C}}, \tilde{c}_l^{\mathrm{Cr}})$ for the iron-rich corner of the Fe–C–Cr phase diagram using 200x200 points tabulation. Note the continuity of the approximation. A solidification path calculated using Thermo-Calc–Scheil module for X30Cr15 alloy is shown for reference.

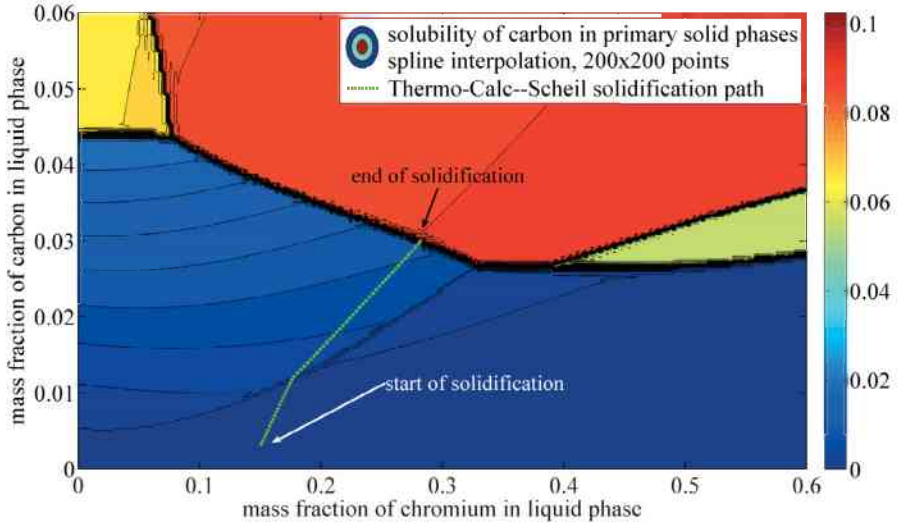

Figure 4.18: Spline interpolation of the solubility of carbon in primary solid phases $\tilde{c}_s^{\mathrm{C}}(\tilde{c}_l^{\mathrm{C}}, \tilde{c}_l^{\mathrm{Cr}})$ for the iron-rich corner of the Fe–C–Cr phase diagram using 200x200 points tabulation. Note that the clear change in the values of the solubility can be seen along the phase borders. A solidification path calculated using Thermo-Calc–Scheil module for X30Cr15 alloy is shown for reference.

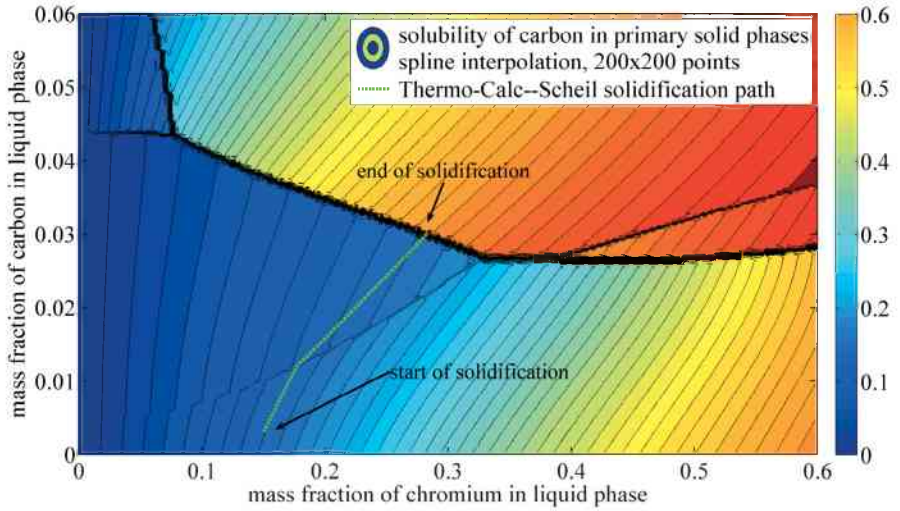

Figure 4.19: Spline interpolation of the solubility of carbon in primary solid phases $\tilde{c}_s^{\mathrm{Cr}}(\tilde{c}_l^{\mathrm{C}}, \tilde{c}_l^{\mathrm{Cr}})$ for the iron-rich corner of the Fe–C–Cr phase diagram using 200x200 points tabulation. Note that the clear change in the values of the solubility can be seen along the phase borders. A solidification path calculated using Thermo-Calc–Scheil module for X30Cr15 alloy is shown for reference.

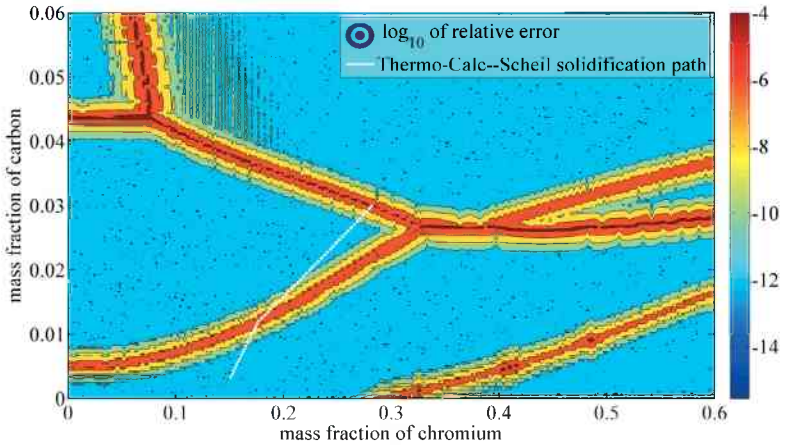

Figure 4.20: Decimal logarithm of the relative error $\log_{10} \epsilon_{\text{rel}}$ for the spline interpolation of the 200x200 tabulation of the liquidus temperature $\tilde{T}_l(\tilde{c}_l^{\text{C}}, \tilde{c}_l^{\text{Cr}})$ for the iron-rich corner of the Fe–C–Cr phase diagram. It can be seen that the error is highest near the phase borders and the error is low away from them. A solidification path calculated using Thermo-Calc–Scheil module for X30Cr15 alloy is shown for reference.

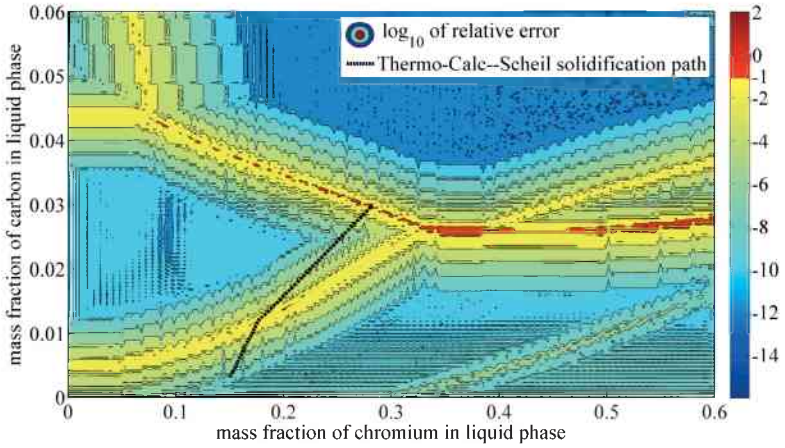

Figure 4.21: Decimal logarithm of the relative error $\log_{10} \epsilon_{\text{rel}}$ for the spline interpolation of the 200x200 tabulation of the solubility of carbon in the primary solid phases $\tilde{c}_s^{\text{C}}(\tilde{c}_l^{\text{C}}, \tilde{c}_l^{\text{Cr}})$ for the iron-rich corner of the Fe–C–Cr phase diagram. It can be seen that the error is highest near the phase borders and the error is low away from them. A solidification path calculated using Thermo-Calc–Scheil module for X30Cr15 alloy is shown for reference.

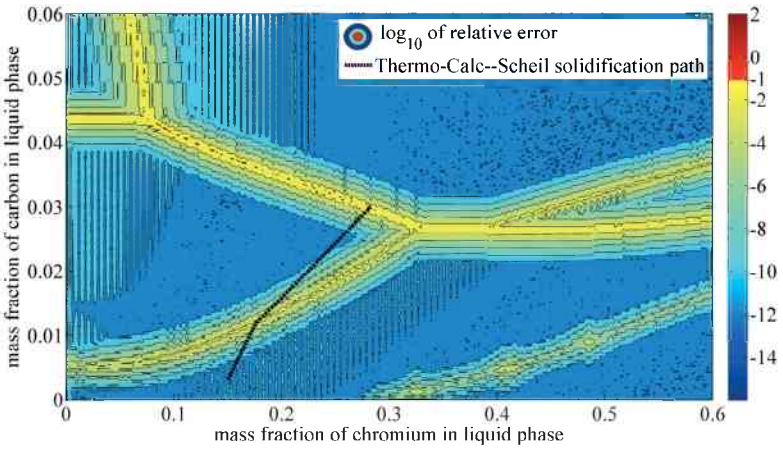

Figure 4.22: Decimal logarithm of the relative error $\log_{10} \epsilon_{\mathrm{rel}}$ for the spline interpolation of the 200x200 tabulation of the solubility of carbon in the primary solid phases $\tilde{c}_s^{\mathrm{Cr}}(\tilde{c}_l^{\mathrm{C}}, \tilde{c}_l^{\mathrm{Cr}})$ for the iron-rich corner of the Fe–C–Cr phase diagram. It can be seen that the error is highest near the phase borders and the error is low away from them. A solidification path calculated using Thermo-Calc–Scheil module for X30Cr15 alloy is shown for reference.

solubilities discontinuities is a good feature of the approximation of the solubilities using splines, which allows using Newton-type iterations for the solving of the nonlinear equation system with these three functions. The approximation using spline interpolation provides both precise and continuous way of representing the thermodynamic functions. The approximation using splines interpolation of the functions tabulated on a 100x100 grid will be used for the solidification simulations.

Chapter 5

Validation of the coupling between solidification thermodynamics, kinetics and Eulerian multiphase flow model

In order to validate the methods of representing the phase diagram information in the form of piecewise-linear approximations and spline interpolations proposed above, the initial value problem consisting of three ordinary differential equations (3.1), (3.9), (3.10) and the initial conditions given by Eq. (3.11) was solved numerically using MATLAB |Grupp04, Gramlich00| incorporating the mass transfer rate for the growth of columnar dendrites by means of the formula (2.34). Piecewise-linear approximations and spline interpolation were used to calculate values of the thermodynamic functions given by Eqs. (3.15), (3.16) and (3.17). The diffusion coefficient in Eq. (2.32) was taken bigger than the real one in order to allow the comparison with curves calculated using Thermo-Calc–Scheil module (infinite diffusion in liquid is one of the assumptions of the Scheil model). These calculations were performed for alloys from Fe–C–Cr, Fe–C–Mn and Cu–Sn–P systems. Resulting $c_l^i - f_c$ curves are plotted together with $\tilde{c}_l^i - f_s$ curves computed using the Thermo-Calc–Scheil module described in the Section 2.2. It is Scheil model on one hand, that does not include any morphological information, thus the resulting phase volume fraction is referred here with f_s, the volume fraction of *solid* (hence index s is used, not c), and on the other hand,

the model described in the previous Chapter 3. The latter model includes the morphological information by means of the expression for columnar growth velocity, Eq. (3.19), so the *columnar* volume fraction f_c notation is used to reflect this fact. Additionally, the solidification paths (curves of the form $c_l^i - c_l^j$, where i and j are alloying components, $i \neq j$) obtained from the solution of the initial value problem (also later referred to as the *zero-dimensional model*) are plotted together with the solidification paths $\tilde{c}_l^i - \tilde{c}_l^j$ obtained from Thermo-Calc–Scheil module.

Note that the variables considered in this chapter are dimensionless, since they are volume fractions (f_c and f_s) and mass fractions (c_l^i and $\tilde{c}_l^i$), which express the amount of volumetric units in volumetric units, for example m^3 in m^3 and mass units in mass units, for example kg in kg.

5.1 0-D solidification using piecewise-linear approximations of thermodynamic functions

Solidification of Fe-0.3wt.%C-15wt%Cr alloy

Here is presented the solution of the initial value value problem (3.1), (3.9), (3.10) and (3.11), which was performed for the Fe-0.3wt.%C-15wt%Cr alloy. The initial conditions in the (3.11) were as follows:

$$\begin{aligned} f_c(0) &= 10^{-5}, \\ c_l^{\mathrm{C}}(0) &= 0.003, \\ c_l^{\mathrm{Cr}}(0) &= 0.15. \end{aligned} \tag{5.1}$$

The three thermodynamic functions, Eqs. (3.15), (3.16), (3.17): liquidus temperature $\tilde{T} = \tilde{T}(\tilde{c}_l^{\mathrm{C}}, \tilde{c}_l^{\mathrm{Cr}})$, solubilities of manganese $\tilde{c}_s^{\mathrm{C}}(\tilde{c}_l^{\mathrm{C}}, \tilde{c}_l^{\mathrm{Cr}})$ and solubility of carbon $\tilde{c}_s^{\mathrm{Cr}}(\tilde{c}_l^{\mathrm{C}}, \tilde{c}_l^{\mathrm{Cr}})$ were represented using piecewise-linear approximation described in Section 3.5.1 with parameters from the Table 4.1. The Scheil–curves calculated using the both Scheil-Gulliver and the zero-dimensional models for carbon are shown in the Fig. 5.1, for chromium in the Fig. 5.2. The corresponding solidification paths are shown in the Fig. 5.3.

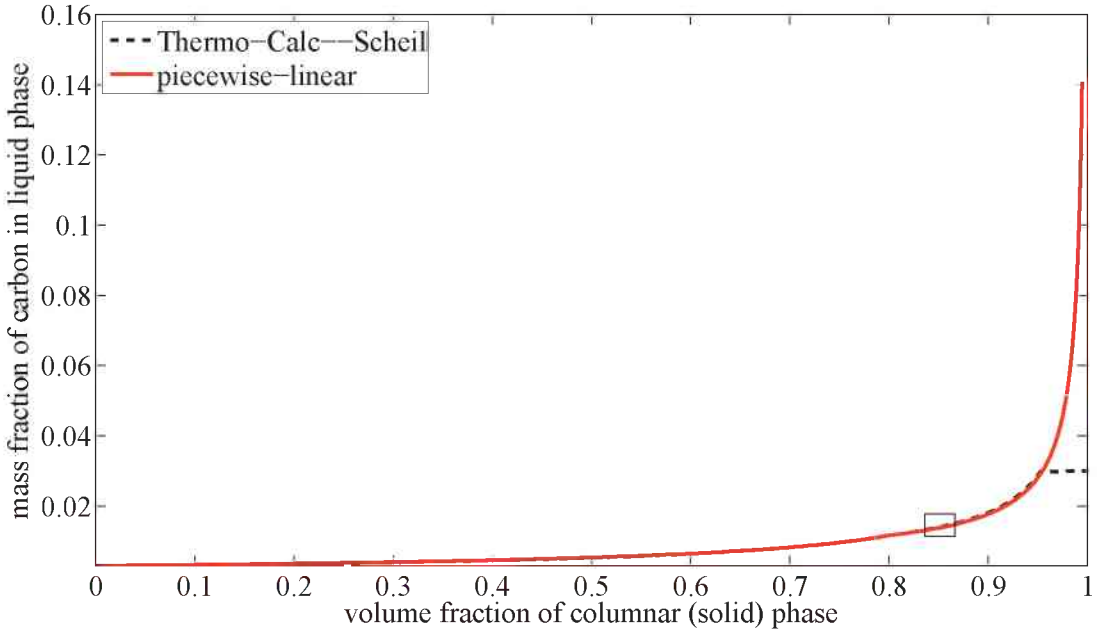

a

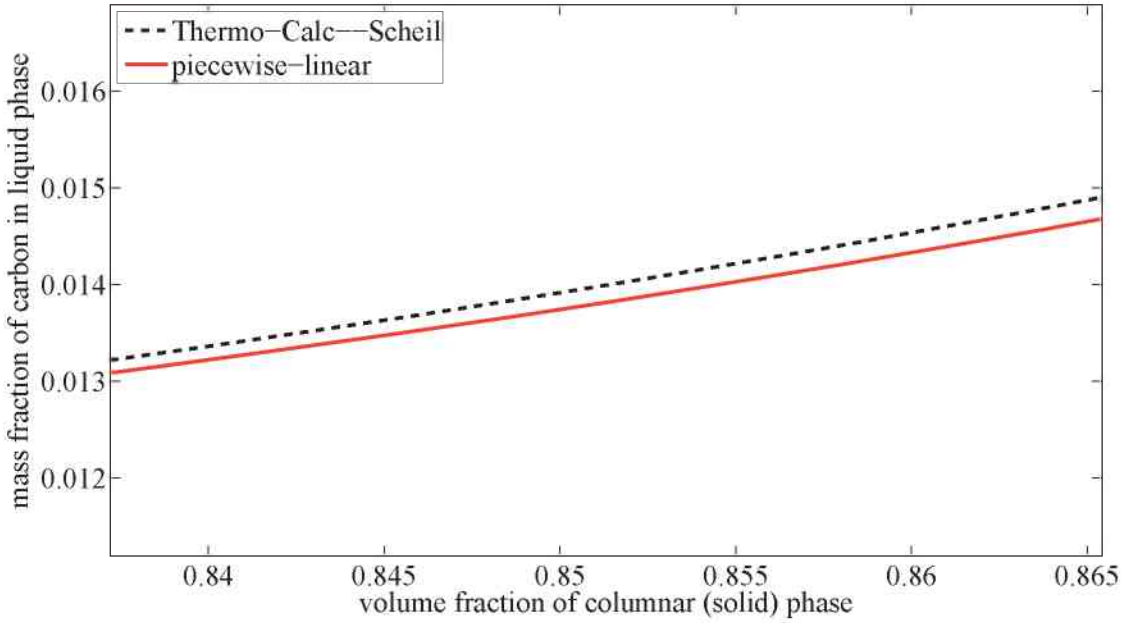

b

Figure 5.1: The $c_l^{\mathrm{C}} - f_s$ curve obtained from the zero-dimensional model using piecewise-linear approximation described in Section 3.5.1 with parameters given in the Table 4.1 (solid red line) plotted together with the corresponding $\tilde{c}_l^{\mathrm{C}} - f_c$ curve calculated using the Thermo-Calc–Scheil module (dashed black line). In the figure (a) the whole graph is shown, the figure (b) shows its enlarged fragment. It shows that the difference between the curves is very small, about 1.5%.

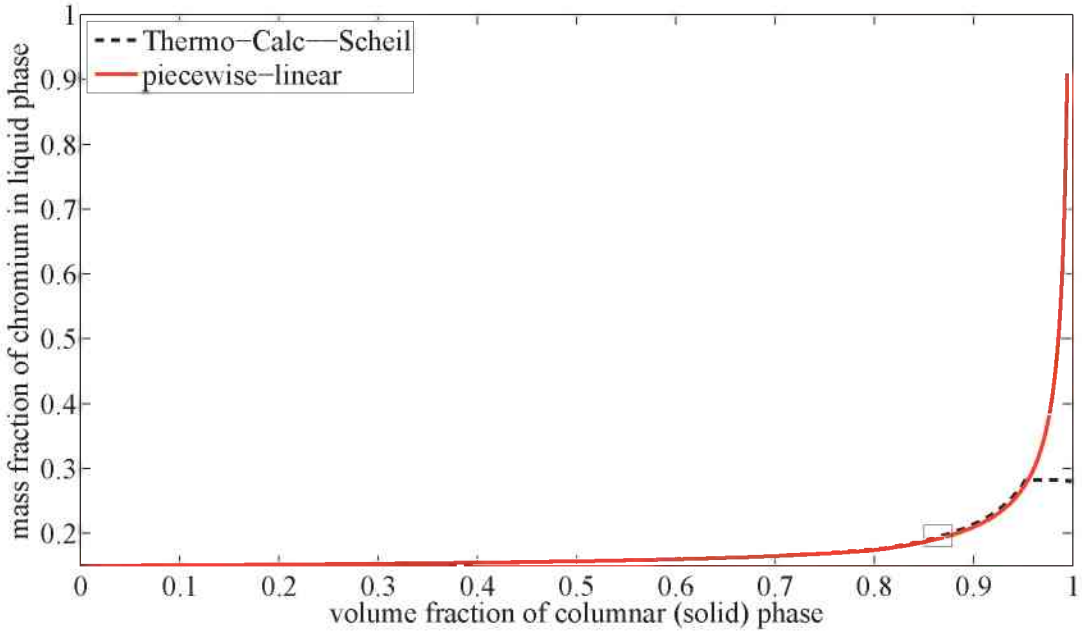

a

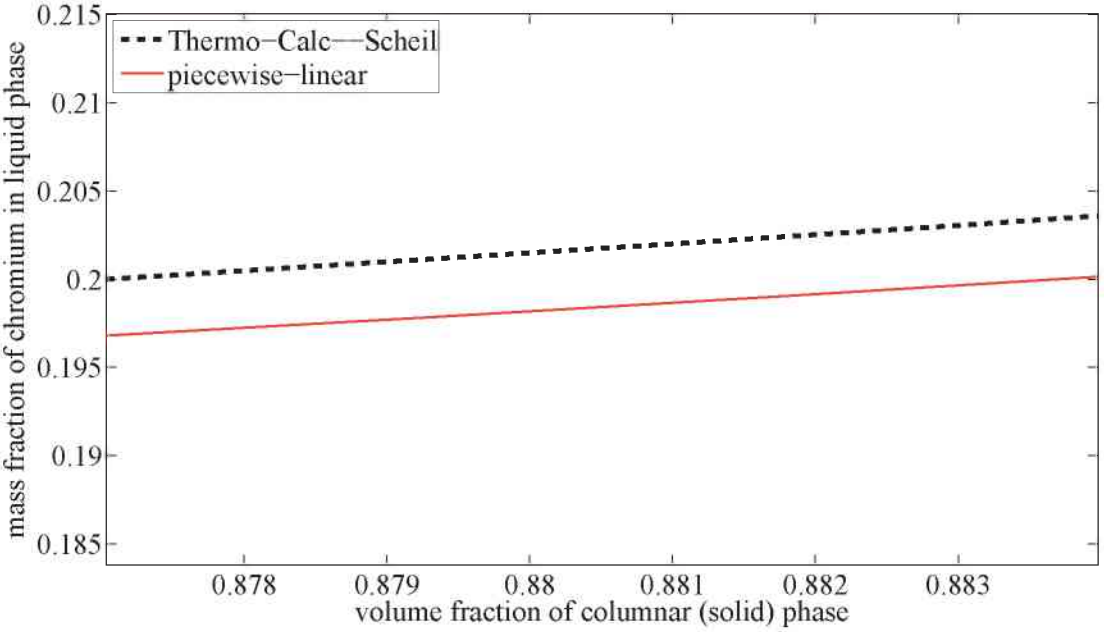

b

Figure 5.2: The $c_l^{\mathrm{Cr}} - f_s$ curve obtained from the zero-dimensional model using piecewise-linear approximation described in Section 3.5.1 with parameters given in the Table 4.1 (solid red line) plotted together with the corresponding $\tilde{c}_l^{\mathrm{Cr}} - f_c$ curve calculated using the Thermo-Calc–Scheil module (dashed black line). In the figure (a) the whole graph is shown, the figure (b) shows its enlarged fragment. It shows that the difference between the curves is very small, about 2.5%.

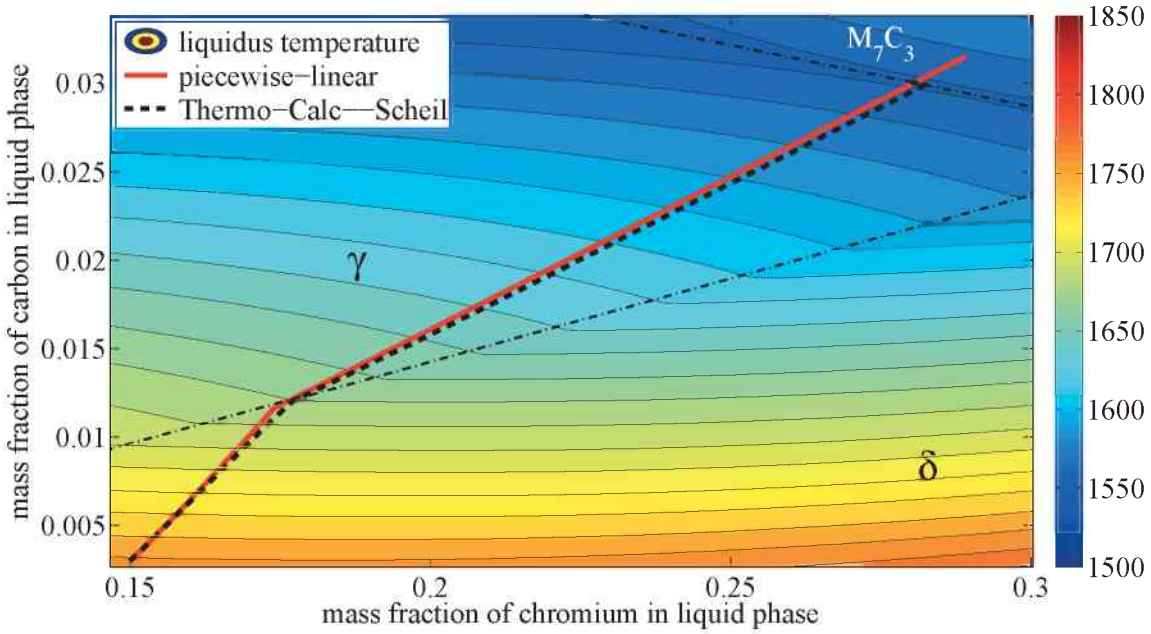

Figure 5.3: The $c_l^{\mathrm{C}} - c_l^{\mathrm{Cr}}$ curve obtained from the zero-dimensional model using piecewise-linear approximation described in Section 3.5.1 with parameters given in the Table 4.1 (solid red line) plotted together with the corresponding $\tilde{c}_l^{\mathrm{C}} - \tilde{c}_l^{\mathrm{Cr}}$ curve calculated using the Thermo-Calc–Scheil module (dashed black line).

Solidification of Fe-0.18wt.%C-1.4wt%Mn alloy

Here is presented the solution of the initial value value problem, Eqs. (3.1), (3.9), (3.10) and (3.11), which was performed for the Fe-0.18wt.%C-1.4wt%Mn alloy. The initial conditions (3.11) for this problem were as follows (note that these numbers are unitless, since f_c is a volume fraction and both c_l^{C} and c_l^{Mn} are mass fractions):

$$\begin{aligned} f_c(0) &= 10^{-5}, \\ c_l^{\mathrm{Mn}}(0) &= 0.014, \\ c_l^{\mathrm{C}}(0) &= 0.0018. \end{aligned} \tag{5.2}$$

The three thermodynamic functions, Eqs. (3.15), (3.16), (3.17): $\tilde{T} = \tilde{T}(\tilde{c}_l^{\mathrm{Mn}}, \tilde{c}_l^{\mathrm{C}})$, $\tilde{c}_s^{\mathrm{Mn}}(\tilde{c}_l^{\mathrm{Mn}}, \tilde{c}_l^{\mathrm{C}})$ and $\tilde{c}_s^{\mathrm{C}}(\tilde{c}_l^{\mathrm{Mn}}, \tilde{c}_l^{\mathrm{C}})$ were represented using piecewise-linear approximation described in Section 3.5.1 with parameters from the Table 4.2. The Scheil–curves calculated using the both Scheil–Gulliver and the zero-dimensional models

for carbon are shown in the Fig. 5.4, for manganese in the Fig. 5.5. The corresponding solidification paths are shown in the Fig. 5.6.

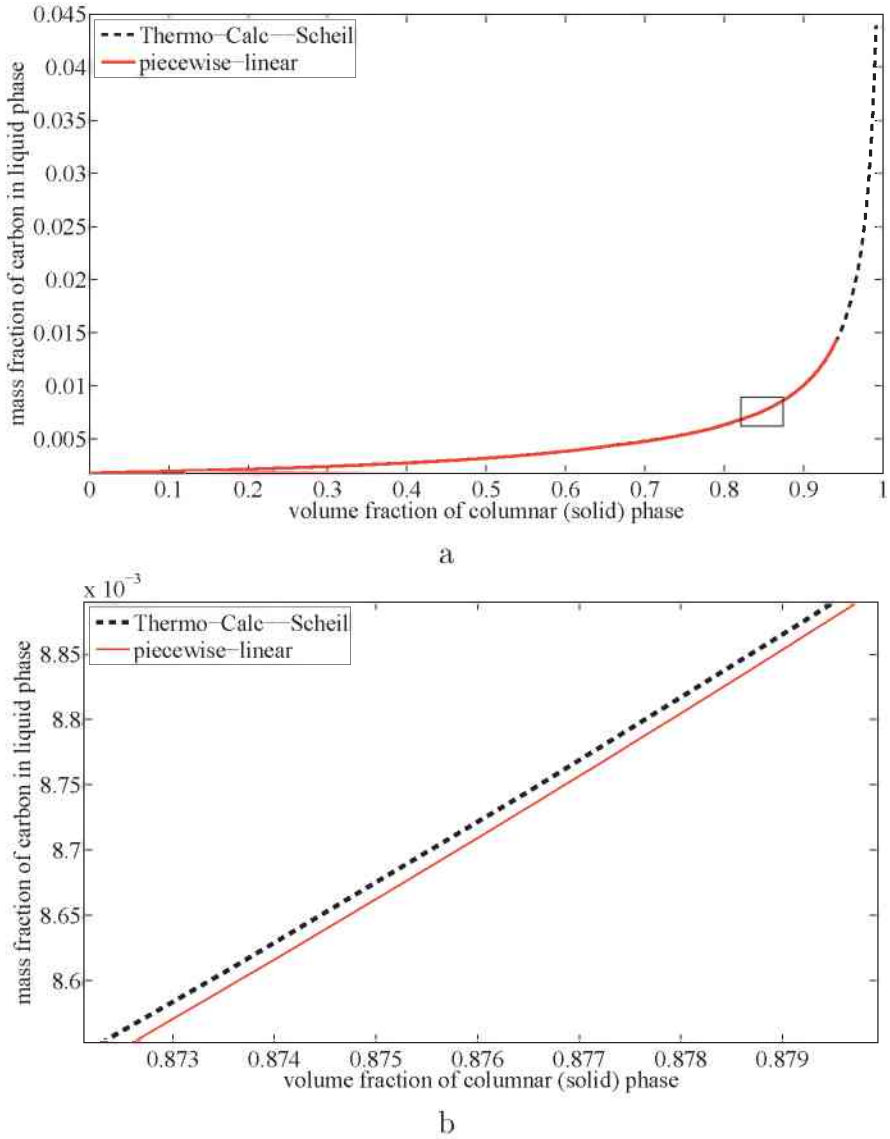

Figure 5.4: The $c_l^C - f_s$ curve obtained from the using piecewise-linear approximation described in Section 3.5.1 with parameters given in the Table 4.2 (solid red line) plotted together with the corresponding $\tilde{c}_l^C - f_c$ curve calculated using the Thermo-Calc–Scheil module (dashed black line). In the figure (a) the whole graph is shown, the figure (b) shows its enlarged fragment, marked in the figure (a) with a black rectangle. It shows that the curves differ, although the difference is very small, about 0.3%.

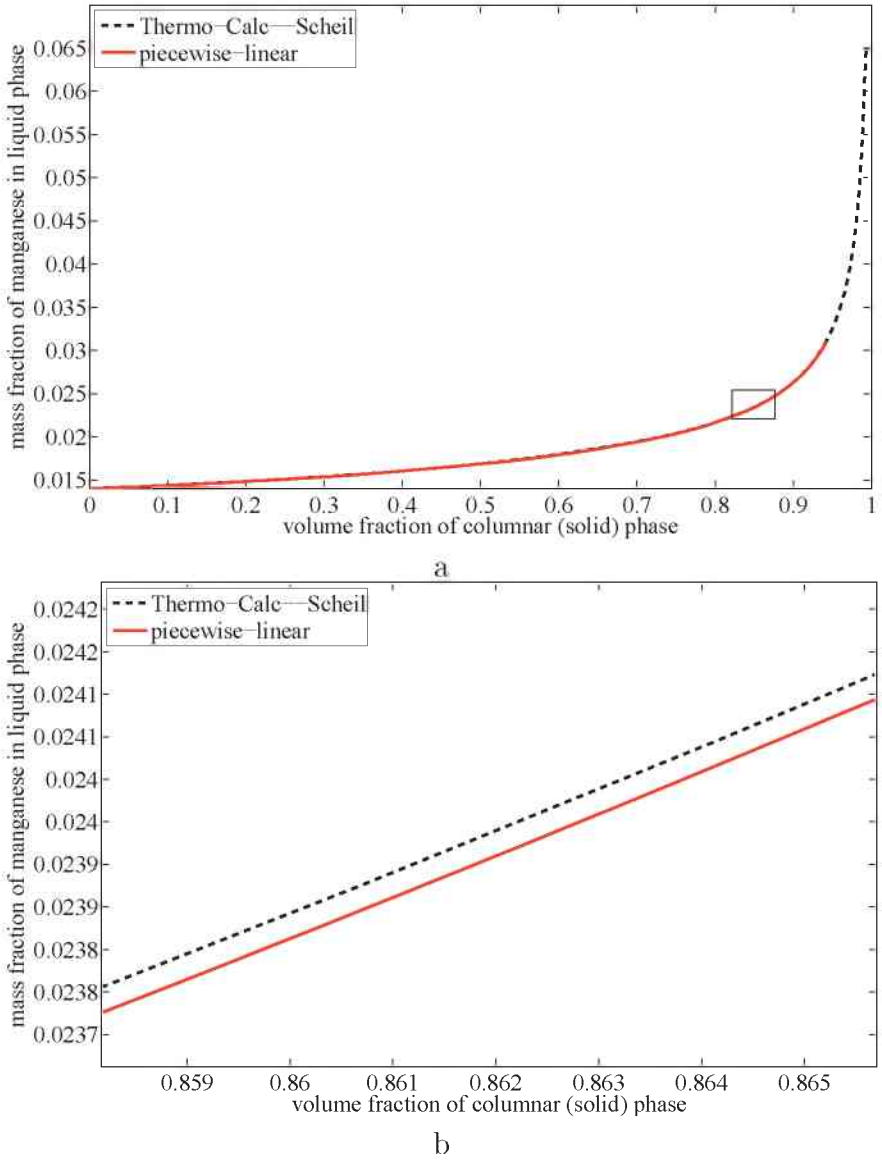

Figure 5.5: The $c_l^{\mathrm{C}} - f_s$ curve obtained from the using piecewise-linear approximation described in Section 3.5.1 with parameters given in the Table 4.2 (solid red line) plotted together with the corresponding $\tilde{c}_l^{\mathrm{C}} - f_c$ curve calculated using the Thermo-Calc–Scheil module (dashed black line). In the figure (a) the whole graph is shown, the figure (b) shows its enlarged fragment, marked in the figure (a) by a black rectangle. It shows that the curves differ, although the difference is very small, about 0.1%.

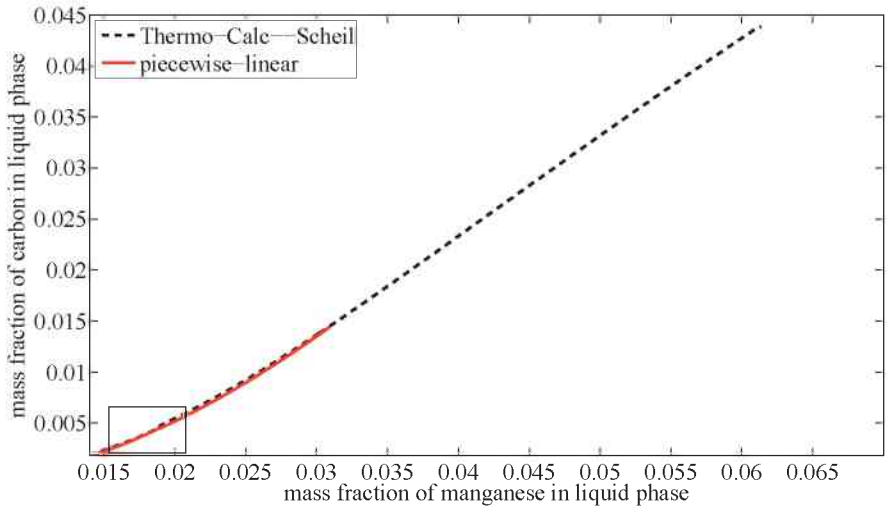

a

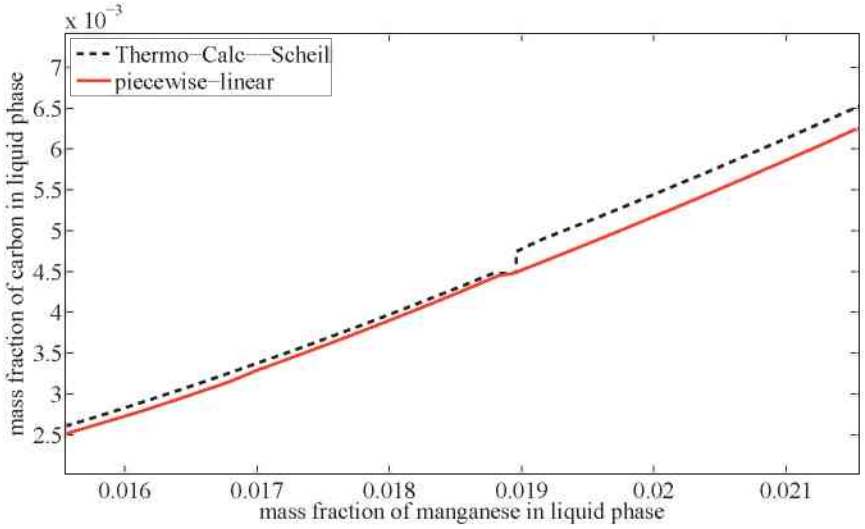

b

Figure 5.6: The $c_l^{\mathrm{C}} - c_l^{\mathrm{Mn}}$ curve obtained from the zero-dimensional model using piecewise-linear approximation described in Section 3.5.1 with parameters given in the Table 4.2 (solid red line) plotted together with the corresponding $\tilde{c}_l^{\mathrm{C}} - \tilde{c}_l^{\mathrm{Mn}}$ curve calculated using the Thermo-Calc–Scheil module (dashed black line). In the figure (a) the whole graph is shown. Note that the solidification path starts at the point corresponding to the initial melt composition. The figure (b) shows the enlarged fragment of the curves in the figure (a) that is marked by the black rectangle. It shows that there is a difference between these curves, although it is very small. The solidification path calculated using the zero-dimensional model does not reach the point of end solidification of Thermo-Calc–Scheil curves because it was calculated only until $f_c = 0.95$.

As these curve comparisons show, the curves calculated using Thermo-Calc–Scheil module for the Fe-0.18wt.%C-1.4wt%Mn alloy can be represented using piecewise-linear approximations of thermodynamic functions with a good precision.

Unfortunately due to the absence of the licence for the Thermo-Calc software for the tabulation of the database containing the thermodynamic data for the Fe–C–Mn phase diagram, it was impossible to provide a liquidus surface in this figure. The licence only allowed the calculation of the thermodynamic functions and their derivatives, which allowed constructing the piecewise-linear approximation.

5.2 0-D solidification using spline interpolation of thermodynamic functions

Solidification of Fe-0.3wt.%C-15wt%Cr alloy

Here is presented the solution of the initial value value problem, Eqs. (3.1), (3.9), (3.10) and (3.11), which was performed for the Fe-0.3wt.%C-15wt%Cr alloy. The initial conditions (3.11) for the problem were as follows:

$$\begin{aligned} f_c(0) &= 10^{-5}, \\ c_l^{\mathrm{C}}(0) &= 0.003, \\ c_l^{\mathrm{Cr}}(0) &= 0.15. \end{aligned} \tag{5.3}$$

The three thermodynamic functions, Eqs. (3.15), (3.16), (3.17): $\tilde{T} = \tilde{T}(\tilde{c}_l^{\mathrm{C}}, \tilde{c}_l^{\mathrm{Cr}})$, $\tilde{c}_s^{\mathrm{C}}(\tilde{c}_l^{\mathrm{C}}, \tilde{c}_l^{\mathrm{Cr}})$ and $\tilde{c}_s^{\mathrm{Cr}}(\tilde{c}_l^{\mathrm{C}}, \tilde{c}_l^{\mathrm{Cr}})$ were represented by interpolating splines, as it is described in Section 4.3.3.

The Scheil–curves calculated using the both Scheil–Gulliver and the zero-dimensional models for carbon are shown in the Fig. 5.7, for chromium in the Fig. 5.8. The corresponding solidification paths are shown in the Fig. 5.9.

Solidification of Cu-6wt.%Sn-0.5wt%P alloy

Here is presented the solution of the initial value value problem, Eqs. (3.1), (3.9), (3.10) for the Cu-6wt.%Sn-0.5wt%P alloy (for the details on the Cu–P–Sn system see |Rogl07|). The initial conditions (3.11) for the problem were as follows:

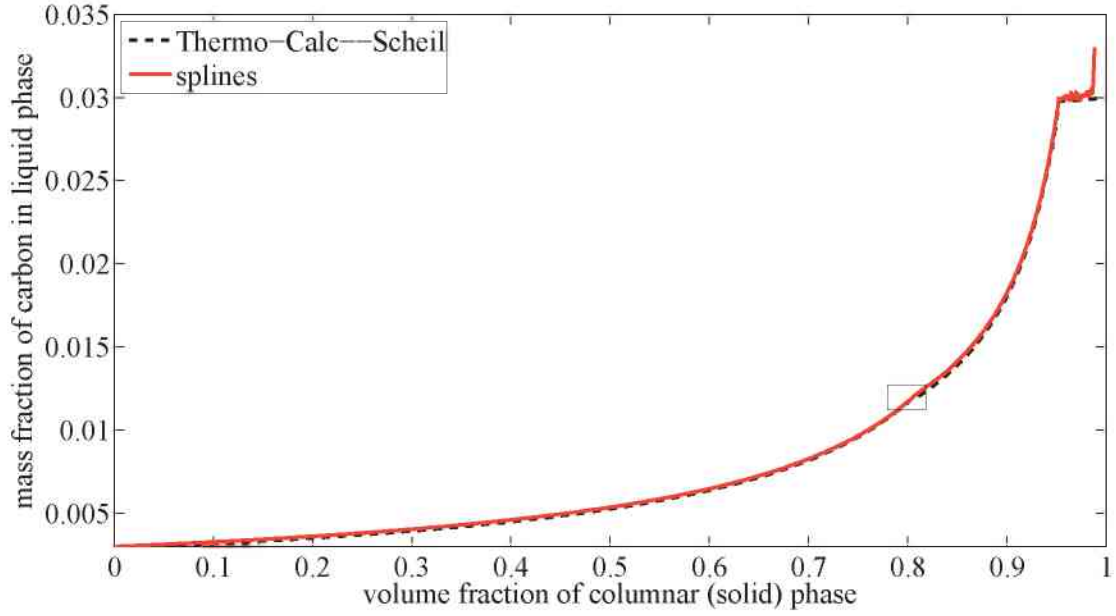

a

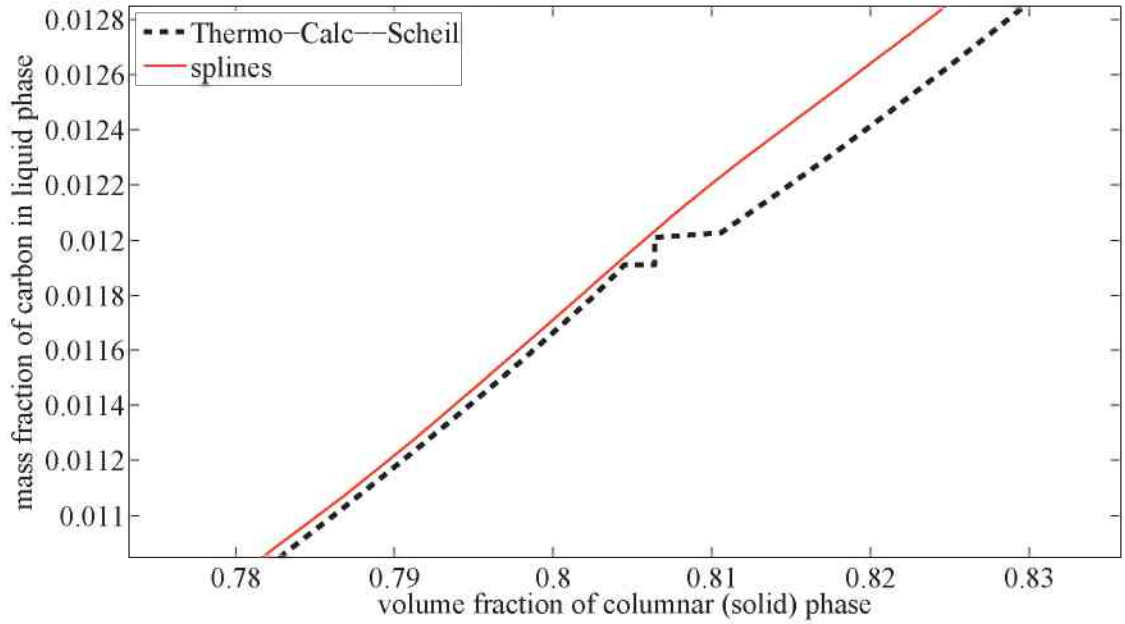

b

Figure 5.7: The $c_l^{\mathrm{C}} - f_s$ curve obtained from the zero-dimensional model using spline interpolated thermodynamic functions as described in Section 4.3.3 (solid red line) plotted together with the corresponding $\tilde{c}_l^{\mathrm{C}} - f_c$ curve calculated using the Thermo-Calc–Scheil module (dashed black line). In the figure (a) the whole graph is shown, the figure (b) shows its enlarged fragment, which shows the difference between the curves, which is in this region is about 1.6%.

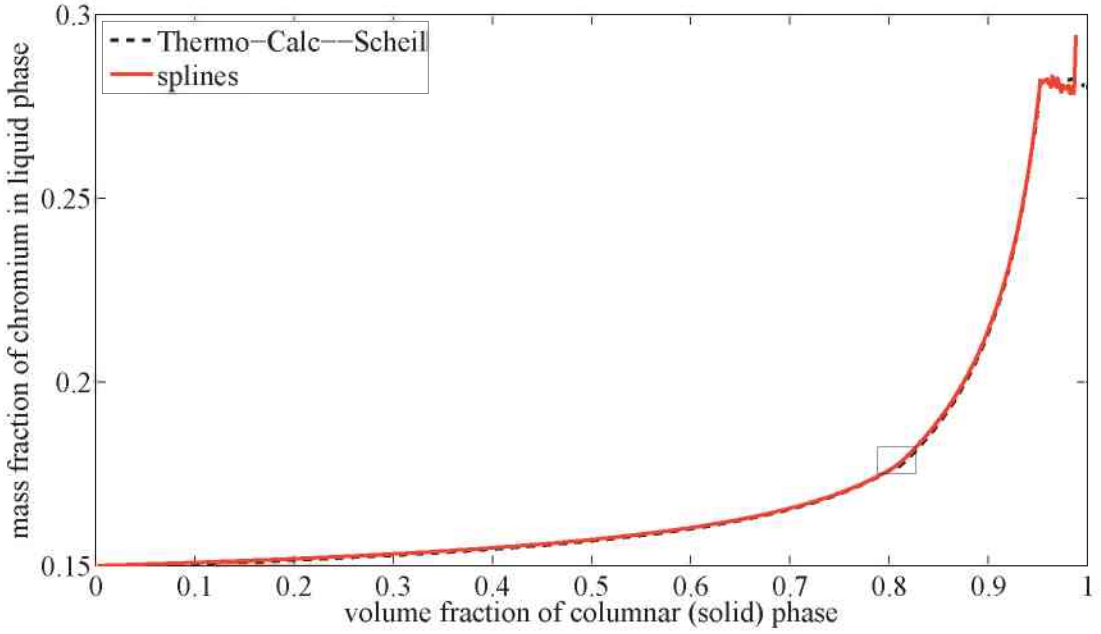

a

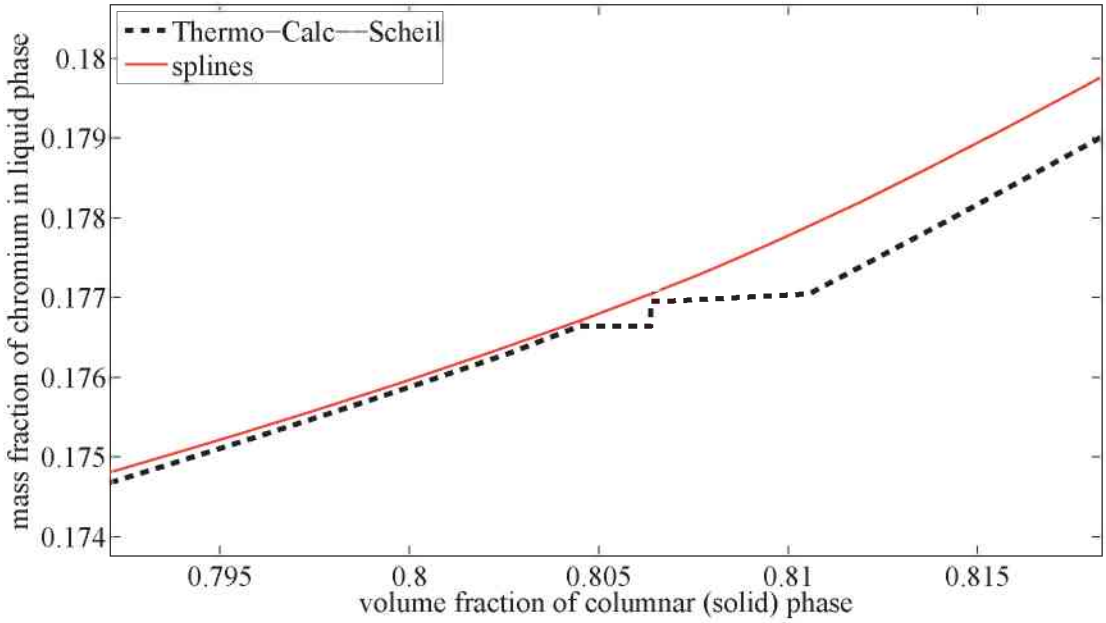

b

Figure 5.8: The $c_l^{\mathrm{Cr}} - f_s$ curve obtained from the zero-dimensional model using spline interpolated thermodynamic functions as described in Section 4.3.3 (solid red line) plotted together with the corresponding $\tilde{c}_l^{\mathrm{Cr}} - f_c$ curve calculated using the Thermo-Calc–Scheil module (dashed black line). In the figure (a) the whole graph is shown, the figure (b) shows its enlarged fragment. It shows that the difference between curves in this interval is at most 0.3%.

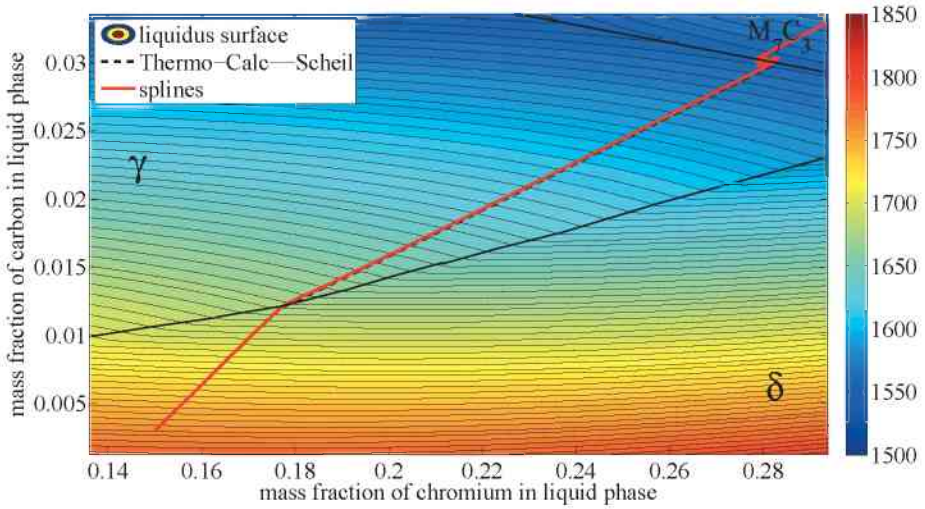

Figure 5.9: The $c_l^{\mathrm{Cr}} - c_l^{\mathrm{C}}$ curve obtained from the zero-dimensional model using spline interpolated thermodynamic functions as described in Section 4.3.3 (solid red line) plotted together with the corresponding $\tilde{c}_l^{\mathrm{Cr}} - \tilde{c}_l^{\mathrm{C}}$ curve calculated using the Thermo-Calc–Scheil module (dashed black line).

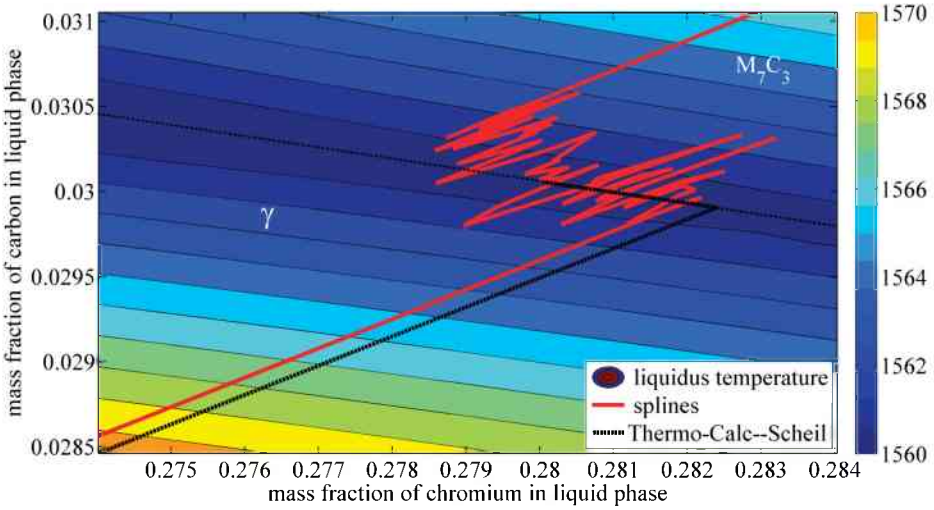

Figure 5.10: enlarged parts of the curves depicted in the Fig. 5.9. The black dash-dot line shows the phase border between the γ and M_7C_3, which is at the same time the eutectic groove in the phase diagram. The zigzag-like end of the solidification path is caused by the fact that the model is not designed to describe two-phase solidification (for details, see Section 3.3).

$$
\begin{aligned}
f_c(0) &= 10^{-5}, \\
c_l^{\mathrm{Sn}}(0) &= 0.06, \\
c_l^{\mathrm{P}}(0) &= 0.005.
\end{aligned}
\tag{5.4}
$$

The three thermodynamic functions, Eqs. (3.15), (3.16), (3.17): $\tilde{T} = \tilde{T}(\tilde{c}_l^{\mathrm{Sn}}, \tilde{c}_l^{\mathrm{P}})$, $\tilde{c}_s^{\mathrm{Sn}}(\tilde{c}_l^{\mathrm{Sn}}, \tilde{c}_l^{\mathrm{P}})$ and $\tilde{c}_s^{\mathrm{P}}(\tilde{c}_l^{\mathrm{Sn}}, \tilde{c}_l^{\mathrm{P}})$ were represented by interpolating splines, as described in Section 4.3.3. The Scheil–curves calculated using the both Scheil-Gulliver and the zero-dimensional models for tin are shown in the Fig. 5.11, for phosphorus in the Fig. 5.12. The corresponding solidification paths are shown in the Fig. 5.13.

5.3 Intermediate conclusions

As it was said before, the zero-dimensional model developed in Section 3.1 is a simplification of the ternary two-phase Eulerian solidification model summarised in Section 3.2, in the sense that it neglects the spatial flow effects, but does not simplify the thermodynamics. The figures presented here plus the error analysis in 4.3.4 prove that the thermodynamics of the Fe–C–Cr and Fe–C–Mn is represented by the piecewise-linear approximations acceptably for the alloys considered in the absence of flow. Combined with the ease of construction of such piecewise-linear approximations it presents an acceptable way of representing the ternary phase diagram data.

The results obtained using the spline approach in Section 5.2 show that the approximation of thermodynamic functions using spline interpolation of tabulated data works well for diffusion-driven simulations of ternary solidification in the absence of flow in two-phase regions. For the X30Cr15 alloy, the difference between the curves calculated using Thermo-Calc–Scheil module and the curves calculated using the zero-dimensional model from the Section 3.1 with the approximation of thermodynamic functions using splines is comparable for the Scheil-curves for carbon (compare Fig. 5.7 for spline approach with $\sim 1.5\%$ error and Fig. 5.1 for piecewise-linear with $\sim 1.6\%$ error) and is much smaller for splines approach in case of chromium (splines in Fig. 5.8 with $\sim 0.3\%$ error and Fig. 5.2 piecewise-linear with $\sim 2.5\%$ error). The example using an alloy from the

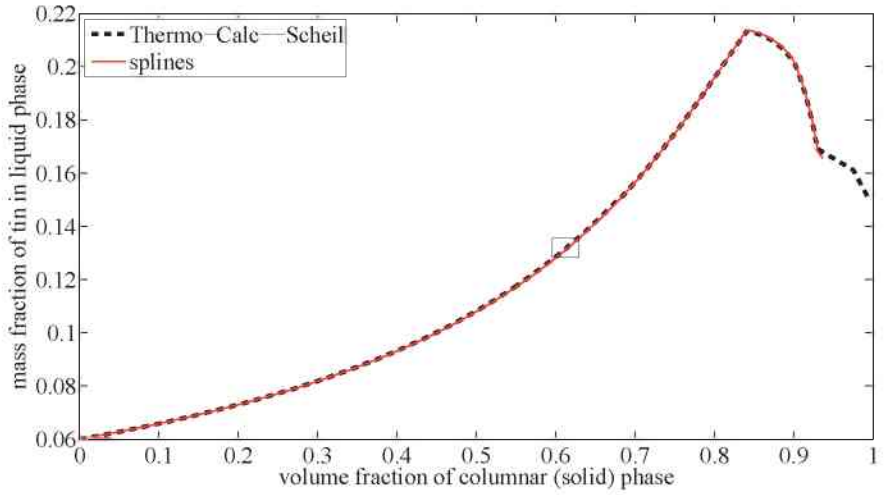

a

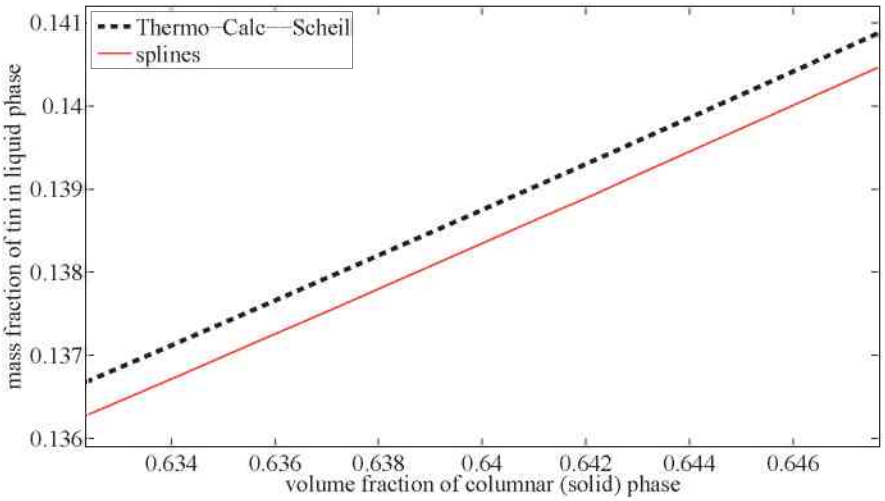

b

Figure 5.11: The $\tilde{c}_l^{\mathrm{Sn}} - f_s$ curve obtained from the zero-dimensional model using spline interpolated thermodynamic functions as described in Section 4.3.3 (solid red line) plotted together with the corresponding $c_l^{\mathrm{P}} - f_c$ curve calculated using the Thermo-Calc–Scheil module (dashed black line). In the figure (a) the whole graph is shown, the figure (b) shows its enlarged fragment. It shows that the difference between these curves is about 0.4%.

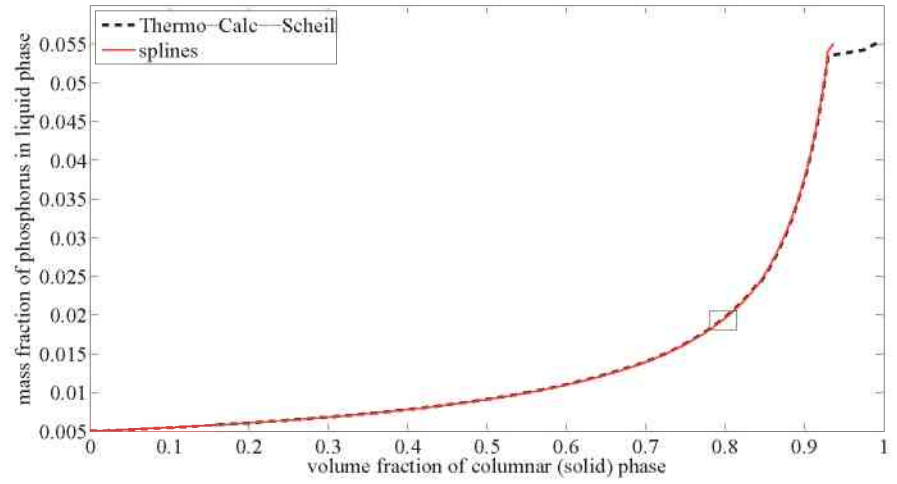

a

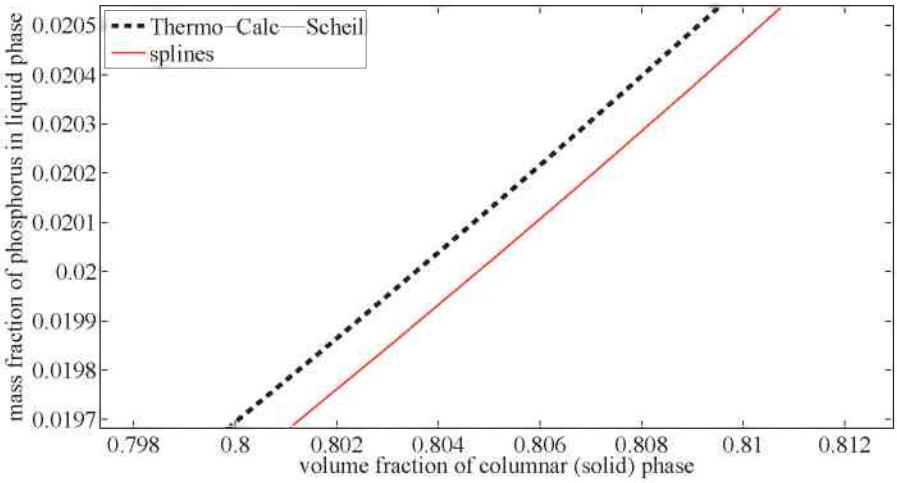

b

Figure 5.12: The $\tilde{c}_l^{\mathrm{P}} - f_s$ curve obtained from the zero-dimensional model using spline interpolated thermodynamic functions as described in Section 4.3.3 (solid red line) plotted together with the corresponding $c_l^{\mathrm{P}} - f_c$ curve calculated using the Thermo-Calc–Scheil module (dashed black line). In the figure (a) the whole graph is shown, the figure (b) shows its enlarged fragment. It shows that the difference between the curves is about 0.5%.

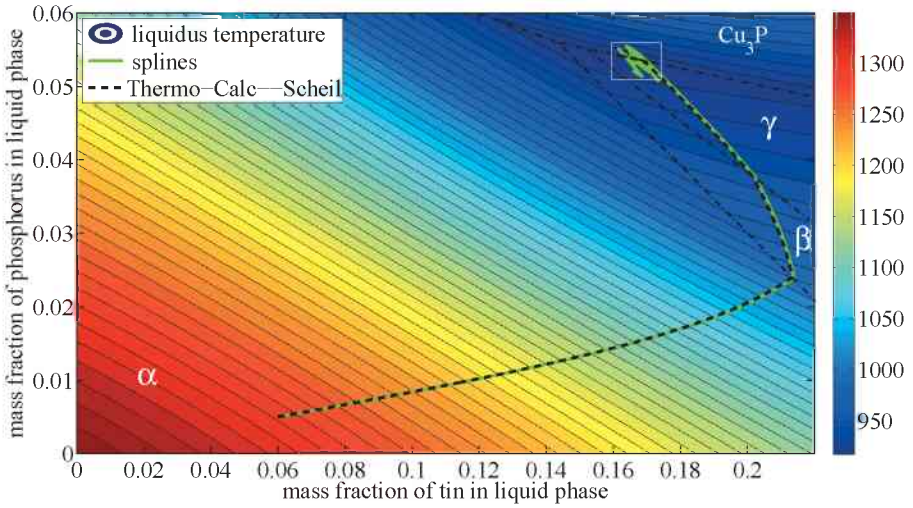

Figure 5.13: The $\tilde{c}_l^{\mathrm{P}} - \tilde{c}_l^{\mathrm{Sn}}$ curve obtained from the zero-dimensional model using spline interpolated thermodynamic functions as described in Section 4.3.3 (solid red line) plotted together with the corresponding $c_l^{\mathrm{P}} - c_l^{\mathrm{Sn}}$ curve calculated using the Thermo-Calc–Scheil module (dashed black line). At the end solidification, the situation in the region marked by a white rectangle is the similar to the end of solidification in the Fe–C–Cr alloy. See the Fig. 5.10 for explanations.

Cu–Sn–P system shows that the spline approach is capable of also representing phase diagrams more complicated (more peritectic reactions, more complicated solidification path trajectory) than Fe–C–Cr in the Fe-rich corner. This fact, combined with the accuracy of the splines and their continuity which is important for solving equation systems numerically, where these functions appear, make the spline approach a precise tool for representing ternary thermodynamics for solidification simulations.

Chapter 6

Simulation of solidification of ingot castings

In order to be able to predict the solidification process correctly, it is necessary to have realistic initial and boundary conditions for the problem. The thermal boundary conditions can be obtained by studying the measured temperature curves collected from thermocouples situated in the mould walls. To acquire the initial conditions for a solidification simulation, a simulation of the process of filling of the ingot with the melt is necessary. After performing such a simulation, it is possible to use the resulting distributions of mass fractions of alloying elements, temperature, velocities profiles and so on as the initial conditions for the multiphase solidification simulation. Such a dissection of the process into two parts, the filling and the subsequent solidification is justified by the complexity of the calculations necessary to simulate the filling stage. The following is true for the filling simulation: the flow is turbulent and it is necessary to solve a free-surface problem, using an interface tracking algorithm such as Volume-of-Fraction (first described in |Hirt81|, also see its application for solidification in |Voller87b, Voller87a, Voller91, Gu99| or level-set. Thus, a simulation of both stages of the process, filling and solidification within one framework is practically impossible. In the work presented, simplified simulations of form filling were performed to determine initial and boundary conditions for subsequent solidification simulations.

We considered two cases of filling: downhill and uphill. The first ingot in question was a benchmark ingot of X30Cr15 alloy, and the only technical pos-

sibility to cast it was by using the downhill filling method. The second filling simulation is of an industrial size ingot of X38Cr16 alloy and the filling is done uphill.

Filling of both of these ingots were performed using the MAGMASOFT [MAG05] software package. Also solidification simulations were performed using this software package, in order to compare the simulated solidification times in experiment and in simulations.

After performing the filling simulations, the necessary time-dependent heat transfer coefficients between the mould and the melt/ingot were found as well as the initial temperatures which are used later in more sophisticated Eulerian multiphase solidification simulations using the models developed in this work (summarised in Section 3.2). The simulations include:

- two-phase ternary 32 kg benchmark ingot solidification simulation with an artificial heat transfer coefficient between the mould and the melt/ingot in order to study the effect of thermosolutal convection
- two-phase ternary 32 kg benchmark ingot solidification simulation with a realistic mould–melt/ingot heat transfer coefficient
- three-phase 2 ton industrial size ingot solidification simulation with the realistic heat transfer coefficient between the mould and the melt/ingot

6.1 Simulation of the downhill ingot filling

6.1.1 Geometry, mesh, initial and boundary conditions

The geometry and meshing of the ingot and mould were created using the CAD capabilities of the MAGMASOFT software package preprocessor. These geometry and mesh are depicted in the Fig. 6.1.

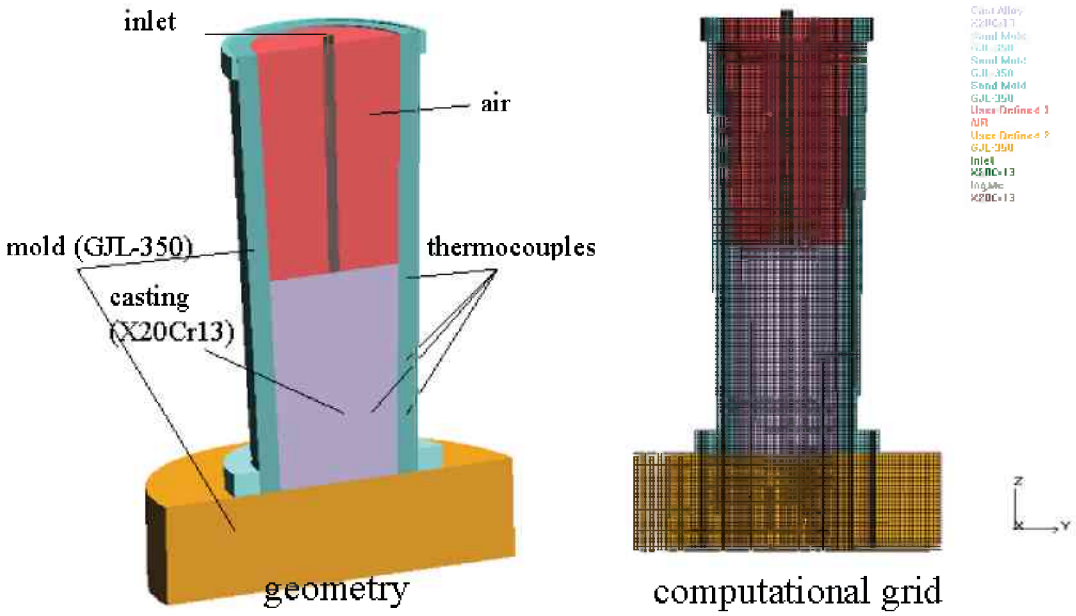

Figure 6.1: Geometry and mesh of the benchmark ingot casting system

The choice of heat transfer coefficients between different parts of the geometry is summarised in Table 6.1.

Material pairs	Heat transfer coefficient, $\mathrm{W \cdot m^{-2} \cdot K^{-1}}$
alloy–mould	temperature-dependent
alloy–bottom plate	temperature-dependent
alloy–cover	10^4
ingate–air	$7 \cdot 10^3$
ingate–cover	10^4
bottom plate–mould	10^4
mould–air	$3.5 \cdot 10^3$
mould–cover	10^4
cover–air	$7 \cdot 10^3$

Table 6.1: Heat transfer coefficients between different parts of the mould, the alloy ingot and the bottom plate

At the beginning of solidification, the heat transfer between the metal and the mould is good due to a good contact, then an gas gap forms between the mould and metal due to shrinkage. The presence of the gas gap hinders the heat transfer,

making heat transfer coefficient between mould and metal dependent on the width of the gap (see, for example |Nishida86, El-Mahallawy88, Assar92, Trovant00, Campbell03|). Since the gap width depends on the temperature, it is possible to represent the mould–metal heat transfer coefficient as temperature–dependent. The temperature-dependent heat trasfer coefficients between the alloy and the mould and the alloy and the bottom plate used in the simulation were as follows:

$$H(T) = \begin{cases} 500\ \mathrm{W \cdot m^{-2} \cdot K^{-1}}, & T \leq 1375\ ^{\circ}\mathrm{C}, \\ (500 + 2.778\ (T - 1375))\ \mathrm{W \cdot m^{-2} \cdot K^{-1}}, & 1375\ ^{\circ}\mathrm{C} \leq T \leq 1483\ ^{\circ}\mathrm{C}, \\ 3500\ \mathrm{W \cdot m^{-2} \cdot K^{-1}}, & T > 1483\ ^{\circ}\mathrm{C}. \end{cases} \tag{6.1}$$

These heat transfer coefficients are chosen this way in order to account for the formation of an air gap between the mould and the alloy, that usually occur at temperatures below liquidus. The heat transfer coefficients were obtained by running trial simulations using MAGMASOFT until the measured temperature curves were in a good agreement with the experimental ones. The comparison between the experimental and simulated curves is shown below in Fig. 6.12.

6.1.2 Material parameters

Material data for X30Cr15

The Table 6.2 shows the general material parameters used in the simulation of filling of 32 kg ingot of X30Cr15 alloy.

Parameter	Value
Solidus temperature	1375 °C
Liquidus temperature	1483 °C
Initial temperature	1600 °C
Latent heat	269.793 kJ · kg^{-1}

Table 6.2: General material parameters used in the MAGMASOFT simulation of filling of 32 kg ingot of X30Cr15 alloy

Thermal conductivity (shown in Fig. 6.2), density (Fig. 6.3), viscosity (Fig. 6.4), evolution of solid fraction (Fig. 6.5) and heat capacity (Fig. 6.6) were taken temperature-dependent from the material database of the MAGMASOFT software package for the closest material available there, namely the X20Cr13 alloy.

Other parameters were taken from the MAGMASOFT materials database as well: thermal conductivity of the mould (Fig. 6.7), heat capacity of the mould (Fig. 6.8), thermal conductivity of the insulation material (Fig. 6.9) and heat capacity of the insulation material (Fig. 6.10). The MAGMASOFT materials database summarises a wide range of physical properties research of liquid and solid steels |Richter83, Richter91, Jer77, Sahm84, Iida93, Lan60, Schneider95a, Davis94, forMetals93|.

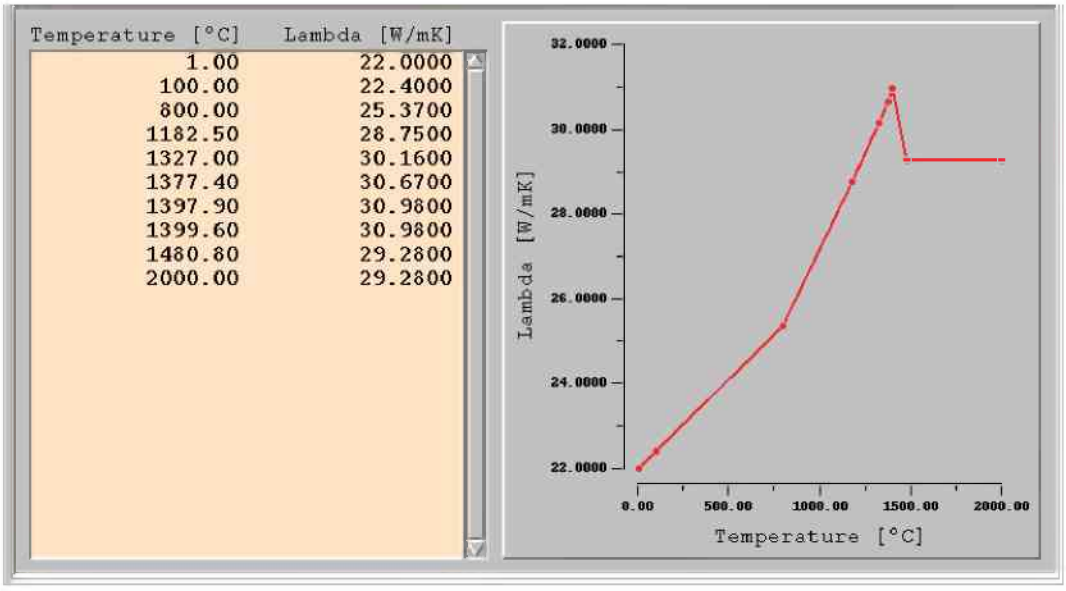

Figure 6.2: Temperature-dependent thermal conductivity of X30Cr15

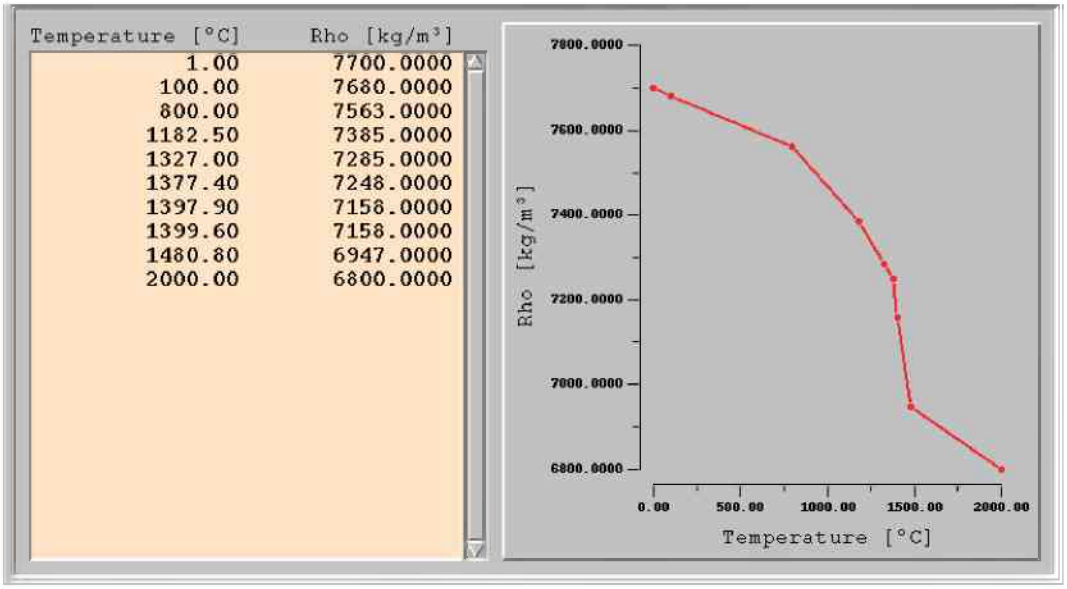

Figure 6.3: Temperature-dependent density of X30Cr15

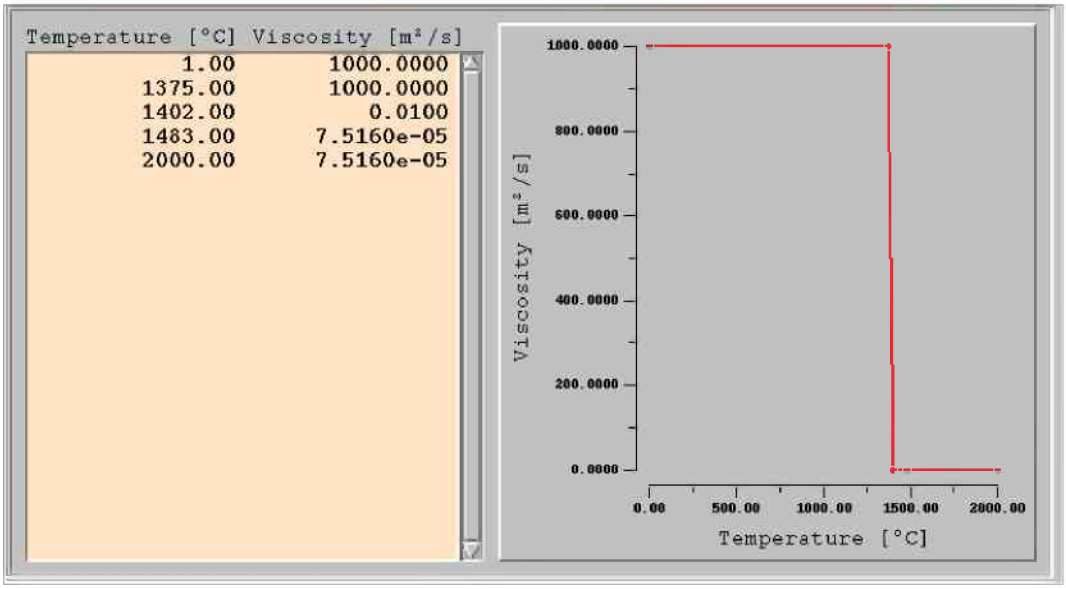

Figure 6.4: Temperature-dependent viscosity of X30Cr15. Note that here the value of $7.5160 \cdot 10^{-5}\mathrm{m}^2\mathrm{s}^{-1}$ is 100 times higher than the actual liquid viscosity of the material, in order to model turbulence occurring during filling. It is necessary, since MAGMASOFT does not allow taking turbulence into account.

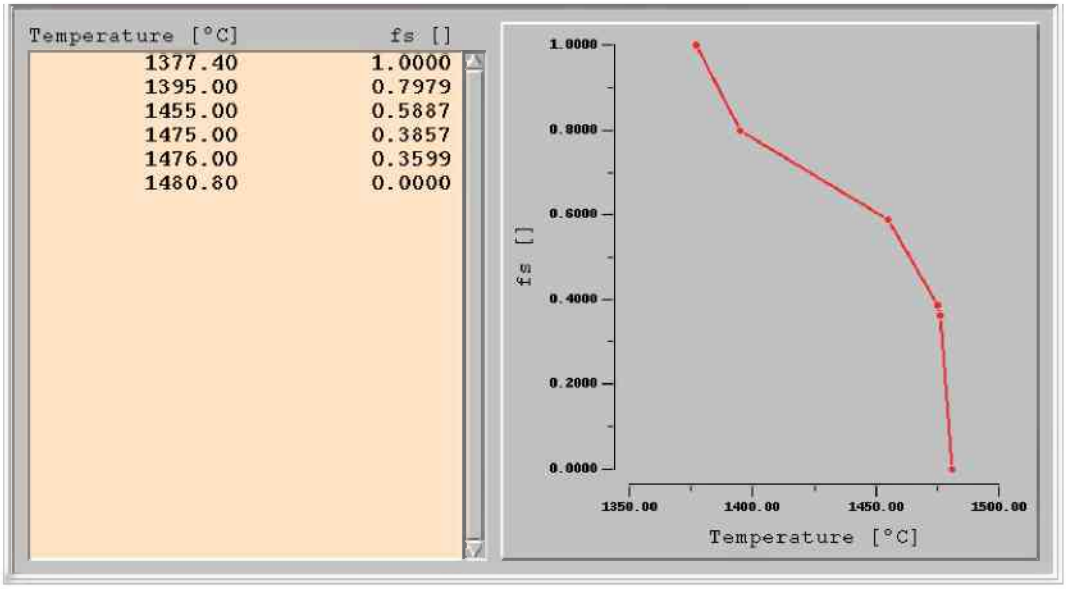

Figure 6.5: Temperature-dependent solid fraction of X30Cr15

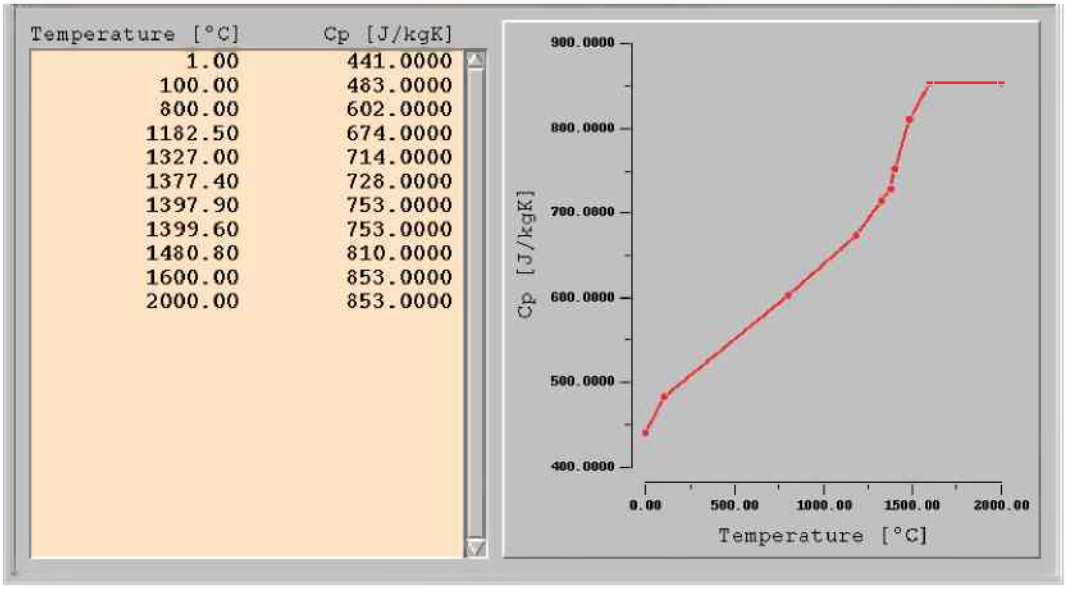

Figure 6.6: Temperature-dependent heat capacity of X30Cr15

Material data for the mould material GJL-350

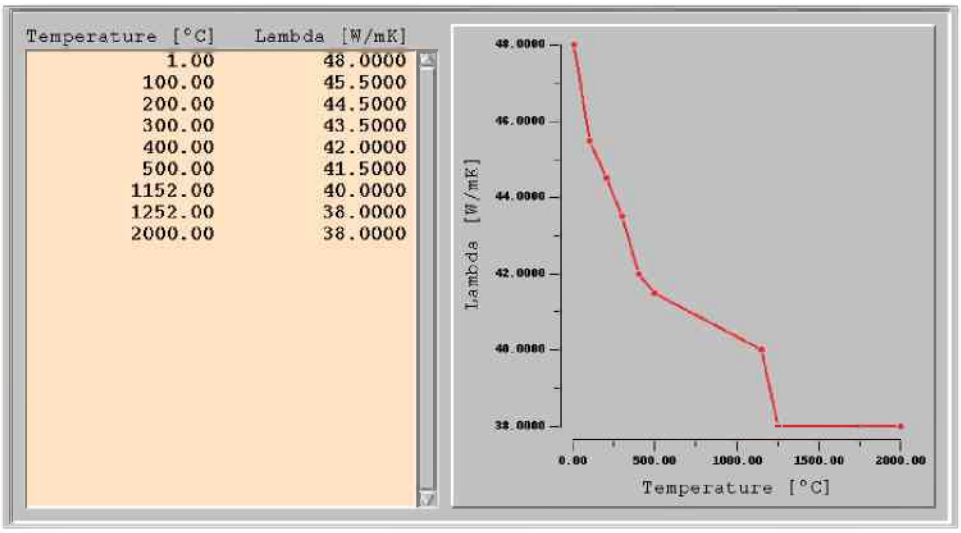

Figure 6.7: Temperature-dependent thermal conductivity of the mould material GJL-350

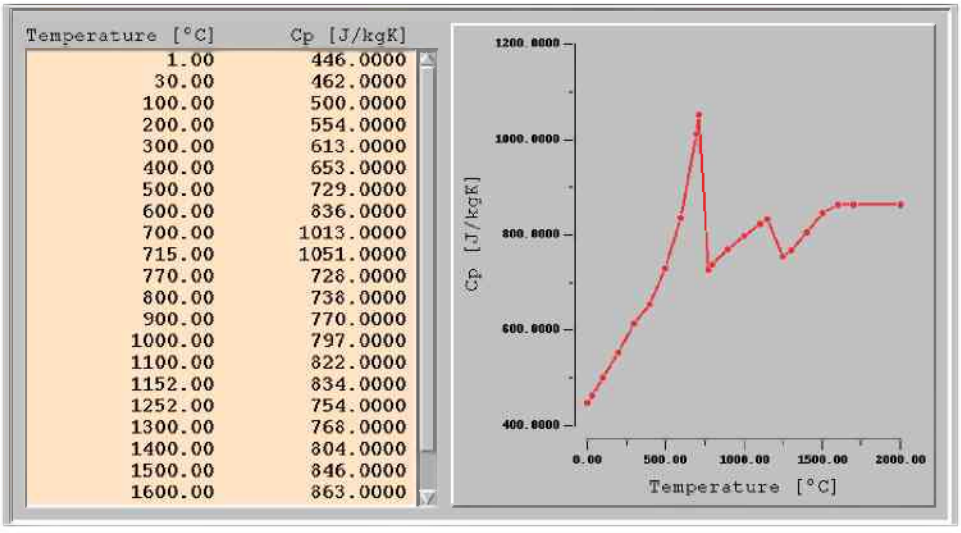

Figure 6.8: Heat capacity of the mould material GJL-350

Material data for the insulation material

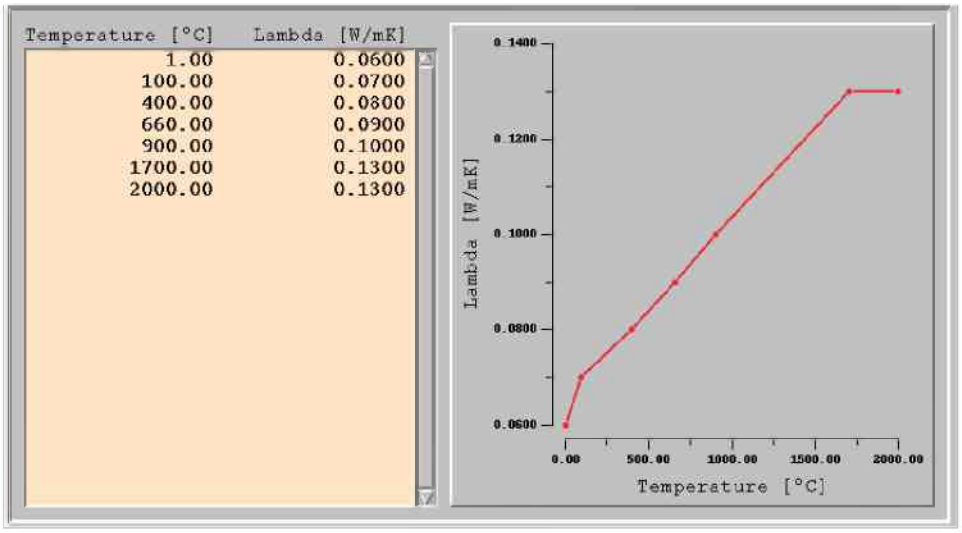

Figure 6.9: Temperature-dependent thermal conductivity of the insulation material

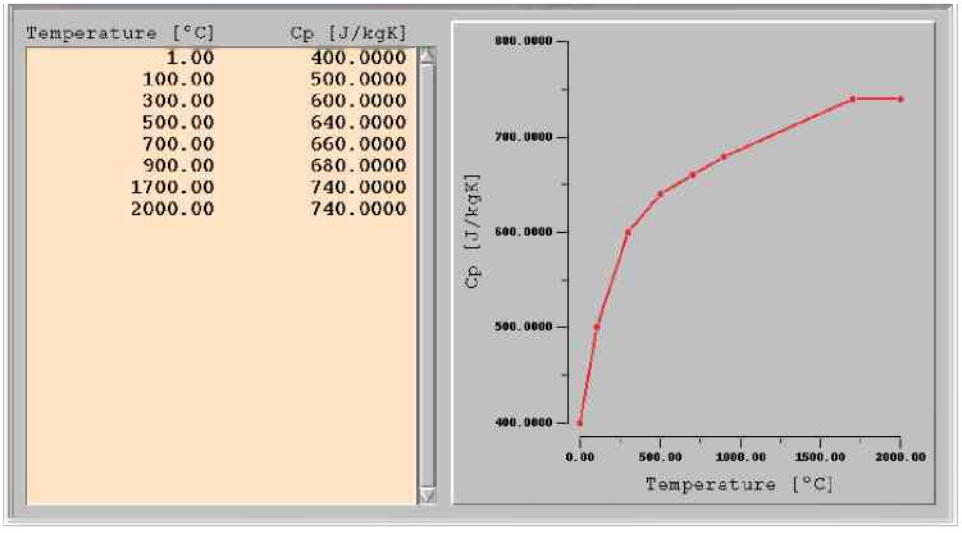

Figure 6.10: Temperature-dependent heat capacity of the insulation material

6.1.3 Results and comparison with the experiment

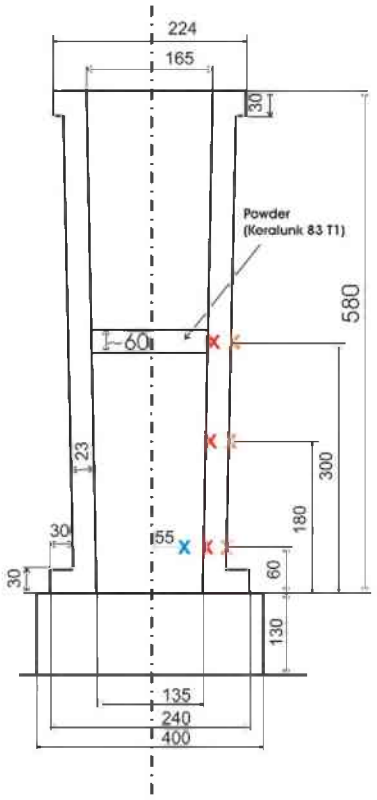

Figure 6.11: Thermocouples placement in the 32 kg mould and ingot. Red crosses indicate the thermocouples placed in the mould wall closer to the inner mould surface (used for the comparison with the simulation in the Fig. 6.12), orange crosses indicate the thermocouples placed on the outer surface of the mould and the blue cross shows the position of the thermocouple placed in the melt region.

In the Fig. 6.12 the comparison of the temperature curves from the experiment and from the solidification simulation using MAGMASOFT [MAG05]. As described in the publication [Tanzer08], several thermocouples were placed in the mould. In the comparison presented the data collected from four thermocouples is used, 3 of them are placed within 5 mm from the inner surface of the mould, at different heights of 60 mm, 180 mm and 300 mm. The fourth thermocouple were placed in the inner space of the mould, 55 mm from its axis and 60 mm from the bottom plate. The last thermocouple was protected with the tube of the

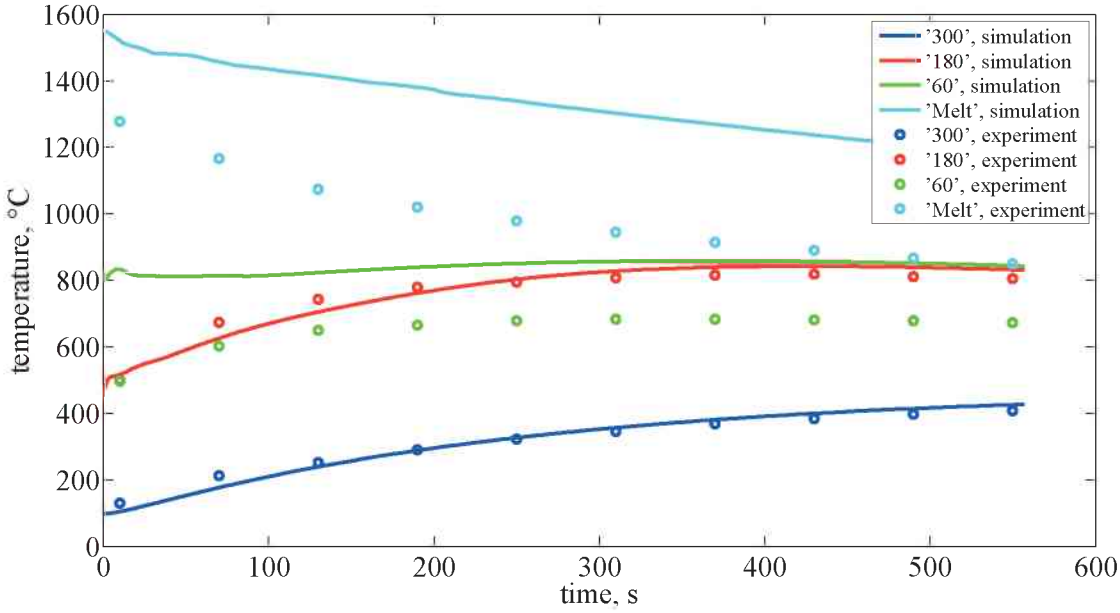

Figure 6.12: Comparison of the temperatures recorded using thermocouples placed in the walls of the mould (circles) with the corresponding curves obtained from the MAGMASOFT simulation (solid lines)

refractory material. At the same positions the temperature curves were recorded during the MAGMASOFT simulation. The position of the thermocouples in the mould is shown in the Fig. 6.11.

As can be seen in the Fig. 6.12, the experimental and simulated curves that correspond to the thermocouples placed within the ingot zone (identifier 'Melt') and the one placed 60 mm from the bottom (identifier '60') differ significantly, whereas the other two curves with identifiers '180' and '300' agree quite well.

The difference between the temperature curve collected by the 'Melt' thermocouple and the curve simulated using MAGMASOFT is approximately constant and is about $200-300$ °C, whereas the thermocouple must have showed the temperature of the melt, which was 1555 °C at the beginning of the casting. Contrary to that, the 'Melt' thermocouple indicated the temperature below 1300 °C in the beginning of the process, which is erroneous. On the other hand, the temperatures obtained numerically and experimentally for the point 'Melt' do not become close with time, as they should if we assume the delay effect caused by the refractory insulation around this thermocouple. Because of these two facts the data

collected from the 'Melt' thermocouple should be considered to be unreliable and will be excluded from the further analysis.

Let us consider the simulated curves for the points marked as '60' and '180' (green and red lines in Fig. 6.12, respectively). These two curves as expected reach almost the same value with time (starting from about 350 s). This is feasible, since the mould wall temperature at different heights becomes equal with time. The same behaviour is expected from the experimental curves for these two points (green '60' and red '180') in the mould wall. However, this is not the case. As can be seen in Fig. 6.12, the experimental values do not reach the same values as they should and have a constant discrepancy of about $200 - 300$ °C starting from the time of about 300 s. On the other hand, it is expected that these two temperature curves differ in the beginning (because they are exposed to heat of the melt at different times) and then start to coincide as the temperature of the mould becomes more and more uniform. The observed behaviour based on the experimental data is however opposite: first the two thermocouples show similar temperatures (around 0 s, the very first experimental points), and then start to show a discrepancy which increases with time and then becomes constant. As it was mentioned before, the simulated and experimental curves for the point '180' agree, but the curves for the point '60' do not. Most probable reason for this is that the thermocouple '60' has lost contact with the mould wall. The results produced by this thermocouple should be excluded from the further analysis.

The remaining two experimental temperature curves (blue '300' and red '180') are in a good agreement with the simulated ones. On the other hand, these two simulated and experimental temperature curves result in the comparable time of about 550 s. Because of these two facts it can be concluded that the temperature-dependent heat transfer coefficient shown above correctly models the heat transfer between the casting and the mould and can be used in the further solidification simulations using the Eulerian solidification model.

For obtaining the initial temperature for the solidification simulation using the model developed (summarised in 3.2) the distribution of the temperature after filling obtained from the MAGMASOFT simulation was used. It is shown in the Fig. 6.13.

As it can be seen in the Fig. 6.13, the temperature after filling is constant in the most of the ingot. Taking into account that the temperature of the ingot

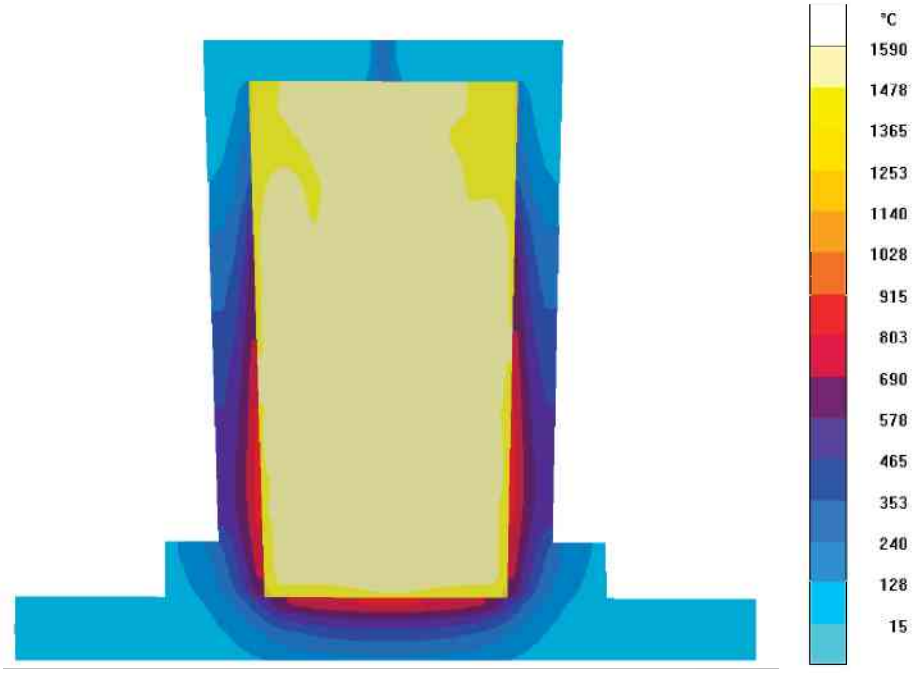

Figure 6.13: Distribution of the temperature of the melt after filling in MAGMASOFT simulation

is nevertheless slightly lower near walls and upper corners, the temperature of 1530 °C was used as initial temperature for multiphase solidification simulations later in Section 6.4.

The MAGMASOFT software package also performs solidification simulations. Such a simulation was performed for the 32 kg ingot and the solidification time was 557.1 s. The temperature distributions at at $t = 543.9$ s and at the end of MAGMASOFT solidification simulation, $t = 557.1$ s are shown in Fig. 6.14.

6.2 Simulation of the uphill ingot filling

Filling simulations of the uphill filling of the 2 ton ingot of Fe-0.38wt.%C-16wt%Cr used in simulations above was performed using the MAGMASOFT [MAG05] software package.

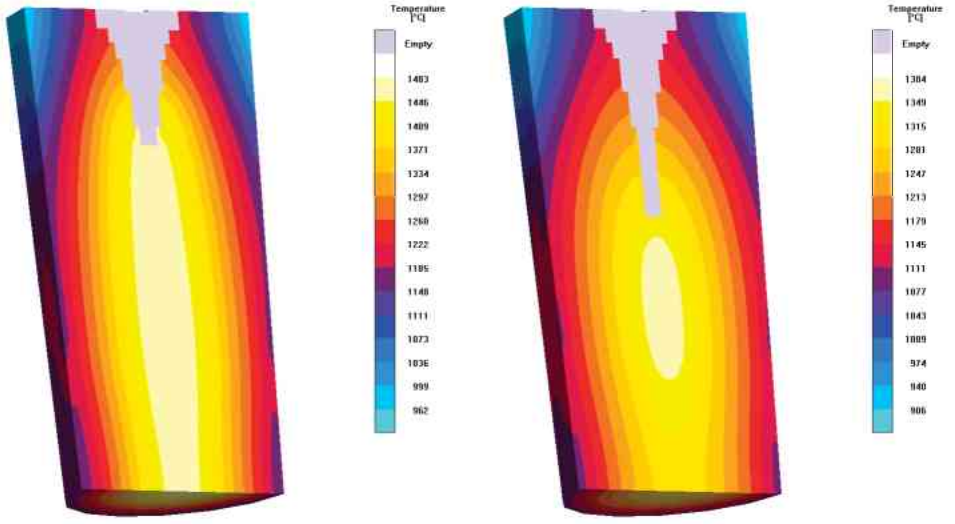

a b

Figure 6.14: Temperature distributions in the 32 kg benchmark ingot at $t = 543.9$ s (a) and at the end of simulation, $t = 557.1$ s (b). The maximal temperatures at these points in time are 1483 °C and 1384 °C respectively.

6.2.1 Material parameters

Material parameters for the alloy X38Cr16 does not differ from the parameters of X30Cr15 so the parameters of the latter were used. They are shown in Section 6.1.2. The only difference for this simulation was that the casting temperature was 1590 °C. The parameters of mould material and insulation were also the same as in the case of the uphill casting MAGMASOFT simulation. They are given in Section 6.1.2 as well.

6.2.2 Geometry, mesh, initial and boundary conditions

The geometry and meshing were prepared using the MAGMASOFT preprocessor. They are shown in Fig. 6.15.

The heat transfer coefficients between the parts of the casting system is shown in Table 6.3.

Just like in the case of downhill simulations, the heat transfer coefficient between the mould and the melt/ingot in the case of uphill casting is temperature-dependent:

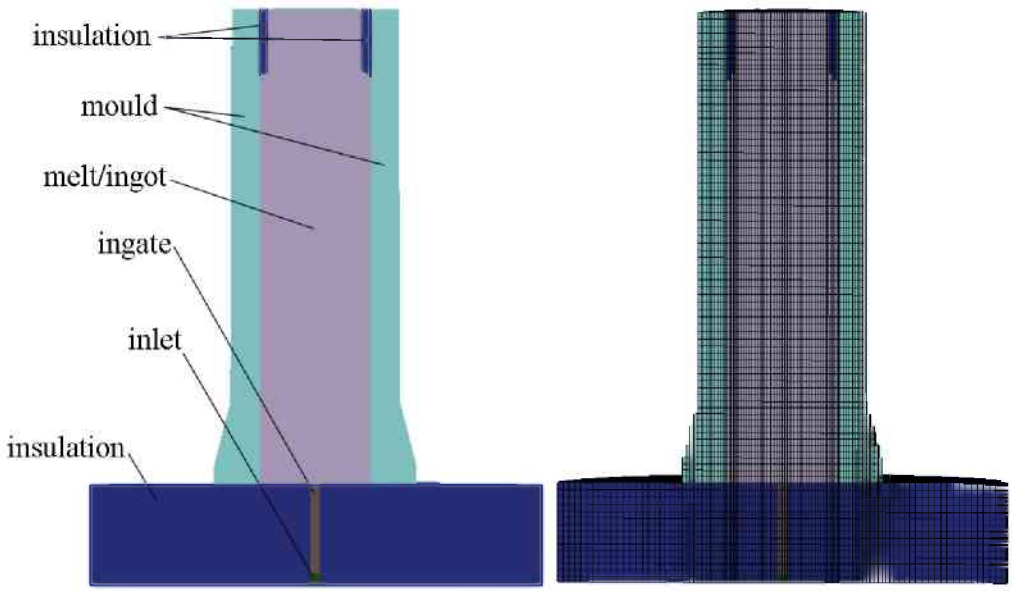

Figure 6.15: Geometry and mesh of the 2 ton ingot casting system

Material pairs	Heat transfer coefficient, $W \cdot m^{-2} \cdot K^{-1}$
alloy–mould	temperature-dependent
alloy–insulation	10^4
inlet–insulation	10^4
ingate–insulation	10^4
mould–insulation	10^4

Table 6.3: Heat transfer coefficients between different parts of the mould, the alloy ingot and the bottom plate for the uphill filling simulation of the 2 ton ingot of X38Cr16 alloy.

$$H(T) = \begin{cases} 1000\ \mathrm{W \cdot m^{-2} \cdot K^{-1}}, & T \leq 1375\ ^{\circ}\mathrm{C}, \\ (1000 + 35.0878\ (T - 1375))\ \mathrm{W \cdot m^{-2} \cdot K^{-1}}, & 1375\ ^{\circ}\mathrm{C} \leq T \leq 1483\ ^{\circ}\mathrm{C}, \\ 5000\ \mathrm{W \cdot m^{-2} \cdot K^{-1}}, & T > 1483\ ^{\circ}\mathrm{C}. \end{cases} \tag{6.2}$$

Again, this heat transfer coefficient was obtained by running a number of trail simulations with different heat transfer coefficient (6.2) so that the temperature curves obtained from the thermocouples in the casting experiment agree with the corresponding simulated curves. The thermocouple placement is shown in the Fig. 6.16.

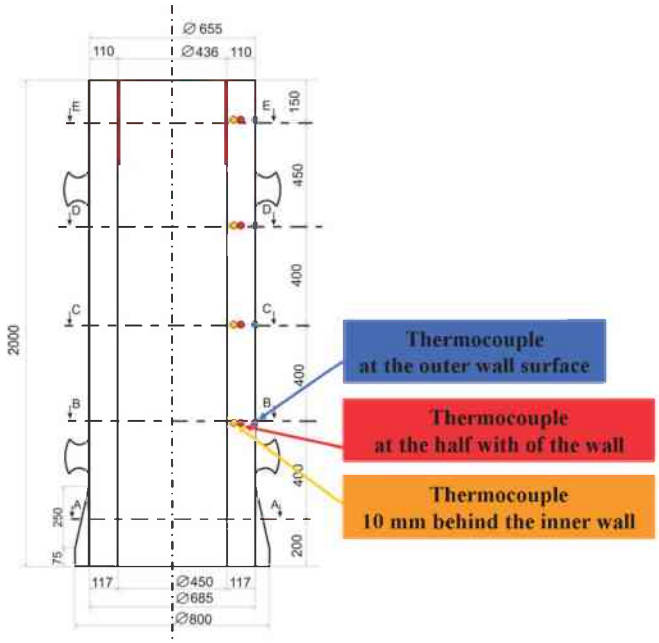

Figure 6.16: Thermocouples placement in the 2 ton mould. At each level (A-A, B-B, C-C, D-D and E-E) there were three thermocouples placed: one on the surface of the mould, one at the half width within the mould wall and one 10 mm away from the inner wall of the mould. The temperatures recorded using the latter two thermocouples were used for the comparison with the MAGMASOFT simulations (see Figs. 6.17-6.20).

6.2.3 Results and comparison with the experiment

The comparison between simulated and experimental temperature curves for cuts[1]B-B, C-C, D-D and E-E are shown in the Fig. 6.17, Fig. 6.18, Fig. 6.19 and Fig. 6.20 respectively. In these figures, the first experimental temperature value is not equal to the initial temperature in the MAGMASOFT simulation. This is because for this comparison the experimental temperature values were used starting from the first value which was not equal to the initial temperature.These figures show that the experimental curves agree with the simulated ones for the cuts B-B, C-C and D-D and have quite a large discrepancy for the cut E-E. The reason for it is that the filling flow rate during the casting becomes smaller at a certain time near the end of filling, so that the hot melt reaches the upper part of the ingot (where the E-E cut is situated) later. The obvious time shift between the curves for the E-E cut in Fig. 6.20 is another argument supporting this point.

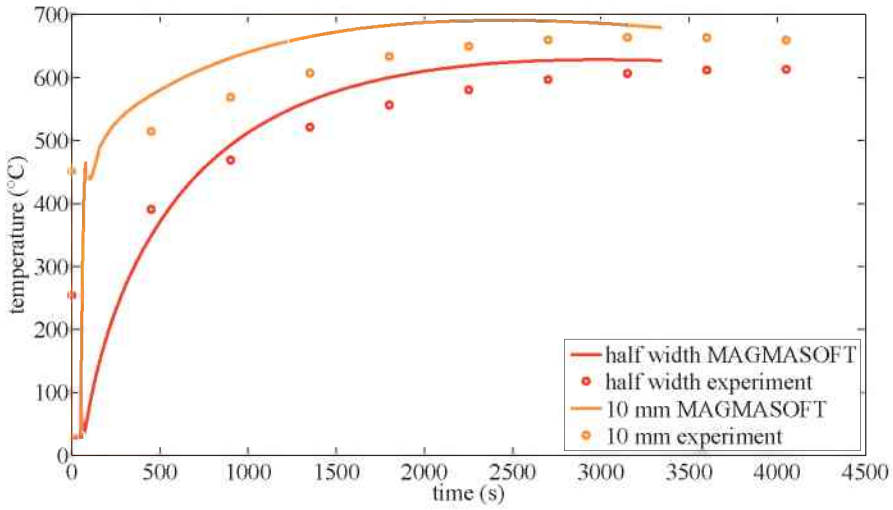

Figure 6.17: Comparison of the temperatures recorded using thermocouples placed in the walls of the mould (circles) with the corresponding curves obtained from the MAGMASOFT simulation (solid lines) for the cut B-B (see Fig. 6.16).

[1]The casting experiment was performed by the industry partner internally and the authors were provided by the experimental data. For an unknown reason the curves for the A-A cut were not among the data provided.

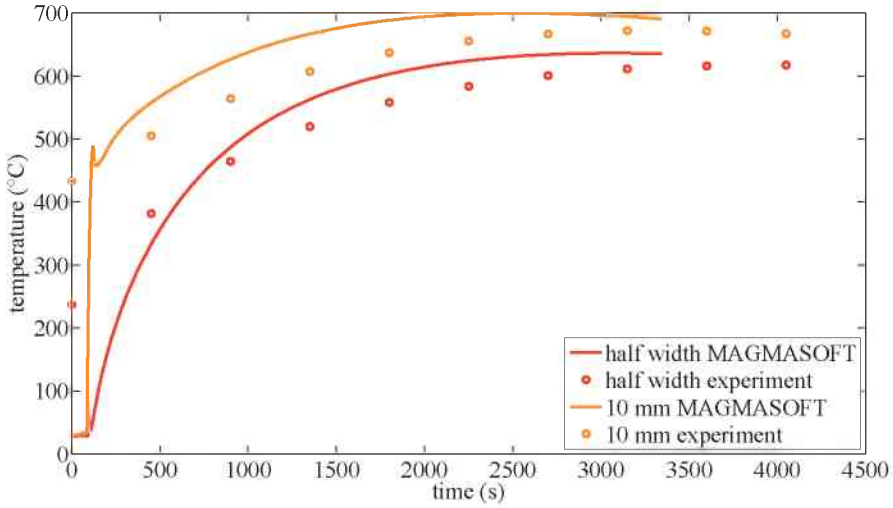

Figure 6.18: Comparison of the temperatures recorded using thermocouples placed in the walls of the mould (circles) with the corresponding curves obtained from the MAGMASOFT simulation (solid lines) for the cut C-C (see Fig. 6.16).

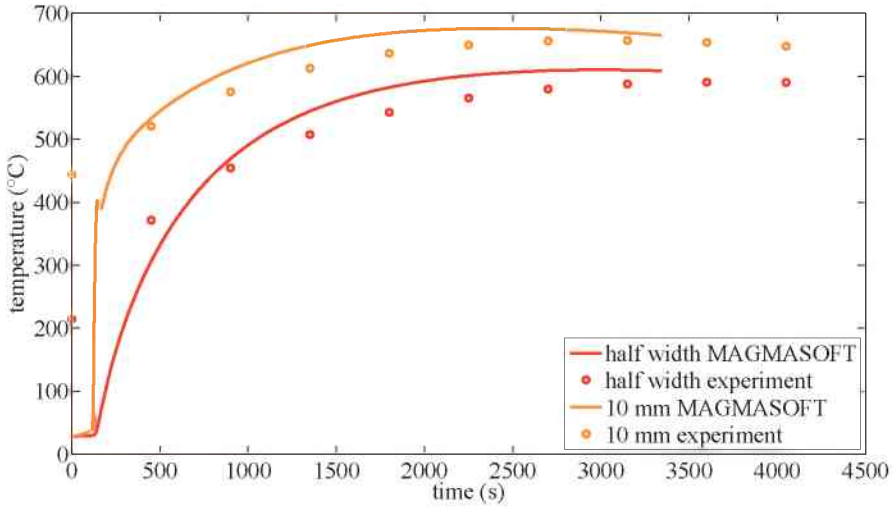

Figure 6.19: Comparison of the temperatures recorded using thermocouples placed in the walls of the mould (circles) with the corresponding curves obtained from the MAGMASOFT simulation (solid lines) for the cut D-D (see Fig. 6.16).

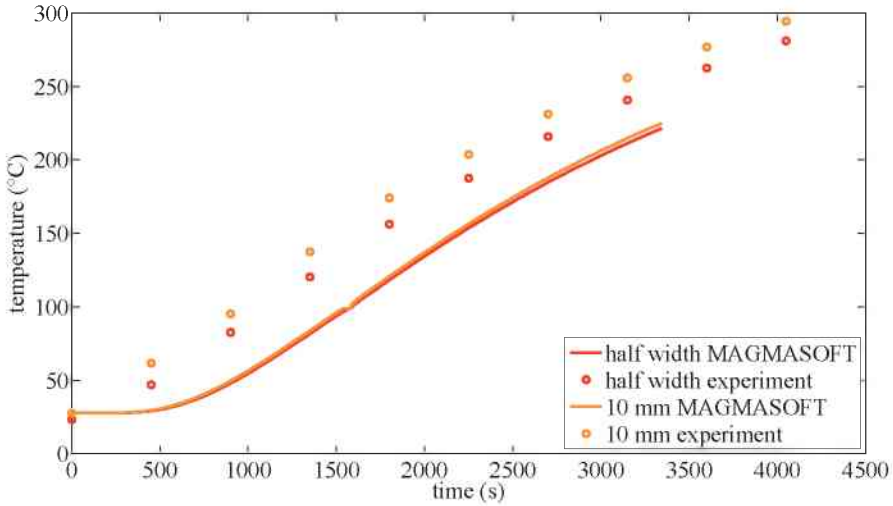

Figure 6.20: Comparison of the temperatures recorded using thermocouples placed in the walls of the mould (circles) with the corresponding curves obtained from the MAGMASOFT simulation (solid lines) for the cut E-E (see Fig. 6.16).

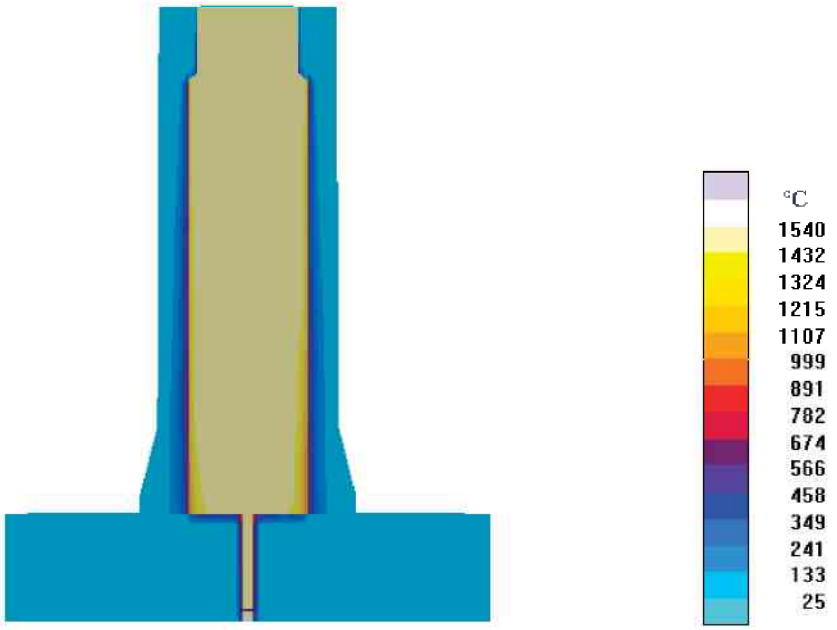

Figure 6.21: Distribution of the temperature of the melt after filling in MAGMASOFT simulation

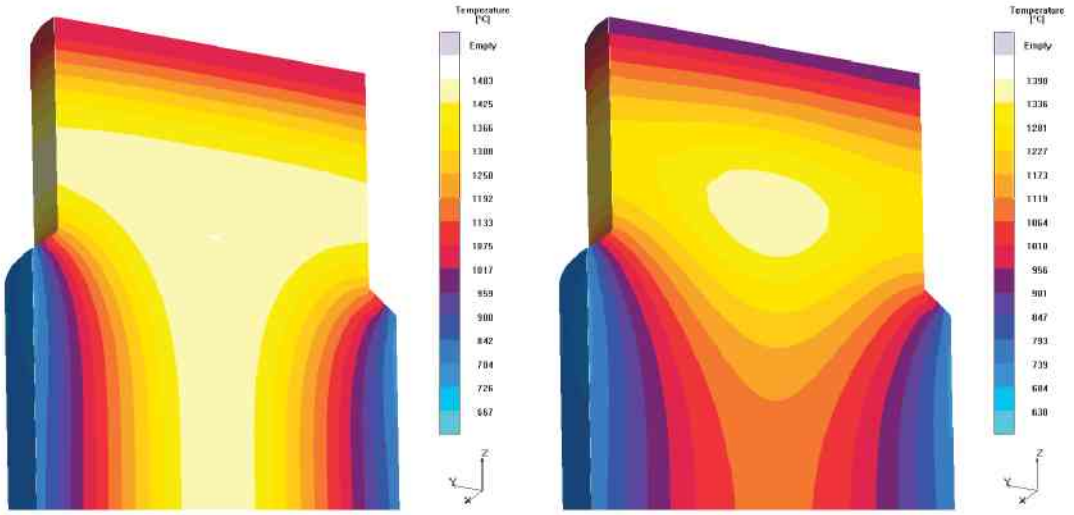

a b

Figure 6.22: Temperature distributions in the 2 ton industrial ingot at $t = 1938$ s (a) and at the end of simulation, $t = 3243$ s (b). The maximal temperatures at these points in time are 1483 °C and 1384 °C respectively.

The MAGMASOFT software package does not allow variable filling flow rate and thus the possibility to fit the experimental curves with the simulated ones is limited. Thus, the agreement between the experimental and simulated temperature curves has to be considered satisfactory and the temperature-dependent heat transfer coefficient, Eq. (6.2), will be used for the ternary three-phase Eulerian solidification simulation using the model developed in this work (summarised in Section 3.2) and implemented in FLUENT flow solver.

The initial temperature for this simulation can be derived from the temperature at the end of filling shown in the Fig. 6.21. The figure shows that in most of the melt the temperature is 1540 °C. and taking into account the small area regions with lower temperatures, the initial temperature for the ternary three-phase Eulerian solidification simulation should be taken a little smaller, namely 1530 °C.

Similarly to the case of 32 kg benchmark ingot, a solidification using MAGMASOFT was performed for the 2 ton industrial ingot. The temperature distributions at at $t = 1938$ s and at the end of MAGMASOFT solidification simulation, $t = 3243$ s are shown in Fig. 6.22.

Property	Value
Diffusion coefficient of carbon in the liquid phase D_l^{C}	$2 \cdot 10^{-8}$ m$^2 \cdot$ s^{-1}
Diffusion coefficient of chromium in the liquid phase D_l^{Cr}	$1.5 \cdot 10^{-9}$ m$^2 \cdot$ s^{-1}
Latent heat L	269793 J $\cdot$ kg^{-1}
Volumetric heat transfer coefficient H^*	10^7 W $\cdot$ m$^{-3} \cdot K^{-1}$
Primary dendrite arm spacing λ_1	10^{-3} m
minimal columnar diameter $d_{\mathrm{c,min}}$	10^{-6} m

Table 6.4: General material properties of X30Cr15 for the two-phase Eulerian solidification simulation of 32 kg benchmark ingot.

6.3 Two-phase 32 kg benchmark ingot simulation with simplified mould-ingot heat transfer coefficient for studying the thermosolutal convection effects

The first case to simulate using the ternary Eulerian multiphase solidification model developed in this work (see Section 3.2) was solidification of a small benchmark ingot X30Cr15 (0.3 wt.% C and 15.0 wt.% Cr) steel of approximately 32 kg in weight. Two phases, liquid and columnar were taken into account. The governing equations of the two-phase Eulerian ternary solidification model are summarised in Section 3.2.

6.3.1 Materials data

Physical parameters of the phases for this simulation were chosen based on the data from the MAGMASOFT database which was used for filling simulations (described in Sections 6.1 and 6.2) and is given in Section 6.1.2. Tables 6.4–6.6 show general properties as well as properties of the solid and the liquid phases. Diffusion coefficients for carbon and chromium in iron were estimated using the literature data from |Kurz98| for carbon and |Saito59, Kubícek75, Kubícek76| for chromium.

Property name	Value
Density ρ_l	$7001\ \mathrm{kg \cdot m^{-3}}$
Heat capacity $c_{p,l}$	$804\ \mathrm{J \cdot kg^{-1} \cdot K^{-1}}$
Thermal conductivity k_l	$29\ \mathrm{W \cdot m^{-1} \cdot K^{-1}}$
Viscosity μ_l	$7.516 \cdot 10^{-7}\ \mathrm{kg \cdot m^{-1} \cdot s^{-1}}$

Table 6.5: Material parameters of the liquid phase

Property name	Value
Density ρ_c	$7001\ \mathrm{kg \cdot m^{-3}}$
Heat capacity $c_{p,c}$	$804\ \mathrm{J \cdot kg^{-1} \cdot K^{-1}}$
Thermal conductivity k_c	$29\ \mathrm{W \cdot m^{-1} \cdot K^{-1}}$

Table 6.6: Material parameters of the columnar phase

6.3.2 Geometry, mesh, initial and boundary conditions

The casting system for the casting of the 32 kg X30Cr15 benchmark ingot had the geometry shown in Fig. 6.16.

After solidification the ingot itself was assumed to have the following geometry (Note that in reality there are cavities in the ingot which are neglected in simulations):

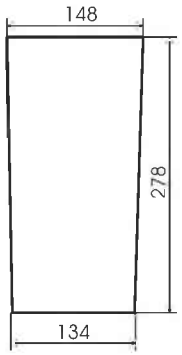

Figure 6.23: A sketch of the resulting 32 kg ingot

In order to perform CFD computations in FLUENT, a two-dimensional finite volume mesh with 690 cells was produced. Such a small number here is

taken because the geometry is small, and the second factor affecting the grid size is the computational effort of numerical solution of the partial differential equation system describing two-dimensional two-phase flow taking into account species transport for two species. Taking into account that in the present section in order to study the effect of thermosolutal segregation 5 different simulations had to be carried out, it was decided to use such a coarse grid. Nevertheless, this amount of cells should be enough to study the influence of thermosolutal expansion coefficients on ternary solidification. The computation time can be decreased by using parallel computing and by optimising spline interpolants (for the details see Section 8.3). Simulation is stopped when f_c reaches the value of 0.95 everywhere in the ingot. This limit for the f_c is set in order to avoid simulation of eutectic reaction which the thermodynamic model is not capable of (see further explanations in Sections 3.3 and 5.2 as well as Fig. 5.10).

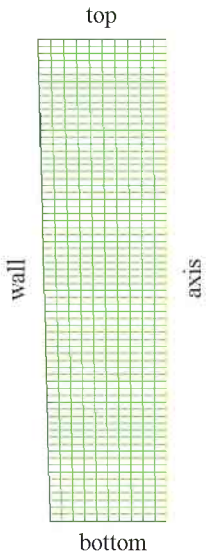

Figure 6.24: The mesh for the 32 kg ingot used for the simulation of the X30Cr15 alloy solidification

In the following simulations two phases were considered: liquid, denoted by lower index l and columnar, denoted by c.

Initial conditions for the equations described in the Section 2.1 were:

- initial volume fraction of columnar was $f_c = 10^{-5}$,

- initial temperature of the both phases was $T_{l,0} = T_{c,0} = 1804$ K (or 1530 °C as it was estimated in the MAGMASOFT filling simulation in Section 6.1),
- initial velocity was $\vec{u}_{l,0} = \vec{u}_{s,0} = 0 \text{ m} \cdot \text{s}^{-1}$ everywhere,
- initial mass fractions of of the liquid species were $c_{l,0}^{\text{C}} = 3 \cdot 10^{-3}$ and $c_{l,0}^{\text{Cr}} = 0.15$, and of columnar $c_{c,0}^{\text{C}} = 4.86 \cdot 10^{-4}$ and $c_{c,0}^{\text{Cr}} = 0.147$.

The boundary conditions for the equation system consisting of equations described in Section 2.1 were set as follows (see also Fig. 6.24 with mesh and boundary names).

Conditions for the boundary *"wall"* and *"bottom"*

- velocity of both phases was set to zero ("no-slip" condition): $\vec{u}_l = 0 \text{ m} \cdot \text{s}^{-1}$ and $\vec{u}_c = 0 \text{ m} \cdot \text{s}^{-1}$.
- for the energy equation the convective heat transfer boundary condition was used, so that the heat flux to the wall is computed as $q = h_{\text{ext}}(T_{ext} - T_f)$, where the external transfer coefficient was set to h_{ext}= 700 $\text{W} \cdot \text{m}^{-1} \cdot \text{K}^{-1}$ and the external temperature was set to T_{ext} =300 K, as the parameters were estimated from experimental data in |Tanzer08| for this geometry and conditions.
- zero diffusive flux through the boundary was assumed for species both in liquid and columnar phase: $\partial c_{l,c}^{\text{C,Cr}}/\partial \vec{n} = 0$, where $\vec{n}$ is the normal to the boundary.

Conditions for the boundary *"top"*

- velocity of both phases was set to zero ("no-slip" condition): $\vec{u}_l = 0 \text{ m} \cdot \text{s}^{-1}$ and $\vec{u}_c = 0 \text{ m} \cdot \text{s}^{-1}$. The choice of the no-slip condition is justified, because the slag on top of the ingot prevents the melt from moving.
- for the energy equation the convective heat transfer boundary condition was used, so that the heat flux to the wall is computed as $q = h_{ext}(T_{ext} - T_f)$, where the external transfer coefficient was set to h_{ext}= 100 $\text{W} \cdot \text{m}^{-1} \cdot \text{K}^{-1}$ and the external temperature was set to T_{ext} =300 K, as the parameters

Case	Convection type	Parameter values
A	no convection	$\beta_T = 0\ \mathrm{K}^{-1},\ \beta_\mathrm{C} = \beta_\mathrm{Cr} = 0$
B	thermal convection only	$\beta_T = 2 \cdot 10^{-4}\ \mathrm{K}^{-1},\ \beta_\mathrm{C} = \beta_\mathrm{Cr} = 0$
C	reduced thermal convection only	$\beta_T = 5 \cdot 10^{-5}\ \mathrm{K}^{-1},\ \beta_\mathrm{C} = \beta_\mathrm{Cr} = 0$
D	solutal convection only	$\beta_T = 0\ \mathrm{K}^{-1},\ \beta_\mathrm{C} = 1.1,\ \beta_\mathrm{Cr} = 0$
E	thermal and solutal convection	$\beta_T = 2 \cdot 10^{-4}\ \mathrm{K}^{-1},\ \beta_\mathrm{C} = 1.1,\ \beta_\mathrm{Cr} = 0$

Table 6.7: Different convection effects taken into account during simulations

were estimated from experimental data in |Tanzer08| for this geometry and conditions.

- zero diffusive flux through the boundary was assumed for species both in liquid and columnar phase: $\partial c_{l,c}^{\mathrm{C,Cr}}/\partial \vec{n} = 0$, where $\vec{n}$ is the normal to the boundary.

Conditions for the boundary *"axis"* Axis boundary condition is set on this boundary.

6.3.3 Simulation parameters

Values of thermal and solutal expansion coefficients

In order to validate and study the simulation possibilities the model suggested offers, five different simulations were carried out for this geometry. In order to study the effect of different types of convection on the resulting distribution of quantities of interest such as mixture mass fractions $c_{\mathrm{mix}}^{\mathrm{C}}$ and $c_{\mathrm{mix}}^{\mathrm{Cr}}$ defined by Eq. (2.20) for $K = 2$ ($i = l, c$, $m = \mathrm{C}, \mathrm{Cr}$), different convection types were taken into account, with parameters shown in Table 6.7.

The value of 1.1 for the solutal expansion coefficient β_C in Eq. (2.8) was taken as in |Sanyal05|. The value $\beta_\mathrm{Cr} = 0$ is taken because the densities of chromium and iron densities are close ($\rho_\mathrm{Cr} = 7150\ \mathrm{kg \cdot m^{-3}}$ and $\rho_\mathrm{Fe} = 7870\ \mathrm{kg \cdot m^{-3}}$) and atomic radii of these elements are also close ($r_\mathrm{Cr} = 124 \cdot 10^{-12}$ m and $r_\mathrm{Fe} = 125 \cdot 10^{-12}$ m), so the diffusion of chromium in iron is considered to be negligible. The thermal expansion coefficient $\beta_T = 2 \cdot 10^{-4}\ \mathrm{K}^{-1}$ used is the same as in the |Sanyal05| or |Qiu04| and does not differ much from the one used for example in |Samoilovich83| ($1.7 \cdot 10^{-4}\ \mathrm{K}^{-1}$) or in |Feng03| ($1.0 \cdot 10^{-4}\ \mathrm{K}^{-1}$).

Characterisation of the simulation cases

Case A no convection. Due to the absence of convection, there is no macrosegregation expected. The final distributions of mixture mass fractions $c_{\text{mix}}^{\text{C}}$ and $c_{\text{mix}}^{\text{Cr}}$ must be uniform and equal to the initial mass fractions of c_0^{C} and c_0^{Cr} respectively.

Case B thermal convection only. Thermal convection causes relative motion of the phases during solidification, thus providing a mechanism for macrosegregation formation. In this case, macrosegregation distributions are expected to be non-uniform, with negatively segregated melt ($c_{\text{mix}}^{\text{C,Cr}} < c_0^{\text{C,Cr}}$) next to the walls and positively segregated melt ($c_{\text{mix}}^{\text{C,Cr}} > c_0^{\text{C,Cr}}$) in the middle of the ingot. During solidification, the solute is rejected into the liquid due to inability of solid phases to incorporate as much of alloying element as liquid phase contains. Since solidification in ingots starts near the walls, the melt there is enriched due to solute rejection and sinks by virtue of the thermal convection. This melt is replaced with a less enriched fresh melt. This way the total amount of alloying elements near the walls of the ingot becomes smaller. This process continues until the end of the solidification, when a highly enriched rest melt solidifies in the middle of the ingot (so-called hot-spot) causing positive macrosegregation ($c_{\text{mix}}^{\text{C,Cr}} > c_0^{\text{C,Cr}}$).

Case C reduced thermal convection only. In this case the same behaviour as in Case B is expected, but to a lesser extent. The macrosegregation patterns are expected to be similar, but not as pronounced as in the Case B.

Case D solutal convection only. When only solutal convection is included only a slight deviations from the uniform distribution (as in Case A) in the final macrosegregation pattern are expected. The reason for solutal convection is the dependence of the density of the melt on its composition. A change in the composition causes a relative motion of the melt. Changes in composition do not cause a strong change in mass of the melt, so the solutal convection is a much weaker effect than the thermal one.

Case E Thermal and solutal convection. Effect of solutal convection on the relative motion of the melt caused by the thermal convection is weak. The small size of the ingot does not allow the development of strong motion due to

the solutal convection. Thus in this case macrosegregation patterns are expected to be similar to those of Case B.

Time step, iterations, and computation time

The simulation was performed with the following settings. The time step was $\Delta t = 10^{-1}$ s, 4000 time steps were carried out with 100 iterations per time step. The number of iterations per time step was fixed to 100 which was enough to achieve acceptable values of residuals.

The simulation is stopped when f_c reaches the value of 0.95 everywhere in the ingot. This limit for the f_c is set in order to avoid simulation of eutectic reaction which the thermodynamic model is not capable of (see further explanations in Sections 3.3 and 5.2 as well as Fig. 5.10).

Thermodynamics representation

Here interpolating spline surfaces of the third order were used to calculate the values of the thermodynamic functions defined by Eqs. (3.15), (3.16) and (3.17). These interpolations were produced by SISL library |SIN06, SIN05| from the values of these functions tabulated from the thermodynamics software package Thermo-Calc |The06a, The06b| as described in Section 4.3.3.

6.3.4 Simulation results

The following figures show change of distributions of different quantities for the case E (see Table 6.7): temperature $T = T_l = T_c$, columnar volume fraction f_c, velocity of the liquid phase $\vec{u}_l$, mass fraction of carbon in the liquid phase c_l^{C}, mass fraction of the chromium in the liquid phase c_l^{Cr}, mass fraction of carbon in the columnar phase c_c^{C}, mass fraction of chromium c_c^{Cr}, mixture mass fraction of carbon $c_{\mathrm{mix}}^{\mathrm{C}}$ and mixture mass fraction of chromium $c_{\mathrm{mix}}^{\mathrm{Cr}}$. Figure 6.25 shows the distribution of these quantities at $t = 4$ s and $t = 10$ s and Fig. 6.26 at $t = 200$ s and $t = 400$ s.

In the following the description of the results is given. There are four sections which describe each of the moments in time: t =4 s, 10 s, 200 s and 400 s. The following descriptions of each moment in time refer to the corresponding figures, where the distributions of process quantities are shown.

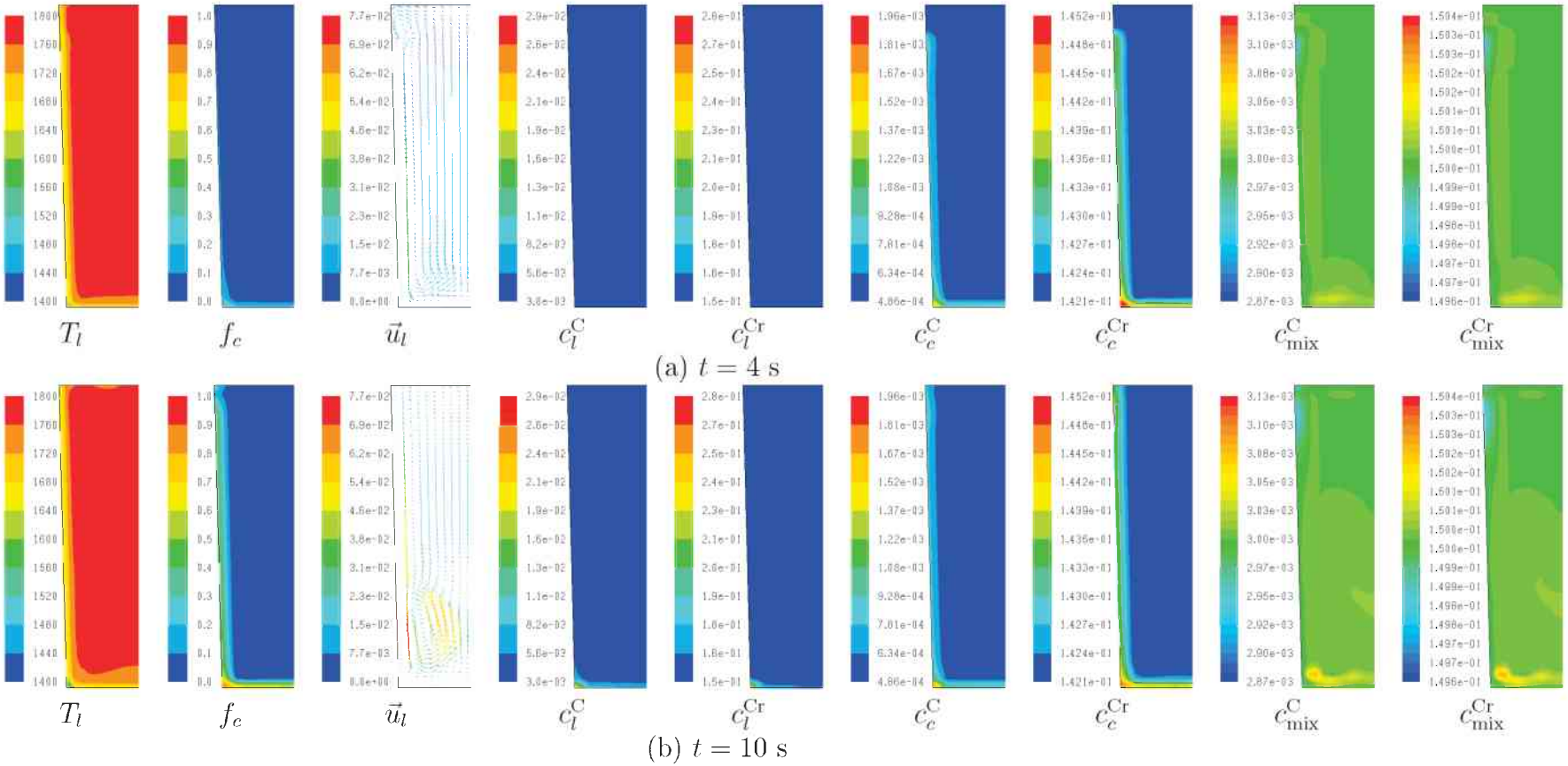

Figure 6.25: Changes in the distribution of process quantities for case E at (a) $t = 4$ s and (b) $t = 10$ s.

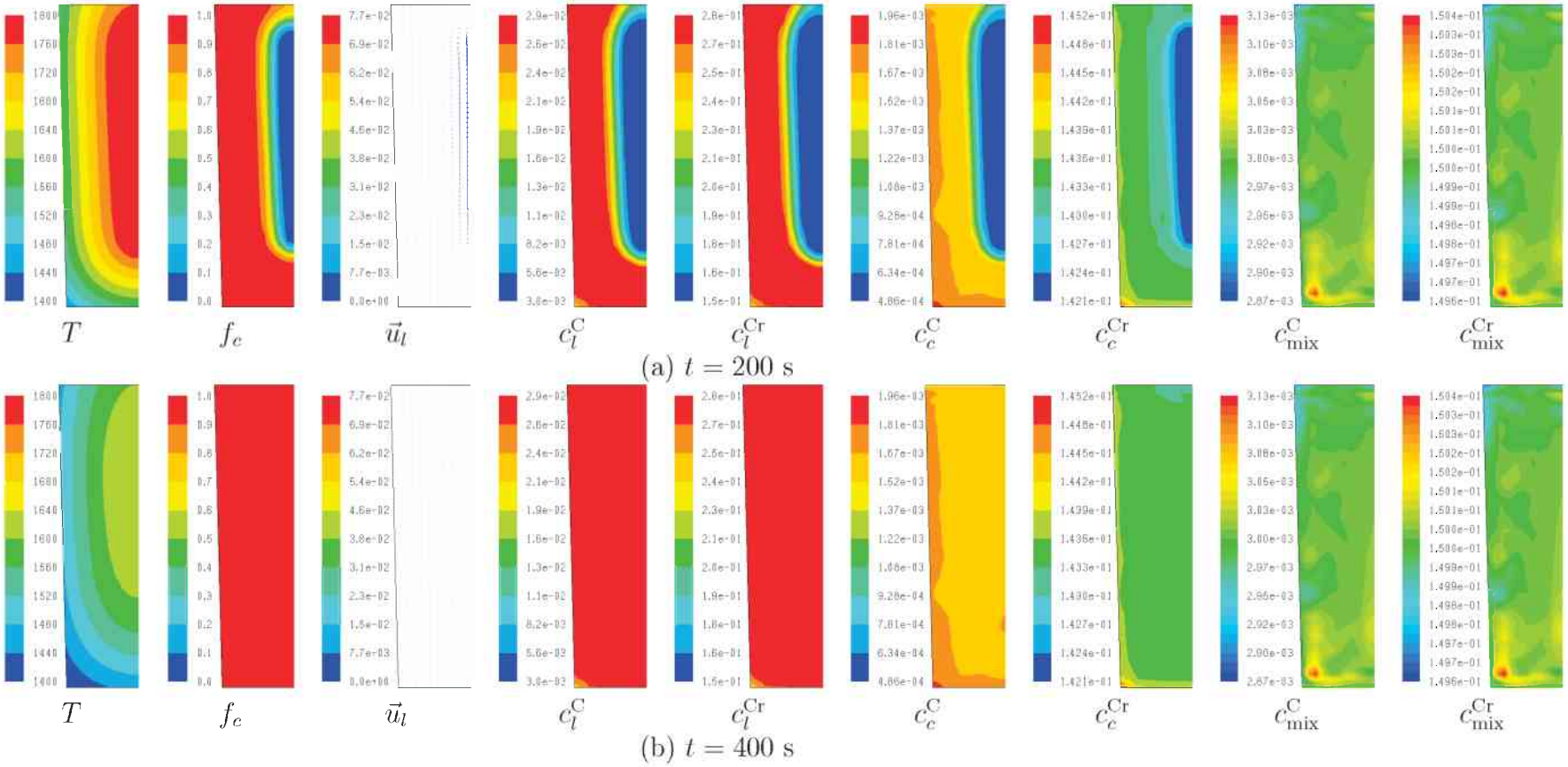

Figure 6.26: Changes in the distribution of different process quantities for case E at (a) $t = 200$ s and (b) $t = 400$ s. Note that the distributions of c_c^{C} and c_c^{Cr} are not the same as $c_{\mathrm{mix}}^{\mathrm{C}}$ and $c_{\mathrm{mix}}^{\mathrm{Cr}}$, since $f_c = 0.05$ at the end of the simulation and $c_c^{\mathrm{C,Cr}} = c_{\mathrm{mix}}^{\mathrm{Cr}}$ only when $f_c = 0$.

Simulation results at $t = 4$ s

The boundary conditions make the melt near the wall of the ingot cool down and due to the thermal convection it flows downwards. This can be seen from the temperature distribution and velocity vectors. At the same time first columnar volume fraction forms in the cooldest part of the ingot, in the bottom corner, which can be seen from the distribution of f_c. Also the mass fractions of both of the alloying elements increase near the wall in both liquid and solid phases. This can be seen again in the same figure, where distributions of c_l^{C},c_l^{Cr},c_c^{C} and c_c^{Cr} are shown. Note that the increase in the liquid mass fractions are very small and cannot be seen in this figure yet due to the colour scale chosen, which ranges from the minimum to maximum value of the liquid mass fractions throughout the whole simulation. The mixture mass fractions of the alloying elements $c_{\mathrm{mix}}^{\mathrm{C}}$ and $c_{\mathrm{mix}}^{\mathrm{Cr}}$ reveal an increase in the bottom area of the ingot. This happens because the enriched melt which flows downwards from the area near the wall increases the macrosegregation in the bottom part of the ingot.

Simulation results at $t = 10$ s

The processes that are described for $t = 4$ s continue, which results in the following: temperature T_l decreases, the columnar volume fraction f_c near the walls increases and the mass fraction of the alloying elements in both liquid and columnar phases c_l^{C},c_l^{Cr},c_c^{C} and c_c^{Cr} increases as well. Also the velocity decreases to zero values very close to the walls, where there is no movement since this part of the ingot has started to solidify. The macrosegregation characterised by the $c_{\mathrm{mix}}^{\mathrm{C}}$ and $c_{\mathrm{mix}}^{\mathrm{Cr}}$ distributions increased in the bottom corner. This happens due to the melt enrichment mechanism described in the previous section for $t = 4$ s and relatively fast solidification in the corner which is accompanied with relatively stronger solute rejection which enriches the liquid phase with the alloying elements there.

Simulation results at $t = 200$ s

At this moment in time, the temperature decreased further, and the solidified shell increased accordingly. There is still a small region of liquid left in the middle of the ingot as it can be seen from the distribution of the columnar volume fraction f_c. The liquid velocity $\vec{u}_l$ is non-zero only in this region. The volume with increased

mass fractions of alloying elements in the liquid and columnar phases c_l^{C},c_l^{Cr},c_c^{C} and c_c^{Cr} continue to grow. These fronts of increased mass fractions fronts coincide with the front of the columnar volume fraction f_c. The macrosegregation in the corners increases due to the processes described in the previous section. The somewhat uneven distribution of liquid velocities $\vec{u}_l$ and columnar mass fractions of alloying elements c_c^{C} and c_c^{Cr} (and thus mixture mass fractions $c_{\mathrm{mix}}^{\mathrm{C}}$ and $c_{\mathrm{mix}}^{\mathrm{Cr}}$ which depend on c_c^{C} and c_c^{Cr} by means of (2.20)) are most probably caused by the relatively coarse grid.

Simulation results at $t = 400$ s

The results at the time $t = 400$ s show the final result, when the whole volume of the ingot has solidified. Figure 6.26 shows the final distribution of the process quantities in the ingot. The temperature T_l decreased further, the columnar fraction f_c is uniform everywhere and is equal to 0.95, the liquid velocity $\vec{u}_l$ distribution shows no movement, mass fractions of the alloying elements in the liquid and columnar phases c_l^{C},c_l^{Cr},c_c^{C} and c_c^{Cr} and thus also their mixture mass fractions c_c^{C} and c_c^{Cr} have reached their final distributions.

Macrosegregation of carbon and chromium in cases with different convection parameters

The following Figs. 6.27 and 6.28 show the distribution of the alloying components carbon and chromium respectively when different convection effects are taken into account. The differences in convection effects are described in Table 6.7.

In case of no convection (all of the expansion coefficients are zero) no macrosegregation was predicted in the simulation, mixture mass fractions of carbon and chromium were distributed uniformly and equal to the initial liquid mass fractions of these elements in every point of the ingot, and there is no need to show this distribution here.

Figures 6.27B and 6.28B show the final distribution of the mixture mass fractions of carbon and chromium when only when the thermal convection is taken into account. One can see that taking into account the thermal convection results in the positive macrosegregations near the bottom corners and very slightly negative near the top corners of the ingot.

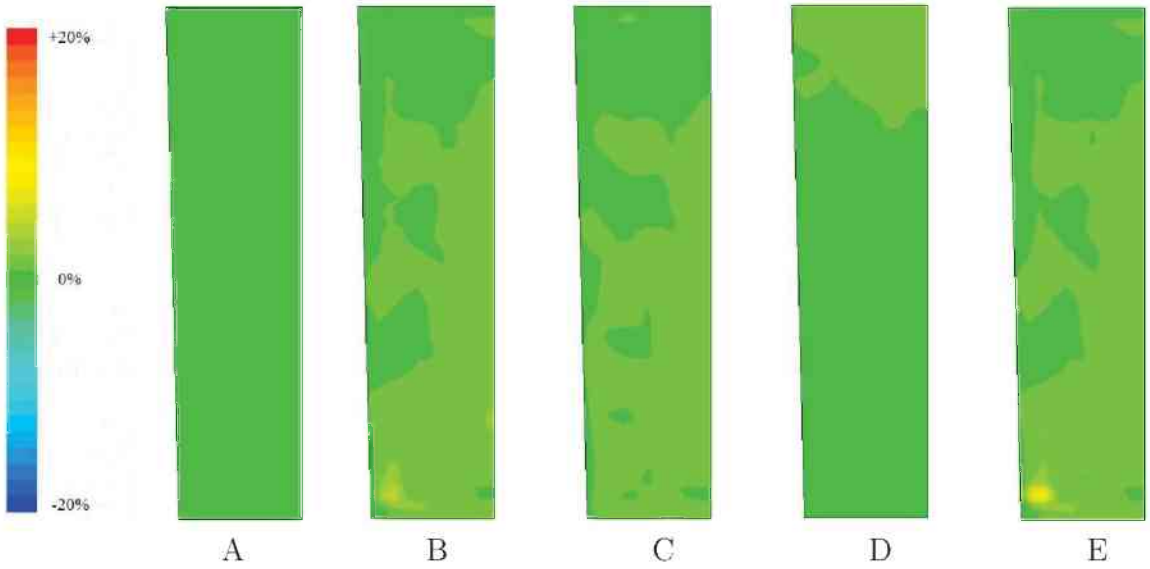

Figure 6.27: The final distributions of c^{C}_{mix} for the cases described in Table 6.7.

The effect of the reduced thermal convection onto the final distribution of the mixture mass fractions of carbon and chromium was so low, that Figs. 6.27C and 6.28C almost cannot reveal it. The same is true for the final distribution of carbon and chromium for the simulation where only solutal convection is taken into account: the distribution of mixture concentrations of carbon and chromium are almost do not differ from the uniform as it can be seen in Figs. 6.27D and 6.28D.

The highest final macrosegregation is achieved in the simulation where both thermal and solutal convection effects are taken into account. The final distributions of the mixture mass fractions of carbon and chromium for this case are shown in Figs. 6.27E and 6.28E. One can see rather strong positive macrosegregation of both carbon and chromium near the bottom corners of the ingot and slightly negative macrosegregation near the top corners.

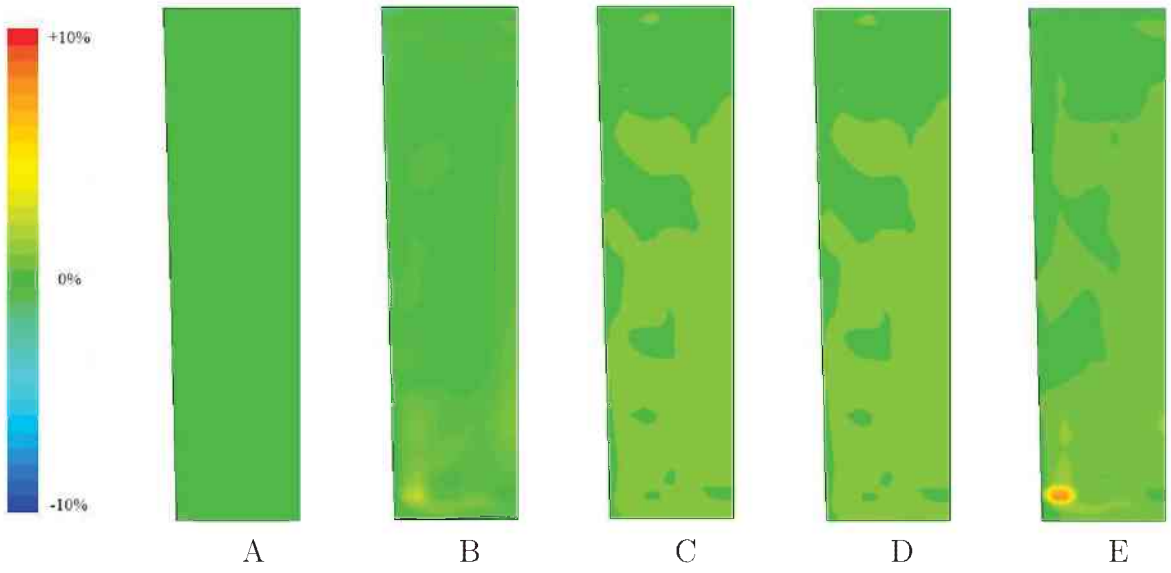

Figure 6.28: The final distributions of $c_{\text{mix}}^{\text{Cr}}$ for the cases described in Table 6.7.

6.4 Two-phase 32 kg benchmark ingot simulation with realistic mould-ingot heat transfer coefficient

6.4.1 Geometry, mesh, initial and boundary conditions

Since the solidification process discussed here was the same as the one simulated in Section 6.3, the only difference to the previous simulation is the use of the realistic heat transfer coefficient between the mould and the ingot, obtained in MAGMASOFT uphill simulation in Section 6.1, given by the formula (6.1) and a finer grid consisting of 2760 cells. The grid is shown in Fig. 6.29.

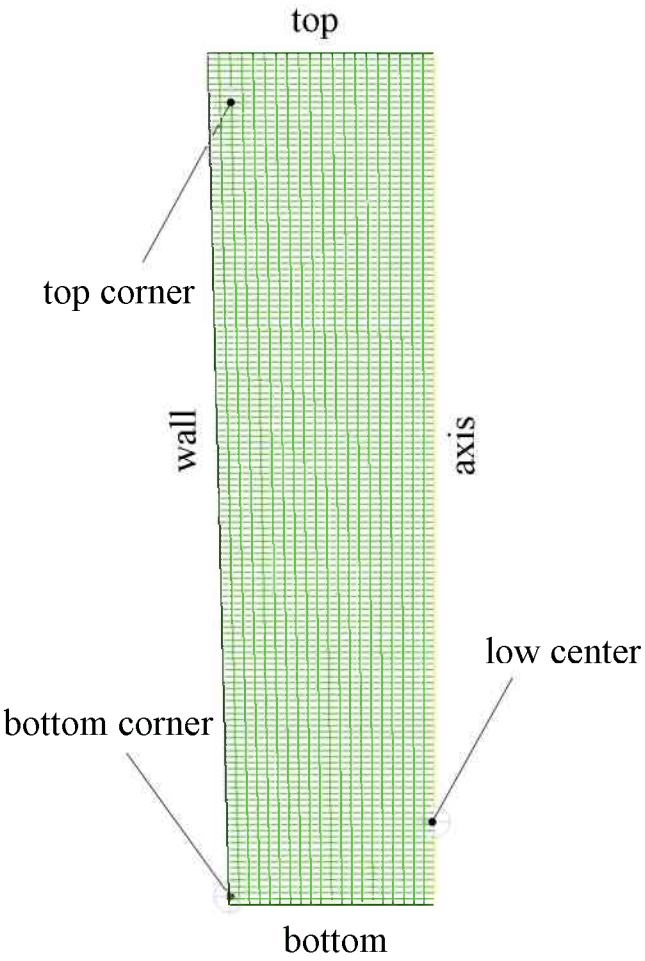

Figure 6.29: Mesh for the solidification simulation of 32 kg ingot of X30Cr15 alloy. Also the points where data were collected for later analysis are shown.

In the following simulations two phases were considered: liquid, denoted by lower index l and columnar, denoted by the lower index c.

The differential equation of the differential equations of the Eulerian two-phase solidification model are summarised in Section 3.2. Initial conditions were as follows:

- initial volume fraction of columnar was $f_c = 10^{-5}$,
- initial temperatures of the all three phases was $T_{l,0} = T_{c,0} = 1804$ K (as it was estimated in the MAGMASOFT filling simulation, see Section 6.1),
- initial velocities were $\vec{u}_{l,0} = 0 \text{ m} \cdot \text{s}^{-1}$ everywhere,

- initial mass fractions of of the alloying components in the liquid phase were $c_{l,0}^{\mathrm{C}} = 3 \cdot 10^{-3}$ and $c_{l,0}^{\mathrm{Cr}} = 0.15$, and in columnar phase $c_{c,0}^{\mathrm{C}} = 4.86 \cdot 10^{-4}$ and $c_{c,0}^{\mathrm{Cr}} = 0.147$.

The boundary conditions for the equation system consisting of equations summarised in Section 3.2 were set as follows (see also Fig. 6.29 with mesh and boundary names).

Conditions for the boundary *"wall"* and *"bottom"*

- velocity of the liquid phase was set to zero ("no-slip" condition): $\vec{u}_l = 0\ \mathrm{m} \cdot \mathrm{s}^{-1}$.

- for temperature the convective heat transfer boundary condition was used, so that the heat flux to the wall is computed as $q = h_{\mathrm{ext}}(T_{\mathrm{ext}} - T_{\mathrm{f}})$. The external transfer coefficient was based on the temperature-dependent heat transfer coefficient $H(T)$ obtained from experimental data and MAGMASOFT filling simulations (see Eq. (6.1) in Section 6.1). In order to take into account the heat transfer through the mould wall it was calculated according to the formula:

$$h_{\mathrm{ext}}(T) = \left(\frac{1}{H(T)} + \frac{l}{k} + \frac{1}{h_{\mathrm{outer}}} \right)^{-1}, \tag{6.3}$$

  where $l = 23{\cdot}10^{-3}$ m is the thickness of the mould wall, $k = 55\ \mathrm{W} \cdot \mathrm{m}^{-1} \cdot \mathrm{K}^{-1}$ its the heat conductivity of the mould (mean value of the heat conductivity of the GJL-350 mould material is taken according to Fig. 6.7) , and $h_{\mathrm{outer}} = 200\ \mathrm{W} \cdot \mathrm{m}^{-2} \cdot \mathrm{K}^{-1}$ is the heat exchange coefficient between the mould wall and the surrounding air. The external temperature was set to T_{ext} =300 K. This is a simplified description of the heat transfer through the mould wall as it does not take into account the heat capacity of the mould.

- zero diffusive flux through the boundary was assumed for species in liquid and columnar phases: $\partial c_{l,c}^{\mathrm{C,Cr}} / \partial \vec{n} = 0$, where $\vec{n}$ is the normal to the boundary.

Conditions for the boundary *"top"*

- velocity of the liquid phase was set to zero ("no-slip" condition): $\vec{u}_l = 0\ \mathrm{m} \cdot \mathrm{s}^{-1}$. This boundary condition was chosen because of the existence of the slag on top of the ingot which prevents the liquid from moving, i.e. it acts as a lid.

- for temperature the convective heat transfer boundary condition was used, so that the heat flux to the wall is computed as $q = h_{\mathrm{ext}}(T_{\mathrm{ext}} - T_{\mathrm{f}})$, where the external transfer coefficient was set to h_{ext}= 100 $\mathrm{W} \cdot \mathrm{m}^{-1} \cdot \mathrm{K}^{-1}$ and the external temperature was set to T_{ext} =300 K, as the parameters were estimated from experimental data in |Tanzer08| for this geometry and conditions.

- zero diffusive flux through the boundary was assumed for species in liquid and columnar phases: $\partial c_{l,c}^{\mathrm{C,Cr}}/\partial \vec{n} = 0$, where $\vec{n}$ is the normal to the boundary.

Conditions for the boundary *"axis"* Axis boundary condition is set on this boundary.

6.4.2 Material data

The materials description necessary for the three-phase Eulerian ternary solidification simulation were the same as in the simulation with simplified ingot/mould heat transfer coefficient (see Section 6.3.1).

6.4.3 Simulation parameters

Thermosolutal convection parameters

The following additional parameters were used: the thermal expansion coefficient was taken as $\beta_T = 2{\cdot}10^{-4}\ \mathrm{K}^{-1}$ and the solutal expansion coefficients were $\beta_{\mathrm{C}} = 1.1$ for carbon, and $\beta_{\mathrm{Cr}} = 0$ for chromium. The choice of these parameters is explained above in Section 6.3.3.

Thermodynamics representation

Thermodynamics representation used for this simulation was the same as in the previous simulation described in Section 6.3. Interpolating spline surfaces of the third order were used to calculate the values of the thermodynamic functions defined by Eqs. (3.15), (3.16) and (3.17). These interpolations were produced by the SISL library [SIN06, SIN05] from the values of these functions tabulated from the thermodynamics software package Thermo-Calc [The06a, The06b] as described in Section 4.3.3.

Time step, iterations, and computation time

The simulation was performed with the following settings. The time step was $\Delta t = 10^{-1}$ s, there was 6150 time steps were carried out with 100 iterations per time step, without convergence check, that is the 100 iterations were done independently of the value of residuals. The achieved residual values were acceptable.

The simulation is stopped when f_c reaches the value of 0.95 everywhere in the ingot. This limit for the f_c is set in order to avoid simulation of eutectic reaction which the thermodynamic model is not capable of (see further explanations in Sections 3.3 and 5.2 as well as Fig. 5.10).

6.4.4 Simulation results

The results of the simulation are shown in Figs. 6.30 and 6.31 which show the distributions of the most important process quantities at times $t = 10$ s, $t = 100$ s, $t = 300$ s and $t = 615$ s. These quantities include: temperature T; columnar volume fraction f_c; velocity of the liquid phase $\vec{u}_l$; mass fractions of the alloying elements in the liquid phase c_l^{C} and c_l^{Cr}; mass fractions of the alloying elements in the columnar phase c_c^{C} and c_c^{Cr} and mixture mass fractions $c_{\mathrm{mix}}^{\mathrm{C}}$ and $c_{\mathrm{mix}}^{\mathrm{Cr}}$.

In the following a description of results at each of the times $t = 10$ s, $t = 100$ s, $t = 300$ s and $t = 615$ s is given. The descriptions are based on Figs. 6.30 and 6.31.

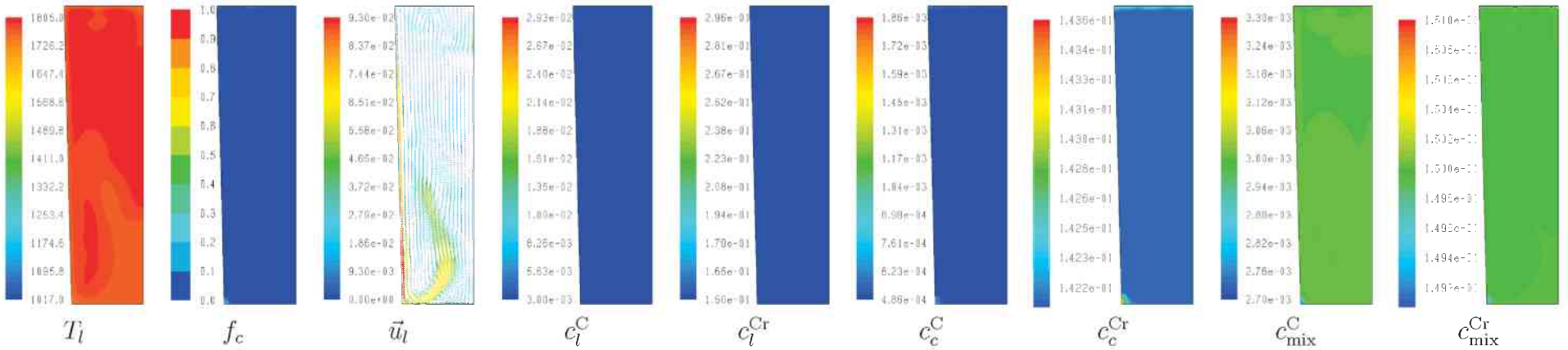

(a) $t = 10$ s

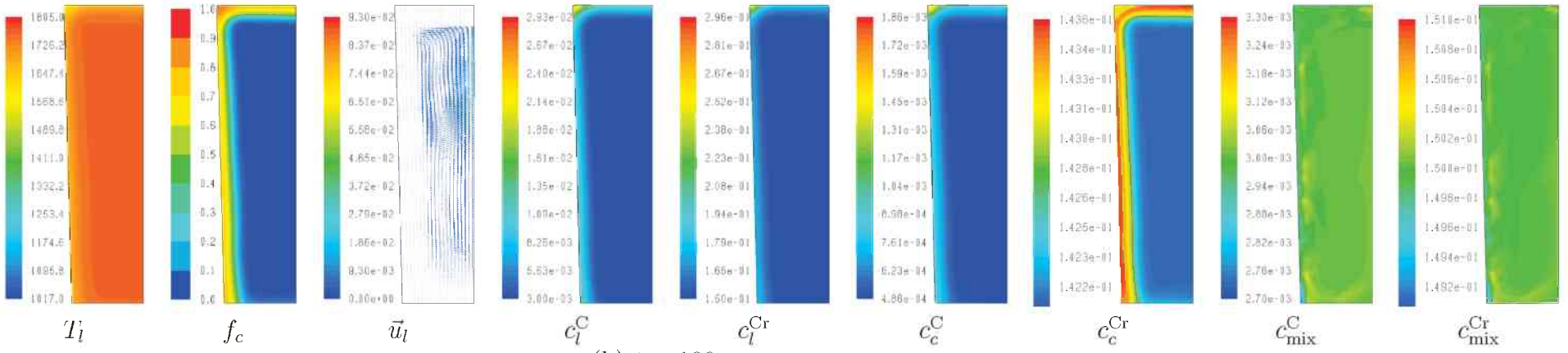

(b) $t = 100$ s

Figure 6.30: Changes in the distribution of different process quantities at (a) $t = 10$ s and (b) $t = 100$ s.

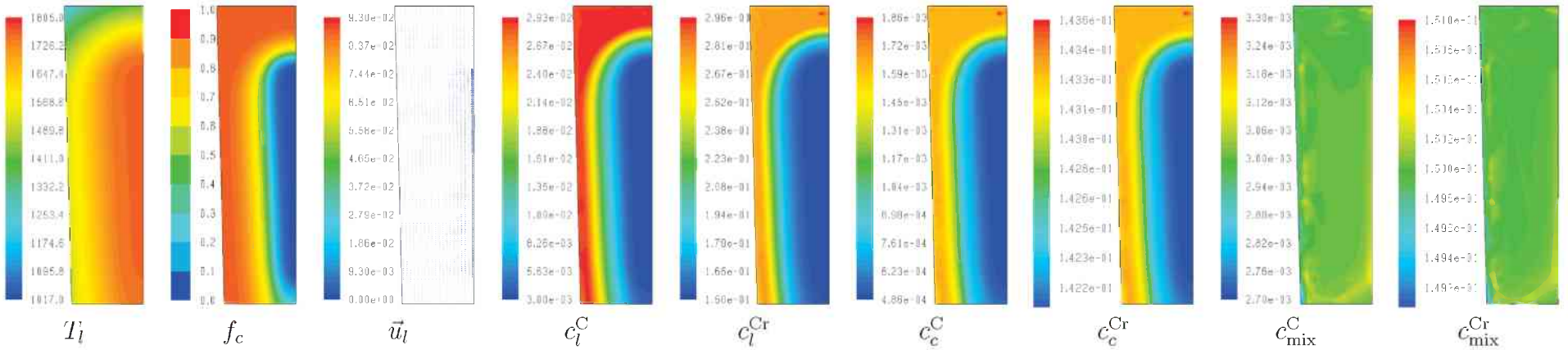

(a) $t = 300$ s

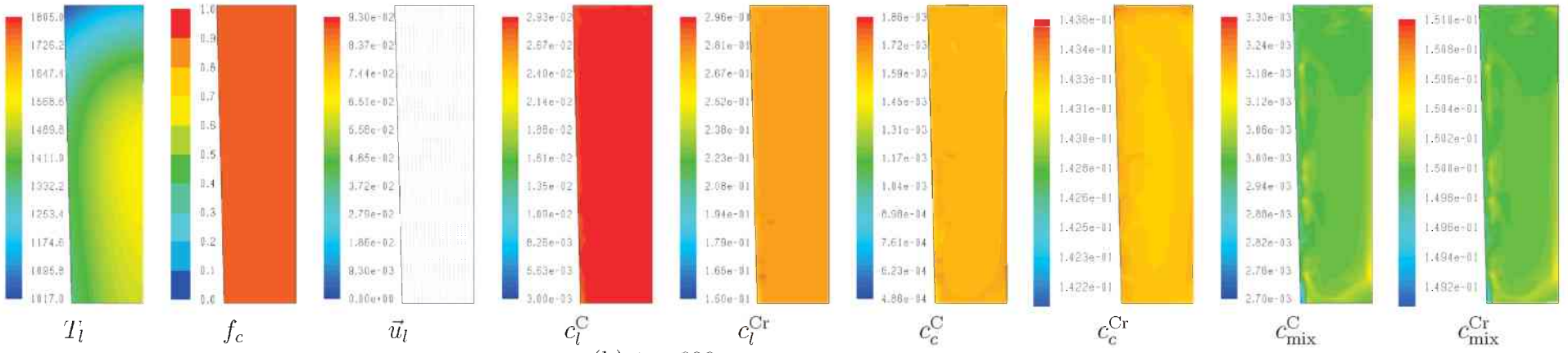

(b) $t = 600$ s

Figure 6.31: Changes in the distribution of different process quantities at (a) $t = 300$ s and (b) $t = 615$ s.

Simulation results at $t = 10$ s

At the early stage of the solidification at $t = 10$ s the temperature T distribution is somewhat uneven as it can be seen from Fig. 6.30a. This is caused by a relatively strong flow near the mould caused by the thermal convection, which is caused by strong cooling of the liquid near the wall.

The changes in mass fractions of the alloying elements in the liquid phase c_l^{C} and c_l^{Cr} can hardly can be seen at this stage. The mass fractions of these elements in the columnar phase c_c^{C} and c_c^{Cr} increase in the bottom corner of the ingot which can be seen only for the mass fraction of chromium c_c^{Cr}, since the change in c_c^{C} is still very small.

No significant change happened in the mixture mass fractions $c_{\mathrm{mix}}^{\mathrm{C}}$ and $c_{\mathrm{mix}}^{\mathrm{Cr}}$ of the alloying elements yet.

Simulation results at $t = 100$ s

After 100 s, the ingot continues to cool down, the temperature T distribution gets more uniform since the flow is not as strong as at $t = 10$ s as the distribution of liquid velocity vectors $\vec{u}_l$ reveals.

The mass fractions of the alloying elements in both liquid and columnar phases c_l^{C}, c_l^{Cr}, c_c^{C} and c_c^{Cr} increase near the top and the wall of the ingot.

The small changes in the mixture mass fractions $c_{\mathrm{mix}}^{\mathrm{C}}$ and $c_{\mathrm{mix}}^{\mathrm{Cr}}$appear: closer to the wall the macrosegregation is negative, then right after that there comes a slightly positively segregated layer. Further to the middle the mixture mass fractions remain equal to the initial liquid mass fractions.

Simulation results at $t = 300$ s

After 300 s, the temperature T continues to decrease. It decreases faster near the top and the wall of the ingot.

The columnar solidification front proceeds further to the centre of the ingot, thus increasing the solidified volume of the ingot and decreasing the volume where liquid is still left, where $f_c \approx 0$.

The flow velocity $\vec{u}_l$ gets smaller in the liquid volume, and zero in the solid volume with $f_c > 0.7$.

The volume with increased mass fractions of carbon and chromium in the liquid and solid phases c_l^{C}, c_l^{Cr}, c_c^{C} and c_c^{Cr} grow, their fronts coincide with the columnar volume fraction f_c front.

The distributions of mixture mass fractions $c_{\mathrm{mix}}^{\mathrm{C}}$ and $c_{\mathrm{mix}}^{\mathrm{Cr}}$ do not change significantly in comparison with $t = 100$ s.

Simulation results at $t = 615$ s

The temperature T is now even more decreased. The columnar volume fraction is uniform everywhere in the ingot and reached its final value of 0.95. The velocity in the liquid phase $\vec{u}_l$ is everywhere equals to zero. The distributions of mass fractions of alloying elements in both liquid and columnar phases c_l^{C}, c_l^{Cr}, c_c^{C} and c_c^{Cr} are more or less uniform, with only minor exceptions: the mass fractions of carbon and chromium in the liquid phase are slightly smaller near the wall and their mass fractions in the columnar phase are slightly higher near the wall and the lower central part of the ingot.

Curves $c_l^{\mathrm{C,Cr}} - f_c$ for different points of the ingot

Also the temporal evolution of the following quantities in three points of the ingot (Fig. 6.29 shows their locations) was recorded: mass fractions of the alloying elements c_l^{C} and c_l^{Cr} as well as the columnar volume fraction f_c. From these data it was possible to plot $c_l^{\mathrm{C}} - f_c$ and $c_l^{\mathrm{Cr}} - f_c$ which are shown in Figs. 6.32 (point 'low centre'), 6.33 (point 'top corner') and 6.34 (point 'bottom corner').

Low centre

The $c_l^{\mathrm{C}} - f_c$ and $c_l^{\mathrm{Cr}} - f_c$ curves for this point lie above the corresponding curve obtained using the Thermo-Calc–Scheil module.

Top corner

In this point the behaviour of the curves $c_l^{\mathrm{C}} - f_c$ and $c_l^{\mathrm{Cr}} - f_c$ is similar to those in the previous point, although in the region of high columnar mass fraction values f_c these two curves practically coincide.

Bottom corner

The curves $c_l^{\mathrm{C}} - f_c$ and $c_l^{\mathrm{Cr}} - f_c$ in this point lie slightly below the corresponding Thermo-Calc–Scheil curves. The absolute distance between curves for this point is higher than for other two points.

6.4.5 Comparison with the experiment

In order to validate the model summarised in Section 3.2, an experimental casting was performed. The experimental procedure is described in |Tanzer08| and in Appendix 8.3.

The composition of the casted steel was $c_0^{\mathrm{C}} = 3 \cdot 10^{-3}$ and $c_0^{\mathrm{Cr}} = 0.1482$. The accuracy of the determination of mass fraction of carbon and chromium were 10^{-4} (3.3% of c_0^{C}) and $5 \cdot 10^{-4}$ (0.34% of c_0^{Cr}) |Tanzer08|. The resulting distribution of alloying elements mass fractions are shown in Figs. 6.35a and 6.36a respectively. Because of the small size of the ingot, in its upper part forms a significant shrinkage cavity. The experimental mass fractions obtained from the cavity region are not reliable and have to be discarded from the analysis |Tanzer08|. The discarded points are marked with crosses in Figs. 6.35a and 6.36a.

6.5 Three-phase solidification simulation of a 2 ton ingot of Fe-0.38wt.%C-16wt.%Cr alloy

6.5.1 Geometry, mesh, initial and boundary conditions

The ingot for the casting of the 2 ton X38Cr16 ingot had the following geometry, shown in the Fig. 6.37.

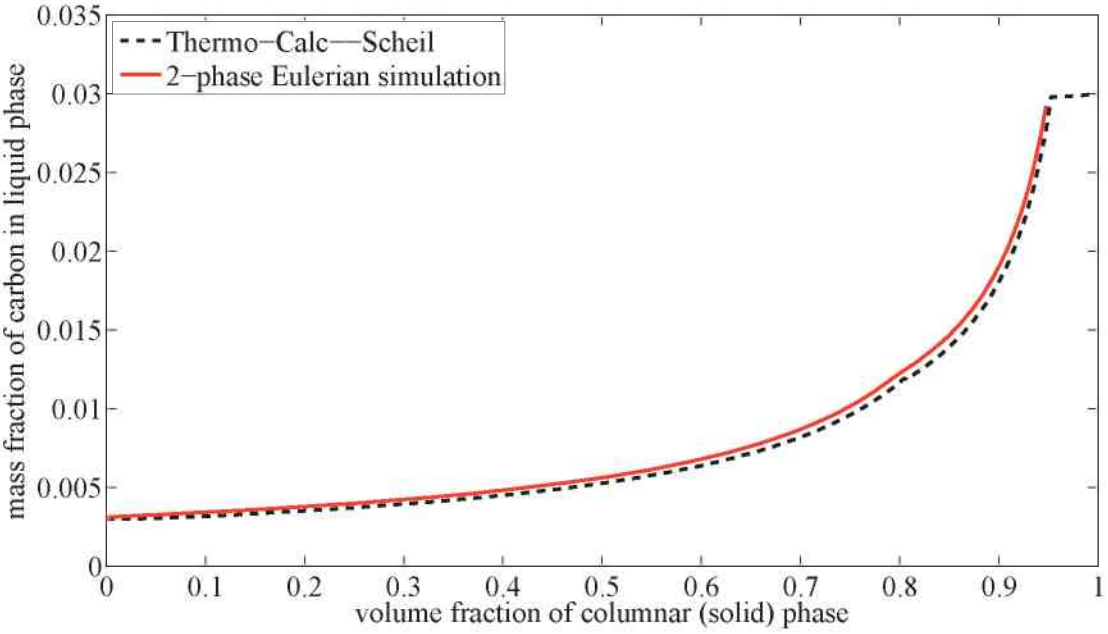

a

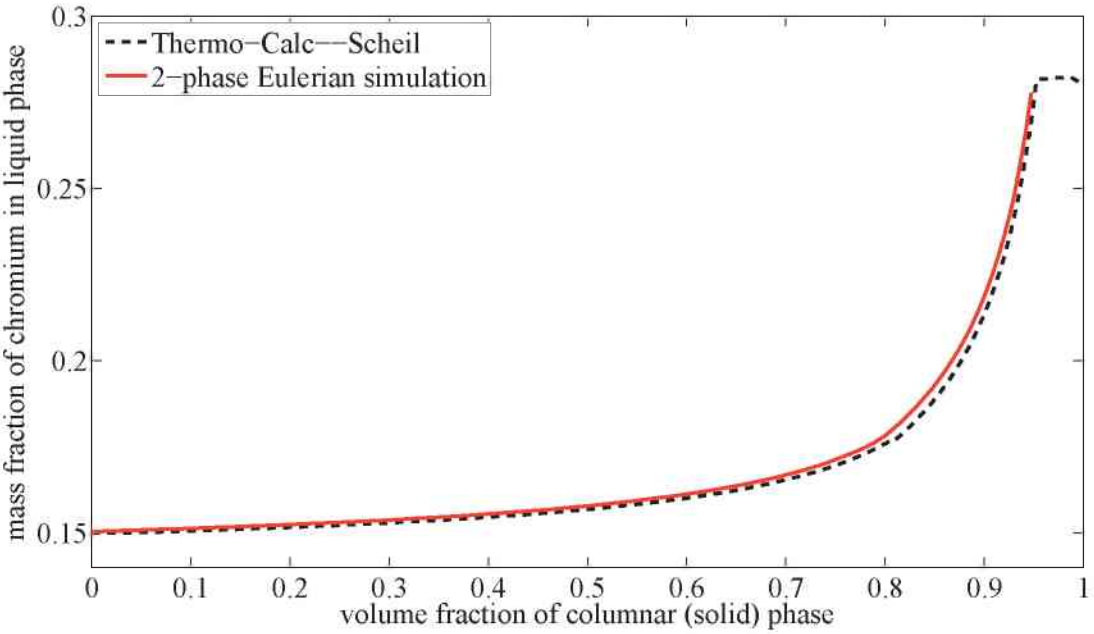

b

Figure 6.32: Curves $c_l^{\mathrm{C}} - f_c$ (a) and $c_l^{\mathrm{Cr}} - f_c$ (b) for the point 'low centre' shown in Fig. 6.29. The red lines represent the curves obtained from the simulation and the black dashed lines represent the corresponding curves obtained using Thermo-Calc–Scheil module.

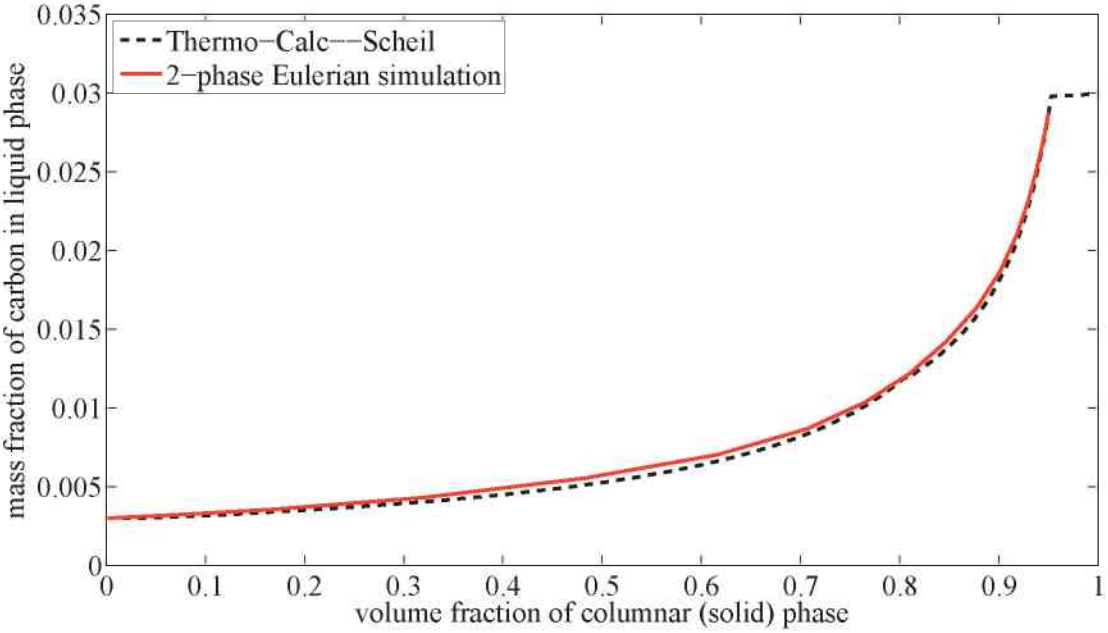

a

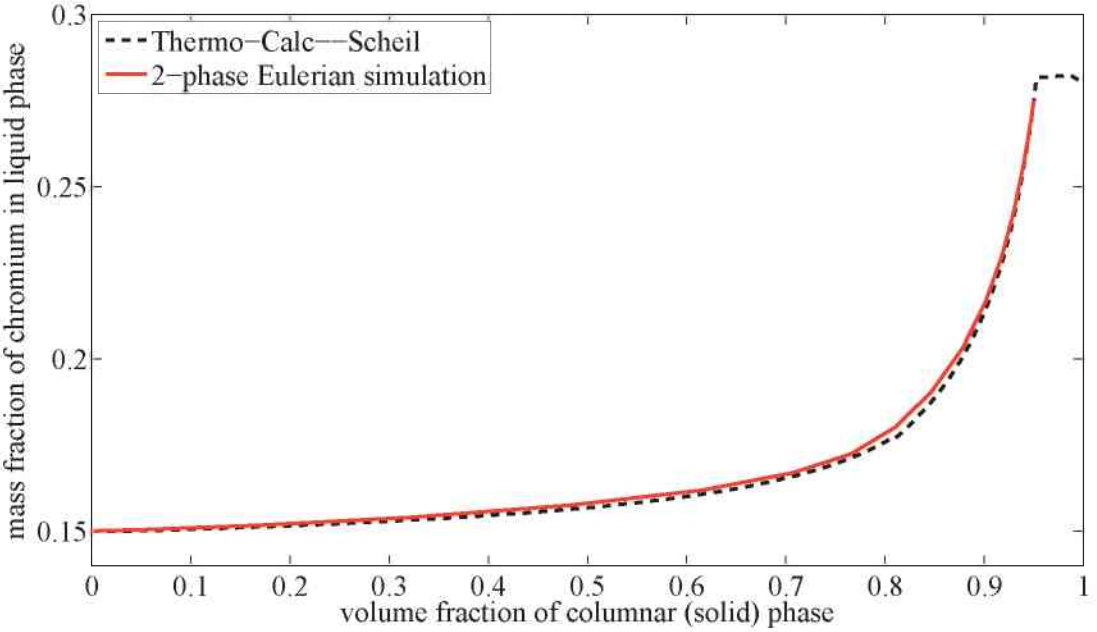

b

Figure 6.33: Curves $c_l^{\mathrm{C}} - f_l$ (a) and $c_l^{\mathrm{Cr}} - f_c$ (b) for the point 'top corner' shown in Fig. 6.29. The red lines represent the curves obtained from the simulation and the black dashed lines represent the corresponding curves obtained using Thermo-Calc–Scheil module.

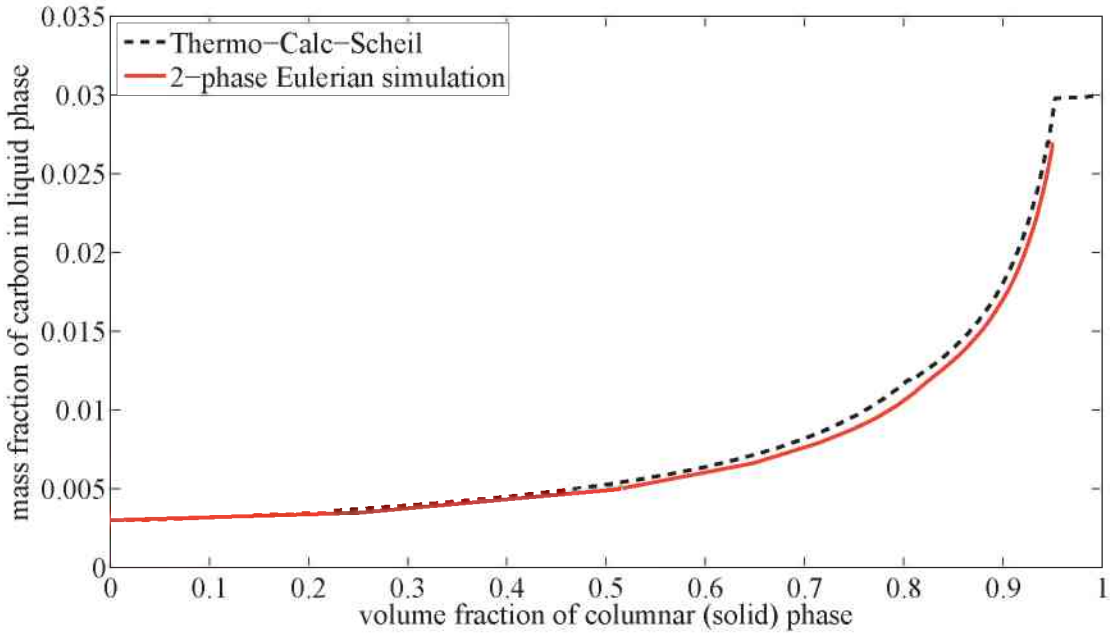

a

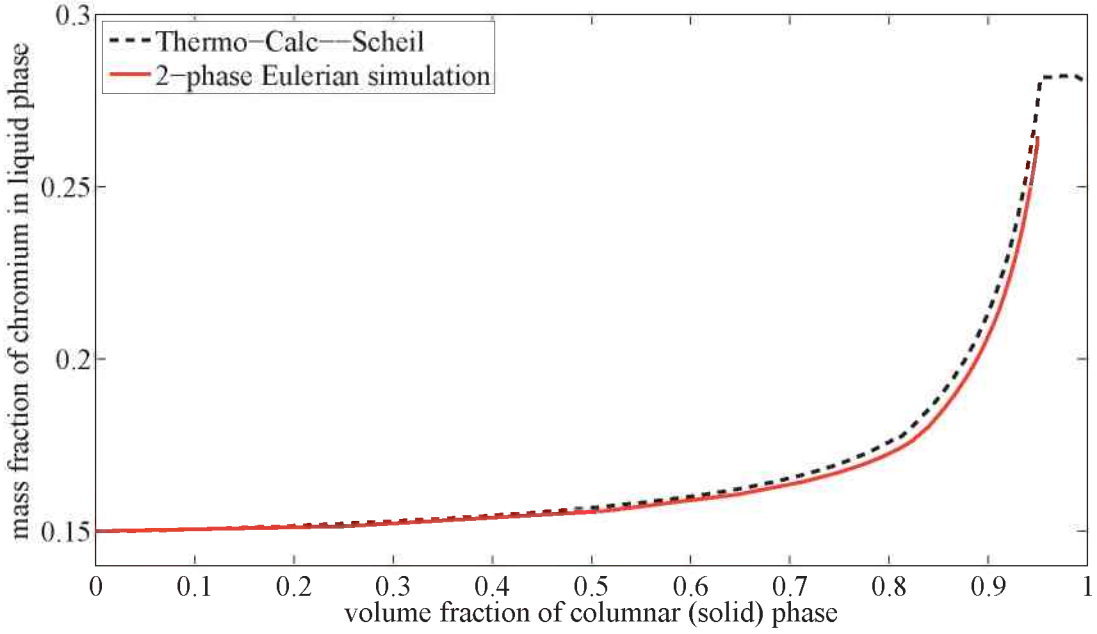

b

Figure 6.34: Curves $c_l^{\mathrm{C}} - f_c$ (a) and $c_l^{\mathrm{Cr}} - f_c$ (b) for the point 'bottom corner' shown in Fig. 6.29. The red lines represent the curves obtained from the simulation and the black dashed lines represent the corresponding curves obtained using Thermo-Calc–Scheil module.

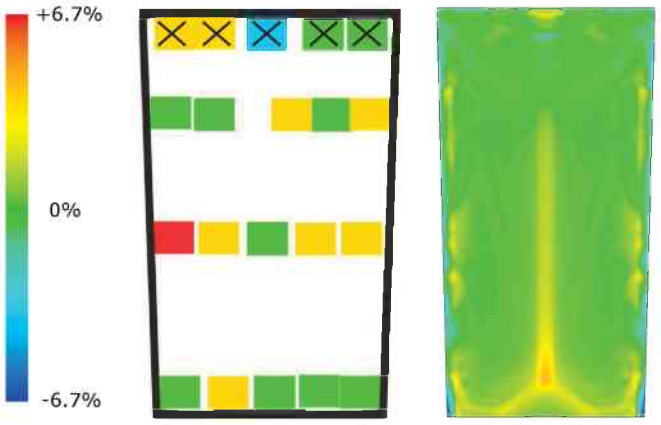

Figure 6.35: Comparison between the mass fraction of carbon in the experiment (a) and the simulation (b). The discarded experimental points are marked with crosses.

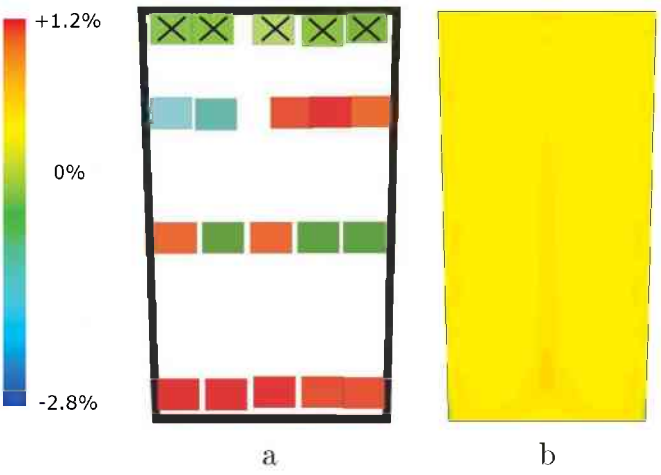

Figure 6.36: Comparison between the mass fraction of chromium in the experiment (a) and the simulation (b). The discarded experimental points are marked with crosses.

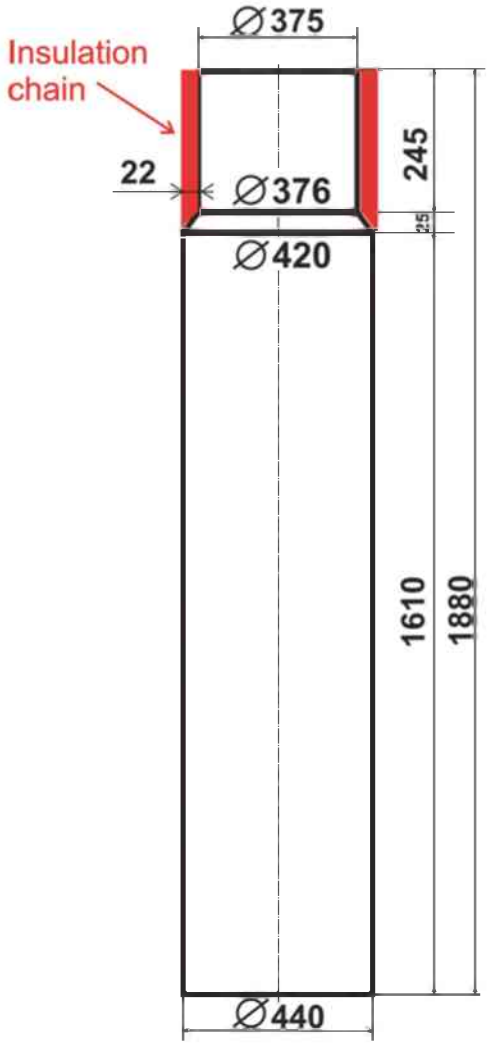

Figure 6.37: The sketch of the mould with an insulation chain

In order to perform CFD computations in FLUENT, a two-dimensional finite volume grid with 4040 cells was created using the GAMBIT preprocessor. Such a small number of cells is taken because the computational effort of numerical solution of the partial differential equation system describing two-dimensional three-phase flow taking into account species transport for three species. The computational grid is shown in the Fig. 6.38. Simulation is stopped when $f_s = f_c + f_e$ reaches the value of 0.95 everywhere in the ingot. This limit for the f_s is set in order to avoid simulation of eutectic reaction which the thermodynamic model is not capable of (see further explanations in Sections 3.3 and 5.2 as well

as Fig. 5.10).

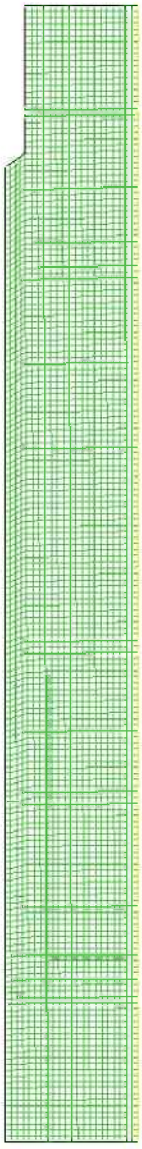

Figure 6.38: Mesh for the 2 t ingot for the X38Cr16 steel solidification simulation.

In the following simulations three phases were considered: liquid, denoted by lower index l, columnar, denoted by the lower index c and equiaxed, denoted by the lower index e.

Initial conditions for the summarised in Section 3.2 differential equations de-

scribing Eulerian three-phase ternary solidification model were:

- initial volume fraction of columnar was $f_c = f_e = 10^{-5}$,
- Initial temperatures of the all three phases was $T_{l,0} = T_{c,0} = T_{e,0} = 1804$ K (as it was estimated in the MAGMASOFT filling simulation, see Section 6.2),
- Initial velocities were $\vec{u}_{l,0} = \vec{u}_{e,0} = 0 \text{ m} \cdot \text{s}^{-1}$ everywhere,
- initial mass fractions of of the alloying components in the liquid phase were $c_{l,0}^{\text{C}} = 3.8 \cdot 10^{-3}$ and $c_{l,0}^{\text{Cr}} = 0.16$, and in both columnar and equiaxed phases $c_{c,0}^{\text{C}} = c_{e,0}^{\text{C}} = 4.86 \cdot 10^{-4}$ and $c_{c,0}^{\text{Cr}} = c_{e,0}^{\text{Cr}} = 0.147$.

The boundary conditions for the equation system consisting of equations summarised in Section 3.2 were set as follows (see also Fig. 6.38 with mesh and boundary names).

Conditions for the boundary *"wall 1"* and *"bottom"*

- velocity of both liquid and equiaxed phases was set to zero ("no-slip" condition): $\vec{u}_l = \vec{u}_e = 0 \text{ m} \cdot \text{s}^{-1}$.
- for temperature the convective heat transfer boundary condition was used, so that the heat flux to the wall is computed as $q = h_{\text{ext}}(T_{\text{ext}} - T_{\text{f}})$. The external transfer coefficient was based on the temperature-dependent heat transfer coefficient $H(T)$ obtained from experimental data and MAGMASOFT filling simulations (see Eq. (6.2) in Section 6.2). In order to take into account the heat transfer through the mould wall it was calculated according to the formula:

$$h_{\text{ext}}(T) = \left(\frac{1}{H(T)} + \frac{l}{k} + \frac{1}{h_{\text{outer}}} \right)^{-1}, \tag{6.4}$$

where $l = 117$ mm is the thickness of the mould wall, $k = 55 \text{ W} \cdot \text{m}^{-1} \cdot \text{K}^{-1}$ its heat conductivity (mean value of the heat conductivity of the GJL-350 mould material is taken according to Fig. 6.7) , and $h_{\text{outer}} = 200 \text{ W} \cdot \text{m}^{-2} \cdot \text{K}^{-1}$ is the heat exchange coefficient between the mould wall and the surrounding

air. The external temperature was set to T_{ext} =300 K. This is a simplified description of the heat transfer through the mould wall as it does not take into account the heat capacity of the mould.

- zero diffusive flux through the boundary was assumed for species in liquid, columnar and equiaxed phases: $\partial c_{l,c,e}^{\text{C,Cr}}/\partial \vec{n} = 0$, where $\vec{n}$ is the normal to the boundary.

Conditions for the boundary *"wall 2"*

- velocity of both phases which are able to move was set to zero ("no-slip" condition): $\vec{u}_l = \vec{u}_e = 0 \text{ m} \cdot \text{s}^{-1}$.

- for temperature the convective heat transfer boundary condition was used, so that the heat flux to the wall is computed as $q = h_{\text{ext}}(T_{\text{ext}} - T_{\text{f}})$. Similarly with the case of the "wall 1" boundary, the following formula was used to calculate the h_{ext}

$$h_{\text{ext}}(T) = \left(\frac{1}{H(T)} + \frac{l}{k} + \frac{l_{\text{insul}}}{k_{\text{insul}}} + \frac{1}{h_{\text{outer}}} \right)^{-1}, \tag{6.5}$$

  where $H(T)$ is the temperature-dependent heat transfer coefficient between the mould and the ingot estimated by means of MAGMASOFT filling simulations in Section 6.2 given by the formula (6.2); l = 117 mm is the thickness of the mould wall, $k = 55 \text{ W} \cdot \text{m}^{-1} \cdot \text{K}^{-1}$ is the heat conductivity of the mould wall, l_{insul} = 22 mm is the thickness of the insulation, $k_{\text{insul}} = 0.11 \text{ W} \cdot \text{m}^{-1} \cdot \text{K}^{-1}$ is the heat conductivity of the insulation, and finally $h_{\text{outer}} = 200 \text{ W} \cdot \text{m}^{-2} \cdot \text{K}^{-1}$ was the heat transfer coefficient between the mould wall and surrounding air. The external temperature was set to T_{ext} =300 K.

- zero diffusive flux through the boundary was assumed for species in liquid, columnar and equiaxed phases: $\partial c_{l,c,e}^{\text{C,Cr}}/\partial \vec{n} = 0$, where $\vec{n}$ is the normal to the boundary.

Conditions for the boundary *"top"*

- velocity of both phases which are able to move was set to zero ("no-slip" condition): $\vec{u}_l = 0 \text{ m} \cdot \text{s}^{-1}$ and $\vec{u}_e = 0 \text{ m} \cdot \text{s}^{-1}$. The choice of the no-slip condition is justified, because the solidified steel at the top of the mould acts as a lid.

- for temperature the convective heat transfer boundary condition was used, so that the heat flux to the wall is computed as $q = h_{\text{ext}}(T_{\text{ext}} - T_{\text{f}})$, where the external transfer coefficient was set to h_{ext}= 100 $\text{W} \cdot \text{m}^{-1} \cdot \text{K}^{-1}$ and the external temperature was set to T_{ext} =300 K, as the parameters were estimated from experimental data in |Tanzer08| for this geometry and conditions.

- zero diffusive flux through the boundary was assumed for species in liquid, columnar and equiaxed phases: $\partial c_{l,c,e}^{\text{C,Cr}}/\partial \vec{n} = 0$, where $\vec{n}$ is the normal to the boundary.

Conditions for the boundary *"bottom"*

- velocity of both liquid and equiaxed phases was set to zero ("no-slip" condition): $\vec{u}_l = \vec{u}_e = 0 \text{ m} \cdot \text{s}^{-1}$.

- for temperature the convective heat transfer boundary condition was used, so that the heat flux to the wall is computed as $q = h_{\text{ext}}(T_{\text{ext}} - T_{\text{f}})$. For this boundary h_{ext} was taken as 100 $\text{W} \cdot \text{m}^{-2} \cdot \text{K}^{-1}$ as it was estimated in |Tanzer08| for similar conditions. The external temperature was set to T_{ext} =300 K.

- zero diffusive flux through the boundary was assumed for species in liquid, columnar and equiaxed phases: $\partial c_{l,c,e}^{\text{C,Cr}}/\partial \vec{n} = 0$, where $\vec{n}$ is the normal to the boundary.

Conditions for the boundary *"axis"* Axis boundary condition is set on this boundary.

6.5.2 Material data

The materials description necessary for the three-phase Eulerian ternary solidification simulation were the same as in the case of 32 kg ingot (see Section 6.3.1),

Property name	Value
Density ρ_e	$7001\ \mathrm{kg \cdot m^{-3}}$
Heat capacity $c_{p,e}$	$804\ \mathrm{J \cdot kg^{-1} \cdot K^{-1}}$
Thermal conductivity k_e	$29\ \mathrm{W \cdot m^{-1} \cdot K^{-1}}$
Viscosity μ_e	defined by Eq. (2.10)

Table 6.8: Material parameters of the equiaxed phase

Property name	Value
mean of the nucleation law ΔT_N	2 K
standard deviation of the nucleation law ΔT_N	5 K
maximum equiaxed grain density $n_{\max}$	$5 \cdot 10^9$

Table 6.9: Nucleation parameters

plus additional data for the equiaxed phase, which is given in Table 6.8.

6.5.3 Simulation parameters

Nucleation parameters

Nucleation parameters enter the equiaxed grain density transport equation (2.21). They are given in Table 6.9. Note that these parameters are not known exactly and has to be determined by means of experiment and parameter study.

Thermosolutal convection parameters

The following additional parameters were used: the thermal expansion coefficient was taken as $\beta_T = 2{\cdot}10^{-4}\ \mathrm{K^{-1}}$ and the solutal expansion coefficients were $\beta_{\mathrm{C}} = 1.1$ for carbon, and $\beta_{\mathrm{Cr}} = 0$ for chromium (same as Case E "thermal and solutal convection", described in Table 6.7). The choice of these parameters is explained above in Section 6.3.3.

Thermodynamics representation

Here the piecewise-linear interpolation for the X30Cr15 alloy was used, as described in Section 3.5.1 and with parameters estimated in Section 4.3.1 which are listed in Table 4.1.

Time step, iterations, and computation time

The simulation was performed with the following settings. The time step was $\Delta t = 10^{-1}$ s, there were 40000 time steps carried out with 100 iterations per time step, without convergence check, that is, the 100 iterations were carried out.

6.5.4 Simulation results

The following figures show change of distributions of different quantities: temperature T , volume fractions of the liquid f_l, columnar f_c , and equiaxed f_e phases; velocity of the liquid $\vec{u}_l$ and equiaxed $\vec{u}_e$ phases; mass fractions of carbon and chromium in the liquid phase c_l^{C} and c_l^{Cr}; mass fractions of carbon and chromium in the columnar phase c_c^{C} and c_c^{Cr}; mass fractions of carbon and chromium in the equiaxed phase c_e^{C} and c_e^{Cr} and finally mixture mass fraction of carbon $c_{\mathrm{mix}}^{\mathrm{C}}$ and chromium $c_{\mathrm{mix}}^{\mathrm{Cr}}$.

Distributions of the quantities listed above are shown in Figs. 6.39–6.44 for $t = 10$ s, $t = 100$ s, $t = 200$ s, $t = 1000$ s, $t = 2000$ s and $t = 3925$ s respectively. The time of 3925 s is considered to be the end solidification, since the majority of the ingot has solidified. The description of the solidification of the upper part is not precise due to the fact that in reality a shrinkage cavity forms. This cannot be described by the model, so the top part of the ingot is excluded from the analysis at the end of solidification.

In the following we describe the results shown in Figs. 6.39–6.44.

Simulation results at $t = 10$ s

At this point in time the temperature T is still uniform almost everywhere, apart from the small region near the bottom, where a strong flow takes place, as can be seen from the distribution of the liquid phase velocity $\vec{u}_l$. The solidification has just started, which can be seen from the distribution of the liquid volume fraction f_l, which is lower in a small area adjacent to the bottom of the ingot. The distribution of the equiaxed phase velocity $\vec{u}_e$ is the same as that of $\vec{u}_l$, since the liquid is dragged by sinking equiaxed crystals. A change in the liquid mass fraction of carbon and chromium (c_l^{C} and c_l^{Cr}) cannot yet be seen. The mass fractions of carbon and chromium in the columnar phase (c_c^{C} and c_c^{Cr}) start to increase in the area adjacent to the bottom of the ingot. The change in the mass

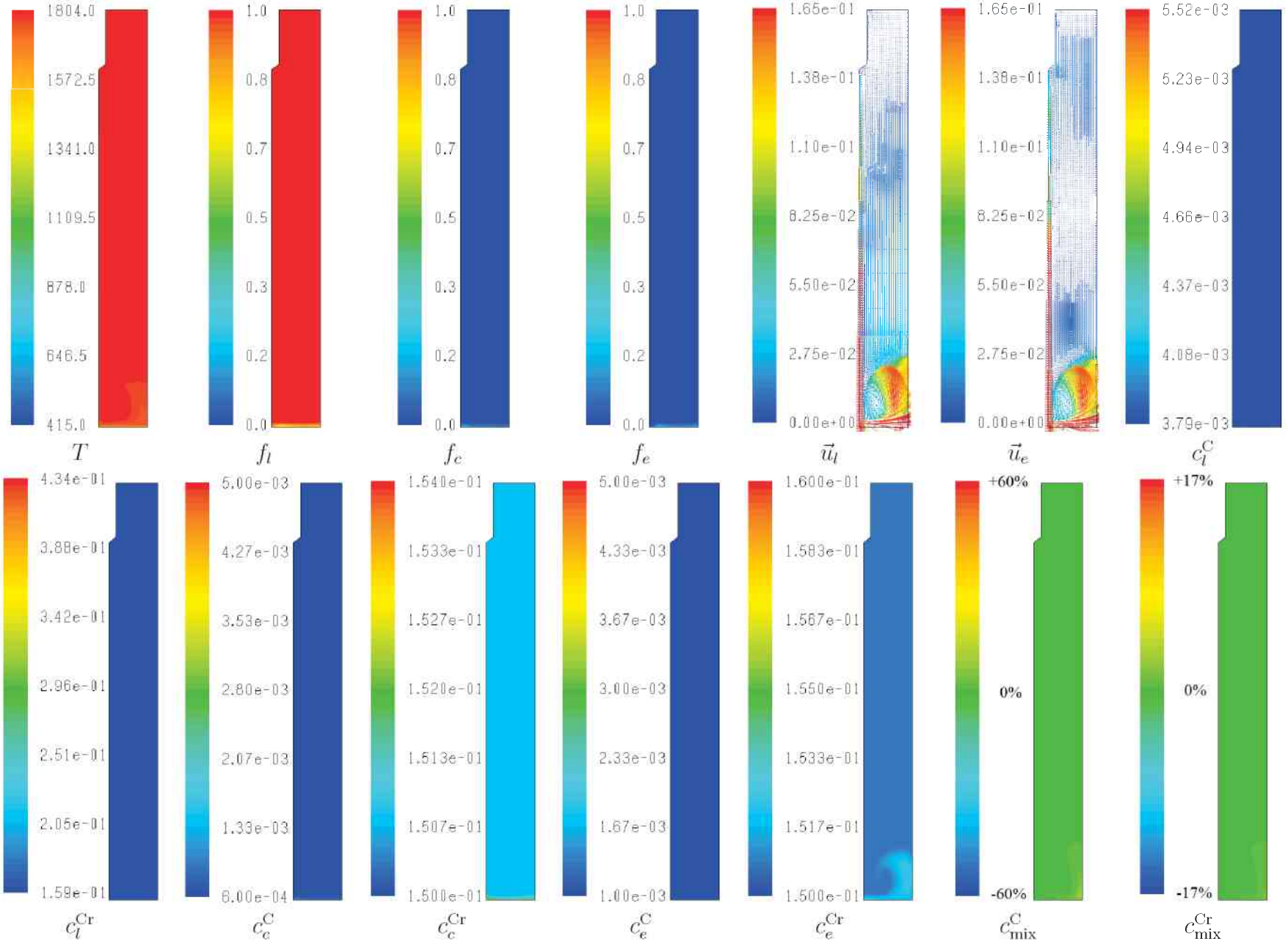

Figure 6.39: Distribution of process quantities at $t = 10$ s

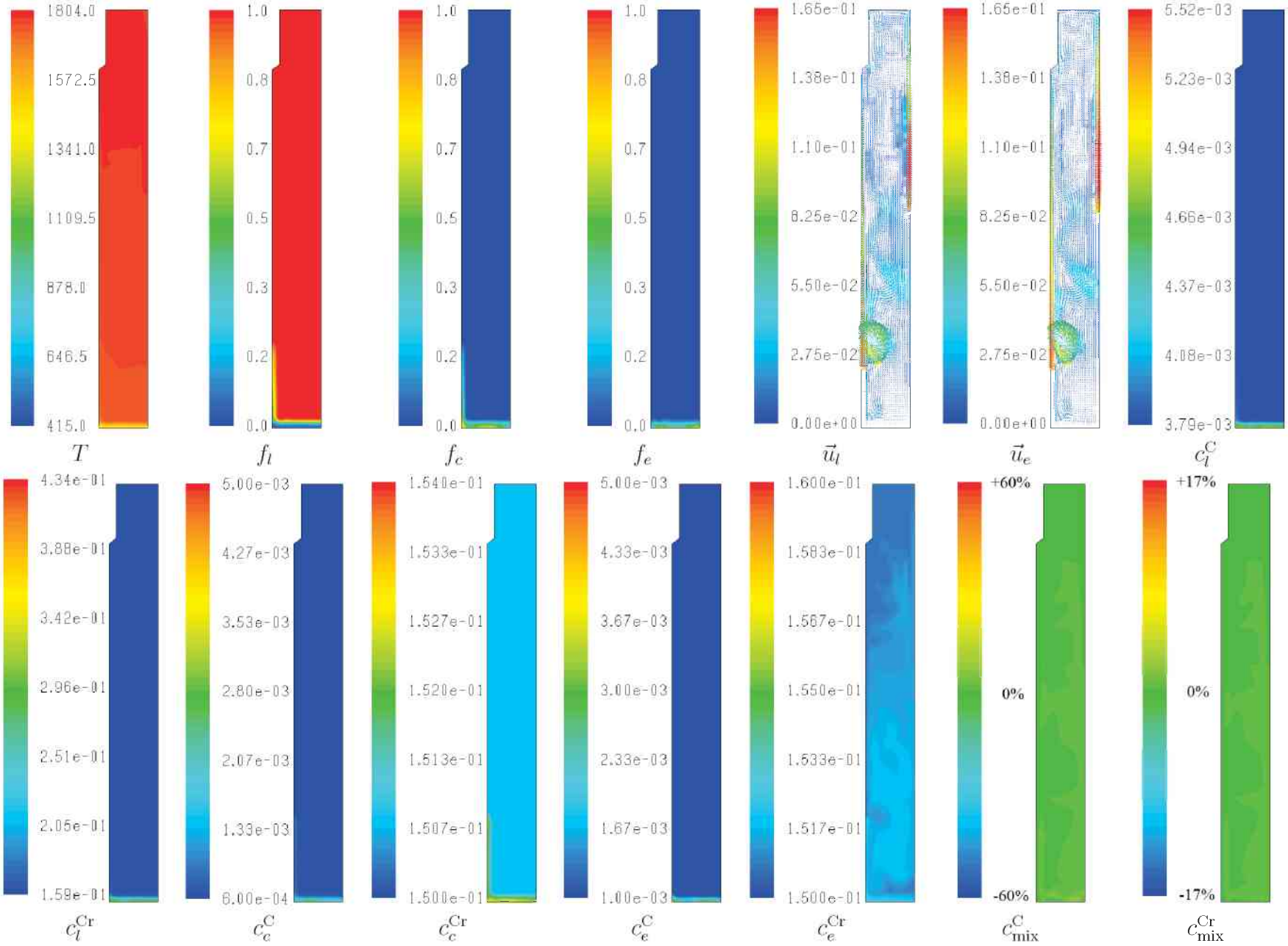

Figure 6.40: Distribution of process quantities at $t = 100$ s

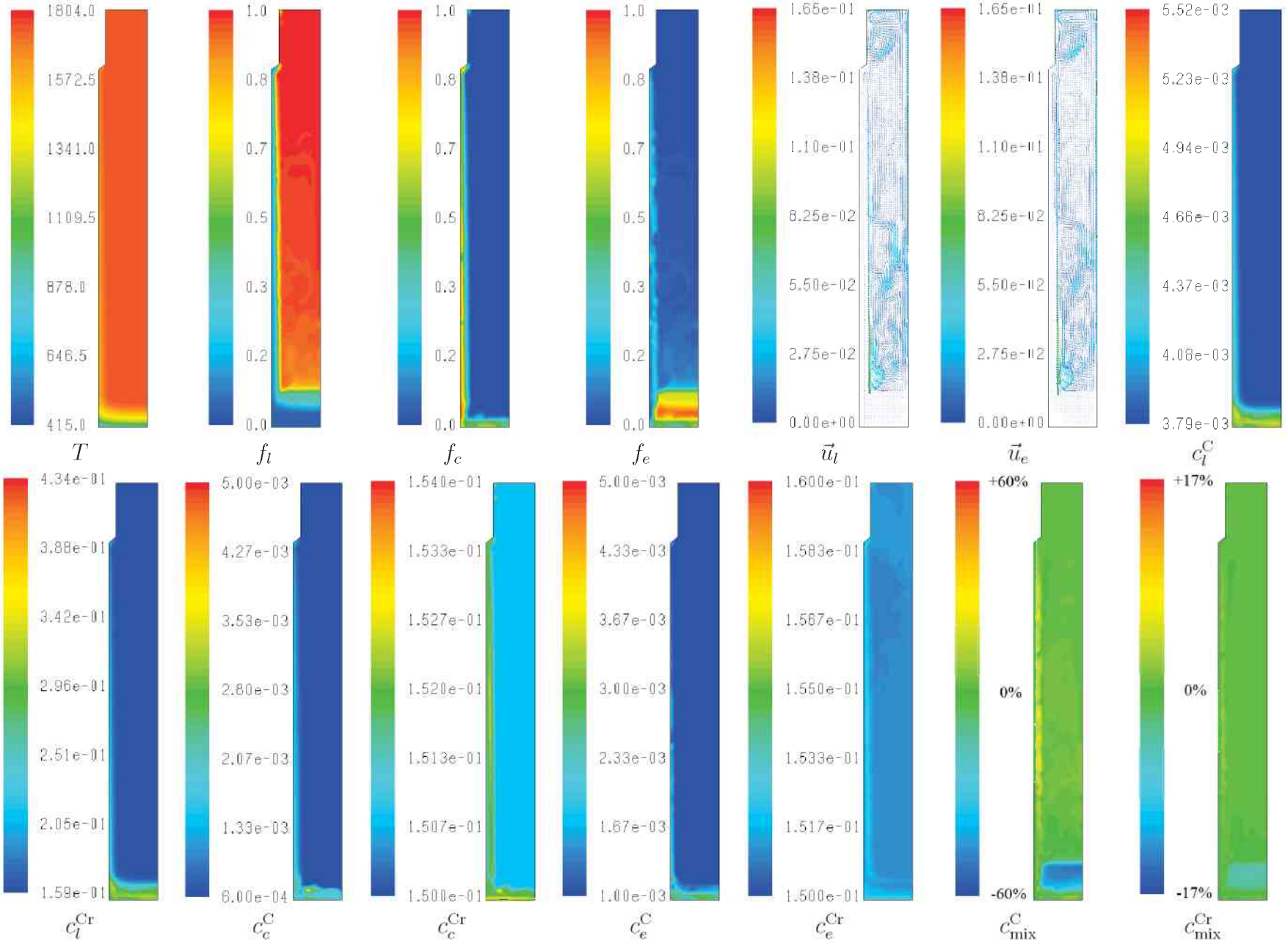

Figure 6.41: Distribution of process quantities at $t = 500$ s

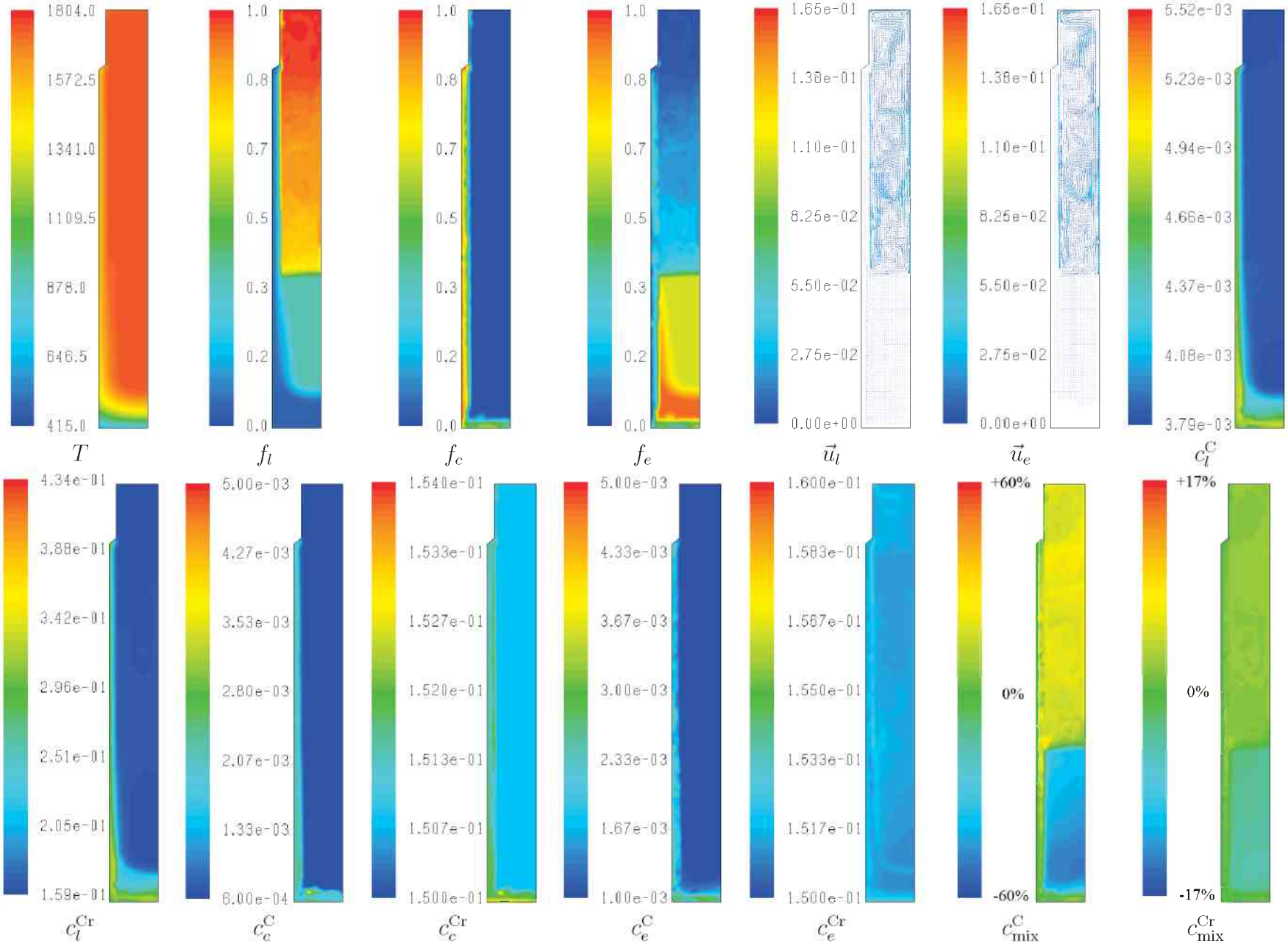

Figure 6.42: Distribution of process quantities at $t = 1000$ s

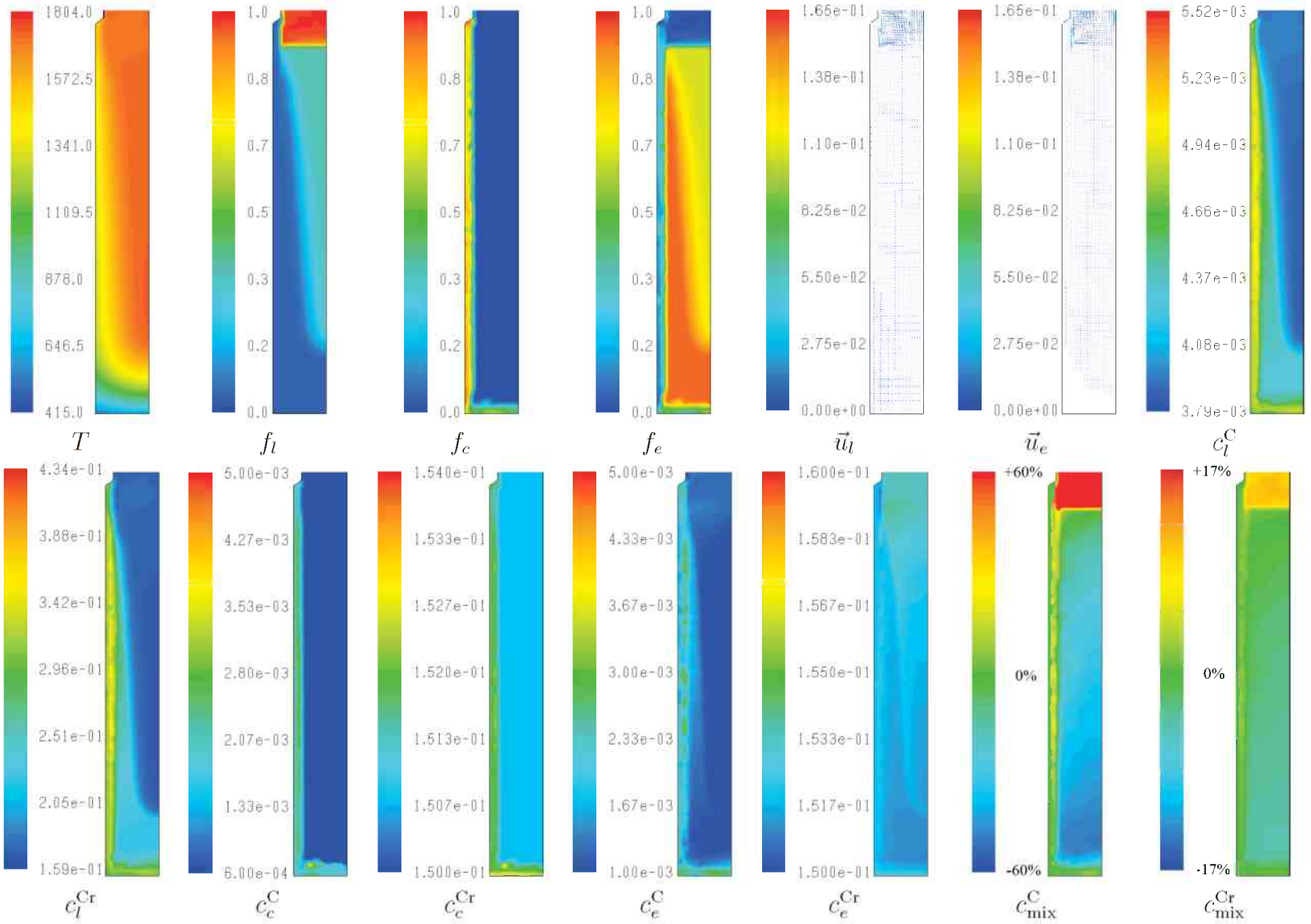

Figure 6.43: Distribution of process quantities at $t = 2000$ s

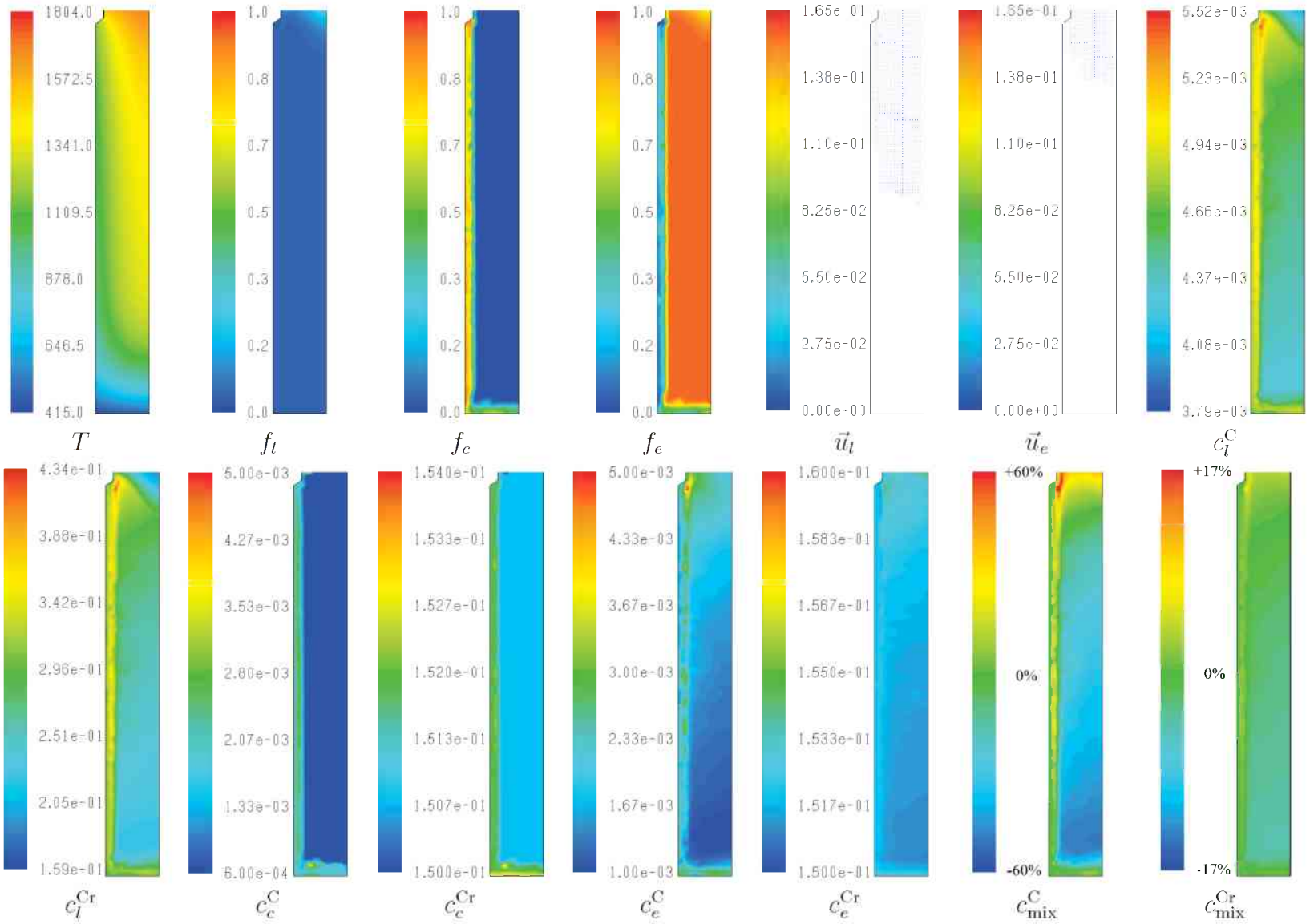

Figure 6.44: Distribution of process quantities at $t = 3925$ s

fraction of chromium in the equiaxed phase c_e^{C} cannot yet be seen, whereas the mass fraction of chromium in the equiaxed phase is increased near the bottom of the ingot and it is possible to see how it is transported by the strong flow. There are almost no changes in the mixture mass fractions of alloying elements $c_{\mathrm{mix}}^{\mathrm{C}}$ and $c_{\mathrm{mix}}^{\mathrm{Cr}}$ yet.

Simulation results at $t = 100$ s

The temperature T decreases in the bottom part of the ingot, and remains relatively high in the middle and the upper part. The reason for this is the formation of a gap between the mould and solidified melt, which is modelled by means of the temperature-dependent heat coefficient given by Eq. (6.2). At the same time more columnar and equiaxed phase is formed in this part of the ingot, and the columnar f_c and equiaxed f_e mass fractions are increased there, whereas the amount of the liquid mass fraction f_l is decreased. The flow becomes weaker overall, especially near the bottom of the ingot, where solidification is occurring. There is still downward movement of the melt along the wall of the ingot caused by the thermal convection (the cold melt sinks). A thin layer of the columnar phase f_c forms at the wall near the bottom, which acts as a step for the downward stream and causes the change in the flow direction and causes the mass transport towards the upper part of the ingot. The height of the ingot is significantly bigger than its width, which prohibits the formation of a stable thermal convection roll. The roll breaks up into a complex system of smaller recirculation zones. This interplay between the complicated liquid and equiaxed phase movements as well as mass conservation cause a downward movement in the centre of the ingot. The distribution of the liquid phase velocity $\vec{u}_l$ and of the equiaxed phase velocity $\vec{u}_e$ are practically the same. Now the increase in the liquid mass fractions c_l^{C} and c_l^{Cr} can be seen near the bottom of the ingot. Mass fractions of alloying elements in columnar phase c_c^{C} and c_c^{Cr} also continue to increase there. The mass fraction of carbon in the equiaxed phase c_e^{C} increases next to the bottom of the ingot and the mass fraction of chromium in the equiaxed phase c_e^{C} increases there and in the lower half of the ingot. The mixture mass fractions $c_{\mathrm{mix}}^{\mathrm{C}}$ and $c_{\mathrm{mix}}^{\mathrm{Cr}}$ increase very slightly in the middle part of the ingot and near the outer ingot wall in its lower part.

Simulation results at $t = 200$ s

The equiaxed phase continues to sediment, and near the bottom, where the temperature is low enough, it starts to grow. The details of this process are given below in Section 7.4. The velocities $\vec{u}_l$ and $\vec{u}_e$ retain the same pattern, although their magnitudes decrease. The liquid mass fractions of the alloying elements c_l^{C} and c_l^{Cr}increase near the bottom, because there the equiaxed phase grows. The mixture mass fractions of the alloying elements $c_{\mathrm{mix}}^{\mathrm{C}}$ and $c_{\mathrm{mix}}^{\mathrm{Cr}}$ are increased near the bottom of the ingot because of the sedimented equiaxed grains.

Simulation results at $t = 1000$ s

The temperature T continues to fall, especially near the bottom and the wall. The equiaxed phase f_e continues to form, filling almost half of the ingot. The columnar phase f_c has grown near the wall and the bottom of the ingot and apparently does not grow further. The liquid and equiaxed velocities $\vec{u}_l$ and $\vec{u}_e$ are almost zero in the solidified part of the ingot (lower half with low f_c values), and in the other part of the ingot they are quite low. The mass fractions of the alloying elements in the liquid phase c_l^{C} and c_l^{Cr} continue to increase and their fronts of increased mass fractions coincide with those of the columnar volume fraction f_e. The mass fractions in the columnar phase, c_c^{C} and c_c^{Cr} are increased only in the area that is adjacent to the bottom and the wall of the ingot, which coincides with the area that has increased columnar mass fraction f_c. The same is true for the distribution of the mass fraction of carbon in the equiaxed phase c_e^{C}. For the mass fraction of chromium in the equiaxed phase c_e^{Cr} it is also true, and additionally it is increased in the middle of the ingot. The mixture mass fractions $c_{\mathrm{mix}}^{\mathrm{C}}$ and $c_{\mathrm{mix}}^{\mathrm{Cr}}$ are higher in the upper, liquid part of the ingot and near its wall.

Simulation results at $t = 2000$ s

As the temperature of the ingot continues to decrease, the processes mentioned for the simulation results at $t = 1000$ s continue. The amount of f_e increases further. Almost all of the volume of the ingot is filled with the equiaxed grains. The columnar phase f_c more or less stops forming. Its mass fraction only increases in the layer near the wall that it formed before. The melt is liquid only in the

upper part of the ingot. Due to solidification of the sedimented equiaxed grains and solute rejection caused by it, the remaining melt is enriched with the alloying elements. This can be seen in the distributions of the mixture mass fractions of the alloying elements $c^{\mathrm{C}}_{\mathrm{mix}}$ and $c^{\mathrm{Cr}}_{\mathrm{mix}}$.

Simulation results $t = 3925$ s

At this point the temperature T has sunk further, near the bottom it is approaching room temperature. The liquid fraction f_l is almost zero everywhere, the columnar volume fraction f_c is high near the wall, and the equiaxed phase f_e occupies the middle part of the ingot. This is the final distribution of the phases in the ingot. The velocities of the liquid and equiaxed phases $\vec{u}_l$ and $\vec{u}_e$ are zero everywhere. The mass fractions of the alloying elements in the columnar phase c^{C}_c and c^{Cr}_c are high only in the areas where the columnar phase is present, that is, where the columnar mass fraction f_c is high. The equiaxed mass fractions of the alloying elements c^{C}_e and c^{Cr}_e are higher near the wall and the bottom on the ingot, and lower in its bottom central part. There is also an increase of these mass fractions towards the top of the ingot. The final distribution of the mixture mass fractions $c^{\mathrm{C}}_{\mathrm{mix}}$ and $c^{\mathrm{Cr}}_{\mathrm{mix}}$shows that they are negative (lower than the initial liquid mass fractions $c^{\mathrm{C}}_{l,0}$ and $c^{\mathrm{Cr}}_{l,0}$) in the central low part of the ingot and positive (higher than the initial liquid mass fractions $c^{\mathrm{C}}_{l,0}$ and $c^{\mathrm{Cr}}_{l,0}$) near the bottom, the wall and the top of the ingot. The macrosegregation of carbon is very high: $\pm 60\%$ of the initial $c^{\mathrm{C}}_{l,0} = 0.003$ and the final macrosegregation of chromium is smaller: $\pm 17\%$ of the initial $c^{\mathrm{C}}_{l,0} = 0.15$.

Chapter 7

Discussion of the results

7.1 Spline interpolants versus piecewise-linear approximations

The results of validation of thermodynamic representation of phase diagram information using spline interpolation and piecewise-linear approximations are presented in the Section 5.

The comparisons between Thermo-Calc–Scheil curves $c_l^{\mathrm{C}} - f_s$ and $c_l^{\mathrm{Cr}} - f_s$ (used as reference) and the curves calculated using the two aforementioned thermodynamics representations are shown for alloys from ternary systems Fe–C–Cr, Fe–C–Mn and Cu–Sn–P. The figures that show the results of the validations are summarised in Table 7.1.

From the figures listed in Table 7.1 we can see that both spline interpolants and piecewise-linear approximations of the ternary solidification thermodynamics data produce results that are very close to those obtained by the reference

Alloy initial composition	Representation	Figures
Fe-0.3wt.%C-15wt.%Cr	linear	5.1, 5.2 and 5.3
Fe-0.18wt.%C-1.4wt.%Mn	linear	5.4, 5.5 and 5.6
Fe-0.3wt.%C-15wt.%Cr	splines	5.7, 5.8, 5.9 and 5.10
Cu-6wt.%Sn-0.5wt.%P	splines	5.11, 5.12 and 5.13

Table 7.1: Figures of the results of validation of different thermodynamics representation methods

computations with the Thermo-Calc–Scheil module.

These figures also show that for certain ternary phase diagrams/initial alloy compositions, the Scheil-curves and solidification paths obtained using the piecewise-linear approximations of the thermodynamic functions do not differ much from those obtained when using spline interpolants.

Note that the results presented in Section 5, which contains the validation of thermodynamics data representation are obtained assuming absence of convection. Taking thermosolutal convection and flow into account makes the process of resolving thermodynamics (calculation of solidification paths) challenging. In the presence of flow, transport of solute components influences the mass fraction fields and so the solidification paths can have a complex shape.

When using piecewise-linear approximations of ternary phase diagram data, the border between the phases has to be defined, as it is done for example for the Fe–C–Cr phase diagram by Eq. (4.6). This unfortunately makes the solubility functions of the alloying elements carbon $\tilde{c}_s^{\mathrm{C}}(\tilde{c}_l^{\mathrm{C}}, \tilde{c}_l^{\mathrm{Cr}})$, chromium $\tilde{c}_s^{\mathrm{Cr}}(\tilde{c}_l^{\mathrm{C}}, \tilde{c}_l^{\mathrm{Cr}})$ and the liquid temperature $\tilde{T}_l(\tilde{c}_l^{\mathrm{C}}, \tilde{c}_l^{\mathrm{Cr}})$ discontinuous, which can be seen in Figs. 4.6, 4.7 and 4.5.

From the thermodynamics point of view the discontinuity of the solubilities $\tilde{c}_s^{\mathrm{C}}(\tilde{c}_l^{\mathrm{C}}, \tilde{c}_l^{\mathrm{Cr}})$ and $\tilde{c}_s^{\mathrm{Cr}}(\tilde{c}_l^{\mathrm{C}}, \tilde{c}_l^{\mathrm{Cr}})$ is not a problem, since these functions are discontinuous in reality. On the contrary, the real liquidus temperature $\tilde{T}_l(\tilde{c}_l^{\mathrm{C}}, \tilde{c}_l^{\mathrm{Cr}})$ is continuous.

In spite of this discontinuity in $\tilde{T}_l(\tilde{c}_l^{\mathrm{C}}, \tilde{c}_l^{\mathrm{Cr}})$, for certain ternary phase diagrams/initial alloy compositions it was possible to use piecewise-linear approximations (alloys Fe-0.3wt.%C-15wt.%Cr and Fe-0.18wt.%C-1.4wt.%Mn considered in this work, see Section 5).

However, for more complicated phase diagrams such as Cu–Sn–P, creating a secure solving procedure to handle the discontinuities at the phase borders is quite complicated due to their complexity in the main element-rich corner. Thus, for this phase diagram piecewise-linear approximations cannot be used. Instead, spline interpolants have to be used. Because of the way in which these are constructed (see Sections 3.5.2, 4.3.3) they are continuous everywhere in the region of interest and do not suffer from the discontinuity problem of piecewise-linear interpolations.

Along with the very useful feature of continuity, spline interpolants also pos-

sess the other useful feature of universality: once constructed, they can be used to simulate solidification of alloys with initial compositions from all of the element-rich corner they were constructed for. Piecewise-linear approximations, in contrast, are not universal: they can be used only for the alloys/initial compositions that they were constructed for (as described in Sections 3.5.1, 4.3.1 and 4.3.2), or in their vicinity. In order to allow simulation of an alloy with a different initial composition, a piecewise-linear interpolation has to be constructed again by choosing different linearisation points and calculating different linearisation coefficients.

The drawbacks of using spline interpolation include: 1) a relatively long time of tabulation of thermodynamic data using Thermo-Calc API |The06b|. Depending on the resolution of the tabulation, it takes between several hours to several days (for example, tabulation of size 100x100 takes 18 hours, 200x200 points takes 1.5 days) and 2) relatively slow operation due to more complicated computations behind it in comparison with those behind the piecewise-linear approximations. The former issue is not prohibitive since it has to be done only once per alloying system, whereas the latter issue can be addressed by reducing the number of points used for interpolation (in these areas where it is sufficient to use less points without sacrificing the accuracy, for instance these areas where thermodynamical functions are close to linear, or of small curvature).

7.2 Simulation of mould filling and determination of boundary and initial conditions for solidification simulations

The results of mould filling simulations and their comparison with casting experiments is given in Sections 6.1 and 6.2. They show that both the downhill as well as uphill mould filling can be performed using the MAGMASOFT software package quite successfully.

The comparisons of the experimental and simulated temperature curves recorded by means of thermocouples placed in the mould wall are shown in Figs. 6.12 for downhill filling of 32 kg benchmark casting and 6.17, 6.18, 6.19 and 6.20 for uphill filling of the 2 ton industrial ingot.

These simulated curves show good agreement with the experimental ones, although there are discrepancies in Figs. 6.12 (downhill casting), and 6.20 (curves for E-E cut of the 2 ton ingot). The position of the thermocouples in the 2 ton ingot are shown in Fig. 6.16. The discrepancies in the curves for the 32 kg benchmark ingot filling are caused by the apparent problems with two of the thermocouples, namely the one labelled as "Melt" and the other labelled as "60", see Fig. 6.12. The reasons for this is questionable behaviour of the experimental curves for these points. For detailed explanations of this questionable behaviour see Section 6.1.3.

The experimental and the simulated temperature curves agree well. This means that the temperature-dependent heat transfer coefficients, Eq. 6.1 and Eq. 6.2 and the final temperature distributions after filling can be used for the solidification simulations. These heat transfer coefficients and initial temperature distributions were used in simulations described in Sections 6.4 (two-phase solidification of Fe-0.3wt.%C-15wt.%Cr alloy) and 6.5 (three-phase solidification of Fe-0.38wt.%C-16wt.%Cr alloy).

Another possibility to simulate the mould filling would be to employ a more sophisticated model including a front tracking algorithm like the VOF method (first described in |Hirt81|. See also its application for solidification in |Voller87b, Voller87a, Voller91, Gu99|) for solving free surface flow combined with the presented Eulerian multiphase model for solidification. Preliminary work is already being carried out in this direction |Fjeld08b, Fjeld08a|. However, because of the complexity of models of this kind and the lack of the ready made simulation tool, the development and application of this method is considered to be beyond the scope of this work.

7.3 Development of macrosegregation in ingot castings

The most important question that the simulations were designed to answer concerns the distributions of the alloying elements (carbon and chromium) in the ingot volume. These distributions are the most decisive factor affecting the quality of the final products that will be produced from this steel.

In this section the formation of macrosegregations in the relevant ingots, that

is, the 32 kg benchmark ingot and the 2 ton industrial ingot as predicted by the simulations performed within the scope of this work (described in Sections 6.4 and 6.5) is discussed.

32 kg benchmark ingot of X30Cr15 alloy

Analysis of the experimentally obtained mass fraction distributions of the alloying elements carbon and chromium and a comparison of the simulation with the experimental data

The final simulated macrosegregation pattern for this ingot is displayed in Fig. 6.31b, which shows the final distributions of the mixture mass fractions of carbon $c^{\mathrm{C}}_{\mathrm{mix}}$ and chromium $c^{\mathrm{Cr}}_{\mathrm{mix}}$. For the purposes of discussion, we show these distributions once again enlarged in Fig. 7.1. The colour bar shows the minimum of the mixture mass fractions in blue, the maximum in red and thus the green colour shows the absence of macrosegregation. The amount of macrosegregation in macrosegregation patterns like these is characterised by the the areas with positive (red) and negative (blue) macrosegregations.

As can be seen from Fig. 7.1, most of the volume of the ingot is green (apart from insignificantly small areas in the bottom corner), both for the mixture mass fractions of carbon $c^{\mathrm{C}}_{\mathrm{mix}}$ and chromium $c^{\mathrm{Cr}}_{\mathrm{mix}}$. This means that there are no significant macrosegregation predicted in the ingot and thus the distribution of alloying elements is predicted to be more or less uniform. If we neglect the insignificantly small areas near the bottom corner of the ingot where mixture mass fractions $c^{\mathrm{C}}_{\mathrm{mix}}$ and $c^{\mathrm{Cr}}_{\mathrm{mix}}$ differ from the neutral values, we can see that the maximum values of $c^{\mathrm{C}}_{\mathrm{mix}}$ and $c^{\mathrm{Cr}}_{\mathrm{mix}}$ are equal to $3.2 \cdot 10^{-3}$ (increase by 6.7% with respect to the initial mass fraction) and $1.504 \cdot 10^{-1}$ (increase by 0.3%), and the minimum values are equal to $2.82 \cdot 10^{-3}$ (decrease by 6%) and $1.496 \cdot 10^{-1}$ (decrease by 0.3%).

Minimum and maximum experimental values of mass fractions of carbon and chromium can be seen in Figs. 6.35 and 6.36 where the results of the chemical analysis of the 32 kg benchmark ingot casting experiment are shown. Because of the small size of the ingot (30 cm in height), several upper centimetres of the casted ingot is shrinkage cavity, and the distribution of the alloying elements there cannot be reliably predicted by the model used, hence the first upper row

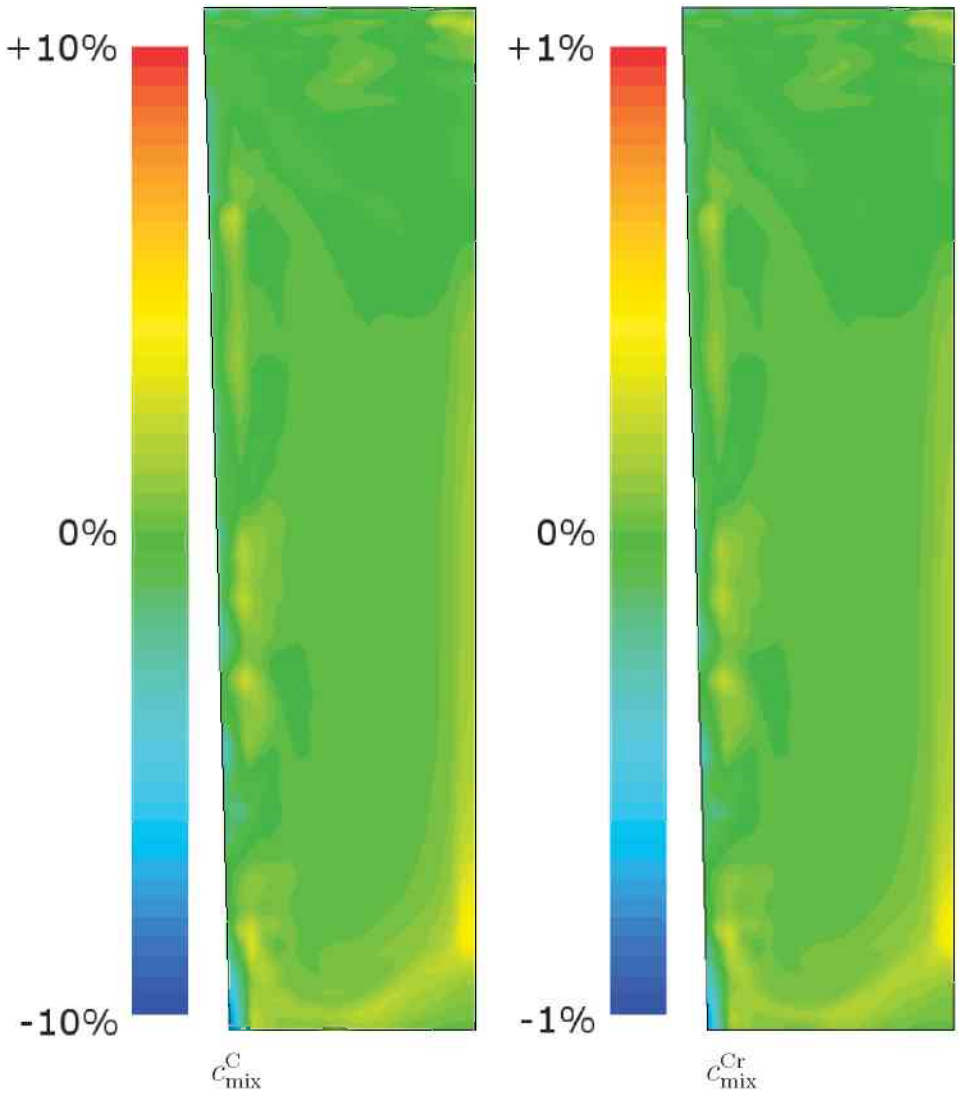

Figure 7.1: Mixture mass fraction distributions (macrosegregation patterns) of carbon c^{C}_{mix} and chromium c^{Cr}_{mix} in 32 kg benchmark ingot of X30Cr15, obtained from the two-phase solidification simulation described in Section 6.4. The colour bars show relative change in percent of initial mass fractions $c^{C}_{0} = 3 \cdot 10^{-3}$ and $c^{Cr}_{0} = 15 \cdot 10^{-1}$. Note that the measurement errors relative to the initial mass fractions of carbon and chromium were 3.3% ($0.1 \cdot 10^{-3}$) for carbon and 0.34% ($0.005 \cdot 10^{-1}$) for chromium. Figures also show that c^{C}_{mix} changes in an approximate interval $\pm 5\%$ and c^{Cr}_{mix} in an approximate interval $\pm 0.5\%$.

element	exp. min.	sim. min.	exp. max.	sim. max.
carbon	$3.0 \cdot 10^{-3}$ (0.0%)	$2.82 \cdot 10^{-3}$ (−6.0%)	$3.1 \cdot 10^{-3}$ (+3.3%)	$3.2 \cdot 10^{-3}$ (+6.7%)
chromium	$1.45 \cdot 10^{-1}$ (−2.2%)	$1.496 \cdot 10^{-1}$ (−0.3%)	$1.50 \cdot 10^{-1}$ (+1.5%)	$1.504 \cdot 10^{-1}$ (+0.3%)

Table 7.2: Minimum and maximum values of the mass fractions of alloying element after solidification in simulation and in experiment for 32 kg benchmark ingot casting of X30Cr15. The relative change in mass fraction with respect to initial mass fractions is given in brackets.

of the points where probes were taken should be excluded from consideration [Tanzer08]. Moreover, the first probe for carbon in the third row from the top in Fig. 6.35 shows a much higher mass fraction of carbon than the neighbouring ones and thus has to be seen as erroneous and also has to be excluded from further consideration.

Taking this into account, the maximum mixture fractions for $c^{\mathrm{C}}_{\mathrm{mix}}$ and $c^{\mathrm{Cr}}_{\mathrm{mix}}$ are $3.1 \cdot 10^{-3}$ and $1.5 \cdot 10^{-1}$, minimum mixture fractions are $3.0 \cdot 10^{-3}$ and $1.45 \cdot 10^{-1}$ respectively.

The minimum and maximum of the mixture mass fractions of alloying elements in simulation and final distribution of the alloying elements in the ingot can now be summarised in Table 7.2.

The measurement error of determination of carbon mass fraction was 10^{-4} (3.3% of c^{C}_0) [Tanzer08]. We conclude that the distribution of carbon has to be considered uniform, since the difference between the minimum and the maximum values of carbon mass fractions are close to the measurement error. The measurement error for the determination of carbon mass fraction was $5 \cdot 10^{-4}$ (0.34% of c^{Cr}_0) [Tanzer08], and spatial distribution of chromium is significant. On the other hand, the experimental macrosegregation of chromium is very small. The simulated macrosegregation of chromium is also very small, which qualitatively agrees with the experimental data.

Note that only one experiment was performed. Thus, reproducibility or statistical significance of the experimental results cannot be investigated.

Peritectic solidification

The proposed model is able to describe the peritectic solidification. Let us consider, for example, the curves shown in Fig. 6.32, which show the $c_l^{\mathrm{C,Cr}} - f_c$ curves obtained during the simulation of solidification. The start of the formation of the phase γ can be seen in these curves: around the value of volume fraction of columnar $f_c = 0.82$ they exhibit a slight change in slope. The slope of the curve in the case of carbon increases, and it decreases for chromium. This is in agreement with the solidification path for X30Cr15 obtained from the 0-D solidification model (described in Section 3.1) and the Thermo-Calc–Scheil module. The solidification path is shown in Figs. 5.3 (piecewise-linear thermodynamics) and 5.9 (spline thermodynamics). As can be seen from these figures, the solidification path changes its direction as it crosses the phase border between the α phase and the γ phase; this is when the peritectic solidification starts. It corresponds to the point on the curve with the mass fraction of carbon $c_l^{\mathrm{C}} = 0.012$ and with the mass fraction of chromium $c_l^{\mathrm{Cr}} = 0.179$, which coincide with the mass fractions of carbon and chromium that correspond to the value $f_c = 0.82$ on curves shown in Figs. 6.32–6.34.

2 ton industrial ingot of X38Cr16 alloy

For the purpose of the discussion, the final macrosegregation patterns of the alloying elements carbon and chromium characterised by the distribution of $c_{\mathrm{mix}}^{\mathrm{C}}$, $c_{\mathrm{mix}}^{\mathrm{Cr}}$, f_c and f_e are shown in Fig. 7.2.

The process of formation of macrosegregation patterns (distributions of $c_{\mathrm{mix}}^{\mathrm{C}}$ and $c_{\mathrm{mix}}^{\mathrm{Cr}}$) as well as the final distributions of f_c and f_e shown in Fig. 7.2 is described in Section 6.5.4.

We can see that most of the ingot volume is occupied by the equiaxed phase, and only the areas adjacent to the wall and the bottom of the ingot reveal the presence of the columnar phase. The amount of the columnar phase is relatively small. This disproportion in the phase distributions is evidently caused by the choice of nucleation parameters $n_{\max}$, ΔT_N and ΔT_σ that describe nucleation in Eq. (2.21). This has to be determined experimentally in conjunction with a parameter study, which is beyond the scope of this work. Preliminary work in this direction has already been performed [Könözsy07, Könözsy08].

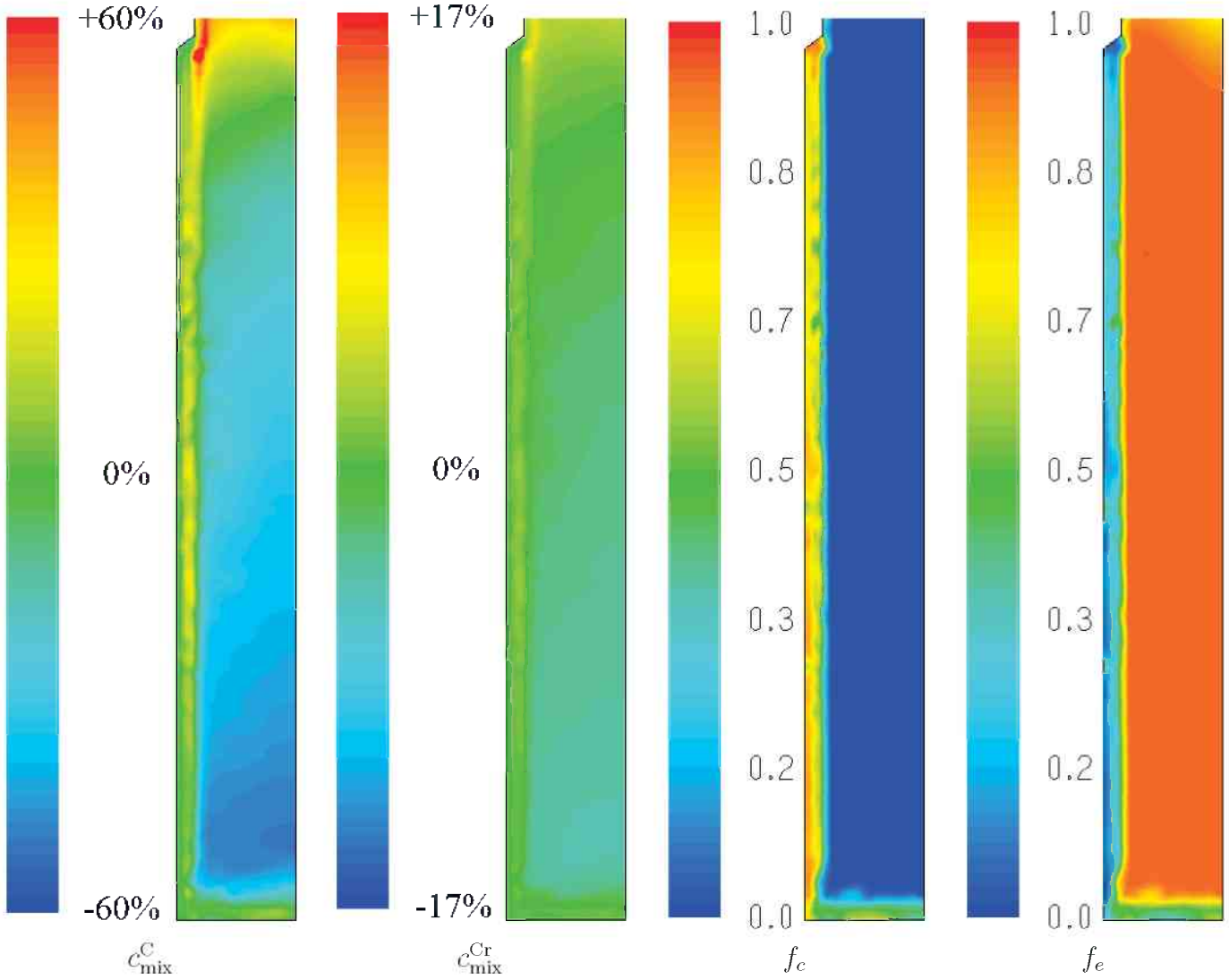

Figure 7.2: Distributions of the columnar f_c and equiaxed f_e phases after solidification in 2 ton industrial ingot of X38Cr16, obtained from the three-phase solidification simulation described in Section 6.5.

Formation of the uneven pattern near the wall of the 2 ton industrial ingot

The uneven pattern in distributions of the volume fraction of the columnar f_c and the equiaxed f_e phases near the outer wall of the ingot can be observed in Figs. 6.42(t=1000 s)–6.44(t =3925 s). Although this uneven distribution of phases cannot be seen on the figures corresponding to earlier points in time, the formation of this pattern takes place earlier, at around t = 100 s. Figure 7.3 shows the formation in detail.

The formation of the pattern happens as follows. Due to the intensive cooling of the wall and the subsequent forced convection, a downward flow develops. Also because of the cooling of the wall the first columnar fraction starts growing at the wall, as can be seen in Fig. 7.3, t =100 s. The columnar layer acts as a step, causing a vortex to appear. By means of the vortex the equiaxed phase is transported towards the wall, as can be seen from the velocity vectors pointing towards the wall in Fig. 7.3, t=115 s, t=120 s, t=125 s and t=130 s. The increasing amount of the equiaxed phase can be seen from the contour plots in Fig. 7.3. After that the equiaxed phase trapped in the gap near the wall continues to grow (Fig. 7.3, t=200 s) and forms the observed pattern.

Formation of the positive-negative segregation near the wall

Examining distributions of the mixture mass fractions of carbon $c^{\mathrm{C}}_{\mathrm{mix}}$ and chromium $c^{\mathrm{Cr}}_{\mathrm{mix}}$ in Figs. 6.42 (in the lower part of the ingot), 6.43 and 6.44 near the wall reveals several layers of differently segregated melt. Adjacent to the wall there is a layer of negatively segregated solid phase, then a positively segregated layer then in the centre the alloy is negatively segregated. The pattern forms as follows.

First of all in the very beginning of the solidification, the columnar phase starts growing at the walls of the ingot. These first crystals are negatively segregated, due to the inability of the solid phase to incorporate all of the alloying elements. This is analogous to the case of binary solidification, where the mass fraction of the alloying element A in the very first solid phase formed is $c^{\mathrm{A}}_s = kc^{\mathrm{A}}_{l,0}$. Here the partitioning coefficient $k < 1$ and $c^{\mathrm{A}}_{l,0}$ is the initial mass fraction of the alloying element A in the melt.

Next, a vortex forms in the bottom part of the ingot, due to the strong forced

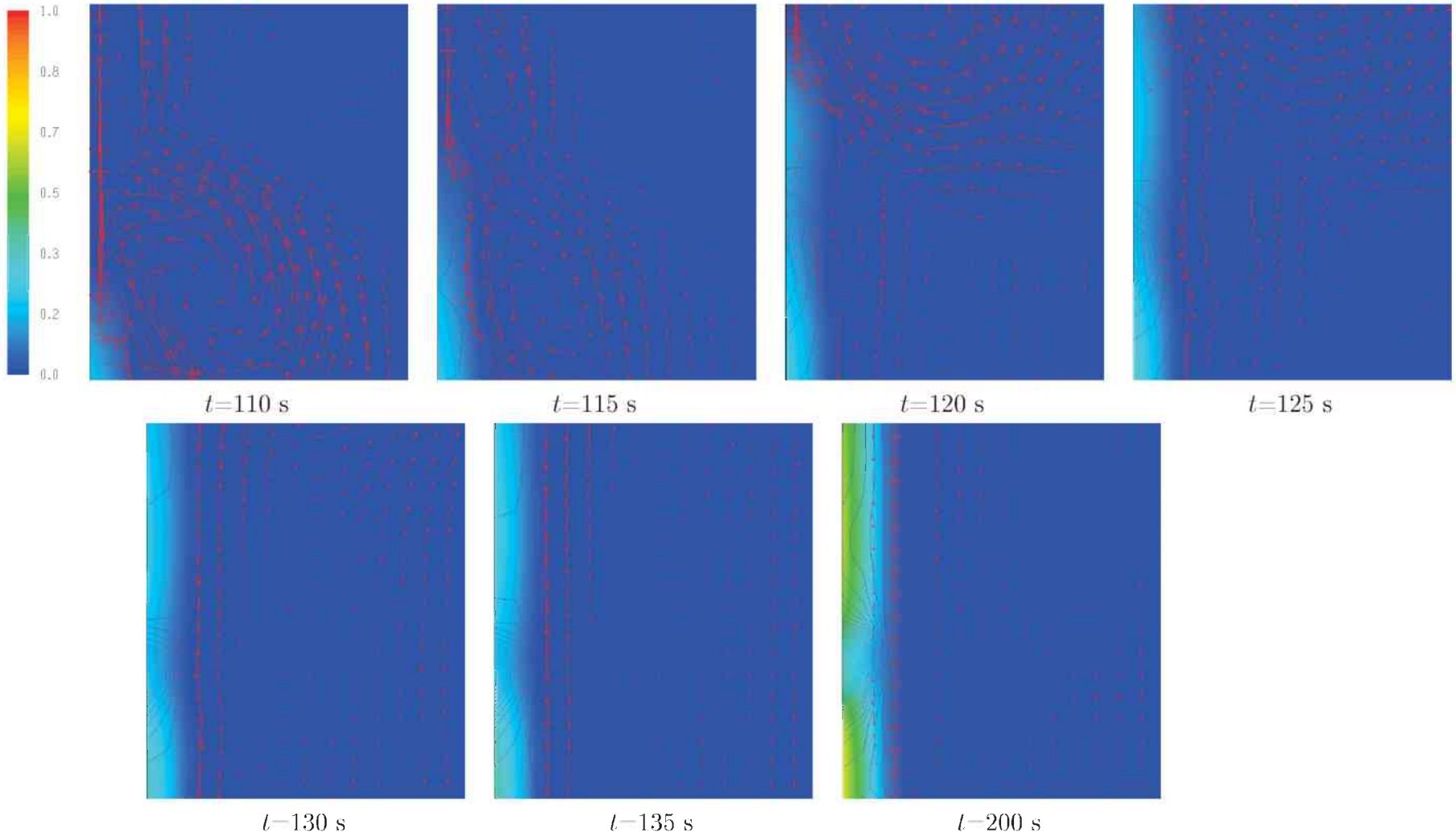

Figure 7.3: Formation of the uneven pattern near the wall of the ingot. An enlarged part of the area near the wall is shown at different points in time. The colour shows the volume fraction of the columnar phase, the contour lines show the volume fraction of the equiaxed phase and the arrows depict the vector field of the velocity of the equiaxed phase.

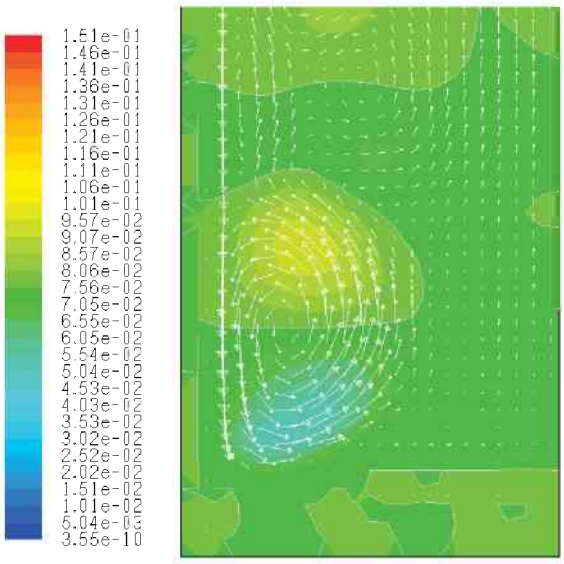

Figure 7.4: Formation of the vortex in the bottom part of the ingot. The colour hue shows the liquid radial velocity in the ingot. The white contour line corresponds to zero liquid radial velocity. The white arrows represent the velocity vector field.

convection of the melt, which flows downwards along the wall. The vortex is shown in Fig. 7.4. Then the vortex moves upwards, as can be seen in Fig. 7.5, and after reaching the top of the ingot it breaks up into a system of smaller vortices.

As the vortex moves up, it transports positively segregated melt from the middle of the ingot towards the wall, which solidifies there, forming a positively segregated layer as shown in Fig. 7.6.

7.4 Solidification of sedimented equiaxed grains

In Figs. 6.42 and 6.43, in the distributions of the volume fraction of the equiaxed phase f_e, an interesting pattern can be seen: almost 100% solidified equiaxed phase region in the bottom of the ingot borders with the region with $f_e \approx 0.637$, which is the packing limit. Let us examine this pattern in greater detail by means of Fig. 7.7. In this figure one can see that in the beginning of the solidification the equiaxed phase just sediments at the bottom of the ingot (approximately t <400 s). The volume fraction of the equiaxed phase is equal to the packing

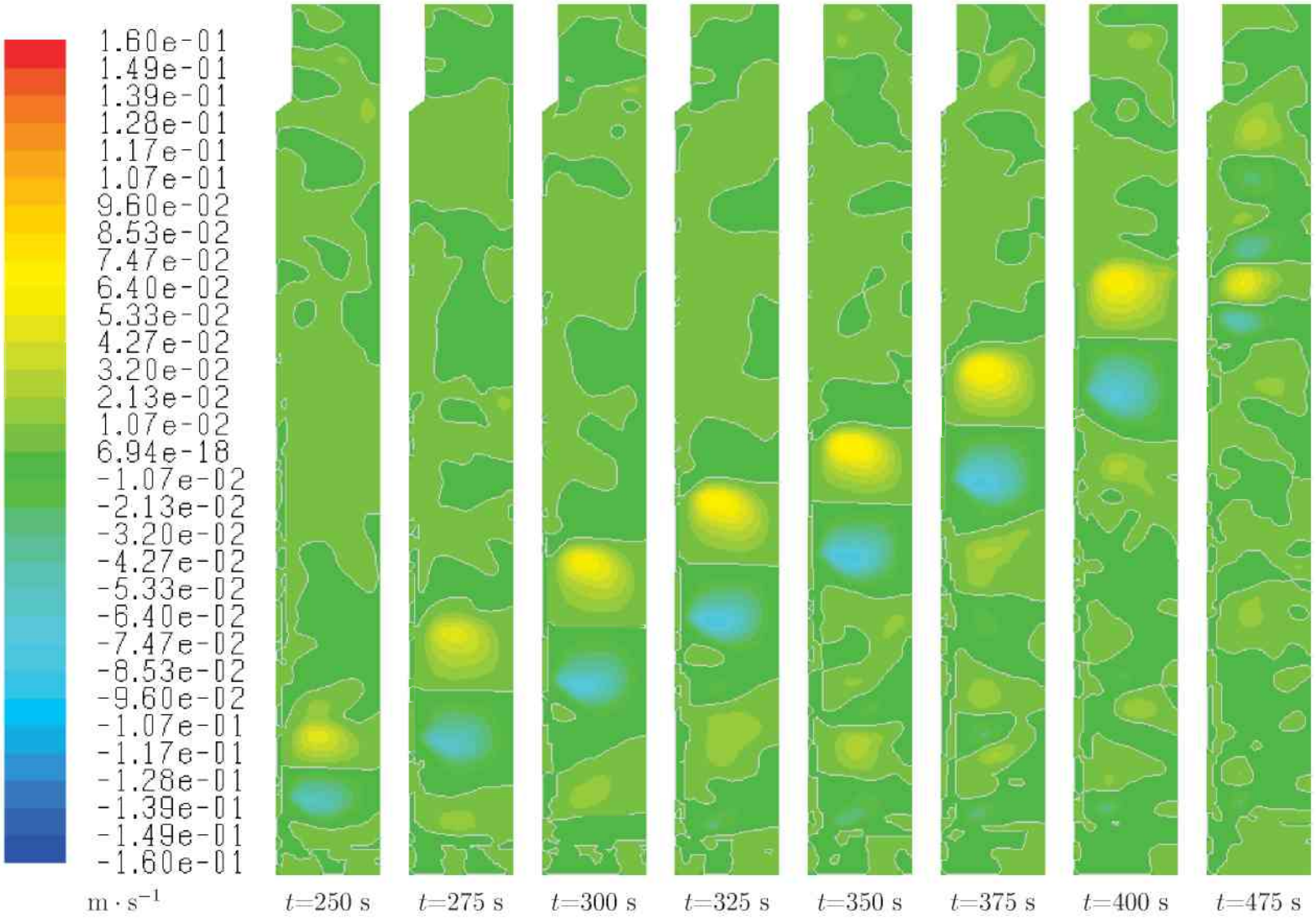

Figure 7.5: The upwards movement of the vortex. The colour hue again shows the liquid radial velocity in the ingot. The white contour line corresponds to zero liquid radial velocity.

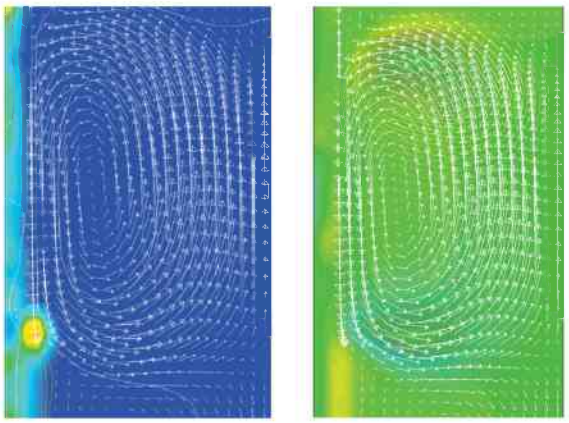

C_{lc}^{C} a $c_{\mathrm{mix}}^{\mathrm{C}}$ b

Figure 7.6: Formation of the positively segregated layer by means of the vortex. In figure (a) the colour shows carbon transfer rate $C_{lc}^{\mathrm{C}} = \bar{c}_s^{\mathrm{C}} M_{lc}$, which represents the mass of carbon incorporated into the columnar phase per unit volume and per unit time. In figure (b) the colour represents the amount of macrosegregation of carbon $c_{\mathrm{mix}}^{\mathrm{C}}$ and the contour lines represent the axial velocity. The white arrows on both of figures (a) and (b) represent the liquid velocity vector field.

limit, 0.637. It remains approximately 0.637 until the temperature in the ingot reaches the liquidus temperature. Once the liquidus temperature is reached, the previously sedimented equiaxed phase starts to grow, forming the aforementioned pattern. This can be seen in Fig. 7.7: the two regions of the equiaxed phase (one with $f_e \approx 0.637$ and the other with $f_e \approx 0.95$) are separated by the contour line T=1760 K, which approximately corresponds to the liquidus temperature of the alloy at the beginning of the solidification. This is true for the time $t < 1400$ s, then the sedimented equiaxed solidification front and the contour line start to deviate. This is because the real liquidus temperature is a function of the mass fractions of the alloying components in the liquid phase, so it changes accordingly.

This effect also explains the increase in the mixture mass fractions of the alloying elements in the top part of the ingot near the end of the solidification. The highly segregated melt that was between the sedimented equiaxed grains is forced to the upper part of the ingot during the course of the solidification, thus causing the increase in $c_{\mathrm{mix}}^{\mathrm{C}}$ and $c_{\mathrm{mix}}^{\mathrm{Cr}}$ observed in Figs. 6.42 and 6.43.

Another result of this solidification behaviour of the sedimented equiaxed phase is the negative mixture mass fractions of the alloying elements $c_{\mathrm{mix}}^{\mathrm{C}}$ and

$c_{\mathrm{mix}}^{\mathrm{Cr}}$ which can be seen in Figs. 6.42, 6.43 and 6.44. The first equiaxed crystals that form cause strong negative segregation for the same reason that the first columnar crystals cause it at the walls. This way the major part of the sedimented equiaxed phase is negatively segregated ($f_e \approx 0.637$ for the negatively segregated sedimented equiaxed phase). Only the remaining fraction of the equiaxed phase $f_e \approx 0.363$ solidifies after the liquidus temperature is reached, which does not have a noticeable effect on the macrosegregation pattern.

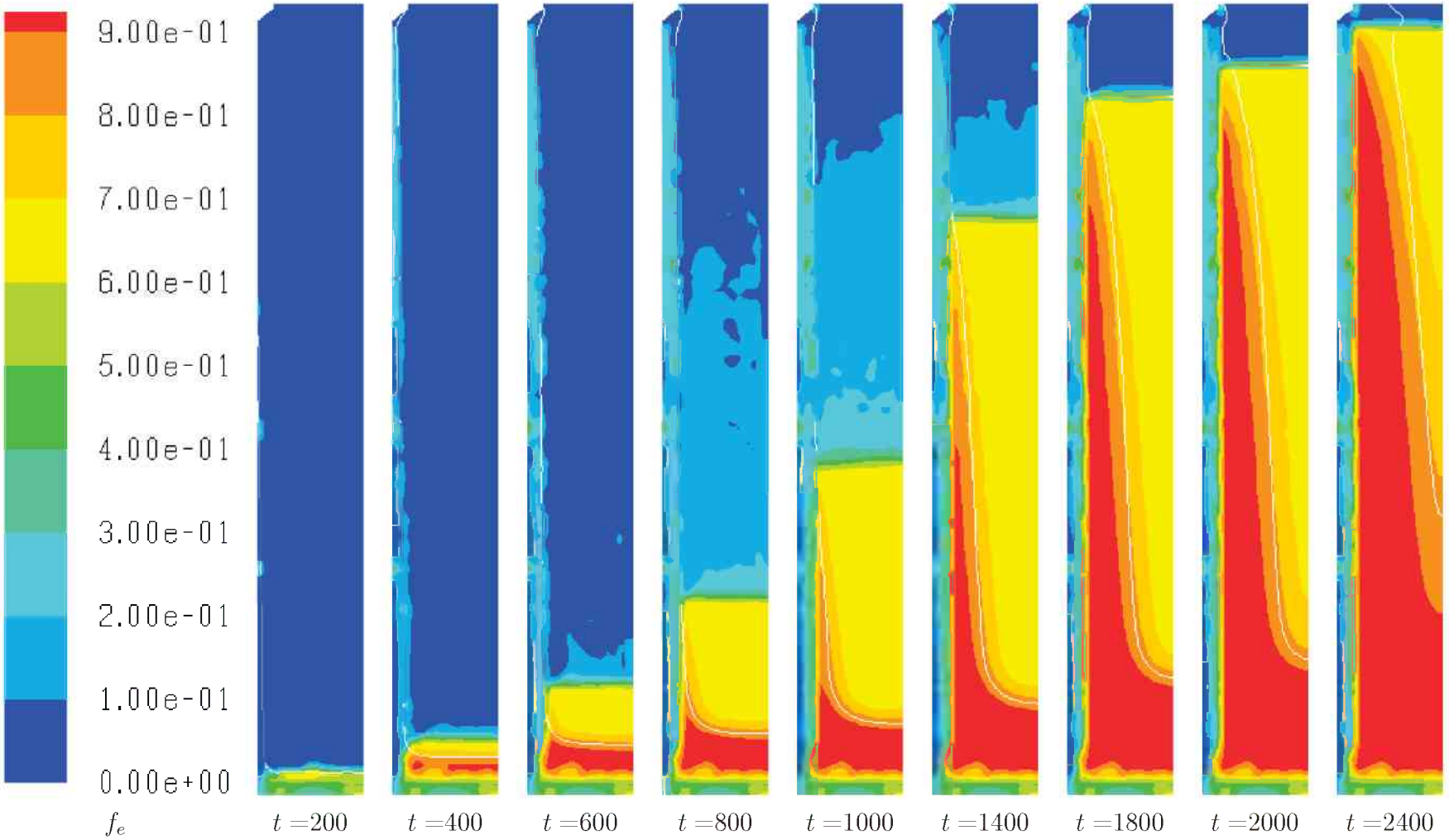

Figure 7.7: Solidification of the sedimented equiaxed phase. The colour represents the volume fraction of the equiaxed phase. The white contour line corresponds to the temperature 1760 K, which approximately corresponds to the liquidus temperature at the beginning of the solidification.

Chapter 8

Conclusions, summary and outlook

8.1 Conclusions

In the presented work a methodology of multicomponent multiphase solidification of ingot steel castings is developed. The work is based on the previous research performed for binary alloys. The extension of the binary model was carried out for the ternary case, including generalisation of the idea of coupling between mesoscale quantities, liquid and solid mass fractions at the phase border on one side and the macroscopic bulk mass fractions and temperature on the other. For this, a mathematical model in the form of a nonlinear equation system was developed, a numerical method for solving this system was implemented and validated using a proposed simplified zero-dimensional solidification model.

A method to overcome the problem of intrinsic discontinuities of solubilities of alloying components in solid phases when using a numerical method was suggested. For this, the spline interpolants were used to interpolate pointwise tabulated thermodynamic data. Spline interpolants smoothen the discontinuities along the phase borders, allowing successful usage of Newton-type methods for solving the nonlinear equation system for coupling.

The developed and implemented model was used to simulate the solidification process in a 32 kg benchmark ingot of X30Cr15 steel and 2 ton ingot of the same X38Cr16 alloy, assuming two and three phase flow. Based on one of the simulations, the effect of thermal and solutal convection was investigated. The effect of the thermal convection was the strongest, affecting the course of solidification, whereas the effect of solutal convection was relatively weak.

The models and methods described in the work were successfully implemented and can be used to simulate ingot casting solidification of ternary steels. The use of the coupling method developed in this work is not limited by the applications to the ingot steel casting solidification. It can and has been used for simulating other solidification processes, for instance, direct-chill casting of bronzes |Ishmurzin08|, continuous casting of steels, and so on. Further parameter study is necessary to increase the reliability of the simulations.

8.2 Summary

A methodology was developed to simulate solidification of multicomponent alloy ingot castings, which was validated and then applied for the simulation of solidification of Fe–C–Cr steel in a 32 kg benchmark ingot and a 2 ton industrial ingot. The results obtained show good qualitative agreement with experimental data.

In order to achieve this, several new developments were made:

- Spherical and cylindrical growth formulations for binary alloys were reformulated for the multicomponent alloys
- A way to take multicomponent phase diagram data into account was developed and implemented, validated and applied for solidification simulations of ternary alloys
- The nonlinear equations system describing the coupling between the phase diagram data, solidification growth kinetics and multiphase flow was investigated, the numerical method for solving it was implemented and successfully applied
- The dependence of mesoscopic quantities (mass fractions of alloying components at the solid-liquid interface) on macroscopic quantities (temperature and mass fractions of alloying components in liquid) was demonstrated
- A simplified zero-dimensional solidification model was introduced, implemented and used to simulate solidification of alloys from Fe–C–Cr, Fe–C–Mn and Cu–Sn–P systems, in order to validate the implementation of algorithms

- Two ways of representing phase diagram information (liquidus temperature and solubilities) were developed, implemented and used for simulations: piecewise-linear approximations and spline interpolations
- The problem of intrinsic discontinuities of the solubility functions was addressed by using spline interpolations, which smoothen the discontinuities mentioned
- Parameters of piecewise-linear approximations of phase diagrams were calculated for Fe–C–Cr and Fe–C–Mn systems and successfully used in simulations
- An investigation of the accuracy of spline-interpolation of thermodynamic data on the order of the splines used was investigated and the optimal order was found and used for simulations
- A simulation of mould filling and solidification using the MAGMASOFT software package was performed; a comparison with experimental cooling was carried out and satisfactory qualitative agreement was found
- Simulations of solidification of ternary Fe–C–Cr alloys were performed, satisfactory qualitative agreement with experimental data was found
- The influence of different convection effects (thermal and solutal) on the final distribution of alloying components was investigated

8.3 Outlook

The coupling strategy presented in this work is valid in the two phase regions of the phase diagram, that is for primary and peritectic solidification. This is sufficient for describing the course of solidification of many alloys. However, there are alloys, for example different tool steels, for which the formation of eutectic phase is of high importance. The next step in this direction should be the implementation of the model describing the formation of eutectics. For the Fe–C–Cr alloying system, the details on the eutectic reaction are given in [VandenBoomgaard72],

and the formation of peritectics can be modelled relatively easily due to the reduction of the degree of freedom by 1 for the eutectic reaction in comparison with primary and peritectic ones.

When using spline interpolants for representing the thermodynamic data, the main issue is the computation time. It can be reduced by decreasing the number of interpolation points in the parts where this is possible. The thermodynamic data represented by splines are two-dimensional surfaces, such as, for example, liquidus temperature $\tilde{T} = \tilde{T}(\tilde{c}_l^{\mathrm{A}}, \tilde{c}_l^{\mathrm{B}})$. It is obvious that in the parts of the surface where its curvature is low it can be approximated using less tabulated data points. Thus, the number of interpolation points necessary for interpolating a surface with sufficient accuracy depends on its curvature. Using less interpolation points for representing the thermodynamic functions should to result in a reduced computational time. One possible way to achieve this is to use an adaptive tabulation procedure, where the density of the data points of the grid is proportional to the curvature of a given thermodynamic function (liquidus temperature or solubilities of alloying elements in solid phases).

Another way of improving the computation time for the simulations discussed in this work is to use parallel processing. This can be performed at the CFD solver level. In this case the computational grid is partitioned, and every grid partition is assigned to a dedicated computing node, which speeds up the computation. By employing modern parallel computers, one can expect a significant increase in computational speed, especially when using fine tuning of the CFD solver.

This model can also be extended to take into account quaternary or more component alloys. The nonlinear equation system consisting of equations for the ternary case (3.16), (3.17), (3.20) and (3.21) can be extended for the n-component case as follows:

$$F(c_l^1, \ldots, c_l^{N-1}, \tilde{c}_l^1, \ldots, \tilde{c}_l^{N-1}, \tilde{c}_s^1, \ldots, \tilde{c}_s^{N-1}) = 0, \tag{8.1}$$

where

$$F = \begin{pmatrix} \tilde{c}_s^1(\tilde{c}_l^1, \tilde{c}_l^2, \ldots, \tilde{c}_l^2, \ldots, \tilde{c}_l^{N-1}) - \tilde{c}_s^1 \\ \tilde{c}_s^2(\tilde{c}_l^1, \tilde{c}_l^2, \ldots, \tilde{c}_l^2, \ldots, \tilde{c}_l^{N-1}) - \tilde{c}_s^2 \\ \ldots \\ \tilde{c}_s^{N-1}(\tilde{c}_l^1, \tilde{c}_l^2, \ldots, \tilde{c}_l^2, \ldots, \tilde{c}_l^{N-1}) - \tilde{c}_s^{N-1} \\ \tilde{T}_l(\tilde{c}_l^1, \tilde{c}_l^2, \ldots, \tilde{c}_l^2, \ldots, \tilde{c}_l^{N-1}) - T \\ r_1 \frac{\tilde{c}_l^1 - c_l^1}{\tilde{c}_l^2 - \tilde{c}_s^2} - \frac{\tilde{c}_l^2 - c_l^2}{\tilde{c}_l^2 - \tilde{c}_s^2} \\ r_2 \frac{\tilde{c}_l^1 - c_l^1}{\tilde{c}_l^1 - \tilde{c}_s^1} - \frac{\tilde{c}_l^3 - c_l^3}{\tilde{c}_l^3 - \tilde{c}_s^3} \\ \ldots \\ r_{N-2} \frac{\tilde{c}_l^1 - c_l^1}{\tilde{c}_l^1 - \tilde{c}_s^1} - \frac{\tilde{c}_l^{N-1} - c_l^{N-1}}{\tilde{c}_l^{N-1} - \tilde{c}_s^{N-1}} \end{pmatrix}, \tag{8.2}$$

with $r_i = D_l^1 / D_l^{i+1}$, $i = 1 \ldots N-2$ are diffusion coefficient ratios. This system consists of $2(N-1)$ unknowns: $\tilde{c}_l^1, \ldots, \tilde{c}_l^{N-1}, \tilde{c}_s^1, \ldots, \tilde{c}_s^{N-1}$, $(N-1)$ equations for solubilities, 1 liquidus hypersurface equation and $(N-2)$ equations expressing growth velocities equality, that is $2(N-1)$ equations. The proof of the existence of the solution for this equation system is analogous to the one for the ternary case. The implementation of the numerical method can be carried out using the same solver that was used for the ternary case and should be straightforward. The representation of the thermodynamic functions using spline interpolation in this case has to be performed incorporating a multivariate spline interpolation.

Another way to improve the model is to take into account the effect of the back-diffusion, which is proven to be an important factor affecting macrosegregation patterns |Hillert99, Turkeli06, Larouche07|. In this case the solute balance equation has to be rewritten to include the diffusive flux into the solid, as follows (compare this to the solute balance without back-diffusion given in Eq. (2.25)):

$$(\tilde{c}_l^A - \tilde{c}_s^A) v = -D_l^A \frac{\mathrm{d}c_l^A}{\mathrm{d}r} + D_s^A \frac{\mathrm{d}c_s^A}{\mathrm{d}r}. \tag{8.3}$$

The growth velocity formula has to be rewritten accordingly and the source terms for the solute transport have to be changed to include the diffusive fluxes from the liquid phase towards the solid one.

With the method of solidification simulation developed in the work presented it is also possible to predict the final solidification microstructure. This is performed by using the alloying element distributions from simulations and subse-

quent deduction of the amount of resulting phases at room temperature |Grasser08|.

Appendix A
Experimental Setup and Procedure for the Benchmark Casting

In order to validate the three-phase Eulerian multicomponent model presented in this work, a casting experiment was carried out by the industrial partner |Tanzer08| and we follow the publication here.

A benchmark ingot with an approximate weight of 32 kg was produced in a laboratory induction furnace. The sketch of the mould is shown in the Fig. 6.16. The melt was built up with pure iron, carbon and ferrochromium in an induction furnace. The chemical composition of the melt was 0.3 wt.% carbon, 14.82 wt.% chromium and iron in balance.

The presence of trace elements such as sulphur or phosphorus are neglected in the analysis. The last temperature measurement before casting revealed a temperature of 1555 °C which was taken as the casting temperature. The laboratory furnace only allowed downhill casting although speaking of industrial processes uphill casting is the common method because of its better surface quality and better yield of material. In this experiment a big end up grey cast mould was used. The mould was placed on a heavy grey cast bottom plate and was instrumented with thermocouples of TypeN in different heights and different depths of the mould wall. Additionally one thermocouple of TypeS was located in the casting room to measure the melt temperature and the cooling behaviour of the ingot.

The experimental data obtained during the experiment were the cooling curves measured by the thermocouples (used in this work are shown in the Fig. 6.12).

Also the solidified ingot was cut as shown in Fig. 8.1a and probes were taken

from the holes drilled as shown in Fig. 8.1b. These probes were used to determine the carbon and chromium mass fractions distributions (shown compared with the simulation results in the Fig. 6.36 and 6.35).

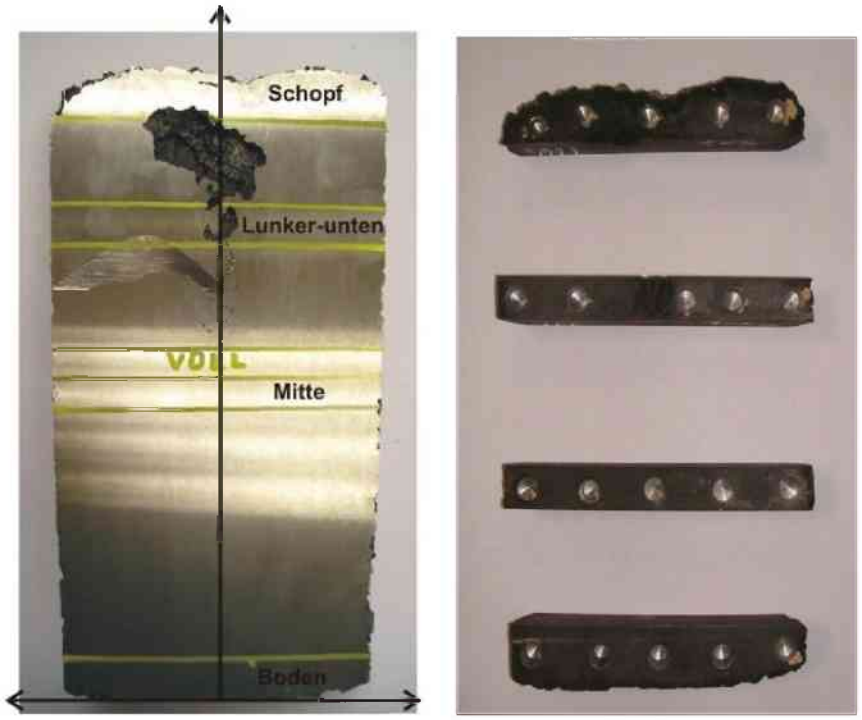

a b

Figure 8.1: The 32 kg benchmark ingot casting. Half of the ingot after cutting (a) and pieces of ingot where probes were taken (b).

Appendix B
Analytical Solution of the Partly Linearised Nonlinear Equation System for Coupling

As it is shown in the main text, in order to compute the growth velocity and then the necessary mass transfer rates, in the case of a ternary alloy, it is necessary to solve a nonlinear algebraic equation system consisting of four equations (3.16), (3.17), (3.20) and (3.21). If we linearise the first three equations (3.16), (3.17), (3.20) of this equation system, it can be written as

$$\tilde{c}_s^A = \tilde{c}_{s,0}^A + m_{AA}(\tilde{c}_l^A - \tilde{c}_{l,0}^A) + m_{AB}(\tilde{c}_l^B - \tilde{c}_{l,0}^B), \tag{8.4}$$

$$\tilde{c}_s^B = \tilde{c}_{s,0}^B + m_{BA}(\tilde{c}_l^A - \tilde{c}_{l,0}^A) + m_{BB}(\tilde{c}_l^B - \tilde{c}_{l,0}^B), \tag{8.5}$$

$$\tilde{T} = \tilde{T}_0 + m_{AT}(\tilde{c}_l^A - \tilde{c}_{l,0}^A) + m_{BT}(\tilde{c}_l^B - \tilde{c}_{l,0}^B), \tag{8.6}$$

$$r\frac{\tilde{c}_l^A - c_l^A}{\tilde{c}_l^A - \tilde{c}_s^A} = \frac{\tilde{c}_l^B - c_l^B}{\tilde{c}_l^B - \tilde{c}_s^B}, \tag{8.7}$$

where $\tilde{c}_{s,0}^A$, $\tilde{c}_{s,0}^B$, $\tilde{T}_0$, m_{AA}, m_{AB}, m_{AA}, m_{BA}, m_{BB}, m_{AT}, m_{BT} are constants,

and r is the diffusion coefficients ratio $r = D_l^A/D_l^B$, which is also a constant.

For this simplified equations system with only one nonlinear equation can be solved analytically, and a way it can be done is shown below.

The first three equations can be written in the matrix form

$$Mc = b, \tag{8.8}$$

where

$$M = \begin{pmatrix} m_{AA} & m_{AB} & -1 & 0 \\ m_{BA} & m_{BB} & 0 & -1 \\ m_{AT} & m_{BT} & 0 & 0 \end{pmatrix} \tag{8.9}$$

$$b = \begin{pmatrix} m_{AA}c_{0,1} + m_{AB}c_{0,2} - c_{0,3} \\ m_{BA}c_{0,1} + m_{BB}c_{0,2} - c_{0,4} \\ \tilde{T} - \tilde{T}_0 + m_{AT}c_{0,1} + m_{BT}c_{0,2} \end{pmatrix}, \tag{8.10}$$

$$c = \begin{pmatrix} \tilde{c}_l^A \\ \tilde{c}_l^B \\ \tilde{c}_s^A \\ \tilde{c}_s^B \end{pmatrix}. \tag{8.11}$$

The equation system (8.8) now can be solved, setting for instance $\tilde{c}_l^B$ to be the parameter, that is $\tilde{c}_l^B = t \in \mathbb{R}$ and other three unknowns are functions of the parameter, so that $\tilde{c}_l^A = \tilde{c}_l^A(\tilde{c}_l^B = t)$, $\tilde{c}_l^B = t$, $\tilde{c}_s^A = \tilde{c}_s^A(\tilde{c}_l^B = t)$ and $\tilde{c}_s^B = \tilde{c}_s^B(\tilde{c}_l^B = t)$. The solution of (8.8) for the three unknowns mentioned is:

$$c = \frac{1}{m_{AT}} \begin{pmatrix} m_{AT}\tilde{c}_{l,0}^A - m_{BT}t + \tilde{T} - \tilde{T}_0 + m_{BT}\tilde{c}_{l,0}^B \\ t \\ (m_{AT}m_{AB} - m_{AA}m_{BT})t - m_{AT}(m_{AB}\tilde{c}_{l,0}^B + \tilde{c}_{s,0}^A) + m_{AA}(\tilde{T} - \tilde{T}_0 + m_{BT}\tilde{c}_{l,0}^B) \\ (m_{AT}m_{BB} - m_{BA}m_{BT})t - m_{AT}(m_{BB}\tilde{c}_{l,0}^B + \tilde{c}_{s,0}^B) + m_{BA}(\tilde{T} - T_0 + m_{BT}\tilde{c}_{l,0}^B) \end{pmatrix}. \tag{8.12}$$

Now it is possible to substitute the expressions $\tilde{c}_l^A = \tilde{c}_l^A(\tilde{c}_l^B = t)$, $\tilde{c}_l^B = t$, $\tilde{c}_s^A = \tilde{c}_s^A(\tilde{c}_l^B = t)$ and $\tilde{c}_s^B = \tilde{c}_s^B(\tilde{c}_l^B = t)$ into the (8.7) and solve it for the $\tilde{c}_l^B = t$.

The resulting equation for the $\tilde{c}_l^B = t$ has two roots. The analytical expressions were found using Maple V symbolical algebraic software package [Maplesoft05, Char93]. One of the roots is negative, thus has to be discarded as not satisfying the physical conditions. The analytical expressions of the solutions are not shown here due to their excessive length (several pages of text). The Maple V file with the analytical solution can be found on the accompanying CD-ROM.

Appendix C
An Example of Using Thermo-Calc for Obtaining the linearization Parameters

Below is an example of using the Thermo-Calc software package for calculating the necessary piecewise-linear approximation parameters is shown.

As an example we will show how to calculate the linearization parameters for the piecewise-linear approximation of the iron-rich corner of the Fe–C–Cr phase diagram in the neighbourhood of the point with the coordinates $\tilde{c}_l^C = 0.003\frac{kg}{kg}$ and $\tilde{c}_l^{Cr} = 0.15\frac{kg}{kg}$ described in Section 4.3.1. The linearization parameters acquired from the Thermo-Calc as described below are listed in the Table 4.1.

The process of acquiring of the necessary linearization parameters can be divided into three parts: 1) initialisation (loading the necessary databases, starting the POLY module); 2) setting up the parameters of the minimisation problem, and finally 3) the minimisation process and the collection of resulting parameters. Firstly, the command sequence and the meaning of the commands will be explained and secondly, a listing of the user input of these commands and Thermo-Calc output will be presented.

Initialisation

After starting Thermo-Calc, we issue the following command in order to select the appropriate database (PTERN) of ternary alloys:

```
go data
```

followed by

```
switch ptern
```

in order to switch to the PTERN database which contains the necessary information for making equilibrium calculations with the ternary system Fe–C–Cr.

Now we select the elements iron, chromium and carbon of the ternary alloy with the following command

```
define-system fe c cr
```

Since the solidification process modelled are not an equilibrium one, the graphite phase has to be rejected with the command

```
TDB_PTERN:reject-phases
PHASES:graphite
```

Now in order to load the necessary data from the database, the following command is issued

```
get
```

After Thermo-Calc has loaded the data, it is necessary to start the POLY module, using which the equilibrium point will be calculated. This is done by issuing the command

```
go poly_3
```

Now Thermo-Calc is ready for setting up the parameters of the minimisation problem for finding the equilibrium point.

Conditions setup for the equilibrium calculation

The next step is to set up the conditions for the calculation of the equilibrium point. With the following commands the composition of the alloy is entered

```
POLY_3:set-condition w(cr)=0.15
POLY_3:set-condition w(c)=0.003
```

The liquid phase has to be fixed, meaning that the equilibrium calculation process has to go on as long as the liquid phase is present in the system. This is achieved by issuing

```
POLY_3:change-status
For phases, species or components? /PHASES/:
Phase name(s):liquid
Status: /ENTERED/: fixed
Number of moles /0/: 1
```

The pressure is atmospheric and is entered to the POLY_3 module with

```
POLY_3:set-condition p=101325
```

The total number of material is taken as 1 mole

```
POLY_3:set-condition n=1
```

Now it is possible to list all of the entered conditions. Note that the degree of freedom that Thermo-Calc indicates (among other parameters) as a response to this command must zero, since is a necessary condition for the solver to start the equilibrium calculation(see the Thermo-Calc output below):

```
POLY_3:list-conditions
```

Equilibrium point computation and data collection

Now when all of the necessary conditions are entered, it is possible to calculate the equilibrium point with the command

```
POLY_3:calculate-equilibrium
```

The computation usually takes not longer that 1 s and the necessary linearization data can be acquired with the commands listed below. Note that all of the linearization parameters are calculated at the linearization point with the coordinates $\tilde{c}_l^C = 0.003\frac{kg}{kg}$ and $\tilde{c}_l^{Cr} = 0.15\frac{kg}{kg}$.

Temperature of the equilibrium point can be shown with

```
POLY_3:show-value t
```

The concentration of carbon and chromium in the solid phase is shown with

```
POLY_3:show-value w(bcc_a2,c)
POLY_3:s-value w(bcc_a2,cr)
```

In order to get the derivative of the temperature at the linearization point with respect to the liquid mass fractions of carbon and chromium the following commands can be used:

```
POLY_3:s-v t.w(c)
POLY_3:s-v t.w(cr)
```

The derivatives of the mass fractions of carbon and chromium in the solid phase at the linearization point with respect to the liquid mass fractions of the carbon and chromium the following commands are used

```
POLY_3:show-value w(bcc_a2,c).w(c)
POLY_3:show-value w(bcc_a2,c).w(cr)
POLY_3:show-value w(bcc_a2,cr).w(c)
POLY_3:show-value w(bcc_a2,cr).w(cr)
```

The resulting Thermo-Calc output listing, together with the user input (shown in italics) is shown below. Note that here shortcut of the Thermo-Calc commands are used, which make using the its command-line interface easier.

```
Thermo-Calc version R on WinNT  Copyright (1993,2006)
Foundation for Computational    Thermodynamics,Stockholm, Sweden
Double precision version linked at Thu Sep 14 09:22:37
```

```
SYS:go data
THERMODYNAMIC DATABASE module running on PC/WINDOWS NT
Current database: SGTE Unary (Pure Elements) TDB v4
VA                        /-  DEFINED
TDB_PURE4:sw ptern
Current database: TCS Public Ternary Alloys TDB v1
VA                        /-  DEFINED
TDB_PTERN:def-sys fe c cr
FE                        C                         CR
DEFINED
TDB_PTERN:reject-phases
PHASES:graphite
GRAPHITE  REJECTED
TDB_PTERN:get
REINITIATING GES5 .....
ELEMENTS .....
SPECIES ......
PHASES .......
PARAMETERS ...
FUNCTIONS ....
 List of references for assessed data
 The list of references can be obtained in the Gibbs Energy System also
 by the command LIST_DATA and option R
 -OK-
TDB_PTERN:go p_3
 POLY version  3.32,  Aug 2001
POLY_3:s-c w(cr)=0.15
POLY_3:s-c w(c)=0.003
POLY_3:c-s
For phases, species or components? /PHASES/:
Phase name(s):liquid
Status: /ENTERED/: fixed
Number of moles /0/: 1
POLY_3:s-c p=101325
```

```
POLY_3:s-c n=1
POLY_3:l-c
W(CR)=0.15, W(C)=3E-3, P=1.01325E5, N=1
FIXED PHASES
LIQUID=1
DEGREES OF FREEDOM 0
POLY_3:c-e
Normal POLY minimization, not global
Testing POLY result by global minimization procedure
Calculated        67904  grid points in            0  s
70 ITS,  CPU TIME USED   0 SECONDS
POLY_3:s-v t
T=1759.7046
POLY_3:s-v w(bcc_a2,c)
W(BCC_A2,C)=4.8618639E-4
POLY_3:s-v w(bcc_a2,cr)
W(BCC_A2,CR)=0.14207627
POLY_3:s-v t.w(c)
T.W(C)=-9198.5831
POLY_3:s-v t.w(cr)
T.W(CR)=-76.214187
POLY_3:s-v w(bcc_a2,c).w(c)
W(BCC_A2,C).W(C)=0.15106564
POLY_3:s-v w(bcc_a2,c).w(cr)
W(BCC_A2,C).W(CR)=-5.2915106E-4
POLY_3:s-v w(bcc_a2,cr).w(c)
W(BCC_A2,CR).W(C)=-2.2273607
POLY_3:s-v w(bcc_a2,cr).w(cr)
W(BCC_A2,CR).W(CR)=1.0438801
POLY_3:
```

alternatively one can use the *list-equilibrium*command for printing most of these values, but the precision of the displayed numbers is lower in this case.

Appendix D
Construction and use of spline-interpolants of thermodynamic functions of in the ternary Fe–C–Cr phase diagram using Thermo-Calc

In order to perform a spline interpolation of the three thermodynamic functions (liquidus temperature, solubility of carbon in the solid phase, solubility of chromium in the solid phase) necessary for the solidification simulations a prior tabulation of these functions is required. In the work presented, the thermodynamics software package Thermo-Calc was used. This section explains how it was used to perform these tabulations and describes the necessary preparation steps for using spline interpolated thermodynamic functions mentioned in simulations at the example of Fe–C–Cr system.

The process of getting the spline interpolations for the thermodynamic functions mentioned can be divided into the following steps: 1) tabulation of the values of the thermodynamic functions into a text file; 2) initialisation of the spline interpolations for the thermodynamic functions and 3) evaluation of the spline interpolations constructed in the Step 2. These necessary steps are described below.

Tabulation of the phase diagram data using the Thermo-Calc software package

The tabulation of the mentioned three thermodynamic functions into a text file is done using a program written using the C programming language and Thermo-Calc C API for calling the necessary Thermo-Calc functions. The calling sequence of the program code in principle repeats the sequence presented in Appendix 8.3, with one exception: the parameters which we called "linearization parameters" are calculated in $N \cdot M$ points in the domain of interest D and not just in one point, as it is described in Appendix 8.3

$$D = \left\{ \left(\tilde{c}_l^A, \tilde{c}_l^B \right) \mid 0 \leq \tilde{c}_l^A \leq a,\ 0 \leq \tilde{c}_l^B \leq b \right\}. \tag{8.13}$$

Numbers N and M are the numbers of tabulation points along the $\tilde{c}_l^A$ and $\tilde{c}_l^B$ directions respectively. In order to start the tabulation, the user has to edit the source code to specify these 4 parameters, namely the grid numbers N and M as well as a and b. Below the parts of the source code (`tabulation.c`) are shown, the parts needing editing are shown in italics.

```
int main() {
    int N = 175; /* number of nodes along the Cr direction */
    int M = 175; /* number of nodes along the C direction */
    double L_c_l_a = 0.4; /* tabulation range for Cr */
    double L_c_l_b = 0.03; /*tabulation range for C */
    /* the code continues here */
```

The following function is called from within `main()` and initialises the Thermo-Calc kernel by means of its C API:

```
static int prepare_tc() {
    /* Initialise the system */
    tc_init_root(); check_tc_error();
    /* Open database */
    tc_open_database("PTERN"); check_tc_error();
    /* Select the elements */
```

```
    tc_element_select("FE"); check_tc_error();
    tc_element_select("CR"); check_tc_error();
    tc_element_select("C"); check_tc_error();
    /* reject Graphite here */
    tc_phase_reject("GRAPHITE");
    /* Get the data from the database */
    tc_get_data(); check_tc_error();
    /* corresponds to the command: s-c n=1 - A.I. */
    tc_set_condition("N", 1.0); check_tc_error();
    /* corresponds to the command: s-c p=101325 - A.I. */
    tc_set_condition("P", 101325.0); check_tc_error();
    /* Calculate the liquidus by setting the liquid to be fixed
    with a certain amount */
    /* corresponds to the command: c-s liquid fixed 1 - A.I. */
    tc_set_phase_status("LIQUID", "FIXED", 1.0); check_tc_error();
    return 0;
}
```

Note that this command sequence is the same as the one described in Appendix 8.3, the only difference is that these commands are executed by means of the Thermo-Calc C API.

After compilation the program is ready to run. in the case of $N = 175$, $M = 175$ for the example shown the tabulation time was approximately 21 hour on a computer with using a Intel Pentium 4 3.2 GHz CPU with 1 GB RAM.

The result of tabulation is saved in a text file using the following line

```
fprintf(fp, "%40.30e %40.30e %40.30e %40.30e %40.30e %40.30e
%40.30e %40.30e %40.30e %40.30e %40.30e %40.30e\n",
state.liquidus_temperature,
state.c_s_carbon,
state.c_s_chromium,
state.liquidus_temperature_d_c_l_carbon,
state.liquidus_temperature_d_c_l_chromium,
state.c_s_carbon_d_c_l_carbon,
```

```
state.c_s_carbon_d_c_l_chromium,
state.c_s_chromium_d_c_l_carbon,
state.c_s_chromium_d_c_l_chromium,
d2t, d2a, d2b);
```

The resulting file thus contains of 12 columns: $\tilde{T}_l$, $\tilde{c}_s^{\mathrm{C}}$, $\tilde{c}_s^{\mathrm{Cr}}$, $\partial\tilde{T}_l/\partial\tilde{c}_l^{\mathrm{C}}$, $\partial\tilde{T}_l/\partial\tilde{c}_l^{\mathrm{Cr}}$, $\partial\tilde{c}_s^{\mathrm{C}}/\partial\tilde{c}_l^{\mathrm{C}}$, $\partial\tilde{c}_s^{\mathrm{C}}/\partial\tilde{c}_l^{\mathrm{Cr}}$, $\partial\tilde{c}_s^{\mathrm{Cr}}/\partial\tilde{c}_l^{\mathrm{C}}$, $\partial\tilde{c}_s^{\mathrm{Cr}}/\partial\tilde{c}_l^{\mathrm{Cr}}$, $\partial^2\tilde{T}_l/\left(\partial\tilde{c}_l^{\mathrm{C}}\partial\tilde{c}_l^{\mathrm{Cr}}\right)$, $\partial^2\tilde{c}_s^{\mathrm{C}}/\left(\partial\tilde{c}_l^{\mathrm{C}}\partial\tilde{c}_l^{\mathrm{Cr}}\right)$ and $\partial^2\tilde{c}_s^{\mathrm{Cr}}/\left(\partial\tilde{c}_l^{\mathrm{C}}\partial\tilde{c}_l^{\mathrm{Cr}}\right)$. Each line corresponds to one of the $N \cdot M$ tabulation points.

Initialisation of the spline interpolants when using FLUENT

The text file produced by the tabulation code has to be placed to the same directory with the FLUENT case file to be used for the simulation. The spline structures are allocated in memory dynamically. There are three of them used in the UDF-code. Below their declarations in the source file `sisl_aux_console.c` are shown

```
static SISLSurf* surf_temperature = NULL;
static SISLSurf* surf_c_s_a = NULL;
static SISLSurf* surf_c_s_b = NULL;
```

The first pointer corresponds to the liquidus temperature, and the other two to the solubilities of the first and second alloying element in the solid phase respectively. If at the moment of calling to the spline-interpolant evaluation function a pointer to one of the three spline objects is null, it is initialised using the data from the text file produced by the tabulation program. Firstly, the data from the text file is read into 12 one-dimensional arrays of double precision float numbers that correspond to the 12 columns of data in the file. These arrays are then used by the SISL function `s1535` for initialising the spline interpolants. For the programming purposes the call to the `s1535` function is wrapped with a function called initialise which is shown below.

```
void initialize(double *points, double *da,
double *db, double *dadb, SISLSurf **f,
```

```
int *jstat)
{
    int i;
    double par1[nodes_num],
    par2[nodes_num];
    for (i=0; i < nodes_num; i++)
    {
        par1[i] = (double) (l_c_l_a / (nodes_num-1) * i);
        par2[i] = (double) (l_c_l_b / (nodes_num-1) * i);
    };
    s1535(points, /* pointer to the array of points to interpolate */
          db, da, dadb, /* 1st and cross derivatives of the function */
          nodes_num, /* number of interpolating points
                        along the 'u' parameter */
          nodes_num, /* number of interpolating points
                        along the 'v' parameter */
          3, /* dimension of the Euclidean space */
          par1, par2, /* parametrisation along both directions */
          0, /* no additional condition along edge 1 */
          0, /* no additional condition along edge 2 */
          0, /* no additional condition along edge 3 */
          0, /* no additional condition along edge 4 */
          4, /* the order of the generated surface
                in the 'u' parameter */
          4, /* the order of the generated surface
                in the 'v' parameter */
          1, /* open surface in the u direction */
          1, /* open surface in the v direction */
          f, /* the generated surface */
          jstat); /* status variable */
}
```

For the details on the parameters of the function `s1525` see the SISL library documentation [SIN06, SIN05]. The solution of the system of nonlinear equations that couples together solidification thermodynamics, kinetics and Eulerian mul-

tiphase flow model that is described above in Section 3.4 and given by Eq. (3.22) is done by a Newton-type method as described in (4.2). During its iterations, the Newton-type method needs evaluating the right-hand side of the equation system (3.22), which includes the evaluation of spline-interpolated functions (3.15)–(3.17) and their derivatives. This is done in the code by calling the `s1527` function of the SISL library. Below a function for evaluating the right hand side of the nonlinear equation system is shown

```
int my_f (const gsl_vector * x, void *params, gsl_vector * f) {
    real c_l_a = ((struct my_f_params *) params)->c_l_a;
    real c_l_b = ((struct my_f_params *) params)->c_l_b;
    real temperature = ((struct my_f_params *) params)->temperature;
    const real x0 = gsl_vector_get (x, 0); /*c_l_a_star*/
    const real x1 = gsl_vector_get (x, 1); /*c_l_b_star*/
    const real x2 = gsl_vector_get (x, 2); /*c_s_a_star*/
    const real x3 = gsl_vector_get (x, 3); /*c_s_b_star*/
    const real r=get_diff_ratio();
    real y0;
    real y1;
    real y2;
    real y3;
    real retv[9] = {0.0, 0.0, 0.0, 0.0, 0.0, 0.0, 0.0, 0.0, 0.0};
    calculate_stars(x0,x1,retv);
    y0 = retv[0] - x2;
    y1 = retv[1] - x3;
    y2 = retv[2] - temperature;
    y3 = r*(x0-c_l_a)/(x0-x2)-(x1-c_l_b)/(x1-x3);
    gsl_vector_set (f, 0, y0);
    gsl_vector_set (f, 1, y1);
    gsl_vector_set (f, 2, y2);
    gsl_vector_set (f, 3, y3);
    return GSL_SUCCESS; }
```

The spline interpolants for the thermodynamic functions are evaluated in the function `calculate_stars`. As input parameters this function gets numbers `x0`

and `x0` which are the mass fractions of the first and the second alloying elements respectively. The resulting 9 numbers consisting of the values of the three thermodynamic functions and its derivatives are stored in the array `retv`. These values are then used for calculating the the variables `y0`, `y1`, `y2`, `y3` which are the components of the right-hand side of the nonlinear equation system. Note that the values of the variables `x0`, `x1`, `x2`, and `x3` are determined by the Newton-type method and change from Newton iteration to Newton iteration.

As one can see, the process of evaluating the right-hand side of the nonlinear equation system using the spline-interpolant evaluation for the three thermodynamic functions is done as follows:

$$\begin{aligned} y_0 &= \tilde{c}_s^A(x_0, x_1) - x_2, \\ y_1 &= \tilde{c}_s^B(x_0, x_1) - x_3, \\ y_2 &= \tilde{T}(x_0, x_1) - T_l, \\ y_3 &= r\frac{x_0 - c_l^A}{x_0 - x_2} - \frac{x_1 - c_l^B}{x_1 - x_3}. \end{aligned} \tag{8.14}$$

Note that here $x_0 = \tilde{c}_l^A$, $x_1 = \tilde{c}_l^A$, $x_2 = \tilde{c}_s^A$ and $x_3 = \tilde{c}_s^B$ are unknowns; T_l, c_l^A and $c_l^B$are known parameters of the bulk melt, available from FLUENT; $\tilde{c}_s^A(x_0, x_1)$, $\tilde{c}_s^B(x_0, x_1)$ and $\tilde{T}(x_0, x_1)$ are thermodynamic functions (solubilities in solid and liquidus temperature) evaluated using spline interpolation of tabulated values of these functions; r is the ratio between the diffusion coefficients of alloying elements in liquid, $r = \frac{D_l^A}{D_l^B}$.

The source code of the tabulation software is provided on the accompanying CD-ROM.

Nomenclature

β_T	thermal expansion coefficient of the liquid phase
ΔT	constitutional undercooling
ΔT_σ	standard deviation of the normal distribution of the nucleation law
ΔT_N	mean of the normal distribution of the nucleation law
ϵ_{rel}	vector of relative errors
κ	constant cooling rate
λ_1	primary dendrite arm spacing
μ_e	viscosity of the equiaxed phase
μ_l	viscosity of the liquid phase
ρ_c	density of the columnar phase
ρ_e	density of the equiaxed phase
$\rho_{l,\text{ref}}$	reference density of the liquid phase
ρ_l	density of the liquid phase
$\tilde{c}_c^A$	columnar equilibrium mass fraction of the element A at the solid–liquid interface
$\tilde{c}_c^i$	columnar equilibrium mass fraction of the i-th element at the solid–liquid phase interface
$\tilde{c}_e^A$	equiaxed equilibrium mass fraction of the element A at the solid–liquid interface

$\tilde{c}_e^i$ equiaxed equilibrium mass fraction of the i-th element at the solid–liquid phase interface

$\tilde{c}_l^A$ liquid equilibrium mass fraction of the element A at the solid–liquid interface

$\tilde{c}_l^i$ liquid equilibrium mass fraction of the i-th element at the solid–liquid interface

$\tilde{T}$ equilibrium temperature at the solid–liquid interface

$\vec{g}$ gravitational acceleration vector

$\vec{u}_c$ velocity of the columnar phase

$\vec{u}_e$ velocity of the equiaxed phase

$\vec{u}_l$ velocity of the liquid phase

A area

A_{cell} area of a hexagonal cell

$A_{\text{imp},c}$ impingement factor for columnar growth

C number of components

c_0 initial mass fraction of the alloying element in the binary case

c_{mix}^m mixture mass fraction of the m-th component

c_{ref}^k reference mass fraction of the k-th element in the liquid phase

c_{l0}^{Cr} initial concentration of chromium

c_{l0}^{C} initial concentration of carbon

C_{lc}^i i-th species transfer rate from the liquid phase to the columnar phase

c_l^i bulk liquid mass fraction of the i-th component

c_l^k mass fraction of the k-th element in the liquid phase

$c_{p(l)}$ isochoric heat capacity of the liquid phase

$c_{p(s)}$ isochoric heat capacity of a solid phase (columnar or equiaxed)

d_c diameter of a columnar dendrite

D_l^A diffusion coefficient of the element A in the liquid phase

f number of degrees of freedom

f_c volume fraction of the columnar phase

f_l volume fraction of the liquid phase

f_e volume fraction of the equiaxed phase

$f_{i,\text{exact}}$ exact value of a function f in the i-th coordinate node

$f_{i,\text{interpolated}}$ interpolated value of a function f in the i-th coordinate node

$f_{l,\text{crit}}$ critical volume fraction of the liquid phase

f_s volume fraction of the solid phase

H^* volumetric transfer coefficient

h_c enthalpy of the columnar phase

h_c^{ref} standard state enthalpy for the columnar phase

h_e enthalpy of the equiaxed phase

h_e^{ref} standard state enthalpy for the equiaxed phase

h_l enthalpy of the liquid phase

h_l^{ref} standard state enthalpy for the liquid phase

J jacobian

$J_{F,y}$ Jacobian with derivatives of F with respect to the independent variables subset y

k binary solute redistribution coefficient

k_c thermal conductivity of the columnar phase

K_{ec} drag coefficient characterizing the drag force between the equiaxed and the columnar phase

k_e thermal conductivity of the equiaxed phase

K_{lc} drag coefficient characterizing the drag force between the liquid and the columnar phase

K_{le} drag coefficient characterizing the drag force between the liquid and the equiaxed phase

k_l thermal conductivity of the liquid phase

m_{rej} mass of the component rejected into the liquid phase

M_{ce} mass transfer rate from columnar phase to the equiaxed phase

M_{lc} mass transfer rate from liquid phase to the columnar phase

M_{le} mass transfer rate from liquid phase to the equiaxed phase

N total number of components

n equiaxed grain density

n_{max} maximal equiaxed grain density

p dynamic pressure

q_{diff} diffusive flux of a solute component in the liquid phase

q_{rej} flux of the component rejected into the liquid phase

q_i^j number of molecules of the component i leaving the phase j per unit surface per unit time

R columnar radius

r radial axis

r ratio between diffusion coefficients of alloying components in the liquid phase in a ternary system

$R_{\max}$ maximal columnar radius

S_c surface concentration (total surface area of all growing columnar dendrites per unit volume)

T temperature

T_0 initial temperature

T_{ref} reference temperature of the liquid phase

T_l temperature of the liquid phase

v solidification growth velocity

v^i growth velocity calculated using concentrations of the i-th alloying component

v_c columnar solidification growth velocity

v_e equiaxed solidification growth velocity

Bibliography

|Aldrich99| **Aldrich**, M.: "The Peril of the Broken Rail": The Carriers, the Steel Companies, and Rail Technology, 1900-1945. *Technology and Culture* (1999) vol. 40 (2), pp. 263–291.

|Andersson02| **Andersson**, J. O., **Helander**, T., **Höglund**, L., **Shi**, P., **Sundman**, B.: Thermo-Calc & DICTRA, Computational Tools for Materials Science. *Calphad* (2002) vol. 26, pp. 273–312.

|Appolaire08| **Appolaire**, B., **Combeau**, H., **Lesoult**, G.: Modeling of equiaxed growth in multicomponent alloys accounting for convection and for the globular/dendritic morphological transition. *Materials Science and Engineering A* (2008) vol. 487 (1-2), pp. 33–45.

|Assar92| **Assar**, A.-w. M.: On the interfacial heat transfer coefficient for cylindrical ingot casting. *Journal of Materials Science Letters* (1992) vol. 11, pp. 601–606.

|Avrami40| **Avrami**, M.: *J. Chem. Phys.* (1940) vol. 8, p. 212.

|Beckermann88| **Beckermann**, C., **Viskanta**, R.: Natural Convection Solid/Liquid Phase Change in Porous Media. *International Journal of Heat and Mass Transfer* (1988) vol. 31, pp. 35–46.

|Beckermann93| **Beckermann**, C., **Viskanta**, R.: Mathematical Mod-

elling of Transport Phenomena During Alloy Solidification. *Applied Mechanics Reviews* (1993) vol. 46, pp. 1–27.

|Beckermann97| **Beckermann**, C.: Modeling Segregation and Grain Structure Development in Equiaxed Solidification with Convection. *JOM* (1997) vol. 49 (3), pp. 13–17.

|Bennon87| **Bennon**, W. D., **Incopera**, F. P.: Continuum model for momentum, heat and species transport in binary solid-liquid phase change systems - I. Model. *International Journal of Heat and Mass Transfer* (1987) vol. 30, pp. 2161–2170.

|Bird60| **Bird**, R. B., **Stewart**, W. E., **Lightfoot**, E. N.: Transport Phenomena, John Wiley & Sons (1960).

|Blondeau91| **Blondeau**, R.: Problems related to use of low alloy steels in H_2S environment: industrial solutions. *Ironmaking and Steelmaking* (1991) vol. 18 (3), pp. 201–210.

|Brennen05| **Brennen**, C. E.: Fundamentals of Multiphase Flow, Cambridge University Press (2005).

|Broyden65| **Broyden**, C.: A Class of Methods for Solving Nonlinear Simultaneous Equations. *Mathematics of Computation* (1965) vol. 19, pp. 577–593.

|Campbell03| **Campbell**, J.: Solidification Structure - Heat Transfer, Butterworth-Heinemann, chap. 5.1 (2003) pp. 117–129.

|Char93| **Char**, B. W., **Geddes**, K. O., **Gonnet**, G. H., **Leong**, B. L., **Monagan**, M. B., **Watt**, S. M.: Maple V Language Reference Manual, Springer, 3rd edn. (1993).

|Chen05| **Chen**, Q., **Engström**, A., **Höglund**, L., **Strandlund**, H., **Sundman**, B.: Thermo-calc program interfaces and their applications - Direct insertion of thermodynamic and kinetic data into modeling of materials processing,

structure, and property. *Materials Science Forum* (2005) vol. 475-479, pp. 3145–3148.

|Chuang75| **Chuang**, Y.-K., **Schwerdtfeger**, K.: Equations for the Calculation of Gravity Segregation in Killed Steel. |ANSAETZE ZUR BERECHNUNG DER SCHWERE-SEIGERUNG VON BERUHIGTEM STAHL.|. *Arch. Eisenhuettenwes.* (1975) vol. 46 (5), pp. 303–310.

|Ciobanas07a| **Ciobanas**, A. I., **Fautrelle**, Y.: Ensemble averaged multiphase Eulerian model for columnar/equiaxed solidification of a binary alloy: I. The mathematical model. *Journal of Physics D: Applied Physics* (2007) vol. 40, pp. 3733–3762.

|Ciobanas07b| **Ciobanas**, A. I., **Fautrelle**, Y.: Ensemble averaged multiphase Eulerian model for columnar/equiaxed solidification of a binary alloy: II. Simulation of the columnar-to-equiaxed transition (CET). *Journal of Physics D: Applied Physics* (2007) vol. 40, pp. 4310–4336.

|Combeau96| **Combeau**, H., **Drezet**, J. M., **Mo**, A., **Rappaz**, M.: Modelling of microsegregation in macrosegregation computations. *Metallurgical and Materials Transactions A* (1996) vol. 27 A, pp. 2314–2327.

|Davis94| **Davis**, J. R. (ed.): ASM Specialty Handbook: Stainless Steels, ASM International (1994).

|DeBoor94| **DeBoor**, C.: A Practical Guide to Splines, Springer Verlag (1994).

|denHartog75| **den Hartog**, H. W., **Rabenberg**, J. M., **Pesch**, R.: Models for Macrosegregation in Rimmed and Semikilled Steel Ingots. Mathematical Process Models in Iron and Steelmaking. *Met. Soc. Book* (1975) vol. 158, pp. 200–212.

|Devillers88| **Devillers**, L., **Kaplan**, D., **Jansen**, J. P.: H. A. Z. Toughness: Metallurgical and Mechanical Points of View. |ASPECTS METALLURGIQUES ET MECANIQUES DE LA TENACITE DES ZONES AFFECTEES PAR LA CHALEUR.|. *Revue de Metallurgie. Cahiers D'Informations Techniques* (1988) vol. 85 (3), pp. 267–282.

|Doré00| **Doré**, X., **Combeau**, H., **Rappaz**, M.: Modelling of microsegregation in ternary alloys: Application to the solidification of Al-Mg-Si. *Acta Materialia* (2000) vol. 48 (15), pp. 3951–3962.

|Du07| **Du**, Q., **Eskin**, D. G., **Katgerman**, L.: Modeling Macrosegregation during direct-chill casting of multicomponent aluminium alloys. *Metallurgical and Materials Transactions A: Physical Metallurgy and Materials Science* (2007) vol. 38 (1), pp. 180–189.

|DuPont06| **DuPont**, J. N.: Mathematical Modeling of Solidification Paths in Ternary alloys: Limiting Cases of Solute Redistribution. *Metallurgical and Materials Transactions A* (2006) vol. 37 A, pp. 1937–1947.

|Ebneth74| **Ebneth**, G., **Haumann**, W., **Ruettiger**, K., **Oeters**, F.: Investigations of Solidification in the Core of Killed Steel Ingots. |UNTERSUCHUNGEN UEBER DIE ERSTARRUNG IM KERN BERUHIGTER STAHLBLOECKE.|. *Arch. Eisenhuettenwes.* (1974) vol. 45 (6), pp. 353–359.

|El-Mahallawy88| **El-Mahallawy**, N. A., **Assar**, A.-w. M.: Metal–Mould heat transfer coefficient using end-chill experiments. *Journal of Materials Science Letters* (1988) vol. 7, pp. 205–208.

|Eriksson71| **Eriksson**, G.: Thermodynamic Studies of High Temperature Equilibria. *Acta Chem. Scand.* (1971) vol. 25, pp. 2651–2658.

|Eriksson90| **Eriksson**, G., **Hack**, K.: ChemSage - a Computer Program for the Calculation of Complex Chemical Equilibria. *Metallurgical Trans. B* (1990) vol. 21B, pp. 1013–1023.

|Ersayin05| **Ersayin**, S.: A Purpose Oriented Magnetic Separator: Skimmer, Tech. Rep. DE-FG26-03NT41933, University of Minnesota Duluth, Natural Resources Research Institute, Coleraine Minerals Research Laboratory, PO Box 188, One Gayley Avenue, Coleraine, Minnesota 55722, USA (2005).

|Felicelli98| **Felicelli**, S. D., **Heinrich**, J. C., **Poirier**, D. R.: Finite element analysis of directional solidification of multicomponent alloys. *International Journal for Numerical Methods in Fluids* (1998) vol. 27 (1-4), pp. 207–227.

|Feng03| **Feng**, Y. H., **Zhang**, X. X., **Xu**, Z. B., **Wang**, X. H.: Mathematical model for turbulent flow, heat transfer, and solidification. *Heat Transfer – Asian Research* (2003) vol. 32 (7), pp. 582–592.

|Fjeld08a| **Fjeld**, A., **Ludwig**, A.: Flow Patterns and Re-melting During the Filling of a Large Composite Casting. *International Journal of Cast Metals Research* (2008) , pp. 111–114.

|Fjeld08b| **Fjeld**, A., **Ludwig**, A.: Modeling and Simulation of a Large Composite Casting, in EPD Congress 2008 Proceedings, The Minerals, Metals, and Materials Society, pp. 281–292.

|Flemings76| **Flemings**, M. C.: PRINCIPLES OF CONTROL OF SOUNDNESS AND HOMOGENEITY OF LARGE

INGOTS. *Scandinavian Journal of Metallurgy* (1976) vol. 5 (1), pp. 1–15.

|FLU01| FLUENT 6.0 User's Guide, FLUENT Inc. (2001).

|FLU06| FLUENT 6.3 UDF Manual, FLUENT Inc. (2006).

|forMetals93| **for Metals**, A. S.: ASM Metals Reference Book, ASM International (1993).

|Fredriksson78| **Fredriksson**, H., **Nilsson**, S. O.: ON THE FORMATION OF MACROSEGREGATIONS IN INGOTS. *Metallurgical and Materials Transactions B* (1978) vol. 9 B (1), pp. 111–120.

|Galassi01| **Galassi**, M., **Davies**, J., **Theiler**, J., **Gough**, B., **Jungman**, G., **Booth**, M., **Rossi**, F.: GNU Scientific Library Reference Manual, Network Theory Ltd. (2001), also available from `http://www.gnu.org/software/gsl`.

|Ganguly07| **Ganguly**, S., **Chakraborty**, S.: A generalized enthalpy-based macro model for ternary alloy solidification simulations. *Numerical Heat Transfer, Part B: Fundamentals* (2007) vol. 51 (3), pp. 293–313.

|Gramlich00| **Gramlich**, G., **Werner**, W.: Numerische Mathematik mit MATLAB, dpunkt.verlag GmbH (2000).

|Grasser08| **Grasser**, M., **Mayer**, F., **Ishmurzin**, A., **Könözsy**, L., **Ludwig**, A.: Numerical modeling of the effect of global transport phenomena on the microstructure formation. *Berg- und Hüttenmännische Monatshefte* (2008) vol. 153 (7), pp. 253–256, submitted.

|Gray56| **Gray**, B.: *J. Iron Steel Inst.* (1956) vol. 182, pp. 366–374.

|Gruber-Pretzler06| **Gruber-Pretzler**, M., **Mayer**, F., **Wu**, M., **Ludwig**, A., **Kuhn**, A., **Riedle**, J.: Modelling of Macrosegregations in DC Casting of Bronze, in 11th Modeling of

Casting, Welding and Advanced Solidification Processes (McWASP XI), Opio, France, pp. 799–806.

|Gruber-Pretzler07a| **Gruber-Pretzler**, M., **Könözsy**, L., **Wu**, M., **Ludwig**, A., **Mathiesen**, R. H., **Schaffer**, P., **Arnberg**, L.: Numerical Study of the Impact of Gravity and Maragoni Force on the Droplet Distribution of Hypermonotectic AlBi Alloys, in Proceedings of the 5th Decennial International Conference on Solidification Processing (SP07), July 23-25, 2007, Sheffield, UK., ed. H. Jones, Tj international Ltd, pp. 249–253.

|Gruber-Pretzler07b| **Gruber-Pretzler**, M., **Mayer**, F., **Wu**, M., **Ludwig**, A., **Riedle**, J., **U.**, H.: Macrosegregation in Continuous Casting of Phosphorus Bronze Impact on Properties and Modeling of Formation, in Proceedings of COM/Cu2007, Toronto, Canada, vol. 1, pp. 265–279.

|Gruber-Pretzler08| **Gruber-Pretzler**, M.: A Study on Macrosegregation in Continuous Casting of Bronze, Ph.D. thesis, University of Leoben (2008).

|Grupp04| **Grupp**, F., **Grupp**, F.: Matlab 7 für Ingenieure, Oldenbourg Verlag (2004).

|Gu99| **Gu**, J. P., **Beckermann**, C.: Simulation of Convection and Macrosegregation in a Large Steel Ingot. *Metallurgical and Materials Transactions* (1999) vol. 30A, pp. 1357–1366.

|Gulliver13| **Gulliver**, G. H.: The Quantitative Effect of Rapid Cooling upon the Constitution of Binary Alloys. *Journal of the Institute of Metals* (1913) vol. 9, pp. 120–157.

|Gulliver22| **Gulliver**, G. H.: Metallic Alloys, Griffin, London (1922).

|Han07| **Han**, Z. Q., **Lewis**, R. W., **Liu**, B. C.: Modelling of the thermosolutal convection and macrosegregation in the solidification of an Fe-C binary alloy. *International Journal*

of Numerical Methods for Heat and Fluid Flow (2007) vol. 17 (3), pp. 313–321.

|Hardin99| **Hardin**, R. A., **Beckermann**, C.: Heat transfer and solidification modeling in the continuous casting of multicomponent steels. *American Society of Mechanical Engineers, Heat Transfer Division, (Publication) HTD 347* (1999) , pp. 9–25.

|Hillert99| **Hillert**, M., **Höglund**, L., **Schalin**, M.: Role of backdiffusion studied by computer simulation. *Metallurgical and Material Transactions A: Physical Metallurgy and Materials Science* (1999) vol. 30 (6), pp. 1635–1641.

|Hirt81| **Hirt**, C. W., **Nichols**, B. D.: Volume Of Fluid (VOF) Method for the Dynamics of Free Boundaries. *J. Comput. Phys.* (1981) vol. 39 (1), pp. 201–225.

|Hultgren29| **Hultgren**, A.: *Journal of the Iron and Steel Institute* (1929) vol. 120, pp. 69–125.

|Hultgren73| **Hultgren**, A.: A AND V SEGREGATION IN KILLED STEEL INGOTS. *Scandinavian Journal of Metallurgy* (1973) vol. 2 (5), pp. 217–227.

|Iida93| **Iida**, T., **Guthrie**, R. I. L.: The Physical Properties of Liquid Metals, Clarendon Press, Oxford, United Kingdom (1993).

|Ishmurzin08| **Ishmurzin**, A., **Gruber-Pretzler**, M., **Mayer**, F., **Wu**, M., **Ludwig**, A.: Multiphase/Multicomponent Modeling of Solidification Processes: Coupling Solidification Kinetics with Thermodynamics. *International Journal of Materials Research* (2008) vol. 6, pp. 618–625.

|Javurek05| **Javurek**, M., **Gittler**, P., **Rössler**, R., **Kaufmann**, B., **Preßlinger**, H.: Simulation of Nonmetallic Inlusions in

a Continuous Casting Strand. *steel research int.* (2005) vol. 76 (1), pp. 64–70.

|Jer77| A Guide to Solidification of Steels, Jernkontoret (1977).

|Jie05| **Jie**, W. Q., **Zhang**, R., **He**, Z.: Thermodynamic Description of Multi-Component Multi-Phase Alloys and its Application to the Solidification Process. *Materials Science and Engineering A* (2005) vol. 413-414, pp. 497–503.

|Könözsy07| **Könözsy**, L., **Mayer**, F., **Ishmurzin**, A., **Kharicha**, A., **Wu**, M., **Ludwig**, A., **Tanzer**, R., **Schützenhöfer**, W.: Parameter study on the formation of macrosegragation in a large steel ingot, in 2nd International Conference on Simulation and Modeling of Metallurgical Processes in Steelmaking STEELSIM 2007, Graz, Austria, ed. A. Ludwig, Knittelfeld: Gutenberghaus GmbH, pp. 126–132.

|Könözsy08| **Könözsy**, L.: Results of a parameter study (Columnar-to-Equiaxed Transition) 21 april 2008 Chair for Simulation and Modeling of Metallurgical Processes, University of Leoben (2008), unpublished work.

|Kohn67| **Kohn**, A.: The Solidification of Metals, 110, The Iron and Steel Institure (1967).

|Kolev02| **Kolev**, N.: Multiphase Flow Dynamics 1,2., Springer Berlin (2002).

|Kounchev01| **Kounchev**, O.: Multivariate Polysplines: Applications to Numerical and Wavelet Analysis, Academic Press (2001).

|Kowalski94| **Kowalski**, M., **Spencer**, P. J., **Granat**, K., **Drziniek**, H., **Lugscheider**, E.: Phase Relations in the C-Cr-Fe System in the Vicinity of the /Liquid+bcc+M23C6+M7C3/ Invariant Equilibrium-Experimental Determinations and Thermodynamic Modelling. *Z. Metallkd.* (1994) vol. 85, pp. 359–364.

|Kraft97| **Kraft**, T., **Rettenmayr**, M., **Exner**, H. E.: Modeling of Dendritic Solidification for Optimizing Casting and Microstructure Parameters. *Progress in Materials Science* (1997) vol. 42 (1-4), pp. 277–286.

|Kubícek75| **Kubícek**, P.: HETERODIFFUSION OF CHROMIUM AND COBALT IN LIQUID IRON. *Czechoslovak Journal of Physics* (1975) vol. 25 (5), pp. 535–541.

|Kubícek76| **Kubícek**, P.: HETERODIFFUSION OF Cr IN MOLTEN Fe IN TEMPERATURE RANGE 1800 TO 1970 K. *Czechoslovak Journal of Physics* (1976) vol. 26 (3), pp. 300–305.

|Kundrat84| **Kundrat**, D. M., **Chochol**, M., **Eliott**, J. F.: Phase relationships in the Fe-Cr-C system at solidification temperatures. *Metallurgical Transactions B* (1984) vol. 15 B, pp. 663–676.

|Kurz98| **Kurz**, W., **Fisher**, D. J.: Fundamentals of Solidification, Trans Tech Publications Ltd (1998).

|Kvasov00| **Kvasov**, B. I.: Methods of Shape-Preserving Spline Approximation, World Scientific Publishing Co. Pte. Ltd. (2000).

|Lan60| Landolt-Börnstein Numerical Data in Science and Technology, Group IV: Physical Chemistry, Springer, 6th edn. (1960).

|Larouche07| **Larouche**, D.: Computation of solidification paths in multiphase alloys with back-diffusion. *Calphad* (2007) vol. 31 (4), pp. 490–504.

|Lee92| **Lee**, B.: On The Stability of Cr Carbides. *Calphad: Comput. Coupling Phase Diagrams Thermochem.* (1992) vol. 16, pp. 121–149.

|Lee04| **Lee**, P. D., **Chirazi**, A., **Atwood**, R. C., **Wang**, W.: Multiscale Modelling of Solidification Microstructures, Including Microsegregation and Microporosity, in an Al–Si–Cu Alloy. *Materials Science and Engineering A* (2004) vol. 365, pp. 57–65.

|Lee07| **Lee**, P. D., **Wang**, J. S.: Simulating tortuous 3D morphology of microporosity formed during solidification of Al-Si-Cu alloys. *International Journal of Cast Metals Research* (2007) vol. 20 (3), pp. 151–158.

|Lesoult05| **Lesoult**, G.: Macrosegregation in steel strands and ingots: Characterisation, formation and consequences. *Materials Science and Engineering A* (2005) vol. 413-414, pp. 19–29.

|Ludwig02| **Ludwig**, A., **Wu**, M.: Modeling of Globular Equiaxed Solidification with a Two-Phase Approach. *Metallurgical and Materials Transactions A* (2002) vol. 33A, pp. 3673–3683.

|Ludwig05a| **Ludwig**, A., **Gruber-Pretzler**, M., **Mayer**, F., **Ishmurzin**, A., **Wu**, M.: A Way of Coupling Ternary Phase Diagram Information with Multiphase Solidification Simulations. *Mat. Sci. Eng. A* (2005) vol. 413-414, pp. 485–489.

|Ludwig05b| **Ludwig**, A., **Wu**, M.: Modeling the columnar-to-equiaxed transition with a three phase Eulerian approach. *Material Science and Engineering A* (2005) vol. 413-314, pp. 109–114.

|Ludwig06a| **Ludwig**, A., **Gruber-Pretzler**, M., **Wu**, M., **Kuhn**, A., **Riedle**, J.: About the Formation of Macrosegregations in Continuous Casting of Sn-Bronze. *Fluid Dynamics and Materials Processing* (2006) vol. 1 (4), pp. 285–300.

|Ludwig06b| **Ludwig**, A., **Wu**, M., **Abondano**, L., **Ratke**, L.: Gravity-Induced Convection during Directional Solidification of Hypermonotectic Alloys. *Material Science Forum* (2006) vol. 508-509, pp. 193–198.

|Ludwig07| **Ludwig**, A., **Ishmurzin**, A., **Gruber-Pretzler**, M., **Mayer**, F., **Wu**, M., **Tanzer**, R., **Schützenhöfer**, W.: How To Combine Ternary Phase Diagram Information with Multiphase Solidification Simulations, in Proceedings of the 5th Decenial International Conference on Solidification Processing, Sheffield, UK, pp. 493–496.

|MAG05| MAGMA Giessereitechnologie GmbH, Kackertstrasse 11 D-52072 Aachen Germany: MAGMASOFT 4.2 Manual Parts 1 and 2 (2005).

|Maplesoft05| **Maplesoft**: Maple User Manual, Maplesoft (2005).

|Marthur97| **Marthur**, S. R., **Murthy**, J. Y.: A pressure-based method for unstructured meshes. *Numerical Heat Transfer, Part B: Fundamentals* (1997) vol. 31 (2), pp. 195–215.

|Mayer07| **Mayer**, F., **Gruber-Pretzler**, M., **Könözsy**, L., **Wu**, M., **Ludwig**, A.: Numerical Study of the Shrinkage Flow Induced Macrosegregation in Continuous Casting of Steel, in 2nd International Conference on Simulation and Modeling of Metallurgical Processes in Steelmaking STEELSIM 2007, Graz, Austria, ed. A. Ludwig, Knittelfeld: Gutenberghaus GmbH, pp. 126–132.

|Moré79| **Moré**, J., **Cosnard**, M.: Numerical Solution of Nonlinear Equations. *ACM Transactions on Mathematical Software* (1979) vol. 5 (1), pp. 64–85.

|Moré81| **Moré**, J., **Garbow**, B., **Hillstrom**, K.: Testing Unconstrained Optimization Software. *ACM Transactions on Mathematical Software* (1981) vol. 7 (1), pp. 17–41.

|Nadella08| **Nadella**, R., **Eskin**, D. G., **Du**, Q., **Katgerman**, L.: Macrosegregation in direct-chill casting of aluminium alloys. *Progress in Materials Science* (2008) vol. 53 (3), pp. 421–480.

|Nakai79| **Nakai**, Y., **Kurahashi**, H., **Emi**, T., **Haida**, O.: DEVELOPMENT OF STEELS RESISTANT TO HYDROGEN INDUCED CRACKING IN WET HYDROGEN SULFIDE ENVIRONMENT. *Transactions of the Iron and Steel Institute of Japan* (1979) vol. 19 (7), pp. 401–410.

|Ni91| **Ni**, J., **Beckermann**, C.: A Volume-Averaged Two-Phase Model for Transport Phenomena During Solidification. *Metallurgical and Materials Transactions B* (1991) vol. 22 (3), pp. 349–361.

|Nishida86| **Nishida**, Y., **Droste**, W., **Engler**, S.: The Air-Gap Formation Process at the Casting-Mold Interface and the Heat Transfer Mechanism through the Gap. *Metallurgical Transactions B* (1986) vol. 17B, pp. 833–844.

|Ohnaka86| **Ohnaka**, I.: State of the Art of Computer Simulation of Casting and Solidification Processes, Les Editions de Physique, Vlis, France (1986) pp. 211–223.

|Oldfield66| **Oldfield**, W.: A Quantitative Approach to Casting Solidification: Freezing of Cast Iron. *Transaction of ASM* (1966) vol. 59, pp. 945–961.

|Patankar80| **Patankar**, S. V.: Numerical Heat Transfer and Fluid Flow, Hemisphere Publishing Corporation (1980).

|Pfeiler05| **Pfeiler**, C., **Wu**, M., **Ludwig**, A.: Influence of argon gas bubbles and non-metallic inclusions on the flow behavior in steel continuous casting. *Materials Science & Engineering A* (2005) vol. 413-414, pp. 115–120.

|Pollack88| **Pollack**: Materials Science and Metallurgy, Prentice-Hall, 4th edn. (1988).

|Powell70a| **Powell**, M. J. D.: A Fortran Subroutine for Solving Systems of Nonlinear Algebraic Equations, Gordon and Breach, London, UK, chap. 7 (1970) pp. 115–161.

|Powell70b| **Powell**, M. J. D.: Numerical Methods for Nonlinear Equations, Gordon and Breach, London, UK, chap. A hybrid method for nonlinear equations. (1970) .

|Qiu04| **Qiu**, S., **Liu**, H., **Peng**, S., **Gan**, Y.: Numerical analysis of thermal-driven buoyancy flow in the steady macro-solidification process of a continuous slab caster. *ISIJ International* (2004) vol. 44 (8), pp. 1376–1383.

|Reddy97| **Reddy**, A. V., **Beckermann**, C.: Modeling of macrosegregation due to thermosolutal convection and contraction-driven flow in direct chill continuous casting of an Ai-Cu round ingot. *Metallurgical and Materials Transactions B: Process Metallurgy and Materials Processing Science* (1997) vol. 28 (3), pp. 479–489.

|Rhie83| **Rhie**, C. M., **Chow**, W. L.: Numerical Study of the Turbulent Flow Past an Airfoil with Trailing-Edge Separation. *AIAA Journal* (1983) vol. 21 (11), pp. 1525–1532.

|Richter83| **Richter**, F.: Physikalischen Eigenschaften von Stählen und ihre Temperaturabhängigkeit. *Stahleisen Sonderberichte* (1983) vol. Heft 10.

|Richter91| **Richter**, F.: Die Physikalischen Eigenschaften von Metallischen Werkstoffen". *METALL* (1991) vol. 45 (6), p. 582.

|Rogl07| **Rogl**, P.: Non-Ferrous Metal Systems. Part 3, Springer Berlin Heidelberg, vol. 11C3 of *Landolt-Börnstein–Group IV Physical Chemistry*, chap. Cu–P–Sn (Copper–Phosphorus–Tin) Non-Ferrous Metal Ternary Systems.

Selected Soldering and Brazing Systems: Phase diagrams, Crystallographic and Thermodynamc Data (2007) pp. 355–367.

|Roques60| **Roques**, C., **Martin**, P., **Dubois**, C., **Bastien**, P.: *Rev. Métall.* (1960) vol. 57, pp. 1091–1103.

|Rousset95| **Rousset**, P., **Rappaz**, M., **Hannart**, B.: Modeling of inverse segregation and porosity formation in directionally solidified aluminum alloys. *Metallurgical and Materials Transactions A: Physical Metallurgy and Materials Science* (1995) vol. 26 A (9), pp. 2349–2358.

|Rudin76| **Rudin**, W.: Principles of mathematical analysis, International series in pure and applied mathematics, McGraw-Hill, Inc., 3rd edn. (1976).

|Sahm84| **Sahm**, P. R., **Hansen**, P. N.: Numerical Sumulation and Modelling of Casting and Solidification Processes for Foundry and Cast-House, CIATF (1984).

|Saito59| **Saito**, T., **Kawai**, Y., **Maruya**, K., **Maki**, M.: Diffusion of Some Alloying Elements in Liquid Iron, Tech. Rep. 112, The Research Institute of Mineral Dressing and Metallurgy (1959).

|Samoilovich83| **Samoilovich**, Y. A., **Yasnitzkii**, **Kabakov**, Z. K.: Mathematical simulation of thermogravitational convection in solidification of liquid steel. *Journal of Engineering Physics and Thermophysics* (1983) vol. 44 (3), pp. 326–333, translated from Inzhenerno-Fizicheskii Zhurnal, Vol. 44, No. 3, pp. 465-473, March, 1983.

|Sanyal05| **Sanyal**, D., **Ramachandra Rao**, P., **Gupta**, O. P.: Modelling of free boundary problems for phase change with diffuse interfaces. *Mathematical Problems in Engineering* (2005) vol. 2005 (3), pp. 309–324.

|Scheil42| **Scheil**, E.: Bemerkungen zur Schichtkrstallbildung. *Zeitschrift für Metallkunde* (1942) vol. 34, pp. 70–72.

|Schneider95a| **Schneider**, M. C.: Modeling the Solidification of Multicomponent Alloys with Convection, Ph.D. thesis, The University of Iowa (1995).

|Schneider95b| **Schneider**, M. C., **Beckermann**, C.: Formation of Macrosegregation by Multicomponent Thermosolutal Convection During the Solidification of Steel. *Metallurgical and Materials Transactions A* (1995) vol. 26 A, pp. 2373–2388.

|Schneider95c| **Schneider**, M. C., **Beckermann**, C.: A Numerical Study of the Combined Effects of Microsegregation, Mushy Zone Permeability and Flow, Caused by Volume Contraction and Thermosolutal Convection, on Macrosegregation and Eutectic Formation in Binary Alloy Solidification. *International Journal of Heat and Mass Transfer* (1995) vol. 38, pp. 3455–3473.

|SIN05| SINTEF ICT, Applied Mathematics: SISL The SINTEF Spline Library Version 4.4 Reference Manual (2005), available from `http://www.sintef.no/sisl`.

|SIN06| SINTEF ICT, Applied Mathematics: SISL The SINTEF Spline Library Version 4.4 User's Guide (2006), available from `http://www.sintef.no/sisl`.

|Sopousek94| **Sopousek**, J., **Vrestal**, J.: Phase Equilibria in the Fe-Cr-Ni and Fe-Cr-C Systems. *Z. Metallkd.* (1994) vol. 85, pp. 111–115.

|Steinberg89| **Steinberg**, A. S.: A report from the alloys world, Nauka, Moscow (1989), in Russian, "Reportazh iz mira splavov".

|Sundman85| **Sundman**, B., **Jansson**, B., **Andersson**, J. O.: The Thermo-Calc Databank System. *Calphad* (1985) vol. 9, pp. 153–190.

[Tanzer08] **Tanzer**, R., **Schützenhöfer**, W., **Reiter**, G., **Fauland**, H.-P., **Könözsy**, L., **Ishmurzin**, A., **Wu**, M., **Ludwig**, A.: Validation of a Multiphase Model for the Macrosegregations and Primary Structure of High Grade Steel Ingots. *Metallurgical and Materials Transactions B* (2008) vol. 40 (3), pp. 305–311.

[The06a] Thermo-Calc Software AB, Stockholm Technology Park, Björnnäsvägen 21 SE-113 47 Stockholm, Sweden: TCC Thermo-Calc Software User's Guide Version R (2006), copyright (c) 1995-2006 Foundation of Computational Thermodynamics, Stockholm, Sweden.

[The06b] Thermo-Calc Software AB, Stockholm Technology Park, Björnnäsvägen 21 SE-113 47 Stockholm, Sweden: Thermodynamic Calculation Interface TC-API Version 4.0 Programmer's Guide and Examples (2006), copyright (c) 1995-2006 Foundation of Computational Thermodynamics, Stockholm, Sweden.

[Thomas90] **Thomas**, B. G., **Mika**, L., **Najjar**, F.: Simulation of Fluid Flow inside a Continuous Slab-Casting Machine. *Metallurgical and Materials Transactions B* (1990) vol. 21B, pp. 387–400.

[Thomas94] **Thomas**, B. G., **Huang**, X., **Sussman**, R. C.: Simulation of argon gas flow effects in a continuous slab caster. *Metallurgical and Materials Transactions B: Process Metallurgy and Materials Processing Science* (1994) vol. 25B (4), pp. 527–547.

[Thomas01] **Thomas**, B. G., **Zhang**, L.: Mathematical modeling of fluid flow in continuous casting. *ISIJ International* (2001) vol. 41, No. 10, pp. 1181–1193.

[Thuinet04] **Thuinet**, L., **Combeau**, H.: Prediction of macrosegregation during the solidification involving a peritectic

transformation for multicomponent steels. *Journal of Materials Science* (2004) vol. 39, pp. 7213–7219.

|Thuinet06| **Thuinet**, L., **Lee**, P. D.: CAFD model for solidification of multicomponent and multiphase alloys, in Modeling of Casting, Welding and Advanced Solidification Processes - XI 1, pp. 457–464.

|Trovant00| **Trovant**, M., **Argyropoulos**: Finding Boundary Conditions: A Coupling Strategy for the Modeling of Metal Casting Process: Part I. Experimental Study and Correlation Development. *Metallurgical and Materials Transactions B* (2000) vol. 31B, pp. 75–86.

|Turkeli06| **Turkeli**, A., **Kirkwood**, D. H.: Back diffusion of manganese during solidification of carbon steels. *Materials Science Forum 508* (2006) , pp. 443–448.

|VandenBoomgaard72| **Van den Boomgaard**, J., **Wolff**, L. R.: Growth and Properties of the Monovariant (Fe,Cr)-(Cr,Fe)7C3 Eutectic System. *Journal of Crystal Growth* (1972) vol. 15, pp. 11–19.

|Vasquez00| **Vasquez**, S. A., **Ivanov**, V. A.: A Phase Coupled Method for Solving Multiphase Problems on Unstructured Meshes, in ASME FEDSM'00: ASME 2000 Fluids Engineering Division Summer Meeting.

|Voller87a| **Voller**, V. R., **Brent**, A. D., **Reid**, K. J.: Computational modeling framework for analysis of metallurgical solidification processes and pheonomena, Tech. rep., Conference for Solidification Processing, Ranmoor House, Sheffield, UK (1987).

|Voller87b| **Voller**, V. R., **Prakash**, C.: A fixed grid numerical modelling methodology for convection-diffusion mushy region phase-change problems. *Int. J. Heat and Mass Transfer* (1987) vol. 30 (8), pp. 1709–1719.

|Voller91| **Voller**, V. R., **Swaminathan**, C. R.: General source-based method for solidification phase change. *Numerical Heat Transfer, Part B* (1991) vol. 19, pp. 175–189.

|Vreeman00a| **Vreeman**, C. J., **Incropera**, F. P.: The effect of free-floating dendrites and convection on macrosegregation in direct chill cast aluminum alloys Part II: Predictions for Al-Cu and Al-Mg alloys. *International Journal of Heat and Mass Transfer* (2000) vol. 43 (5), pp. 687–704.

|Vreeman00b| **Vreeman**, C. J., **Krane**, M. J. M., **Incropera**, F. P.: The effect of free-floating dendrites and convection on macrosegragation in direct chill cast aluminum alloys Part I: Model development. *International Journal of Heat and Mass Transfer* (2000) vol. 43 (5), pp. 677–686.

|Wang03| **Wang**, Y., **Sridhar**, S.: *Ironmaking and Steelmaking* (2003) vol. 30, p. 223.

|Weiss99| **Weiss**, J. M., **Maruszewski**, J. P., **Smith**, W. A.: Implicit Solution of Preconditioned Navier-Stokes Equations Using Algebraic Multigrid. *AIAA Journal* (1999) vol. 37 (1), pp. 29–36.

|Westgren28| **Westgren**, A., **Phragmén**, G., **Negresco**, T.: On the Structure of the Iron-Chromium-Carbon System. *J. Iron Steel Inst.* (1928) vol. 117, pp. 383–406.

|White58| **White**, W. B., **Johnson**, S. M., **Dantzig**, G. B.: Chemical Equilibrium in Complex Mixtures. *J. Chem. Phys.* (1958) vol. 28, pp. 751–755.

|Wu03| **Wu**, M., **Ludwig**, A., **Bührig-Polaczek**, A., **Fehlbier**, M., **Sahm**, P. R.: Influence of Convection and Grain Movement on Globular Equiaxed Solidification. *International Journal of Heat and Mass Transfer* (2003) vol. 46, pp. 2819–2832.

[Wu06] **Wu**, M., **Ludwig**, A.: A Three-Phase Model for mixed Columnar-Equiaxed Solidification. *Metallurgical and Materials Transactions A: Physical Metallurgy and Materials Science* (2006) vol. 37 (5), pp. 1613–1631.

[Wu07] **Wu**, M., **Ludwig**, A.: Using a Three-Phase Deterministic Model for the Columnar-to-Equiaxed Transition. *Metallurgical and Materials Transactions A: Physical Metallurgy and Materials Science* (2007) vol. 38 A (7), pp. 1465–1475.

[Yu02] **Yu**, K.-O. (ed.): Modeling for Casting and Solidification Processing, Marcel Dekker, Inc. (2002).

[Yuan05] **Yuan**, Q., **Thomas**, B. G.: Transport and Entrapment of Particles in Continuous Casting of Steel, in 3rd Int. Cong. Sci. and Tech. Steelmaking Conf. Proceedings, AISTech, Warrendale, PA, pp. 745–762.

[Yuji99] **Yuji**, M., **Thomas**, B. G.: Modeling of inclusion removal in a tundish. *Metallurgical and Materials Transactions* (1999) vol. 30B, pp. 639–654.

[Zhang00] **Zhang**, L., **Taniguchi**, S., **Cai**, K.: Fluid flow and inclusion removal in continous casting tundish. *Metallurgical and Materials Transactions* (2000) vol. 31B, pp. 253–266.